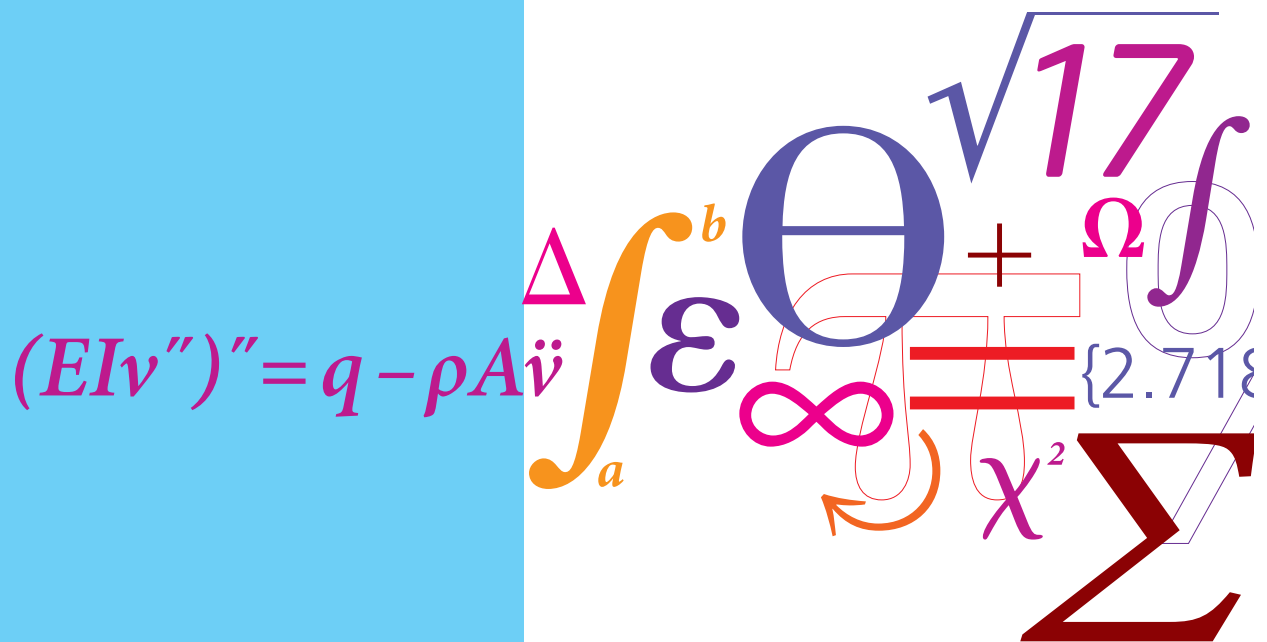


Accurate dimensional measurements in production environment using Dynamic Length Metrology

PhD Thesis



Giuseppe Dalla Costa
September 2017

Accurate dimensional measurements in production environment using Dynamic Length Metrology

by
Giuseppe Dalla Costa

Department of Mechanical Engineering
Technical University of Denmark
September 2017

“As for the future, your task is not to foresee it, but to enable it.”

Antoine de Saint-Exupéry

*“One does not work better under pressure,
One works exclusively under pressure.”*

Abstract

The work described in this thesis concerns accurate dimensional measurements performed in a production environment with particular focus on injection moulded polymer parts. The work has encompassed the development of probing solutions to be implemented with the new method of Dynamic Length Metrology (DLM) introduced by DTU Mechanical Engineering.

A state of the art review on the topic of accurate dimensional measurement outside a temperature and humidity controlled metrology laboratory (directly in production environment) has been carried out, with particular focus on traceability and measurement uncertainty of length measurement technologies and temperature sensors.

Experimental investigations on non-conventional probing systems have been performed with focus on assessing the uncertainty in DLM applications. The uncertainty contribution of the probing force of contact measurements is studied in devices with passive and active force application system. A cutting-edge interferometric system with wide absolute measurement range is investigated as an alternative to contact devices. Infrared thermography is studied as a valid non-contact system for measuring non-uniform temperature fields; measurements from a thermal imager are compared with reference measurements performed using a RTD contact sensor.

Methods for the concurrent acquisition of data for dimensions, temperature, forces, humidity, etc. over time, dynamically, have been investigated, and probing solutions developed. Probing solutions involve both the measurement operation as well as the data analysis. An innovative solution for elastic deformation compensation is proposed using a measuring device with active force control. The effect of temperature is investigated on polymer parts replicating the thermal conditions after injection moulding. The compensation of thermal effects is implemented through the definition of an apparent coefficient of thermal expansion from the analysis of length and temperature information. A study on the optimal measuring time, regarding starting time and measurement period, is performed. A highly non-uniform temperature field on the workpiece allows the study of the influence of the sensor location on the measurement results. The investigations on hygroscopic swelling involve study on polymer parts in saturated conditions to verify the relationship between moisture absorption, dimensional expansion and ambient relative hu-

midity. Subsequently the focus is moved on the transient state typical of the post-production period of injection moulded parts. A strategy for compensation of hygroscopic swelling is then proposed.

An optical solution using a vision system with integrated 2d reference grid has been proposed to provide fast and traceable length measurement. The integration of the reference artefact in the measuring system provides direct traceability with uncertainties ideally independent from the measured dimension. The methodology involves image processing with edge detection routines which have been studied and optimized using an artefact with ideal edges. The solution is then validated on an industrial polymer part.

A novel method based on digital image correlation (DIC) has been proposed for producing transient displacement data. The influence on the accuracy of different computational choices and of the surface appearance of the measured workpiece has been assessed using a industrial ABS part. The benefits of the method applied to DLM measurements have been verified.

Finally an industrial POM part produced by injection moulding has been investigated in an industrial environment using the DLM method. Dimensional instabilities due to temperature, moisture absorption and residual stresses are analysed in a preliminary study. A set of probing strategies to consider the abovementioned factors has been developed and validated with a comparison between DLM prediction and reference measurements carried out under controlled conditions in a metrology laboratory.

Resume

Arbejdet beskrevet i denne afhandling vedrører højpræcision dimensionsmålinger udført i et produktionsmiljø med særlig fokus på sprøjtestøbte polymerdele. Arbejdet har omfattet udviklingen af en metode til taktil opmåling, der skal implementeres med den nye metode ”Dynamic Length Metrology” (DLM), der introduceres af DTU Mekanik.

En gennemgang af nyeste teknologi vedrørende højpræcision dimensionsmålinger uden et temperatur- og fugtighedskontrolleret metrologi laboratorium (direkte i produktionsmiljø) er blevet udført, med særlig fokus på sporbarhed og måleusikkerhed af længde opmåling og temperaturfølere.

Eksperimentelle undersøgelser af ikke-konventionelle taktile måle metoder er blevet udført med fokus på at vurdere usikkerheden i DLM applikationer. Usikkerhedsbidraget fra kontaktkraften ved taktil opmåling studeres i systemer med passiv og aktiv kraftpåvirkning. Et banebrydende interferometrisk system med bredt absolut måleområde undersøges som et alternativ til taktil opmåling. Infrarød termografi studeres som et gyldigt ikke-kontakt system til måling af ikke-ensartede temperaturfelter; målinger fra et termisk billede sammenlignes med referencemålinger udført ved hjælp af en RTD kontaktføler.

Metoder til dynamisk indsamling af data omkring dimensioner, temperatur, kræfter, fugtighed osv. er blevet undersøgt, og den taktile måleteknik er blevet udviklet. Taktile måleteknikker involverer både selve måleoperationen såvel som dataanalysen. En innovativ løsning til elastisk deformationskompensation er foreslået ved hjælp af en måleanordning med aktiv kraftstyring. Temperatureffekten på polymerdele undersøges, ved at de termiske tilstande efter sprøjtestøbning efterlignes. Kompensationen for den termiske virkning gennemføres ved at definere en tilsyneladende termisk ekspansionskoefficient fra analysen af længde- og temperaturinformation. En undersøgelse af den optimale måle-tid vedrørende starttid og måleperiode udføres. Et meget uensartet temperaturfelt på emnet gør det muligt at undersøge hvordan placeringen af sensoren influerer måleresultatet. Undersøgelserne vedrørende hygroskopisk hævelse indebærer undersøgelse af polymerdele i mættede forhold for at verificere forholdet mellem fugtabsorption, dimensional ekspansion og ambient relative luftfugtighed. Derefter flyttes fokus til den transiente tilstand, der er typisk for postproduktionsperioden af sprøjtestøbte emner. Der foreslås derfor en strategi for kompensation for hygroskopisk hævelse.

En optisk løsning, der anvender et visionssystem med integreret 2d-referencegitter, er blevet foreslået for at tilvejebringe hurtig og sporbar længdemåling. Integrationen af referencegenstanden i målesystemet giver direkte sporbarhed med usikkerheder, der er ideelt uafhængige af den målte dimension. Metoden indebærer billedbehandling med kantdetekteringsrutiner, som er blevet undersøgt og optimeret ved hjælp af en artefakt med ideelle kanter. Den optiske løsning er herefter valideret på et industriel polymeremne.

En ny metode baseret på ”Digital Image Correlation” (DIC) er blevet foreslået til fremstilling af transient forskydningsdata. Indflydelsen på nøjagtigheden af forskellige beregningsmæssige valg og overfladen af det målte emne er blevet vurderet ved anvendelse af et industrielt ABS-emne. Fordelene ved metoden anvendt til DLM målinger er blevet verificeret.

Endelig er et industrielt POM-emne fremstillet ved sprøjtestøbning blevet undersøgt i et industrielt miljø ved anvendelse af DLM-metoden. Dimensionelle ustabiliteter på grund af temperatur, fugtabsorption og restspændinger analyseres i en indledende undersøgelse. Et sæt taktile opmålings strategier er blevet udviklet med henblik på førnævnte faktorer og valideret med en sammenligning mellem DLM-forudsigelse og referencemålinger udført under kontrollerede betingelser i et metrologi laboratorium.

Preface

This thesis was prepared as one of the requirement for the fulfilment of the Ph.D. degree in mechanical engineering. The work was carried out at the Department of Mechanical Engineering at the Technical University of Denmark (DTU) in the period from September 2014 to September 2017 under the supervision of Prof. Leonardo De Chiffre, Prof. Hans Nørgaard Hansen and Dr. Daniel Gonzalez Madruga, in collaboration with the Danish company Metrologic ApS.

The work was financially supported for 2/3 by Innovation Fund Denmark, through the project “Accurate Manufacture” and for 1/3 by DTU Mechanical Engineering.

Kgs. Lyngby, October 2017

Giuseppe Dalla Costa

Acknowledgements

The financial supports of DTU-MEK, Innovation Fund Denmark and Otto Mønsted Fund are gratefully appreciated.

I would like to express my gratitude to my supervisors for giving me the opportunity to fulfil the PhD studies at DTU and for the support and guidance during these three years. In particular I would like to thank Prof. Leonardo De Chiffre for the constant motivational support, unlimited patience and great contribution on my work. My gratitude goes also to Dr. Daniel Gonzalez Madruga for his helpful and highly valuable collaboration and discussions. I would like to thank also Prof. Hans Nørgaard Hansen for the guidance and insightful inspiration.

Great thanks Mr. Ali Mohammadi, Dr. Mads Rostgaard Sonne and Prof. Jesper Henri Hattel for the fruitful and pleasant collaboration in the development of analytical and numerical modelling.

I want to thank the partner company Metrologic ApS, in particular Mr. Jørgen and Christian Meinertz, for the fruitful collaboration and for providing the equipment and software necessary for the experimental work in the project. Thanks to Dr. Angela Cantatore, Mr Masoud Meftahpour and Dr. Kamran Mohaghegh for the pleasant collaboration.

I want to thank the staff of Lego A/S, Dr. Stefania Gasparin and Mr. Luis Monteiro Neves, for the pleasant collaboration and for providing material and experience to the project.

I would like to thank Prof. Giulio Barbato and Dr. Gianfranco Genta, from Politecnico di Torino, for the fruitful collaboration and discussion over the topic of statistical analysis and uncertainty evaluation, in particular in calibration procedures.

I want to thank the team of DMS Metrology at Novo Nordisk A/S for giving me the opportunity to perform field experiments in their facilities.

My gratitude goes also to all the staff of DTU which I had the pleasure to collaborate with. In particular I would like to thank Mr. Rene Sobiecki for the wise guidance and expert assistance in the numerous metrological issues encountered during the project.

Thanks to M.Sc. Ida Jespersen, M.Sc. Aikaterini Alexiou and M.Sc. Alberto Santaniello for their contribution in the experimental work during their M.Sc. projects.

Finally I would like to thanks all my colleagues (and friends) for their support, the many hours of brainstorming and sharing of ideas and for the enjoyable work environment.

Table of contents

Abstract.....	i
Resume.....	iii
Preface	v
Acknowledgements.....	vii
Table of contents.....	ix
List of figures.....	xiii
List of tables.....	xix
List of abbreviations	xxi
List of symbols.....	xxiii
1 Introduction and objectives.....	1
1.1 Industrial needs and background.....	1
1.2 Dynamic Length Metrology.....	4
1.3 The Accurate Manufacture project.....	6
1.4 Task identification.....	7
1.5 Thesis outline	8
2 State of the art of accurate measurements in production environment	11
2.1 Influence factors in dimensional metrology.....	11
2.1.1 Reference conditions.....	13
2.1.2 Temperature	14
2.1.3 Humidity	14
2.1.4 Stresses.....	16
2.2 Contact sensors for dimensional measurements	19

2.2.1	1-D contact devices	20
2.2.2	CMMs, probes and stylus	23
2.3	Optical sensors for dimensional measurements	24
2.3.1	Intensity based sensors	26
2.3.2	Interferometric systems	27
2.3.3	Triangulation systems	32
2.3.4	Applicability to DLM.....	43
2.4	Reference artefacts	45
2.5	Metrology frame and structure	46
2.6	Temperature sensors.....	47
2.6.1	Contact sensors.....	48
2.6.2	Infrared sensors	52
2.7	Conclusion.....	55
3	Experimental investigation on probing systems for DLM	59
3.1	A measuring device with active force control.....	59
3.1.1	Measuring process.....	60
3.1.2	A priori uncertainty evaluation.....	63
3.1.3	A posteriori uncertainty evaluation	67
3.2	Multi-wavelength interferometer	69
3.2.1	Procedure description.....	69
3.2.2	Data analysis	70
3.2.3	Uncertainty budget and discussion.....	72
3.3	Infrared temperature sensors	74
3.3.1	Accuracy of temperature measurement.....	74
3.3.2	Temperature field on polymeric parts	77
3.3.3	Conclusions on thermal camera	79
3.4	Conclusion.....	79
4	Probing strategies for DLM.....	81
4.1	The need for novel probing strategies	81
4.2	Effect of forces	85
4.3	The influence of temperature	88
4.3.1	Calculation of apparent CTE.....	88
4.3.2	The influence of the measurement time	90
4.3.3	Non-uniform temperature field with contact sensors and simulations ..	94
4.3.4	Discussion	99
4.4	Influence of humidity	99
4.4.1	Hygroscopy and swelling	100

4.4.2	Transitory period.....	106
4.4.3	A proposed method for considering humidity uptake.....	111
4.5	Conclusions.....	112
5	Optical solution for DLM using a vision system and digital image correlation	115
5.1	Optical solution for profile measurements.....	115
5.1.1	Method	115
5.1.2	Edge detection algorithm	118
5.1.3	Investigation set up	121
5.1.4	Camera calibration	121
5.1.5	Measurement strategy	126
5.1.6	A preliminary investigation on a calibrated scale	127
5.1.7	Measurements of polymer parts.....	130
5.2	Optical solution for displacement measurements	130
5.2.1	Motivation.....	130
5.2.2	Digital Image Correlation	131
5.2.3	Algorithm development	132
5.2.4	Experimental setup.....	133
5.2.5	Performance assessment	134
5.2.6	Applicability to DLM.....	139
5.3	Conclusion	142
6	Industrial case	145
6.1	Introduction.....	145
6.2	Experimental work.....	146
6.3	Data analysis	152
6.3.1	The effect of probing force	152
6.3.2	The effect of temperature.....	153
6.3.3	The effect of moisture uptake	155
6.3.4	The effect of residual stresses	158
6.4	Validation.....	159
6.5	Conclusion	163
7	Summary and conclusions	165
7.1	Summary	165
7.2	Conclusions.....	172
7.3	Outlook	174
	Bibliography	177

List of publications.....	187
Appendix A: Matlab codes.....	189
Appendix B: Instruments	215

List of figures

Figure 1.1 Central role of metrology in modern manufacturing [2].	2
Figure 1.2 Dimensional metrology can be performed with: a) hand tools ;b) fixtures with gauges [6]; c) CMM.	4
Figure 1.3 Main elements composing a DLM system: metrology frame and calibrated workpiece ensure traceability.	5
Figure 1.4 Dynamic Length Metrology: the length at reference condition L_0 is estimated from measured quantities L in production through the identification of different influence contributors dL_i .	6
Figure 1.5 The Accurate Manufacture project. Four working areas are identified in the development of a Dynamic Length Metrology solution.	7
Figure 2.1 Influence factors in dimensional metrology according to ISO 14253-2 [10].	12
Figure 2.2 Dimensional behaviour of a generic object under transient state.	13
Figure 2.3 Three elements model of a viscoelastic material: a) schematic representation; b) mechanical behaviour under constant load.	18
Figure 2.4 Electronic inductive probes: LVDT working principle [24], common inductive probe [26]; radial miniaturized probe [27].	21
Figure 2.5 Length measurement with encoders: a) length gauges [29]; b) linear actuator.	22
Figure 2.6 Error sources of CMM measurements [37].	24
Figure 2.7 Summary of optical metrology techniques, according to different working principle (modified from [40]).	25
Figure 2.8 Bundle layout of optical fibres in intensity based sensors [41]	26
Figure 2.9 Typical response to displacement variation of intensity based sensors [41].	27
Figure 2.10 Schematic representation of a Michelson interferometer [44].	29
Figure 2.11 Lumphos smart probe [50].	30
Figure 2.12 Gauge block calibration: a) NPL interferometer layout; b)Fringe counting method [16].	31
Figure 2.13 Conoscopic holography working principle [38]	32
Figure 2.14 Laser triangulation sensors: a) point sensor [38], b) line sensor [74].	34
Figure 2.15 3D optical metrology: laser scanner [61] and structured light scanner [62].	35
Figure 2.16 Working principle of chromatic confocal sensors [78].	36
Figure 2.17 Artefacts used for camera calibration: a) grid [72], b) dot matrix [88], c) 3d artefact [70].	38

Figure 2.18 Photogrammetry scanners using a DSLR camera and a) translation movements [91] b) rotation movements [63].	39
Figure 2.19 Experimental set up for DIC [67].	40
Figure 2.20 Optical CMMs: a) multisensory CMM [98]; b) laser scanner probe [33]; c) opto-tactile fibre probe [39]; d) multisensory CMM application [99].	42
Figure 2.21. Structure of a roundness tester. The metrology loop is highlighted with a red dashed line [104].	46
Figure 2.22 Temperature profiles during dynamic temperature measurement: T_B =object temperature, T_1 =measured temperature [117].	49
Figure 2.23 Thermistors (NTC,PTC) response compared to RTDs [117].	50
Figure 2.24 Thermocouples: a) basic measuring circuit; b) type of junctions [120].	51
Figure 2.25 Infrared temperature measurement: radiation model [124].	55
Figure 3.1 The measuring setup for actuator calibration (e.c. = encoder counts, d_{block} = dimension of gauge block).	61
Figure 3.2 Box-plots of residuals $R_{corr,F}$ vs. measuring length.	68
Figure 3.3 Box-plots of residuals $R_{corr,FL}$ vs. measuring length (a) and measuring force (b).	68
Figure 3.4 Normal probability plot for residuals $R_{corr,FL}$.	69
Figure 3.5 Step gauge measurement with a MWLI system.	70
Figure 3.6 Levelling of main orientation of MWLI measurement.	71
Figure 3.7 Data processing: definition of measuring point on the step gauge.	71
Figure 3.8 Comparison of measurement results with reference lengths for SG1 before (a) and after (b) compensation of systematic linear trend (error bars represent the expanded uncertainty).	73
Figure 3.9 Comparison of measurement results with reference lengths for SG2 (error bars represent the expanded uncertainty).	73
Figure 3.10 Experimental set up for infrared temperature measurements: a) thermal camera position; b) heating plate with targets.	74
Figure 3.11 Measured temperatures on heating plate: a) with thermocamera, area 1=metallic surface, area 2=black matt label, area 3= contact sensor RTD 1, area 4= contact sensor RTD 2; b) with contact sensors.	76
Figure 3.12 Difference between infrared and contact temperature measurements of the heating plate: ΔT_1 refers to RTD 1 while ΔT_2 to RTD 2.	76
Figure 3.13 Infrared temperature measurements: temperature profiles in three locations for three different orientations of an ABS workpiece during cooling.	77
Figure 3.14 Infrared temperature measurements: temperature fields of an ABS workpiece during cooling positioned at different orientations.	78
Figure 4.1 Schematic DLM measuring system showing the main elements of the method.	82
Figure 4.2 DLM method: from dimensional measurements to length prediction.	82
Figure 4.3 Comparison between conventional and apparent coefficient of thermal expansion. Conventional CTE is calculated from measurements of a standardized specimen under stationary condition. Apparent CTE is defined for a specific part of any shape and for specific measurement procedure in transitory condition.	83

Figure 4.4 The DLM measuring strategy is defined by three main elements mutually connected.	85
Figure 4.5 Experimental setup for length measurements at variable contact force.	86
Figure 4.6 Elastic deformation due to probing force: a) absolute values; b) residual from linear trend. Blue points correspond to the experimental data while the continuous line to the fitting curves uses different models.	87
Figure 4.7 Creep effect for a prolonged measurement contact.	87
Figure 4.8 Definitions of the coefficient of thermal expansion: a) mean value; b) instantaneous value.	89
Figure 4.9 Considerations of DLM measurement during cooling of a mono dimensional beam.	90
Figure 4.10 Heating device: the adjustable temperature is achieved with a closed loop temperature control.	91
Figure 4.11 Experimental set up for investigation on influence of measuring time on DLM results.	91
Figure 4.12 Measurements of cooling of an ABS workpiece: a) length and temperature variation vs time; b) length variations vs temperature.	92
Figure 4.13 Set-up for multipoint temperature measurements on a ABS workpiece: L_i = inductive probes, T_i = thermocouples.	95
Figure 4.14 Sum of square of residuals of the regression of cooling curve.	97
Figure 4.15 Temperature fields estimated from numerical model after 30 s (a) and 600 s (b) after the beginning of the measurement.	98
Figure 4.16 Apparent CTEs estimated with analytical and numerical tools.	98
Figure 4.17 Experimental set-up for moisture uptake and moisture expansion measurements.	101
Figure 4.18 Fixture for simultaneous length measurements of 8 parts.	101
Figure 4.19 Test 1 on hygroscopy: relative length (dL) and water content (dW) variations for 8 parts. The values are zeroed at the 50 % relative humidity condition.	102
Figure 4.20 Test 1 on hygroscopy: relative length dL vs relative ambient humidity RH (a) and relative water content dW (b). The dashed line represents the linear regression of the data.	103
Figure 4.21 Test 2 on hygroscopy: relative length dL vs relative ambient humidity RH (a) and relative water content dW (b). The dashed line represents the linear regression of the data.	104
Figure 4.22 Merged data sets of length variations at different ambient humidity. The continuous and dashed line represent the regression line performed with data sets of test 1 and test 2 respectively.	105
Figure 4.23 Linear (continuous black line) and quadratic (dashed red line) regression of the merged data set of two tests on hygroscopy.	105
Figure 4.24 Calculated apparent CMEs for two separated tests and for the merged data set considering: a) relative humidity RH ; b) relative water content dW . The error bars represent the estimated expanded uncertainties.	106
Figure 4.25 Equipment for moisture absorption measurements: a) sealed bags with desiccant; b) electronic scale; c) length measurement fixture.	106

Figure 4.26 Experimental results on moisture uptake: a) weight variation dW vs time t ; b) length variation dL vs time t ; c) length variation dL vs weight variation dW ; d) length variation dL vs temperature T	107
Figure 4.27 Weight variation due to moisture uptake (continuous line represents the exponential regression model): a) three batches measured after production; b) batch from production compared with a dried aged batch.....	109
Figure 4.28 Parameters of the exponential regression models of moisture absorption: comparison between principal measured samples and dummy parts.	111
Figure 5.1 Methodology for directly traceable profiles measurements with a vision system.....	116
Figure 5.2 Gradient based edge detection: position of the edge (a) corresponds to the maximum of the first derivative (b) and to the zero crossing of the second derivative (c) [149].	119
Figure 5.3 Horizontal (a) and vertical (b) Sobel convolution masks.....	119
Figure 5.4 Edge detection algorithm: a) searching window selection; b) Sobel edge enhancement; c) column analysis, regression of maximum neighbourhood for subpixel detection; d) linear fitting of calculated data point.....	120
Figure 5.5 Bilateral telecentric lenses model [152].	122
Figure 5.6 Reference chessboard: a) calibration artefact; b) 6 locations used for pixel size estimation, indicated with coloured lines (appearance of the chessboard after Sobel filter application).....	124
Figure 5.7 Detection of control points on the picture of the chessboard after Sobel filter.	124
Figure 5.8 Pixel size calculated with pixel size estimation (a) and with the formal calibration (b). The error bars represent the expanded uncertainty.....	125
Figure 5.9 Difference coordinate systems defined for a two points length measurement of the optical method under development: (x_{im}, y_{im}) = image coordinate systems, (x_{rel}, y_{rel}) = relative reference systems, (x_{abs}, y_{abs}) = absolute reference system, l, r =left or right picture.	127
Figure 5.10 Example of measuring strategy of the optical method under development: red continuous line= detected edges, blue dots= measuring points.....	127
Figure 5.11 Influence of the regression model on performance of the optical method. .	128
Figure 5.12 Influence of the regression DOF on measurement performance of the optical method.....	129
Figure 5.13 Influence of the subpixel resolution on measurement performance of the optical method.....	129
Figure 5.14 Experimental set-up for DIC experimental test campaign.	134
Figure 5.15 Average calculation times for a DIC algorithm: a) pure cross-correlation; b) regression of correlation function with Gaussian model; c) regression of correlation function with polynomial model.	135
Figure 5.16 Surfaces used during DIC performance assessment of a DIC algorithm. ...	135
Figure 5.17 Comparison between average displacement ΔL and reference displacement ΔL_{ref} as function of subset size (s_{31} ÷ s_{121}): a) surface A Gaussian regression; b) surface	

A polynomial regression; a) surface B Gaussian regression; d) surface B polynomial regression.	137
Figure 5.18 Residuals of the spatial linear regression of the displacements as function of subset size ($s_{31} \div s_{121}$): a) surface A Gaussian regression; b) surface A polynomial regression; a) surface B Gaussian regression; d) surface B polynomial regression.	137
Figure 5.19 Expanded uncertainty of displacement measurement with the developed DIC method.	138
Figure 5.20 Experimental layout for a DLM application of the DIC method.	139
Figure 5.21 Displacement distribution of a linear thermal expansion model.	140
Figure 5.22 Differential thermal expansions: the vertical red lines represent the workpiece edge progression during cooling.	141
Figure 6.1 The POM component selected as industrial case.	145
Figure 6.2 Measuring setup of the industrial case: a) station for length (and temperature) measurements; b) scale for weight measurements.	147
Figure 6.3 Station for length measurement: a) measurement on polymer tube; b) zeroing using reference gauge block.	147
Figure 6.4 Length measurement of the POM tube using the comparator method.	149
Figure 6.5 The “column type” metrology frame of the length measuring station. Thermal expansion is limited by the use of a combination of Invar and steel components.	150
Figure 6.6 Zeroing of measuring equipment using a gauge block: probe reading vs temperature.	151
Figure 6.7 Post moulding cooling of POM tube: a) length and temperature measurements over time; b) length variation vs temperature variation. The black continuous line delimits the dataset used in the data processing.	153
Figure 6.8 Calculated apparent CTE of 7 POM tubes. In the upper horizontal scale the production day is indicated. The error bar represents the expanded uncertainty.	154
Figure 6.9 Weight variation measured on: a) single parts; b) groups of dummy parts, the black dashed line correspond to the fitting model (equation 6.4). The different batches are indicated with progressive numbers.	155
Figure 6.10 Post moulding length and weight variation for 7 samples of POM tubes. A clear correlation is not visible.	156
Figure 6.11 Post moulding length variation (blue), weight variation (red) and ambient humidity (green) referred to the measurements on sample n. 1. A change in ambient humidity in the fifth day after moulding causes a change in dimensions and weight of the part.	157
Figure 6.12 Calculated apparent CME of 7 POM tubes. In the upper horizontal scale the production day is indicated. The error bars represent the expanded uncertainty.	157
Figure 6.13 Post moulding length measurement of POM tube: probe reading of tube n.1 (blue); after thermal expansion correction (red); after moisture expansion correction (green). The logarithmic fitting is represented by the dashed black line. The measurements after several weeks are also indicated.	158
Figure 6.14 Shrinkage during a week after production for 7 parts. The black dashed line corresponds to the logarithmic model fitting all the data points.	159

Figure 6.15 Predicted length $L_{20,Wref,t}$ for 4 workpieces compared to reference measured values $L_{20,Wref}(t)$. The error bars represent the expanded uncertainties according to table 6.4 and 6.5..... 163

List of tables

Table 1.1: Difference between shop floor and laboratory metrology.	3
Table 1.2: Main requirements in conventional metrology and Dynamic Length Metrology [8].	6
Table 2.1: CTE values for common materials used in metrology and engineering [15], [16], [17].	15
Table 2.2: Moisture absorption of some polymers measured according to ISO 62A [12], [17].	16
Table 2.3: Young modulus of common materials used in metrology and engineering [15], [17].	17
Table 2.4: Example of measurement systems based on measuring technique and dimensionality [2].	20
Table 2.5: MPE values of common manual instruments.	21
Table 2.6: Applicability of optical technologies to DLM.	44
Table 2.7: Types of thermocouples [118].	51
Table 3.1: Nominal characteristics of the actuator under calibration (from catalogue)...	60
Table 3.2: Estimated values of the independent variables of the actuator model.	64
Table 3.3: Estimated variability of the independent variables of the actuator model. The variability range is given for Type B evaluations, while the standard uncertainty is given for Type A evaluations.	65
Table 3.4: Uncertainty table for the length L (expressed in millimetres) measured with the actuator for a specific working condition.	66
Table 3.5: Systematic effects (deformation) due to measuring force.	67
Table 3.6: Uncertainty budget of step gauge measurement with MWLI according to [10].	72
Table 3.7: Thermal camera characteristics.	75
Table 4.1: Expanded uncertainty of the estimated reference lengths of the ABS workpiece using a DLM approach and following formula 4.2 (values in μm).	94
Table 4.2: Weights used in the averaging of the temperature measured in three location of the ABS workpiece.	96
Table 4.3: Estimated average CTEs for analytical and FEM models. Values in $\mu\text{m}/\text{mm}^\circ\text{C}$	98
Table 4.4: Coefficients of the non-linear regression of the post moulding moisture uptake. The uncertainty U is referred at 95 % level of confidence.	109

Table 5.1: Advantages and disadvantages of the proposed profile optical measurement solution.....	118
Table 5.2: Maximum value and root mean square value of image distortions calculated during the camera calibration (values in μm).....	126
Table 5.3: Standard deviation of optical measurements on two polymeric components.	130
Table 5.4: Subset sizes (in pixels) considered in the performance assessment of DIC algorithm.	136
Table 5.5: Apparent CTE calculated from contact displacement measurement (CTE_1) and DIC optical measurements using a global approach (CTE_2) and a local approach (CTE_2).	141
Table 6.1: Characteristics of the selected POM workpiece.....	146
Table 6.2: Generic properties of POM [17].....	146
Table 6.3: Uncertainty contributors for the predicted length at reference conditions of the POM tube.	150
Table 6.4: Uncertainty budget according to [10] for reference measurement $L_{20,Wref}(t_1)$ of POM tube n.8.	161
Table 6.5: Uncertainty budget according to [10] for estimated length measurement $L_{20,Wref,t1}$ of POM tube n.8.	162

List of abbreviations

<i>Abbreviation</i>	<i>Name</i>
ABS	acrylonitrile butadiene styrene
ACM	Accurate Manufacture project
AFM	atomic force microscope
CCD	charge-coupled device
CME	coefficient of moisture expansion
CMM	coordinate measuring machine
CMS	coordinate measuring system
CT	computer tomography
CTE	coefficient of thermal expansion
DIC	digital image correlation
DLM	dynamic length metrology
DOF	degrees of freedom
DSLR	digital single-lens reflex
DTU	Danish Technical University
FEM	finite element method
FOV	field of view
GPS	geometrical product specification
GRR	gauge repeatability and reproducibility
GUM	guide to the expression of uncertainty in measurement
HBT	half bridge transducers
HDPE	high-density polyethylene
ISO	International Organization for Standardization
LCD	liquid crystal display
LVDT	linear variable differential transducer
MPE	maximum permissible error
MWLI	multi wavelength interferometry
NETD	noise equivalent temperature difference
NPL	National Physical Laboratory
NTC	negative temperature coefficient
NUC	non-uniformity correction
PEEK	polyether ether ketone
PMMA	poly methyl methacrylate

<i>Abbreviation</i>	<i>Name</i>
POM	polyoxometalate
PP	polypropylene
PRT	platinum resistance thermometer
PTB	Physikalisch-Technische Bundesanstalt
PTC	positive temperature coefficient
PUMa	procedure for uncertainty management
PVC	polyvinyl chloride
RH	relative humidity
RMS	root mean square
RTD	resistance temperature detectors
SEM	scanning electron microscope
TMA	thermomechanical analysis

List of symbols

<i>Variable</i>	<i>Name</i>	<i>Unit</i>
A	area	mm^2
c	sensitivity coefficient	-
CME	coefficient of moisture expansion	ppm/% ppm/g
CTE	coefficient of thermal expansion	ppm/°C
δ	deformation/displacement	mm
df	degrees of freedom	-
E	elastic modulus	MPa
e	strain	ppm
ε	emissivity	-
er	encoder reading	-
F	force	N
k	coverage factor	-
L	length	mm
M	radiance	W/m^2
n	Poisson modulus	-
r	electrical resistance	Ω
R	residual of correlation	
ra	radius	mm
RH	relative humidity	%
σ	Stefan Boltzmann constant	$5.670367 \times 10^{-8} \text{ Wm}^{-2}\text{K}^{-4}$
t	time	s
T	temperature	°C
u	standard uncertainty	-
U	expanded uncertainty	-
V	volume	mm^3
W	weight	g

1

Introduction and objectives

1.1 Industrial needs and background

Modern manufacturing constantly faces new challenges to maintain competitiveness and to accommodate the market needs. In the case of mass production, manufacturing technologies must guarantee fast and high output volumes and at the same time limit the scrap rate to minimize costs.

Material traditionally used for precision components, such as steel and brass, have been replaced in many cases by dimensionally less stable materials such as polymers, both for functionality reasons, polymers are lighter than metals, and for manufacturing reasons, they are faster and cheaper to produce. Polymer parts are to a great degree produced by injection moulding. This process is characterized by low process variation and high production rates therefore it is very suitable for mass production of precision components. Examples of precision components made with injection moulding are medical devices, gears and pumps.

Geometrical tolerances are often reduced to ensure reliable final products. Consequently, measuring equipment used to assess product conformity must guarantee lower and lower measurement uncertainties in order to meet the general rule of thumb in metrology where the measuring uncertainty should be one tenth of the tolerance.

The role of metrology in the modern industrial context is crucial for maintaining high quality and reducing scrap rate. Metrology is a necessary tool for acquiring information and transferring knowledge at any step of the product life-cycle from the product development to the final production [1]. **Figure 1.1** illustrates the central role of metrology as the link between design, manufacture and function of a product [2].

Despite the established importance of metrology in manufacturing the benefits of the implementation of metrology in production are not easily noticeable. Benefits include improvement in the development of product and process, improvements of the production process with in line measurements and closed-loop control and improvement of the product functionality through a better characterization [3].

Nevertheless the costs related to metrological facilities are easily accounted causing companies to reconsider investments for metrology. Thus the reduction of metrology related costs is crucial both to limit the unitary costs of a single product and to ensure an adequate diffusion of metrology in the manufacturing field.

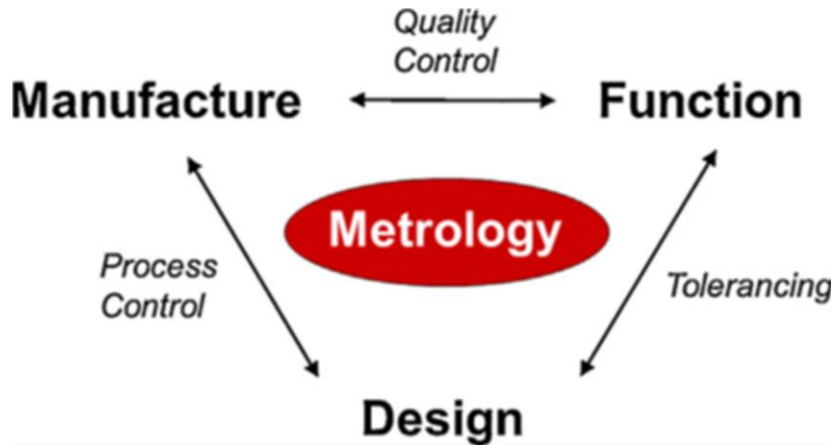


Figure 1.1 Central role of metrology in modern manufacturing [2].

Metrology dedicated to production can be divided into two main categories depending on the location of the measurement activity. The first category consists of production floor measurement performed on the premises of the production line. These types of measurements are typically fast and simple, such as a two point length or diameter, often performed with manual instruments (**Figure 1.2**). The main advantage of this category is that, in the instance of an out-of-tolerance production, the process can be quickly adjusted to restore conformity. On the other hand measurements performed in such conditions, i.e. non-controlled environment, presence of contaminants, untrained operator, lead to less accurate results. Whenever higher accuracies are required, for instance in the case of verification of tight tolerances, the measurements must be performed in a dedicated metrology facility. In this second category the part to be measured must be transferred to a controlled environment and stored for the time necessary to guarantee complete acclimatization, namely the state where the part reaches a uniform condition of equilibrium with the ambient. It is common practice to wait for one day (24 hours) before performing the measurement. Controlled environment facilities usually consist of metrology laboratories where temperature and often humidity are kept stable within narrow ranges. ISO standard 1[4] fixes the reference temperature at 20 °C and divides the metrology laboratory in classes according to the ambient temperature interval. Typically in industrial facilities the temperature is kept slightly higher than 20 °C and within an interval of $\pm 1-2$ °C for the comfort of the operators. Reference value for relative humidity is usually 50 % [5] and a typical variation interval is ± 15 %. Metrology laboratories are generally cleaner than the production floor limiting the effect of contaminants. Moreover, in metrology laboratories, only qualified operators perform the measurements reducing the contribution of the oper-

ator to the final measurement uncertainty **Figure 1.2 c**. Hence a metrology laboratory allows achieving more accurate measurement with the disadvantage of costs and overall measuring time, **Table 1.1**.

Table 1.1: Difference between shop floor and laboratory metrology.

<i>Measurement in production floor</i>	<i>Measurements in metrology laboratory</i>
Fast and simple measurements	Both simple and complex measurements
Fast response for process control	Need for acclimatization time
Untrained operator	Trained operator
Non controlled ambient conditions	Controlled conditions
Presence of contaminants	High level of cleanness

To accommodate the need of reducing metrology costs, dimensional and quality control is more and more assigned to production floor measurements. Besides, measurements in production provide outcomes in an immediate period of time after the production process allowing faster process control than measurements in dedicated metrology facilities. On the other hand production floor measurements face a higher uncertainty due to the environment conditions, which affect to a greater degree relatively less stable materials, such as polymers. As opposed to metals and ceramic materials, polymers have poor dimensional stability, particularly immediately after production, since they are highly affected by environmental conditions and are subjected to time dependent deformations attributable to residual conditions from the production process. They therefore require a further stabilization time to assimilate these time dependent post-production instabilities as well as an acclimatization time. All in all, moving dimensional and quality control means developing new measurement systems and methodology able to provide the necessary information to control the production within the given tolerances.

Speeding up the control validation of the production (avoiding stabilization and acclimatization time) also means measuring the parts in unstable state when they are still influenced by the production process conditions, e.g. for injection moulding: higher temperature than ambient, low moisture content, residual stresses. Measurements at this stage must also address these influence factors. Traditionally, measurements at non-standard conditions make use of systematic error compensation exploiting generic material properties from data sheets or material properties parameters obtained in additional specific tests, not directly performed on the produced parts.

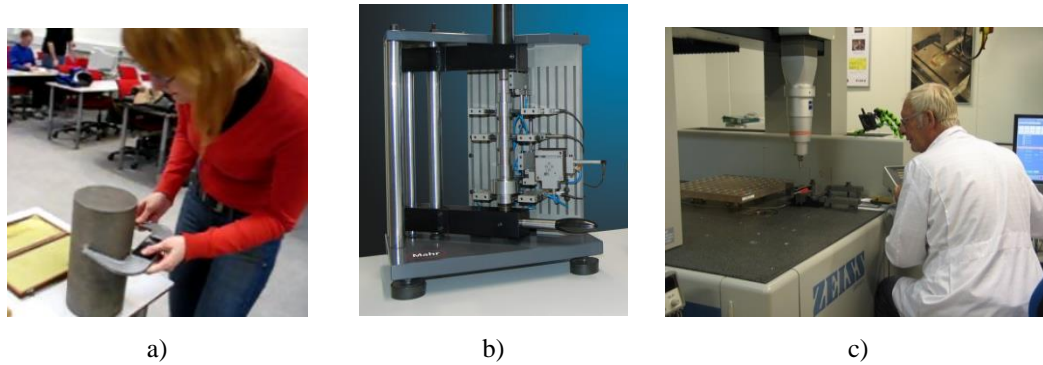


Figure 1.2 Dimensional metrology can be performed with: a) hand tools ;b) fixtures with gauges [6]; c) CMM.

The production control and validation is achieved by different technologies (contact or non-contact) and measurement set-ups. Coordinate Measuring Machines (CMMs) are among the most flexible measuring systems. CMM producers are developing measuring solutions specifically meant for shop floor application. These solutions exploit complex compensation of thermal effects and vibration insulation. Ad-hoc measurement systems are also used when a simple measurand is the production validation parameter. A dedicated fixture allows simplifying and speeding up the measurement process and at the same time keeping the uncertainty and the cost to a minimum.

A new trend in industry is to implement new technology for increase communications and data exchange (Industry 4.0). Similarly in dimensional metrology the research is focused on improving the result of a measurement by benefitting from information obtained with different technologies. This methodology, referred to as data fusion [7], can go from the combination of 2 different measurement systems e.g. contact and non-contact in order to get the precision of the contact method and the amount of data from non-contact method or the quantification of the dimensional behaviour of machines during the measurement process. Additional information on the influence parameters at an earlier stage of the measurement process would provide accurate information for the validation process. A new method, named Dynamic Length Metrology, for achieving a higher degree of information from a measurement is introduced below.

1.2 Dynamic Length Metrology

To address the industrial need for cost reduction and early-stage measurement a new measuring methodology called Dynamic Length Metrology (DLM) was conceived by DTU [8] [9]. The concept of a DLM measuring unit is depicted in **Figure 1.3**. In contrast to conventional metrology, DLM consists of dimensional measurements under non-constant conditions when the measuring workpiece is not yet stabilized and acclimatized.. Dimensions and all the quantities affecting them are measured concurrently and over time

(dynamically). In **Figure 1.3** the length of the workpiece is supposed to be affected by mechanical stresses (contact force), temperature and humidity (moisture uptake). Traceability of the measurement is established comparing the measurement of a workpiece to the measurement of a reference calibrated artefact. The use of a temperature invariant metrology frame and calibrated workpiece is a fundamental aspect of a DLM platform as it ensures traceable and accurate measurements even in non-constant and non-standard temperature states. The DLM measuring procedure can be divided into three consecutive steps. Initially the length sensor is zeroed using the calibrated workpiece, successively the required measurements of length and influence factors are concurrently performed. Finally, by applying analytical and numerical calculations, the dimensional instabilities can be identified, as well as condition-specific material properties, and the dimensions at any conditions can be predicted (**Figure 1.4**). The DLM measuring concept relies only on information acquired during the measurement and does not require previous knowledge about the material behaviour. It can be implemented alone or in a hybrid measuring system which takes advantage of both DLM and conventional metrology. **Table 1.2** compares the requirements for conventional metrology and DLM. The concept of DLM can be implemented at different levels in the industrial measuring process:

- stand-alone unit including sensors and software for use in the production;
- solution of sensors and software for use with a measuring fixture in the production;
- solution of sensors and software for use with a Coordinate Measuring Machine (CMM) or another Coordinate Measuring System (CMS) in the production.

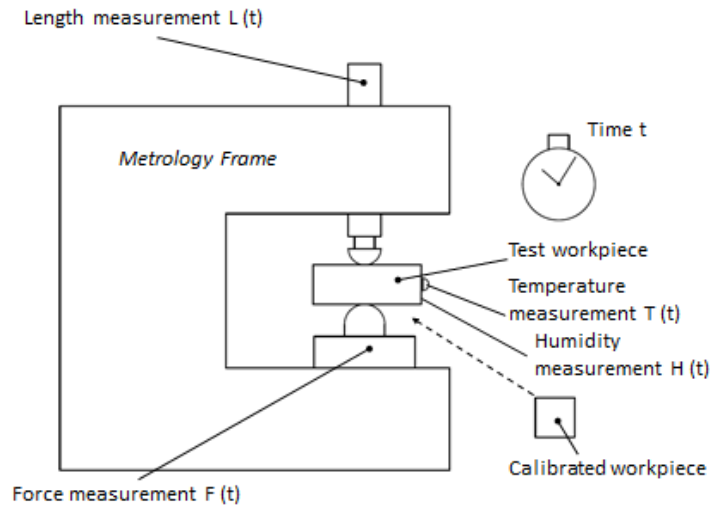
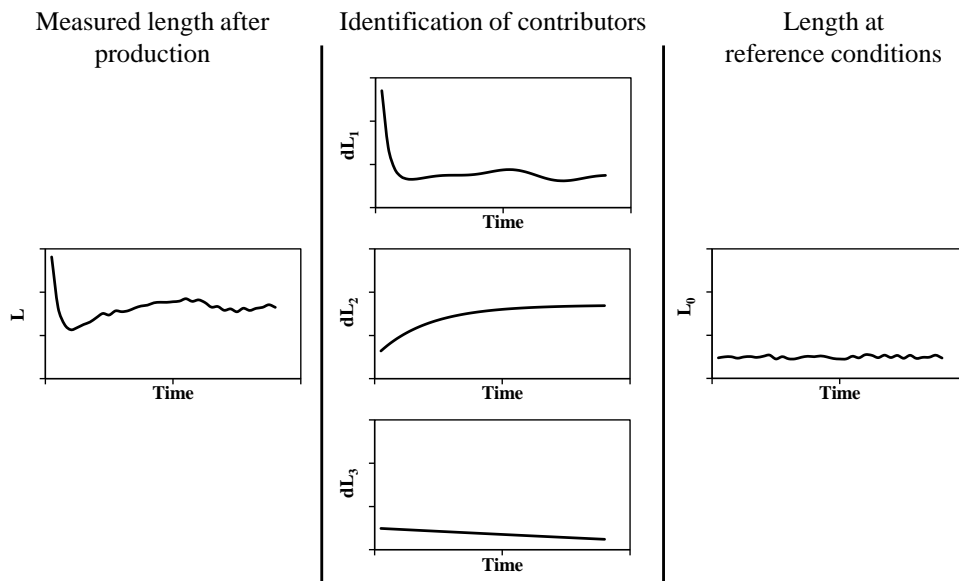


Figure 1.3 Main elements composing a DLM system: metrology frame and calibrated workpiece ensure traceability.

Table 1.2: Main requirements in conventional metrology and Dynamic Length Metrology [8].

<i>Conventional metrology</i>	<i>Dynamic Length Metrology</i>
Costly temperature controlled facilities	Directly in production environment
Long waiting time for part acclimatization	Reference and multi-sensing system
Separate part material characterization	Analytical and numerical modelling

**Figure 1.4** Dynamic Length Metrology: the length at reference condition L_0 is estimated from measured quantities L in production through the identification of different influence contributors dL_i .

1.3 The Accurate Manufacture project

This PhD thesis incorporates work performed as part of the Accurate Manufacture project (ACM). The project concerned the development of the innovative concept of DLM in collaboration with Danish industries. The goal of the project has been to achieve narrow uncertainties for dimensional measurements on parts made of metal as well as less stable material, such as polymers, when measured directly in production environment. Uncertainties lower than $1\text{ }\mu\text{m}$ for metal parts and lower than $5\text{ }\mu\text{m}$ for polymer parts have been selected as target uncertainties. Production environment is considered as an environment where temperature and humidity are not controlled and fluctuate from 15 to 35 °C for temperature and 15 to 70 % for relative humidity. The project focused on parts

with dimensions smaller than 250 mm. The project was divided into four working areas (**Figure 1.5**):

1. A metrological analysis of a selected measuring process for a given part taking all relevant influence factors and uncertainties into account.
2. Development of a system for traceably measure over time local displacements fields, forces and temperatures on the part in 1.
3. A modelling tool to predict the thermo-mechanical conditions over time of the part in 1, as well as the related uncertainties, using input data from 2.
4. A data acquisition and software platform which makes use of the results from the previous areas, integrated into a measuring unit and validated in a production environment.

This work encompasses working area 2 and to a lesser extent part working areas 1 and 3.

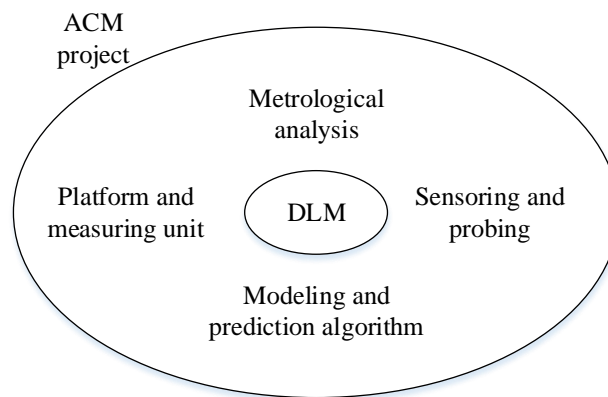


Figure 1.5 The Accurate Manufacture project. Four working areas are identified in the development of a Dynamic Length Metrology solution.

Main partners of the project were two research groups at DTU Mekanik, with competence in dimensional metrology and simulation respectively, and Metrologic ApS, a Danish company specialized in quality management and metrology. The Accurate Manufacture project running from May 2014 until March 2018, has received financial support from the Innovation Fund Denmark.

1.4 Task identification

The DLM concept is a new idea being developed for the first time during the Accurate Manufacture project. For establishing a solid guideline for DLM, a wide range of questions has to be addressed regarding sensing and probing strategies. DLM requires measurements of dimensions and other quantities performed over time. The information

from the measurements has to be merged in a solid modelling to predict the dimensions at reference conditions. Issues regarding the number and the position of the sensors, the acquisition time and rate, and the data fusion strategy have to be solved.

This thesis encompasses works on probing system selection and their implementation, considering contact sensors as well as optical systems, data acquisition, signal conditioning, positioning, fixing and articulation of probes. Dimensional instability due to thermal effects, moisture uptake, viscoelastic creep and shrinkage are investigated, and uncertainty models for simple and complex parts are developed. The research work has included the following main tasks:

- A thorough review of the state of the art concerning sensing techniques and probing strategies for displacement, forces and temperatures distributions and other factors affecting the dimensional measurement uncertainty, traceability of sensors and dimensional measurements, and uncertainty models has been carried out to produce a base line for the project.
- A second task has comprised possible methods for the simultaneous acquisition over time of necessary data from measuring equipment and components for dynamic length measurement. This part includes the study of several types of sensors and the evaluation of the uncertainty connected to probing and signals.
- Probing solutions have been investigated to determine distributions of displacements, forces and temperatures (among other influence parameters) with particular focus on accessibility and traceability. Several probing systems have been studied, including optical sensors and infrared thermography. Data acquisition and signal conditioning to achieve low uncertainty have been investigated along with probing strategies for optimum data extraction.
- Probing systems and fixtures have been also investigated for measurements on industrial parts. The higher complexity of measurements on such objects requires additional investigations and the consideration of multidimensional models (3D models). Uncertainty budgets and estimations have been developed for an industrial case as a final result of the project.

1.5 Thesis outline

The structure of this thesis addresses the tasks identified above as follows.

A broad insight on the subject of industrial dimensional metrology is introduced in chapter 2. Contact and optical methods for dimensional measurements are described as well as an introduction to factors influencing dimensional measurements. Advantages and disadvantages of each measuring method are outlined to draw a framework for the selection of the most suitable technologies to apply in DLM

A selection of probing systems and sensors is presented in chapter 3. Contact and non-contact solutions for dimensional measurements and temperature measurements are investigated to assess the applicability to a DLM solution.

Probing strategies are presented in chapter 4. Issues such as the sampling time and frequency and the number of sensors necessary for achieving a target uncertainty are tackled in this chapter. The definition of an adequate measuring procedure requires the knowledge of the analytical/numerical model used for length prediction. In this chapter each influence factor is treated separately and for each of them guidelines for defining the measuring strategies are defined.

In chapter 5 two solutions for measuring surface displacement and absolute dimensions are introduced. These solutions were conceived and developed during the project. A laboratory set up is used to validate the methods for conventional and dynamic measurements.

An industrial case is presented in chapter 6. Knowledge obtained about probing strategies is applied in measurements in production in a Danish company. Plastic products are measured just after moulding during a transitory state and dimensions at reference conditions are predicted. Comparison with measurements under reference conditions has validated the approach. Uncertainties lower than 6 μm were obtained.

The conclusive chapters summarize findings and outcomes of the thesis. In addition future work and suggestions for improvements are outlined.

2

State of the art of accurate measurements in production environment

2.1 Influence factors in dimensional metrology

The output of a dimensional measurement is always influenced by external factors, such as, e.g., temperature. It is therefore of fundamental importance to take all the influence factors into account when providing a measurement result. ISO 14253-2, from the family of ISO standard dealing with Geometrical Product Specification (GPS) presents a broad list of factors influencing dimensional measurements (**Figure 2.1**) divided in categories including environment, measuring equipment and set up, and measurement object [10]. The following section focuses on the factors to consider during the development of a DLM methodology. In particular they consist of elements that change over time and affect the dimensions during measurement of the workpiece in industrial environment. Many other relevant factors, such as surface texture, influence dimensional measurement contributing with static systematic effects and they are omitted in the discussion.

Both the measured object and the measuring equipment can change their properties under different external conditions. While the dimensional instability of the workpiece represents the objective of the measurement procedure in DLM, the instabilities related to the equipment must be reduced, for instance using low expansion materials, or removed with a compensation routine.

Among all quantities influencing length measurements in such conditions the most important are identified to be:

- Temperature of the measuring object and equipment

- Ambient humidity and moisture content of measuring part
- Stresses applied to the part differentiated in:
 - Residual stresses from previous production processes
 - Stresses induced by the measuring equipment.

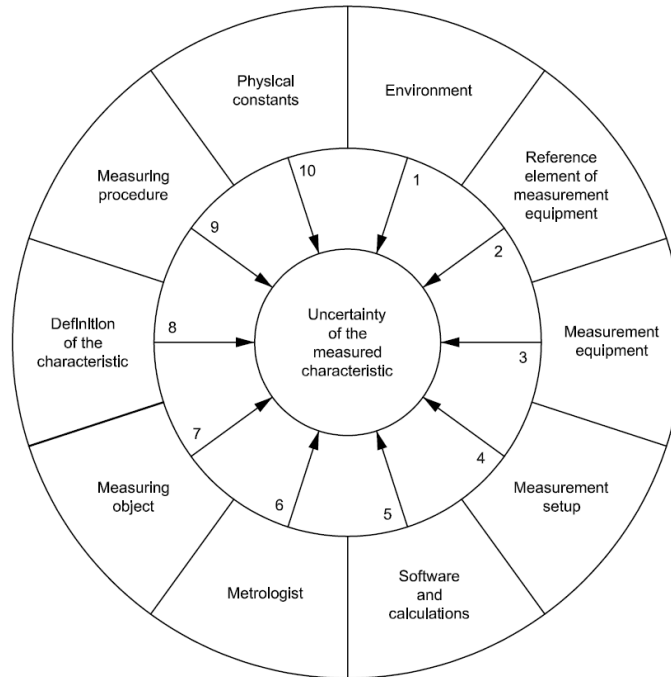


Figure 2.1 Influence factors in dimensional metrology according to ISO 14253-2 [10].

In a time-transient situation, the non-constant state of an object is influenced by its initial state and by the external environment, defined as boundary conditions, as illustrated in **Figure 2.2**. The state of the object, mainly consisting of the temperature field, the moisture absorbed and the stresses acting on the object directly influence the dimensional features of the object. Indirectly dimensions are therefore influenced also by boundary and initial conditions. The elements mentioned above contribute to change the dimensions (expansion) and the shape (warping) of any object especially if made from less stable materials like polymers. The way they affect a specific object's dimensions depends on both material properties and geometry of that object. Thus the relationship between external quantities and dimensions cannot be synthesized only by a material property coefficient, such as the coefficient of thermal expansion, but it must be described by a more comprehensive sensitivity coefficient, representing the extrinsic object's behaviour.

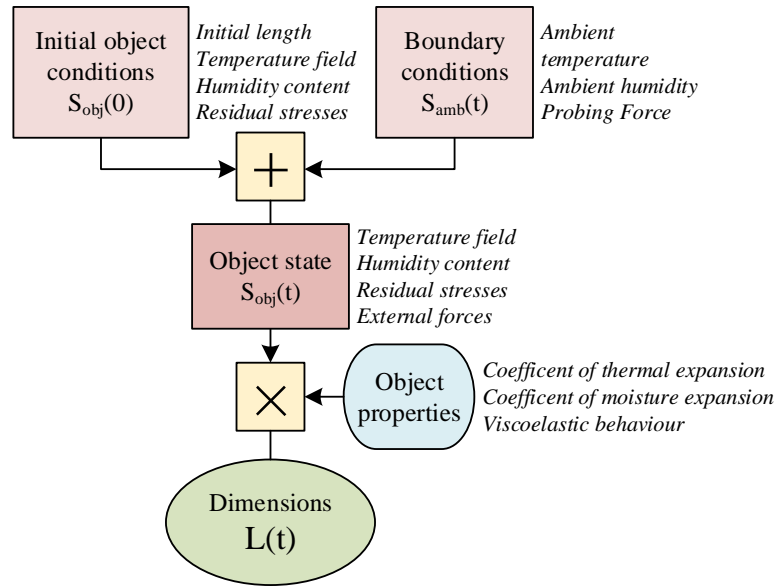


Figure 2.2 Dimensional behaviour of a generic object under transient state.

2.1.1 Reference conditions

Conventionally in dimensional metrology temperature is considered the main influence factor and uncertainty contributor. ISO 1 [4] regulates the temperature conditions for dimensional and geometrical measurements. It defines the concept of reference temperature as “the temperature of an object, having a uniform temperature, specified in the definition of a geometrical or dimensional property” and the concept of standard reference temperature as the “internationally agreed-upon reference temperature”. The standard reference temperature is fixed at 20 °C and any measurement must be referred to that temperature value. The case where the reference temperature of a measurement is different than the standard reference temperature of 20 °C is however allowed.

In other metrology fields different standard reference conditions are defined also considering additional influence factors. In the case of measurement on polymer it is necessary to regulate the ambient humidity as well as the temperature since polymer physical properties change with humidity and water absorption. Reference ambient condition for polymer testing are fixed to 23 °C for temperature and 50% for relative humidity [5]. GPS standards acknowledge the influence of humidity in dimensional measurements as a secondary factor, however they leave the eventual definition of the reference ambient humidity to the product designer without defining any standardized value [11]. It is reasonable therefore to adopt the requirement regarding ambient humidity present in [5] also in dimensional measurements.

When dealing with contact measurements ISO standards define the principle of perfectly rigid workpiece, that is a measuring object must always be considered with infinite stiffness and undeformed by external solicitations [11]. In a real application all workpiece-

es are deformed by the measuring force, therefore to reach an infinite stiffness condition the elastic (or sometimes plastic) deformation must be compensated and the measuring force considered zero [10].

2.1.2 Temperature

Every material, from metals to polymers, expands and shrinks with the change of temperature making it the most influential quantity in dimensional metrology. The influence of temperature on dimensions can be represented by the formula of thermal expansion:

$$L_T = L_{20} + L_{20} \cdot CTE \cdot (T - 20) \quad 2.1$$

Where:

L_T is the length of the object at the temperature T ;

L_{20} is the length of the object at 20 °C;

CTE is the coefficient of linear thermal expansion;

T is the temperature of the object.

This simple formula is massively used in dimensional metrology for compensating systematic errors and for estimating measuring uncertainties.

In metrological application thermal expansion of fixture components and reference artefacts affects the measurement result and measurement uncertainty. The most used material in metrology equipment is steel both for fixtures and for reference artefacts. However, when specific requirements must be fulfilled, such as low measurement uncertainty or possibility to work with wider temperature variations, other materials with lower CTE can be employed. **Table 1.2** lists the values for the coefficient of thermal expansion for some materials employed in metrology.

2.1.3 Humidity

Humidity represents an issue mainly for polymers since they are prone to absorb water. ISO standards regulate experimental procedure to define how polymers absorb water and define some quantities for comparing different materials, such as the water absorbed by a sample exposed to an atmosphere at 50% of relative humidity [12]. A generally acceptable acclimatization time necessary for a specimen to reach the equilibrium is about 24 hours. The phenomenon of water absorption in polymers involves both thermodynamic and kinetics aspects [13]. Diffusion in polymers can be described with a Fick law (equation 2.2) which correlates the penetrant flux J with the concentration gradient ∇C and the molecular diffusion coefficient. The latter is constant for low concentration levels and temperatures [14].

Table 2.1: CTE values for common materials used in metrology and engineering [15], [16], [17].

<i>Type</i>	<i>Material</i>	<i>CTE /ppm/°C</i>
Metal	Steel	10.2-17.2
	Invar 36 (Ni-Fe alloy)	1.6
	Cu alloys	16.2-20.5
	Al alloys	21.5-23.6
Ceramic	Zirconia	9.6
	Glass	3.3-9.0
	Zerodur	0.05
Polymer	High density polyethylene HDPE	106-198
	Polypropylene PP	146-180
	Acrylonitrile butadiene styrene ABS	75-95
	Polymethylmetacrilate PMMA	90-162
	Polyoxymethylene POM	110-130
	Polyether-ether-ketone PEEK	72-85

$$J = -D \cdot \nabla C \quad 2.2$$

The absorbed moisture is quantified with the water content C , as the weight variation due to the absorption dW referred to the total volume V or to the total weight W of the component [18], [19]:

$$C_w = \frac{dW}{W} \quad 2.3$$

$$C_v = \frac{dW}{V}$$

The absorption of water causes an obvious increase in the mass of the polymer part but also an increase of the dimensions and distortion, similarly to temperature. The quantification of the hygroscopic swelling of a part can be treated similarly to the thermal expansion with the introduction of the coefficient of moisture expansion CME , often

called also coefficient of hygroscopic swelling [19]. For a linear one dimensional analysis the expansion dL of a dimension L can be calculated as:

$$dL = L \cdot CME \cdot \left(\frac{dW}{W} \right) \quad 2.4$$

Table 2.2: Moisture absorption of some polymers measured according to ISO 62A [12], [17].

<i>Material</i>	<i>%</i>
High density polyethylene HDPE	0.01
Polypropylene PP	0.02
Acrylonitrile butadiene styrene ABS	0.1-0.3
Polymethylmetacrilate PMMA	0.3-0.4
Polyoxymethylene POM	0.2 – 0.28
Polyether-ether-ketone PEEK	0.1-0.3

2.1.4 Stresses

Measuring Force

When dealing with contact measurements the force applied by the measurement instrument causes a deformation on the measuring object. Measurement instruments apply small contact forces usually in the order of tenths of a newton to compromise between the limitation of the deformations and the necessity of having an unambiguous contact between instrument and workpiece.

The deformations occurring during the measurement are often elastic and recover after the contact is released. Since the stress field is locally confined the simple Hooke law is insufficient. The contact can be modelled using the Hertz contact mechanics theory. According to Hertz the local stress field and consequent deformation depends on the geometry of the bodies in contact besides the amplitude of the force and the elastic properties of the bodies. In geometrical metrology common types of contact consist of contact between a half-space and a sphere or a cylinder, where the half-space represents the measuring object with an approximated flat surface and the sphere (or the cylinder) the probing instrument. The contact between an elastic half-space and an ideally rigid sphere causes an indentation on the half-space equal to [20]:

$$\delta = \left(\frac{9 \cdot F^2 \cdot (1 - \nu^2)^2}{16 \cdot E^2 \cdot ra} \right)^{1/3} \quad 2.5$$

Where:

δ is the depth of indentation (deformation);

F is the contact force;

E is the Young modulus;

ν is the Poisson ratio;

ra is the radius of the sphere;

Values of Young modulus for commonly used material are listed in **Table 2.3**. Polymers usually have elasticity 30 to 100 times smaller than steel and metals.

Table 2.3: Young modulus of common materials used in metrology and engineering [15], [17].

<i>Type</i>	<i>Material</i>	<i>E /MPa</i>
Metal	Steel	193-207
	aluminium alloys	69-72
	Copper alloys	97-150
	Invar 36	141
Ceramic and Glass	Zirconia	205
	Glass	70
Polymer	High density polyethylene HDPE	1.08
	Polypropylene PP	1.14-1.55
	Acrylonitrile butadiene styrene ABS	2.4-2.7
	Polymethylmetacrilate PMMA	2.24-3.24
	Polyoxymethylene POM	2.7
	Polyether-ether-ketone PEEK	1.10

In contrast to metals, polymer components exhibit viscoelastic behaviour. A simple way to describe the viscoelastic characteristics is a model composed by elastic and viscous element combined in parallel or serial way [21]. The deformation δ of elastic elements occurs instantaneously to the application of an external stress F (equations 2.6) while viscous elements deform in time according to and 2.7, where E represents the elastic constant of the modular element.

$$\text{elastic element} \quad F = E \cdot \delta \quad 2.6$$

$$\text{viscous element} \quad F = E \cdot \frac{d\delta}{dt} \quad 2.7$$

This modular model allows the creation of simple or more complex models depending on the type of material and the particular application. As an example a model composed of two elastic elements and one viscous element is depicted in **Figure 2.3 a**. It explains the behaviour of a polymer component during a contact measurement: as soon as the contact is engaged the pure elastic deformation occurs (element A) while the deformation of element B is restrained by element C. If the contact is held throughout time element C activates and the deformation of the progress with an exponential trend since the force is progressively absorbed by the deformation of element B. When the contact is released the element A recovers its deformation instantaneously while the element B forces the recovery of the deformation of element C with a negative exponential trend because B is progressively unloading (**Figure 2.3**).

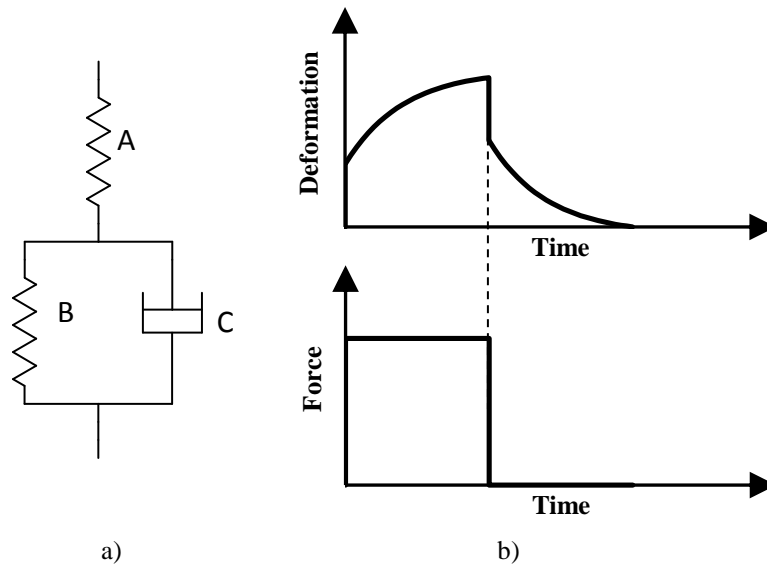


Figure 2.3 Three elements model of a viscoelastic material: a) schematic representation; b) mechanical behaviour under constant load.

Residual stresses relaxation

Manufacturing processes often create stresses in the bulk material of a part that can remain embedded in the material even after production. In the case of metallic parts residual stresses, coming from example from a cold deformation process, cause problems especially regarding material strength but usually not regarding dimensional stability over time. Differently residual stresses present in polymer parts cause dimensional instabilities, especially in the lapse of time following the production process. Due to the viscoelastic behaviour typical of polymers, in this period the part deforms to reach an unstressed condition. The time necessary to achieve a stable condition varies depending on the amplitude of the stresses and on the mechanical properties of the part. In the case of injection moulding residual stresses are caused by the material flow and differential solidification in the cavity. An inhomogeneous cooling of the material inside the mould cavity creates strain-driven stresses in the solidified sections. Distortions due to residual stresses are a well-known issue in the polymer manufacturing industry [22]; in fact dimensional measurements are usually performed days after the production occurs to ensure a stable condition. Thus to limit dimensional instability due to residual stresses the dimensional inspection must be consistently postponed. The minimization of residual stresses through process optimization has been widely investigated with experimental work and simulations [23] as it represent a key issue in the production of precision components.

2.2 Contact sensors for dimensional measurements

An overview of technologies used in industry for dimensional measurements is presented. This section focuses on contact measurement instruments while section 2.3 deals with optical technologies.

The geometrical characteristics of a component can be defined and measured as the position and distance of the selected surface points in reference to a datum position. The measuring approach of contact devices consists of establishing contact between the probing element of the instrument and workpiece and measuring the probe position. According to the number of axes in which contact sensors operate (measured movements of the probing device), they can be classified as one, two or three dimensional systems [24]. **Table 2.4** presents a short list of measurement devices grouped according to number of working dimensions and type of measuring technique.

Contact sensors can be divided into absolute and relative measurement methods. A comparative approach is necessary when dealing with relative measurement techniques. The measurement result is obtained as a difference of readings between measurement on the workpiece and on a reference artefact with known dimension. Absolute measurement devices, such as callipers or CMMs do not require a reference artefact to produce an absolute measurement result. Nonetheless the measurement procedure can be performed for both workpiece and reference artefact to improve the results accuracy. In absolute meas-

uring systems the measurement accuracy is related to the maximum permissible error (MPE), which considers among other things linearity, resolution and axis errors (in case of CMMs); on the contrary by following a comparative procedure the uncertainty is related to the calibration uncertainty of the reference artefact and the repeatability of the instrument [25]. A discussion of reference artefacts is presented in section 2.4.

Several aspects influencing a contact length measurement arise from the analysis of the contact between probe tip and workpiece measurement. Surface texture and form error of the two bodies affect the position of the probe tip during the measurement. The size of the probe tip influences the measurement as well. Smaller probe tips can reach position corresponding to deeper valley on the surface texture. Another source of error is represented by the elastic deformation of the probe. In section 2.1 the focus is mainly on the workpiece. However for long stem probes or less stiff frames and fixture, elastic deformation and bending occur [24].

Table 2.4: Example of measurement systems based on measuring technique and dimensionality [2].

<i>Measuring technique</i>	<i>1D</i>	<i>2D</i>	<i>3D</i>
<i>Contact</i>	Ruler, calliper, micrometre, dial gauge	stylus profilometer, roundness tester	CMM, form tester
<i>Optical</i>	Laser point triangulation, laser interferometer	optical profilometer, video CMM	optical scanner
<i>other</i>	ultrasonic probe	AFM, SEM	3D SEM, CT-scanner

2.2.1 1-D contact devices

Manual instruments

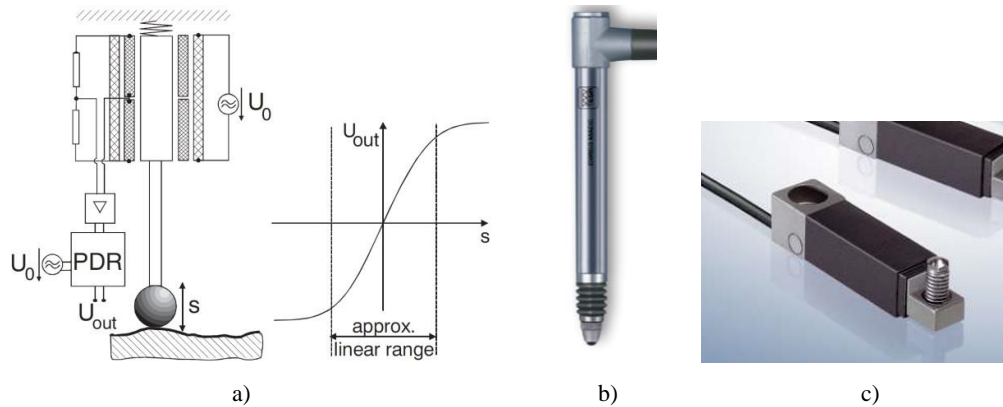
Manual instruments are widely used in industry for performing simple and fast measurements in production. Callipers and micrometres offer absolute length measurements, while dial gauges are often used in comparator setup. Automatic acquisition allows the registration of the measurement for a direct estimation of conformity. Maximum permissible errors for the most common manual instrument are listed in **Table 2.5**.

Table 2.5: MPE values of common manual instruments.

<i>Instrument</i>	<i>MPE /μm (L in mm)</i>
Vernier calliper	$50+L/10$
Vernier calliper (0.01 mm resolution)	$30+L/20$
Micrometre	$4+L/50$
Dial gauge (0.01 mm resolution)	$10+L/100$

Electronic inductive probe

Electronic inductive probes are instruments providing a relative displacement measurement. They are widely used in dimensional metrology in similar application as dial gages. The working principle is described in **Figure 2.4 a**. The probe head is connected to a ferromagnetic core which slides inside a coil changing its inductance. The coils are connected to an half Wheatstone bridge in Half Bridge Transducers (HBT) circuit, which becomes a full bridge in the case of Linear Variable Differential Transducers (LVDT) [26].

**Figure 2.4** Electronic inductive probes: LVDT working principle [24], common inductive probe [26]; radial miniaturized probe [27].

They provide a continuous analogue output which is converted in digital signal typically with resolution of $1\ \mu\text{m}$ or $0.1\ \mu\text{m}$. The usual maximum working range is $\pm 0.2\ \text{mm}$ when using the fine resolution. The output of inductive probes is referred to the electrical zero, which is a position located in the middle of the tip travel. Probes are characterized

by high linearity in the correspondence of the electrical zero which worsens at the extremity of the working range. Typical MPEs are $0.2+3 \cdot L^3 \mu\text{m}$, which can go as low as $0.07+0.4 \cdot L \mu\text{m}$ (L being the electronic reading in mm). A spring connected to the probe head, or a pneumatic system, ensure the automatic application of a contact force. Depending on the probe model the force applied goes from a minimum of 0.09 N to 4 N [26]. The tip shape is usually spherical; nonetheless it can be interchanged with cylindrical, flat or sharp tips. Typically inductive probes come with a cylindrical shape and axial stroke. Other shapes are available to offer also radial strokes [26], [27].

Inductive probes are used in comparative applications on standard column stands, for example for measurements of height or diameters, or in fixtures (**Figure 1.2b**) for measurements of more complex components, such as a crankshaft. The possibility of defining several set-ups gives flexibility to the inspection with probes which are usually used in inline production for fast inspection. For this reason, it is common to find the working temperature range and thermal drift in their technical specifications.

Encoder based measurement devices

Another method to measure the position of the probing element in a 1D device consists of using encoder scales (**Figure 2.5**). Thermal expansion is a limiting factor for the accuracy of encoder based sensors, which can be limited by compensation or using a scale made of low CTE materials [28]. Glass encoder scales are employed for general applications, providing accuracies in the order of $1 \mu\text{m}$, while high accuracy probes are equipped with Zerodur scales and can reach accuracies of $0.03 \mu\text{m}$ over a range of several millimetres. Differently from inductive probes, encoder based systems have a longer measuring range up to 100 mm [29]. The contact with the measuring object can be engaged with a spring, a pneumatic system or an active linear motor.

Linear actuators can be included in this last category. Specific models are equipped with a glass scale, with resolutions up to $0.1 \mu\text{m}$ [30]. The active control allows the implementation and the direct measurement of an adjustable contact force.



Figure 2.5 Length measurement with encoders: a) length gauges [29]; b) linear actuator.

2.2.2 CMMs, probes and stylus

A coordinate measurement machine (CMM) is a 3D dimensional measurement device. The system is composed of a measuring probe connected to three moving guideways oriented orthogonally to form a cartesian coordinate system. The moving axes are equipped with encoders to measure the absolute position of the measuring head. Several configurations of frame and guideways are available and are described in ISO 10360-1 [31]. The most common configurations are the moving bridge and fixed bridge types [32]. Other types of coordinate measuring machine, namely articulated arm, are based on polar coordinate systems instead of Cartesian systems. CMMs can be grouped based on the working range achievable. Usual working ranges are in the order of 0.5-2 m, however large volume CMMs are available as well as micro and nano-CMMs [32].

The contact probe is generally composed by a stylus and a ruby sphere tip. The measurement of the surface points of a workpiece is performed by touching the surface with the probe tip and measuring its position in respect to the absolute coordinate system. The measuring point position can be determined by correcting the measurement for the tip radius. The definition of a workpiece datum is necessary to convert the measurement of the position of the object surface points into dimensional measurement. The system can be operated manually or automatically after the definition of the working path. A completely rigid probe suits manual operations as the engagement of the contact has to be defined by the operator. Touch-trigger probes, instead, provide a Boolean signal when the contact with the workpiece occurs. A third type of probe is composed of measuring probes which can provide information on the contact force applied to the workpiece and on the position of the tip with respect to a fixed probe point. It is the case of complex probing systems, like the articulated head [24]. Non-contact probing techniques can be implemented as well as in the case of video probe or laser triangulation probes (see section 2.3.3). CMMs can be employed in single point measurements or in scanning mode, where the measuring probe is moved while keeping contact with the workpiece for collecting clouds of points. Simple geometries, like prism or cylinders, can be measured with single point measurement while complex shapes, like freeform surfaces, are usually measured in scanning mode [33]. Several sources of errors are present in CMMs measurements, as depicted in **Figure 2.6**, and a single definition of measurement uncertainty is not achievable. The moving axes introduce 21 geometrical errors (7 for each moving axis) which can be identified and mapped with a calibration procedure. ISO 10360 series define acceptance and reverification tests considering these geometrical errors [31]. Other sources of errors are related to the probing system, such as elastic deformations, pretravel of trigger and measuring probes and tip radius definition [24]. The spherical tip can be qualified, to determine radius and geometrical errors, by measuring a high quality sphere [32]. Thermal inputs are also relevant in case of measurements in non-standard conditions. Modern CMMs implements temperature measurements for thermal error compensation [34], [35]. Other sources of errors are introduced by the specific measuring strategy [36]. ISO 15530-3 defines a procedure using calibrated artefact for the estimation of measurement accuracy considering the contribution of measuring procedure and workpiece [25].

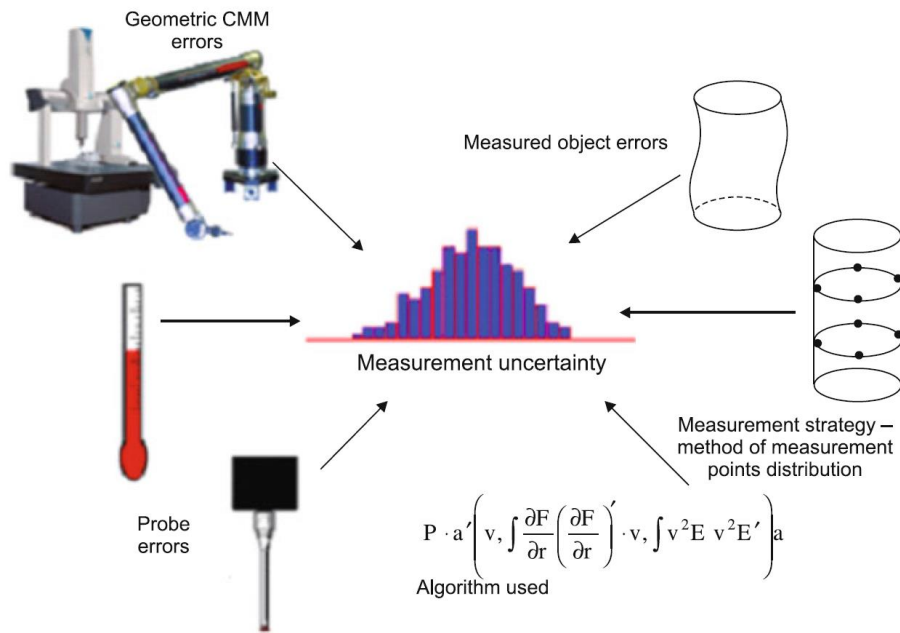


Figure 2.6 Error sources of CMM measurements [37].

2.3 Optical sensors for dimensional measurements

Optical methods for dimensional metrology exploit different properties of visible light for measuring and scanning objects of dimensions from the nanometer scale (i.e. confocal microscopes) to several meters scale (i.e. fringe projection scanners). In industrial metrology and quality inspection they are replacing traditional contact methods whenever possible. Compared to contact systems they can acquire higher volumes of data in less time being suitable to measure complex and freeform shapes like turbine blades. Another advantage of optical measuring systems is the absence of contact with the sample to be measured, making them suitable for applications involving brittle and soft materials, such as a polymer. The absence of a touching probe increases the accessibility for small feature measurements. Nonetheless limitations occur when the light path is hindered, like in the case of deep holes or undercuts. A strong limitation of optical methods consists in the sensitivity to the surface appearance. The accuracy of the measurement can be influenced by the colour, reflectivity and transparency of the object surface. In many cases the surface texture prevents the use of specific techniques as in the case of rough surfaces not suitable for laser interferometer measurements. In other cases the measurements can be reliably performed after a surface treatment such as paint spraying or target application as in the case of photogrammetry. The measurement is influenced also by the characteristic

of the ambient conditions, such as air temperature and humidity and presence of dust, as they change the condition in which the light is propagated and transmitted.

Despite the fact that optical methods, as techniques exploiting visible light to measurement, are commonly considered non-contact measurement methods, in some particular cases light is used together with a touching probe to measure displacements. It is the case of touching probes (similar to inductive probes) where the displacement can be assessed with an linear optical encoder or an interferometric measurement [38]. Another hybrid system consists in CMM equipped with an opto-tactile fibre probe [39].

Visible light is a narrow interval on the electromagnetic field. Thus in a broader sense any other system using a generic electromagnetic wave can be considered as an optical measuring system. For example computer tomography scanners use x-rays to measure components and assemblies. In this review however these systems are not considered

The optical systems can be categorized according different characteristics. A first distinction can be made according to the working principle of the system and more precisely to the light property exploited by the system. Four main systems can be identified (see **Figure 2.7**):

- Intensity based sensor.
- Triangulation systems: their working principle is based on the geometrical nature of light, linear propagation and reflection and refraction laws.
- Interferometric systems: the wave characteristic of light is exploited to create constructive and destructive interference.
- Time of flight: the constant propagation speed is used to measure length.

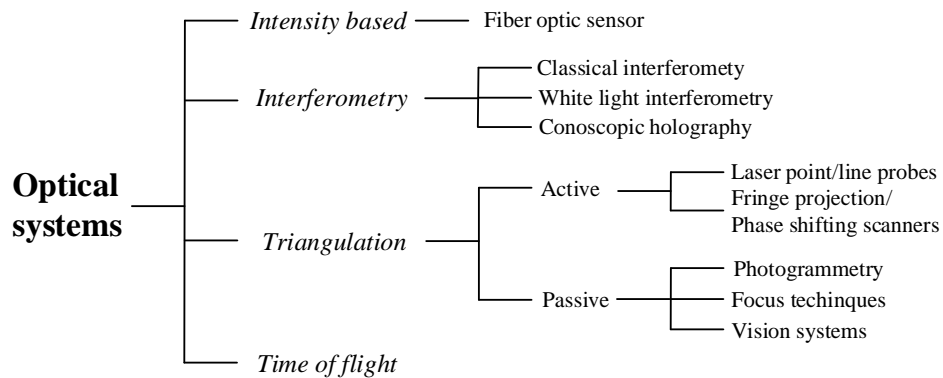


Figure 2.7 Summary of optical metrology techniques, according to different working principle (modified from [40]).

Another possible subdivision is based on the measuring range and resolution of the optical systems:

- Micro-nano scale (sub-millimetre scale)
- Meso scale
- Large scale.

All microscopes can be classified in the micro scale. Some optical CMM can measure small features as well. Triangulation systems belong to the meso-large scale. Considering that the resolution and measuring range often depend on the types of lenses used it is easy to understand how a technique can be easily implemented to measure small as well as big objects. Portable scanners using photogrammetry have few limitations in the measuring range since each measurement is composed by several pictures of a portion of the measuring object. Time of flight is used to measure large distances.

A particular group of optical technics consists in vision systems. They can be defined as the systems that use a picture to extract dimensional information. Their working principle is based on the triangulation. Photogrammetry systems and some optical CMMs belong to this category.

In the following chapter the most used optical systems for dimensional measurements are reviewed with a particular attention for the meso and micro scale. For such a reason time of flight systems are not considered and microscopy is partially introduced. In the final section the applicability to DLM is discussed.

2.3.1 Intensity based sensors

This type of sensors consists simply in a source of light and a detector. When the light source is projected towards a surface of an object it is partially reflected into the detector. The intensity of the reflected light depends on the distance between sensor and surface. These sensors use optical fibre to transmit the light. The transmitting and receiving fibres are bundled together in different layouts, see **Figure 2.8**.

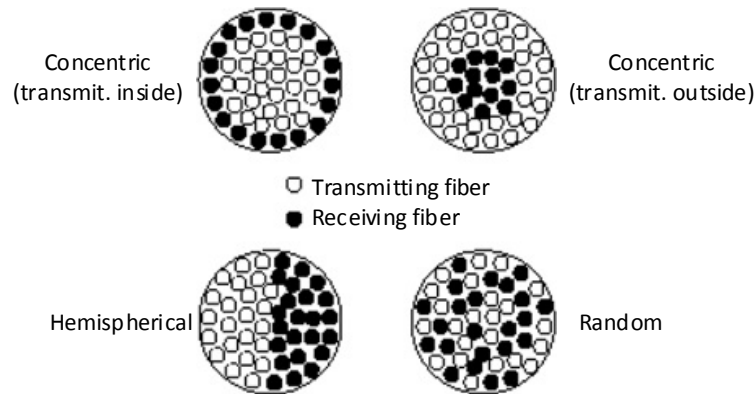


Figure 2.8 Bundle layout of optical fibres in intensity based sensors [41]

Their main advantages are the limited cost and possibility to reach high acquisition rate. Their typical response is highly nonlinear and non-monotonic. An example is depicted in **Figure 2.9**. It can be divided in two zones, the near side and the far side. As they have different slopes the sensors show different resolutions if working in the different

zones. For having an absolute distance measurement it is also necessary to perform a precalibration on every target to assess slope and amplitude of the response curve.

As they rely on the reflected light of a surface these sensors are sensitive to the reflectance and diffusivity of the specific target. The surrounding light conditions influence the measurement as well. Another influence factor is the angular slope of the measuring surface.

The working distance is in the order of few micrometres up to 50 mm. Typical resolutions on the far side is around 1 μm and repeatability worse than 3 μm [41], [42].

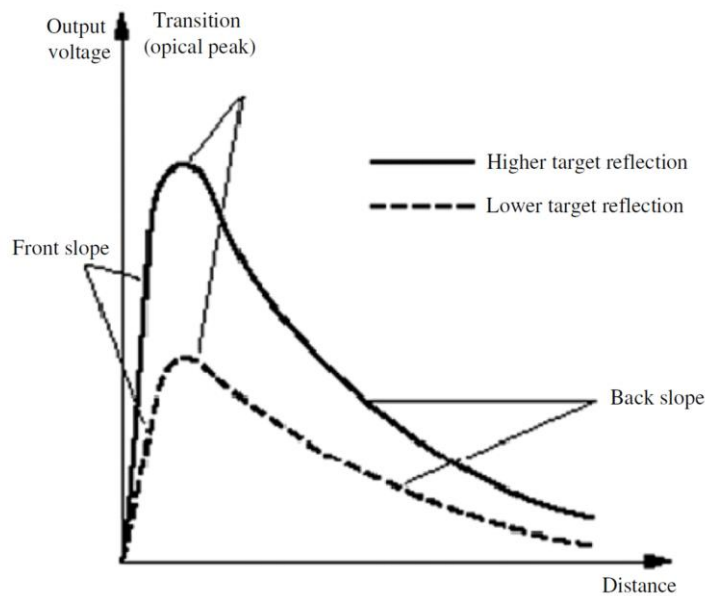


Figure 2.9 Typical response to displacement variation of intensity based sensors [41].

2.3.2 Interferometric systems

Several applications in the field of dimensional metrology and displacement measurements are based on the interferometry principle. Interference fringes originate when two coherent light signals with different phase are superimposed. The basic components of an interferometric system are a monochromatic coherent light source, a series of mirrors and lenses, a target object or a reflector and a receiver. The light emitted by the source is split into two beams. One beam is used as reference and reaches the detector through a fixed length path. The other beam first reaches the measuring object and then it is reflected into the detector. Due to the coherence of the light when the two beams are recombined together at the detector they create interference fringes. When the path of the measuring beam changes, due to a movement of the target or a variation on the surface position, the relative phase of the two light beams changes, thus the interference fringes change as well. The signal arriving at the detector is therefore only a series of shadows

and light signals. When a 2d detector is used the interference fringes can be represented in a picture called interferogram. The pitch between two fringes corresponds to a difference in the light paths of a multiple of the wavelength. The length measurement, performed by counting the fringes, is therefore a comparison between the wavelength of the light used and the quantity under investigation. The proper count of the number of fringes and the knowledge of the light wavelength is necessary to obtain an accurate measurement.

Interferometric systems can reach the highest accuracies among all length measuring systems. However their high accuracy is bonded to the knowledge of the refractive index of the transmission mean, i.e. air. Air refractive index is not constant and depends on temperature, pressure and humidity of air. It can be calculated with the Edler formula[43] to compensate the measurement for ambient conditions. This compensation could be not sufficient to achieve low uncertainties in the case of long beam path and in presence of strong air fluctuation. The uncertainty of the refractive index of air in fact represents a major contribution to the measurement uncertainty in non-laboratory conditions[38].

Despite their high nominal accuracy interferometric systems require costly and dedicated hardware (light sources, lenses, electronic fringe counts) and specific environmental conditions that makes them not appealing to a wide range of users.

As mentioned above coherent light must be used to obtain interference fringes. Coherence is a property related to the light frequency bandwidth. Coherence length is defined as the opposite of the light bandwidth. Only if the difference of the travel path of two split beams is smaller than the coherence length then interference occurs. Coherent light is often associated with monochromatic light or narrow bandwidth light since its coherence length is long. However, also large bandwidth light, such as white light, can show interference effects. Another advantage of using monochromatic light is the resulting high contrast of the interferogram [44].

A broad range of measuring solutions exploits the interferometric principle. Laser interferometry (mono or multi wavelength) is used to detect difference in height/distance (out of plane displacement) on a surface. White light interferometry is used in surface topography measurements. Speckle and holographic interferometers are used for detecting deformations and vibrations (in plane and normal) of a surface[45]–[47].

Laser interferometer

Also known as classical interferometry [48] uses a monochromatic coherent light source to create the interference fringes. The first and most diffuse layout is the Michelson interferometer (see **Figure 2.10**). Several other layouts with the same working principle have been developed, like the Fizeau interferometer. These interferometric systems are used to measure displacements on optically smooth surfaces. Rough surfaces create speckles that predominate over the interference fringes, reducing the measurement accuracy or even making the fringes impossible to recognize.

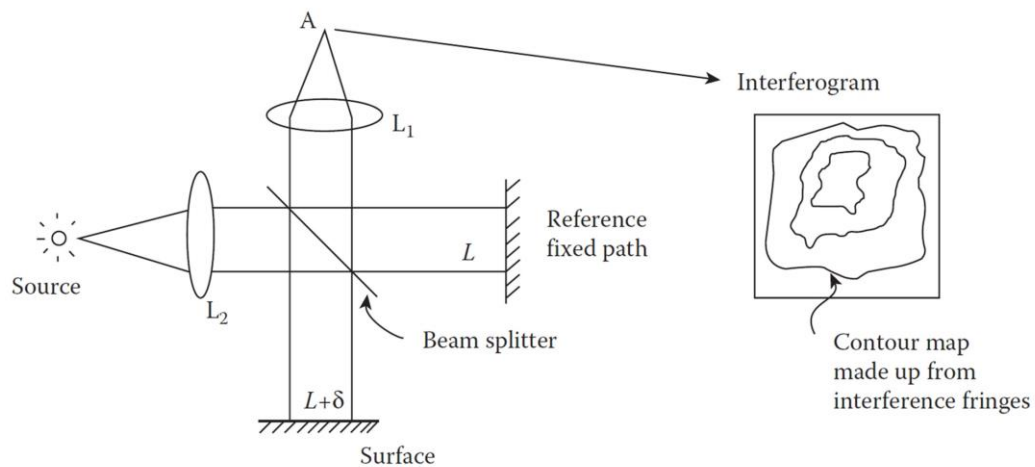


Figure 2.10 Schematic representation of a Michelson interferometer [44].

Classical interferometers can measure the position of a single point when the laser light is concentrated in a small area. The detector receives only one amplitude signal as the average over the small area. This creates a low pass filter in scanning application, i.e. measurements of lenses. The light beam can also pass through divergent lenses to create a collimated extended beam. The measuring area becomes wider and an interferogram is received by the 2d detector. This is the case in gauge block calibration.

The direct link to the fundamental definition of the length makes interferometry an important technology for traceable measurement. In fact it is widely exploited in calibration activity (gauge block calibration, laser tracker for machine tool calibrations). To obtain a traceable measurement a single wavelength light has to be used. For many light sources a frequency filter, i.e. an optical prism, has to be introduced in the light path. Other types of light sources, such as HeNe lasers, are widely used since their narrow bandwidth and high stability does not require filters.

One disadvantage of classic interferometry is the ambiguity of the measurement. The displacement measurement can be unambiguous only if it is within the range of half of a wavelength, since the absolute fringe counting is limited to half of a pitch. As an example if a HeNe laser is used (wavelength of 633 nm) the unambiguity range is only 158 nm. For longer displacements the interferometric measurement suffers from the ambiguity problem and the knowledge of the relative position of each fringe in respect to a reference one is necessary to ensure proper measurement. In the case of heterodyne counting system the reference fringe is the first fringe counted therefore the absolute measurement can be performed as long as the light beam is not interrupted.

To overcome the weakness of the narrow unambiguous working space a multi-wavelength system can be used. These systems are also referred to as absolute distance interferometers. They exploit the phenomena of the beat frequencies. If two waves with different but close wavelengths are superimposed a synthetic wave with a much longer wavelength arises. The interference fringes created from this synthetic light corresponds to a much longer displacement. Multi-wavelength interferometric systems use two or

more monochromatic diode light sources. Tunable diodes are used because of the possibility to modify the wavelength according to the input current. The range of unambiguity can be enlarged to 0.5 mm. They can achieve sub-nanometer uncertainties in a range of $10^2 \mu\text{m}$ [44],[49].

A commercial example of multi-wavelength interferometer is represented by the LumphosSmart probe, depicted in **Figure 2.11** [50]. This system is composed by an electronic unit connected with optical fibres to a probe which contains the interferometer optics. The small size of the probe and the fibre connection make it easy to move and rotate. Thus it can be used in scanning systems such as a profilometer and roundness tester. In scanning mode it can reach measurement uncertainties of 50 nm (at 3σ level).

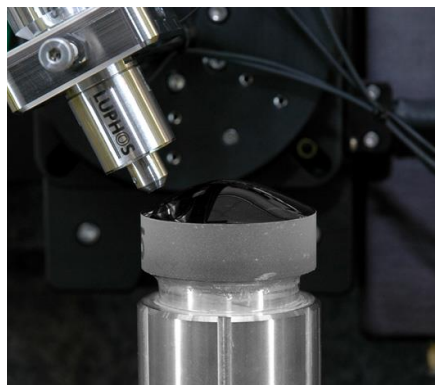


Figure 2.11 Lumphos smart probe [50].

Calibration of gauge blocks has already been mentioned as laser interferometry application. Particular attention is paid to calibrate the laser source to ensure traceability. Michelson and Fizeau interferometers are equally used. The gauge block to be measured is wrung to a flat surface with similar characteristics to the block surface to minimize phase shifts. The length of the gauge block is defined as the orthogonal distance between a point on the top surface of the block and the reference bottom plane. It is done by measuring the shift of the fringes on the plate and on the block, see **Figure 2.12**. To remove the ambiguity of the measurement the gauge blocks are premeasured with a contact probe to roughly assess the length thus the position of the reference fringe. Thermal stability of the measurand (gauge block and platen) and of the measuring system is ensured by measuring the temperature at several points and performing the measurement in an insulated cabinet. Uncertainty contributors come from the light wavelength (calibration of laser, refractive index of air), the geometry of the interferometer (alignment), the gauge block (temperature, thermal expansion coefficient, phase shift measurement) [16].

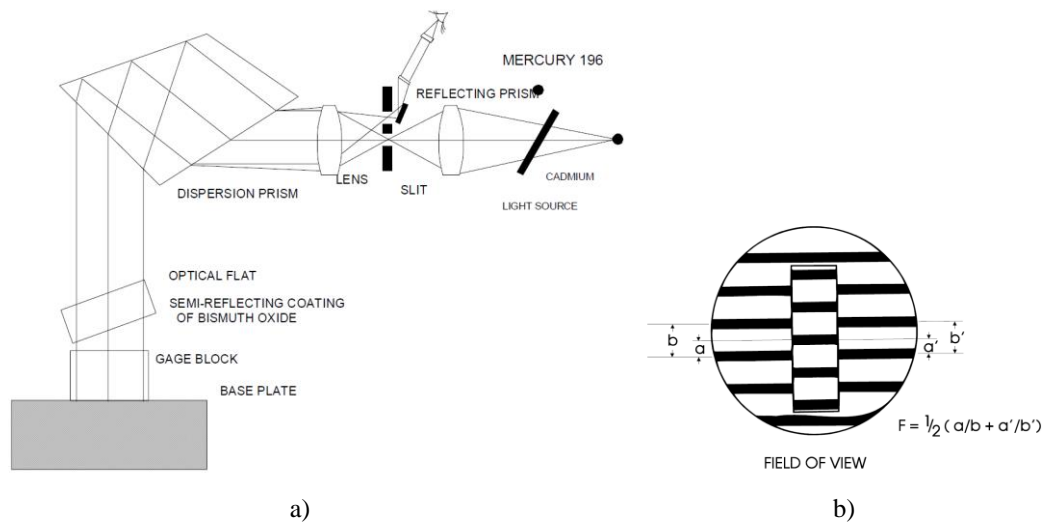


Figure 2.12 Gauge block calibration: a) NPL interferometer layout; b) Fringe counting method [16].

Another application of classical interferometry regards calibration and testing of machine tools, CMMs and guideways. The moving part, e.g. the machine tool spindle, is equipped with a retroreflector while the laser and the beam splitter are fixed. With a single beam setup it is possible to measure the distance between the retroreflector and the beam splitter. With a two beam setup the angular movements due to straightness of the guideways are detected [51], [52].

Laser trackers [53] and laser tracers [54] are widely used in large scale metrology and machine testing. They are a polar coordinate system composed of an interferometer linked to two rotational axes. The interferometer rotates around a reference sphere and measures the distance between a spherical retroreflector and the reference sphere. The rotation is measured separately by two angle sensors [55].

Laser interferometry is also used as an integrated measuring system in x-y stages. They are widely used in high precision positioning systems, such as ultraprecision CMMs [56]. Contact gauging probes can be equipped with an interferometric measuring system instead of the usual inductive system [52].

Conoscopic holography

Conoscopic holography exploits the properties of double refraction of uniaxial crystals. The working principle is depicted in **Figure 2.13**. A monochromatic laser light is reflected from a surface into the detecting device. It is firstly composed by a polarizer that creates two rays with orthogonal polarization. These two rays propagate through a uniaxial crystal oriented in the same direction of the optical axis. The propagation speeds of the two rays result differently because of the different polarization, i.e. orientation respect to the crystal axis. A circular analyser (another polarizer) brings back the two beams at the same polarization. The phase shift occurred in the crystal causes the formation of interference fringes on a detector positioned after the second polarizer. The distance between

the fringes is proportional to the distance between the sensor and the measuring surface [38], [57].

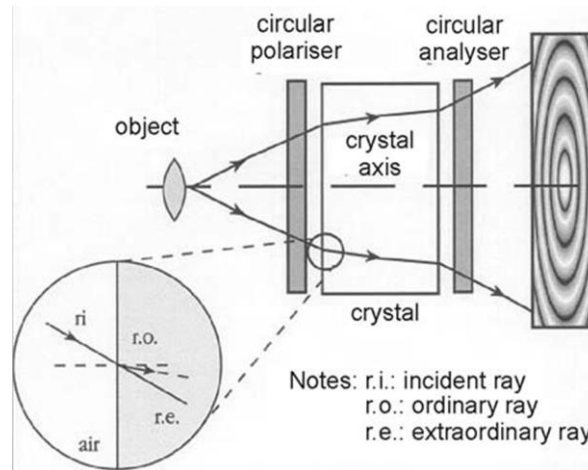


Figure 2.13 Conoscopic holography working principle [38]

Conoscopic holography can be used in single point distance measurements or implemented in a 3D scanner. Steep surfaces can be measured up to 85° of tilt angle. Typical ranges for these sensors are from 0.5 mm to 180 mm having measuring accuracies respectively of 2 and 100 μm [58].

2.3.3 Triangulation systems

Triangulation systems differ from interferometric systems by exploiting the geometrical behaviour of light and the triangulation principle. They can be divided in active and passive systems. Active triangulation systems include in the measuring device a light projector that can be as simple as a single point laser (laser triangulation systems) or a more complicated structured light projector, like a fringe projector. Passive methods do not require a specific illumination system. They are widely used in industry due to the low costs and high versatility. The most used technologies in industry are:

- Focus techniques
- Laser scanners[59][60][61]
- Structured light scanners [38][62]
- Photogrammetry systems [63][64][65][66]
- Digital image correlation systems (DIC) [67][68][69]
- Other vision systems.

All of these triangulation systems are composed by:

- An acquisition device: most of the time consisting of a photographic or industrial camera, such as DSLR (Digital single-lens reflex) camera, or simply by a photo-sensitive chip, e.g. a charge-coupled device CCD. The main features are the di-

mension of the chip, measured in pixels, and the colours (monochromatic or 3 colour channels). Stereo vision systems use two or more cameras.

- A system of lenses: a proper combination of lenses is required to have a good trade-off between magnification (i.e. resolution) and field of view. Other characteristics such as depth of view and focal length are important as well.
- A lighting system: as mentioned above the lighting system can be represented by a simple series of white lights (e.g. ring light [65]) to guarantee a uniform illumination of the measuring part, or it can be a more sophisticated structured light projector. In the case of photogrammetry and DIC system white light projectors (diffusive or coaxial) are sufficient.
- A post processing software or algorithm: several algorithms are used to extract dimensional information from the acquired pictures.

The camera and the lens unit introduce in the acquired pictures an inevitable distortion (such as barrel distortion). It is fundamental therefore to perform a calibration of the system to quantify this distortion (usually represented by a polynomial surface) and implement compensation in the post processing algorithm. Usually a square grid is used as reference for defining the lens distortions [70][71][72].

All triangulation methods suffer from the problem of spatial coherence interaction when a light spot is reflected and scattered from a rough surface. This interaction creates a speckle noise at the detector and an error in the definition of the mean point of the light spot. The amplitude of this error is proportional to the working distance of the measuring system [48]. The lateral maximum resolution achievable by geometrical optical systems is limited to a value higher than half of the wavelength used for illumination due to diffraction phenomena. For a visible light illumination (wavelength of 400-800 nm) the lateral resolution cannot be lower than 200 nm.

The matter of the traceability of optical systems is still a discussed topic in literature. Several artefacts have been developed to transfer traceability. In [73] a review of artefacts is presented.

Active triangulation system

Point and line sensor

Point and line sensors belong to the active triangulation sensors class. Due to the low cost and fast measurement rate (up to 10^5 Hz) they are widely used in industry and in in-line measurements [38], [41]. Their working principle is depicted in **Figure 2.14**. The sensor is composed of a collimated light source (diode) and a detector unit displaced at a fixed angle from the light source. The light emitted by the source is reflected by the measuring surface into the detector. The position of the light spot in the detector is proportional to the distance from the surface. The geometric construction of these sensors imposes a minimum and a maximum sensing distance. While point sensors detect the position of a single spot on the surface, line sensors, also called light sectioning, detect the coordinates of a line on the surface from the deformed reflection of a straight laser line.

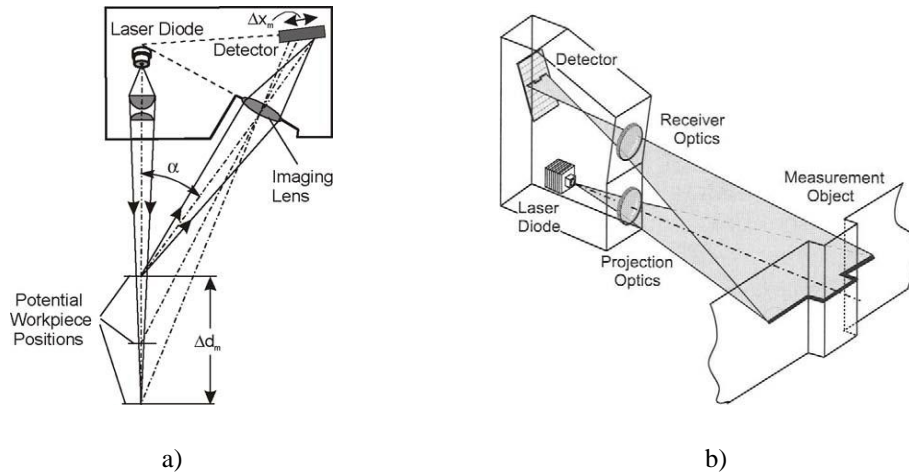


Figure 2.14 Laser triangulation sensors: a) point sensor [38], b) line sensor [74].

Point and line sensor measurements are highly influenced by the surface appearance being measured. A first error source consists in the speckle noise already mentioned in the section above. Volume scattering, occurring for measurements on polymers, and inhomogeneous surface texture introduce an error in the measurements. Smooth and transparent surfaces cannot be measured due to the low diffusive reflected light. Moreover orientation and curvature of the surface deform the laser spot received by the detector. Another limitation regards inevitable shading, caused by the non-aligned source of light and detector, and the impossibility to measure deep and narrow features [38], [41], [74].

Many commercial triangulation laser sensors are available on the market. They are designed for general or specific application, such as high frequency measurements, measurement of shiny or matt surfaces. Typical measuring ranges go from 2 mm to 1000 mm and typical repeatability goes from 0.2 μm upwards, depending on the range [75], [76].

Triangulation sensors can be used in a static application as a distance sensor for 1D and 2D or they can be implemented in a scanning system, such as a on a machine tool/CMM, a robot arm or a simple linear stage, for 3D scanning measurements.

Laser scanners and structured light scanners

This category of optical sensors is composed of active triangulation devices capable of measuring 3D shapes. Stereo-vision, i.e. a vision system composed of two cameras, is often used in 3D scanners for detecting 3D surfaces from a single position.

Laser scanners, such as the 3Shape scanner [61] (**Figure 2.15 a**), are composed of a laser that illuminates the surface of an object and a stereo vision system able to detect the position of the illuminated spot. By controlled movement of the light source and of the object it is possible to illuminate the whole surface.

Differently structured light scanners project onto the object surface an extensive structured light. The detector registers at once the whole field of view for a 3D reconstruction without the need for any movement (**Figure 2.15 b**). The projected patterns can consist of

speckle patterns, lines, grids, sine grids or more complex coded light. Two main approaches can be identified for structured light scanners. In the first approach the projected light is used only to create a homologous point on the object surface to be used in the triangulation reconstruction from the image of the stereo-vision system, as in photogrammetry. The second approach instead estimates the position of the surface points as function of the deformation of the light pattern projected on the surface. This method requires only a single camera, but several coded lights have to be generated by a computer controlled LCD projector. Different type of coded light can be used in structured light sensors, such as a single-frequency sine pattern with different phases (phase shifting technique) or binary grey coded light [33], [74]. The complete scan of complex objects may require the measurement from several orientations to avoid shaded areas not being recognized.

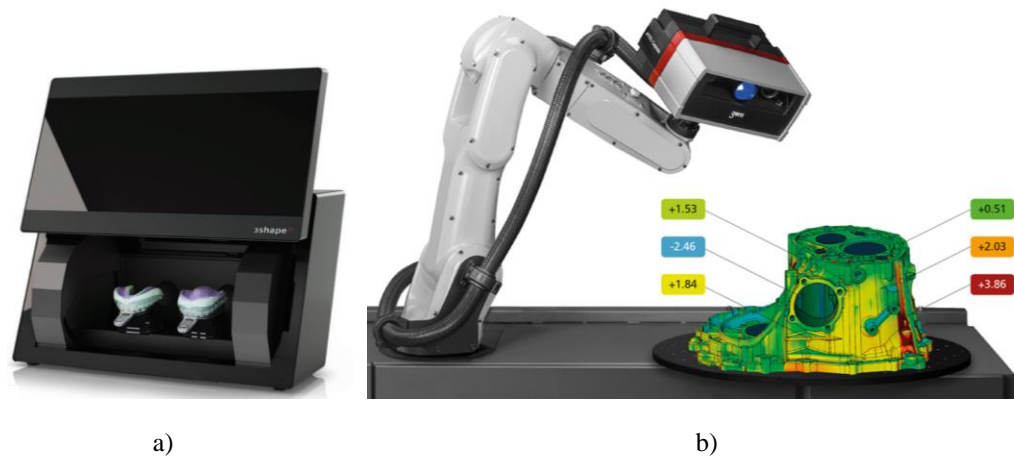


Figure 2.15 3D optical metrology: laser scanner [61] and structured light scanner [62].

Focus techniques

Focus techniques are a class of geometric optical sensors that exploit the concept of in-focus and out-of-focus imaging. In particular these techniques measure the distance of the surface from the sensor in the direction of the axis of the optics. Four main types of focus technique are identified, namely:

- Chromatic confocal sensors
- Confocal microscopy [48], [77]
- Focus variation microscopy[48]
- Autofocus sensors [38], [44].

Chromatic confocal sensors

They are also called polychromatic confocal sensors or chromatic white light sensors. These sensors use a highly broadband or multi-wavelength light source and exploit the

property of chromatism, typical of almost all optical components. Chromatism refers to the creation of different focal planes for different wavelengths (**Figure 2.16**). This creates a chromatic dispersion of light along the optical axis. In a confocal configuration therefore the light arriving at the detector has a specific wavelength that has the focal plane coincident to the surface plane. Using a decoding device like a spectrometer it is possible to measure the axial position of the surface. The great advantage of these sensors is that they do not require a scanning movement along the optical axis as for the confocal scanning microscopy. They also offer the advantage of being insensitive to ambient light and to work both on reflective or diffusive surfaces, even though low reflective surfaces cannot achieve high signal to noise ratio. The resolution of the sensors is linked to the amplitude of the chromatic dispersion, from $0.015\ \mu\text{m}$ to $0.25\ \mu\text{m}$. The measuring range goes from $0.5\ \mu\text{m}$ to $5\ \mu\text{m}$ [41], [48], [77].

Chromatic confocal sensors can be used in a surface topography measurement or as distance sensors in length measurement applications. Commercial systems usually consist of an optoelectronic controller (composed of light source, beam splitter and a spectrometer) linked to the optical probe (optical head) with an optical fibre. Multisensor CMMs are often equipped with a chromatic confocal sensor [48].

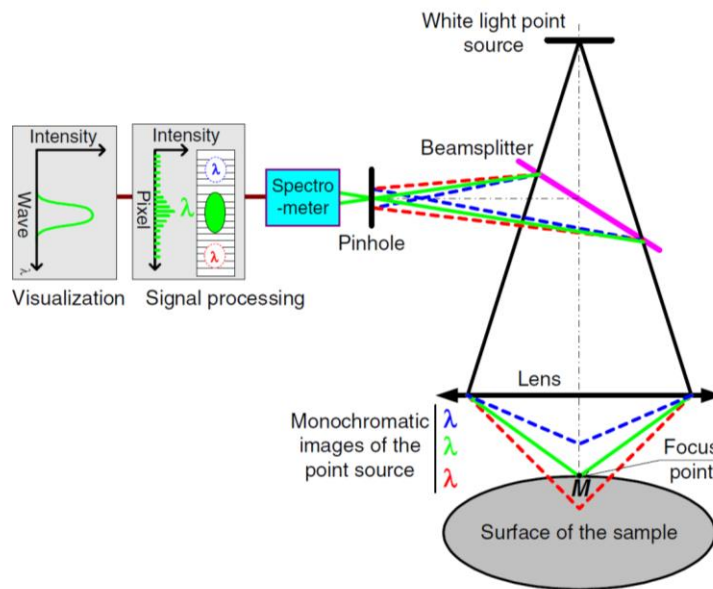


Figure 2.16 Working principle of chromatic confocal sensors [78].

Photogrammetry

Photogrammetry is a particular vision method in which several pictures are matched together to generate a 3D model of the object. Historically photogrammetry has been used in non-industrial applications, such as geology and civil engineering. Nowadays it is widespread as well in manufacturing engineering especially in the field of large scale

metrology [55]. Recent works have documented the possibility to apply photogrammetry also to small scale metrology [63], [79]–[81] and microscopy [82]. Several other applications regard process monitoring [83], medical applications (body and facial scanners[70], [84]), material testing[64], cultural heritage[85].

Photogrammetry applications can be separated according to different features [86] such as:

- Distance between the object and the camera sensor: from satellite photogrammetry to close range photogrammetry (distance less than 300 m).
- Number of pictures used in the reconstruction: stereo photogrammetry (two pictures), multipicture photogrammetry.
- Offline - online measurements: in offline systems the image acquisition stage is decoupled from the processing; one camera is sufficient for taking several pictures. Online systems require a synchronized stereo or multi camera layout; they are suitable for dynamic measurements, such as robot trajectory tracking. Online systems are generally more precise than offline systems [66].

Photogrammetry systems consist of dedicated hardware and software or, alternatively, of off-the-shelf components coupled with dedicated software. The first group consists of stereo photogrammetry or multi-camera scanners. The second group is composed of systems often self-made by the consumer employing DSLR cameras and commercial/open source software. Dedicated hardware is more expensive but better performing and gives several advantages such as the possibility to run online measurements (fast and synchronized photo acquisition). Thanks to their stable structure they require less frequent calibrations. In some cases they are equipped with light projectors, such as fringe projectors, to help the model reconstruction. Self-made systems are considerably cheaper but they rely on the software algorithm for calibration and error compensation. Calibration procedures must be performed frequently to have a beneficial error compensation, especially considering thermal instability of the camera system[87]. These systems gained popularity in recent years thanks to the increasing performances of commercial digital camera and the increasing of computational power of modern computers.

An advantage of photogrammetry is the possibility, to some extent, of measuring large and small objects with the same technique. In fact the calculation algorithm is independent of the size of the object in the picture. Considering the case of a photogrammetry system using a DSLR camera, the same camera equipped with different lenses with different magnification can be used for scanning objects of different size. The downscaling process however creates some issues especially regarding the camera calibration of lenses with different characteristics [80].

Calibration

When using general purpose cameras and lenses, the distortions on the image due to lenses defects must be identified and compensated using a camera calibration procedure. This step gives a series of parameters for reducing the radial and decentring distortions [71]. It is generally performed by acquisition of pictures of a grid, a chess-board or a matrix of dots and a comparison of pictures and real object (**Figure 2.17**).

When more precise measurements are required a more complex 3 dimensional artefacts can be used for lens calibration [70].

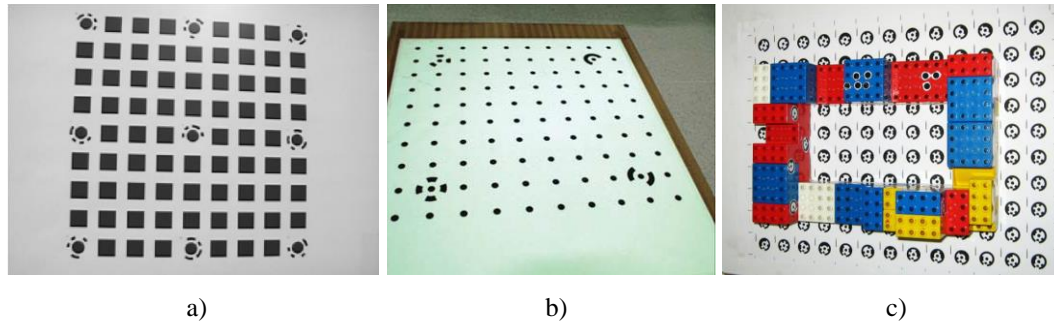


Figure 2.17 Artefacts used for camera calibration: a) grid [72], b) dot matrix [88], c) 3d artefact [70].

Measurement procedure

The procedure to create a virtual model of the object under measurement starts with the acquisition of several images of the object from different angles. At least two pictures are necessary (stereo photogrammetry), however several pictures are needed to ensure a certain level of redundancy especially when the surface of a complex object has to be scanned [89]. The total scanning and reconstruction time depends on the application. It can be negligible as in the case of online stereo photogrammetry, or as long as several minutes [63]. The total measuring time increases with the accuracy required since the number of necessary pictures increases (both scanning and reconstruction time increase).

The images are then merged together through a bundle adjustment algorithm. The algorithm simultaneously estimates the optimal parameters of position and orientation of the camera for each picture through a minimization of a cost function [90].

For a successful bundle adjustment and reconstruction of the 3D model some distinctive control points must be available in the camera field of view. They can consist in distinct features the object surface. Artificial markers or projected light can be used as well as control points. They are preferred to natural object features since they provide a substantial improvement in the accuracy [55]. The surface appearance of the workpiece is crucial for obtaining low measurement uncertainties when markers are avoided. In some cases it might be necessary to treat the part with special paints to obtain a cooperative surface for a better measurement uncertainty [63].

Alternatively to markers and structured light some reference objects or scales can be placed in the field of view of the scanner. If a calibrated object is chosen, such as a grid a scale or a sphere, it also helps to establish a traceable measurement. The issue of the surface appearance is however still a problem.

Large scale metrology

As mentioned before, photogrammetry is widely used in large scale metrology applications. The availability of portable scanners makes it possible to measure an object, or portion of an object, of any dimensions. As it is the most developed application in industrial metrology many commercial solutions are available.

Although using the same principle of image based measurement, several different measuring methods can be found [66]:

- Single point measurements: the position of a single point on the surface of the object is measured using a hand touching probe with coded markers. The system can detect position and orientation of the probe using several cameras.
- Multi-point measurements: the scanner detects the position of coded targets placed on the object. This method is used in dynamic measurements, for instance for robot movement tracking.
- Surface scanning measurements: The whole surface of the object is detected during the measurements. Cooperative surface and proper lighting are two necessary features.

Commercial scanners often combine photogrammetry measurements with phase shift measurements using fringe projection light, as in the case of the ATOS Triple Scan [55].

Small objects

When dealing with small size object (less than 0.5 m) photogrammetry is employed as a surface scanning system. Commercial scanners with a relatively large field of view, such as the Atos Triple Scan, can be used for measuring small objects. Long measuring distance and not-optimized resolution are however expected. Many efforts are addressed to develop scanning systems employing DSLR cameras and dedicated software.

Galantucci et al. developed several scanners using only commercial photographic cameras (**Figure 2.18**).

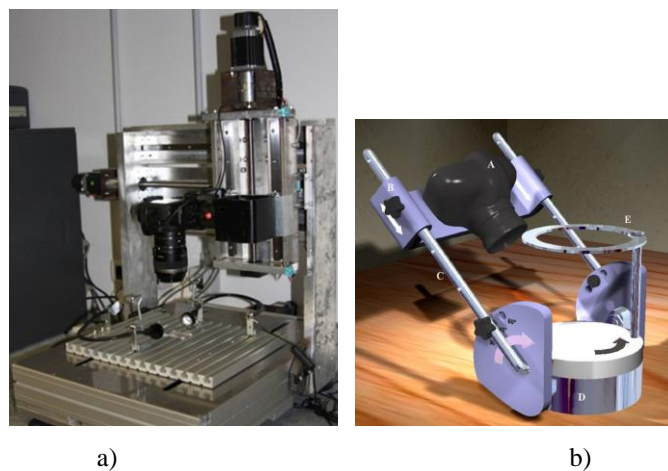


Figure 2.18 Photogrammetry scanners using a DSLR camera and a) translation movements [91] b) rotation movements [63].

A typology of scanners has been developed for measuring small objects with sub-millimetre surface features. They employ a single camera and a movement system, translation or rotation for measuring objects smaller than 50 mm [65], [91]. Measurements with precision better than 5 μm have been documented [65].

Digital image correlation DIC

Digital image correlation is a technic used to detect surface strain and displacements of a specimen. It is widely used and accepted as non-contact measuring method in mechanical testing. It is a valid alternative to other optical techniques such as interferometric or holographic techniques since it requires less sophisticated hardware and lower environmental requirements [67]. Typical applications are related to experimental solid mechanics, such as measurements of strain field of a loaded specimen and measurement of the mechanical properties like Young modulus; it can be used in thermomechanical applications, such as measurements of the coefficient of thermal expansion or measurements of thermal strain [69]. DIC is not widespread in the field of dimensional metrology; however it represents a valid technique in the specific application of dynamic length metrology where the dimensions of a part are changing through time.

The method of DIC consists of a comparison of a picture of the surface of the sample at the initial reference state with a picture of the same detail at the final state. The experimental setup is very simple since it requires only a camera and a light source besides the specimen and a computer for the image processing (**Figure 2.19**). The imaging system can consist of a digital camera as well as a microscope (optical, SEM, AFM) or a thermocamera.

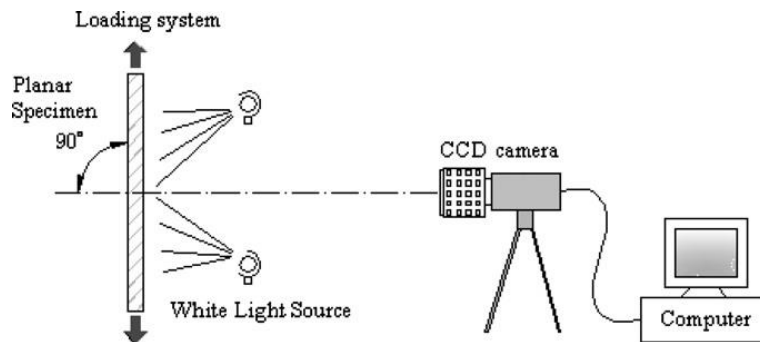


Figure 2.19 Experimental set up for DIC [67].

DIC can be used to detect in plane 2D displacement or 3D displacements. The first case requires only a single camera oriented orthogonally to the surface to be measured. Despite its simplicity the system has to ensure that the distance between the camera sensor and the surface remains constant to avoid changes in the magnification of the pictures. To meet this requirement the sample surface must be flat and parallel to the sensor plane. Moreover the out of plane displacements must be minimized. To reduce the influence of the out of plane displacements the camera can be equipped with a series of telecentric

lenses or can be placed far from the measuring object to make the incoming light beams as parallel as possible [92].

Digital image correlation can detect 3D displacement fields as well when a stereovision system composed by at least two cameras is used. Exploiting the stereovision properties the system is also able to detect the out of plane displacements. The higher geometrical freedom is ensured however by a more complex system and by a longer computation time.

The surface of the sample must have some distinctive features. The quality of the surface patterns plays a fundamental role on the effectiveness of the DIC. Ideally the surface pattern must be random, isotropic and with a high density of features. Random speckle patterns represent therefore the optimal pattern type. In a few cases speckles already appear on the sample surface [93]. However in most cases the speckles must be created artificially using a coherent light source to create interferometric laser speckles or spraying the surface with a black and white paint. Other types of surface features can be accepted with a consequent loss of performance. Periodic features may compromise the results of the correlation process because of their similarity over a shift of a period. Directional features instead are suitable for measure displacement in the direction orthogonal to the features.

The accuracy of the DIC method depends on different aspects of the measuring process. A first source of errors can come from the experimental setup. The alignment between camera and sample is an important factor to consider when 2D-DIC is implemented. As mentioned before the sample should be parallel to the camera sensor. Misalignment of less than 5° give errors lower than 0.01 pixels [67]. Also the out of plane displacement must be limited. Errors can come from distorted images caused by imperfections in lenses and camera sensors. When low-cost hardware is used it is important to perform a camera calibration procedure to determine and compensate the picture distortion. Self-heating of the camera may induce a variation of the distance sensor-sample and could create a not negligible error [95]. The quality of the specimen surface is another important factor to consider in improving the quality of the DIC method. It has already been mentioned how the surface patterns interact in the displacement method. The quality of the surface pattern is influenced by features such as the dimension and density of the speckles and the contrast between bright and dark spots. Another important category of errors is related to the image processing. First of all the subset size must be chosen adequately and mostly based on the dimension of the speckle pattern. Bigger subsets contain more features and therefore are less sensitive to noise and lead to more accurate results. On the other hand adopting a small subset increases the spatial resolution of the resulting displacement field [96]. Moreover the accuracy of DIC can be increased by choosing normalized correlation criteria and more precise subpixel registration methods.

Optical CMM and articulated arm

Traditionally coordinate measuring machines and articulated arms are equipped with contact probes. They are well established in the field of industrial metrology due to the high versatility and high accuracy achievable. Optical probes have been introduced in the CMM systems to fulfil the requirement of high scanning speed, high density of measuring

points and need to measure flexible and small parts. The uncertainty however increases for measurement performed using an optical probe. Different types of optical measuring devices can be integrated into CMMs. The most common are video probes, triangulation probes, autofocus systems and conoscopic holography [33] (**Figure 2.20**).

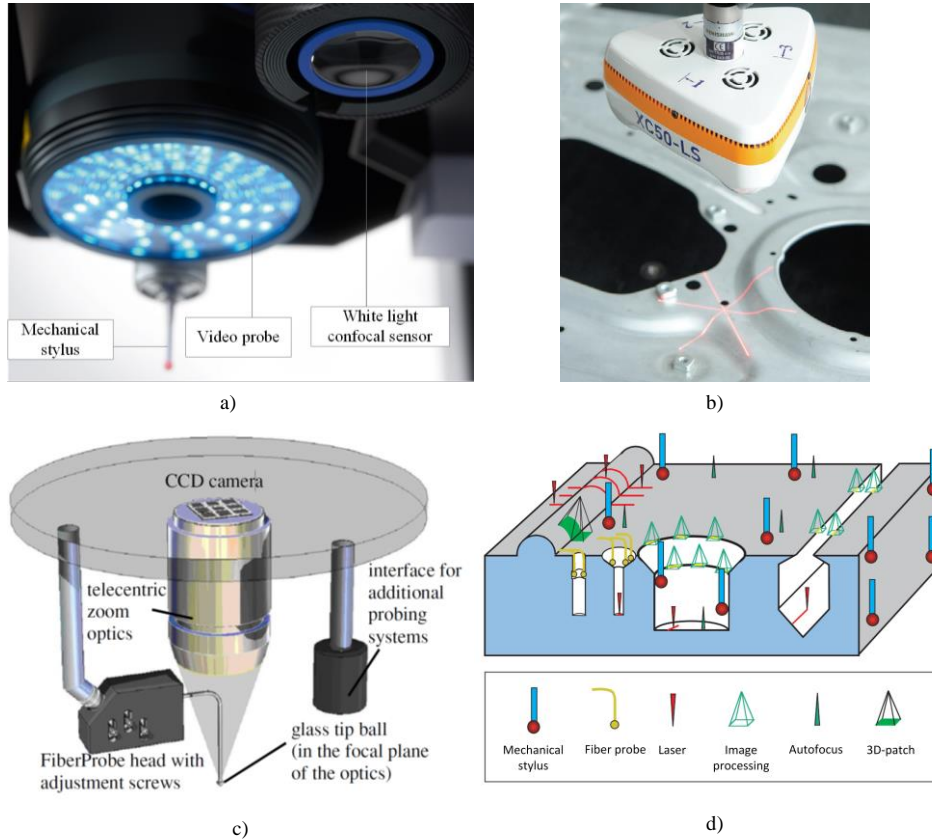


Figure 2.20 Optical CMMs: a) multisensory CMM [98]; b) laser scanner probe [33]; c) opto-tactile fibre probe [39]; d) multisensory CMM application [99].

Video probes are composed by a digital camera and adequate microscope optics and illumination. Usual magnification factor stands between 2x and 20x with consequent resolution up to 0.5 μm per pixel. Subpixel image processing helps to achieve an effective resolution several times higher. Telecentric lenses are used to ensure the same magnification for all the features in the depth of focus of the system. Video probes are usually equipped with three types of illumination: coaxial top light, diffusive top light (ring light) and back light. The combined use of the three lights allows for bright field, dark field and mixed measurement conditions. The measurement consists of the detection of the edges in the field of view of the camera. The measurement accuracy is therefore influenced by the performed digital image processing aside from the measuring hardware (camera, optics distortion, CMM movements, and illumination) and the measuring object [38]. Accu-

racy of 10-20 μm can be achieved by video probes under general working conditions [97].

Laser scanners, autofocus, chromatic confocal sensors and conoscopic holography can be used as distance sensor (point sensor), line sensor or area sensor. Major CMM producers offer optical scanning probes as an alternative to contact probes.

An opto-tactile fibre probe has been designed by PTB and Werth Messtechnik GmbH for measurements of micro features, such as micro holes in conventional CMM. The working principle is depicted **Figure 2.20 c**. The probe is composed of a micro sphere supported by an optical fibre stylus. The sphere is illuminated with light travelling through the fibre and its position can be detected by a measuring microscope. The diameter of the sphere can be as small as 0.25 μm . The high radial flexibility of the fibre stylus allows the measurement with a probing force in the order of μN . The measurement uncertainties are in the range of 0.2-0.3 μm

Multisensor CMMs combine several measuring devices, usually a contact probe a video probe and a distance sensor, in a common coordinate system to exploit the benefits of the different technologies [38].

2.3.4 Applicability to DLM

The requirements for the application of an optical system in Dynamic Length Metrology can be summarized as:

- Suitability to shop floor application. In this sense the optical system has to be robust, not affected by vibration and ambient condition changes.
- The system must be easy to use and user-friendly to avoid the necessity of a specially trained operator.
- Limited costs of the optical system are important in order to offer an attractive alternative product to the industry.
- The possibility to be integrated in a more multisensory measuring device. Therefore the size of the optical system must be limited and the connection to a sensor net must be easy. The use of off the shelf components might be useful to simplify the multisensory network development.
- A resolution in the order of 0.1 μm and a measuring accuracy below 1 μm to be a valid alternative to contact probes, especially inductive probes.
- Relatively fast acquisition and processing rates to allow length measurement in a dynamic range.
- Suitability to measure polymer parts.

Table 2.6 compares the various measuring techniques described in the chapter according to the DLM requirements. Interferometric systems have the best performance regarding accuracy. However their performances are sensitive to the ambient conditions and therefore they are not suitable for shop floor applications. Laser scanners, structured light scanners and photogrammetric systems are sturdy technologies meant for industrial applications. The measuring procedure however is quite long considering the scanning phase and the post processing. Moreover as standalone systems they can not be easily combined in a multisensory measurement station. Similar considerations can be done for CMMs.

Photogrammetric systems have the advantage that they can be designed by the users with the possibility to develop particular integrated photogrammetric systems. Point and line laser sensors on the other hand are cheap and flexible devices but they lack in measurement accuracy especially when measuring polymer parts. Chromatic confocal sensors seem a valid alternative besides the high costs of the optoelectronic controller. Digital image correlation and in general digital image processing result in a cheap, fast and easy to integrate in a multisensory device.

Table 2.6: Applicability of optical technologies to DLM.

	<i>Fast acquisition</i>	<i>Resolution/accuracy</i>	<i>Multisensory integration</i>	<i>Shop floor suitability</i>	<i>Costs</i>	<i>Measurements on polymer</i>
Intensity based sensors	++	--	+	+	++	+
Laser interferometry	+	++	-	-	--	+
Conoscopic holography	+	+	-	+	--	+
Chromatic confocal sensors	++	++	+	+	-	+
Point/line laser sensor	++	-	+	+	++	-
Laser scanner	-	-	+	+	+/-	-
Structured light scanner	-	-	-	+	-	-
Photogrammetry	-	+	-	+	++	-
Digital image correlation	++	-	+	+	++	+
Optical CMMs	+	+	-	+	--	+

Note:

- ++ Very suitable for DLM
- + Suitable for DLM
- Unsuitable for DLM
- Very unsuitable for DLM

2.4 Reference artefacts

Reference calibrated artefacts are used in dimensional metrology in calibration and acceptance tests. They represent a fundamental link in the traceability chain. Traceability is defined as *the property of a measurement result whereby the result can be related to a reference through a documented unbroken chain of calibrations, each contributing to the measurement uncertainty* [100]. A calibration procedure for a specific measurement, such as in the case of task specific CMM measurements, consists of the measurement of the calibrated artefact using the same equipment and similar procedure as in the measurement of the workpiece [25]. Hence reference artefacts have to resemble as much as possible the geometrical characteristics of the measuring workpiece. Reference artefacts have to provide documented traceability, namely through a calibration certificate, without introducing further measurement errors and uncertainties due to form errors and surface texture. Gauge blocks are widely used as reference artefacts and they comply with the abovementioned requirement. In fact the surfaces involved in the calibration are polished with limited flatness deviation [16], [101]. Material used for gauge blocks are usually steel, ceramic (Zirconia) and material with low thermal expansion (such as Zerodur). In the case of freeform parts with complex geometries like turbine blades, the reference artefact can be composed by an assembly of components with simple geometries (cylinders, spheres) to resemble the curvature of the workpiece [102]. Reference objects must be dimensionally stable over time to limit the variations occurring between two consecutive recalibrations. Another important requirement in the case of reference artefact for contact measurements is a high hardness to avoid scratches or plastic deformations due to repetitive probing. Invar represents an alternative to steel as material for reference artefacts to be employed in industrial conditions due to its low thermal expansion. Nonetheless its higher sensitivity to corrosion and oxidation reduces its stability over time. Other types of reference object that can be used in contact metrology are step gauges, spheres, ball bars and holeplates. An important aspect when choosing or designing the proper reference artefact is its dimension compared to the measuring object. The working range of the measuring sensor must ensure that it covers both reference and measuring objects. For instance in the case of a measuring device based on inductive probe, with limiting range of ± 0.2 mm, the reference artefact has often to be specially designed.

Artefacts for optical measurements have to comply with different requirements. Dimensional stability is still a requirement however hardness and geometrical errors become less important. The surface appearance plays a central role in optical artefacts as the measurement depends on the interaction between surface and light (both in active and passive measuring methods). When dealing with 2D measuring methods the reference artefacts are often composed by scales, grids or patterns deposited on a glass plate [103]. In this case the edges of the different shapes must be sharp and with limited burrs.

2.5 Metrology frame and structure

The frame and the structural components holding measuring probe and measuring object play an important role in the overall measurement accuracy of an instrument especially in the case of application in non-constant and non-reference temperature conditions. Two main elements, in particular, are to be considered in the development of a measuring instrument: the metrology frame and the positioning fixture.

The metrology frame consists of a series of elements connecting probe and measuring object and which constitute the metrology loop, defined as an imaginary continuous line passing through solid components of the measuring instrument (frame and sensor) and determining the position of the measuring object with respect to the probe (**Figure 2.21**) [104].

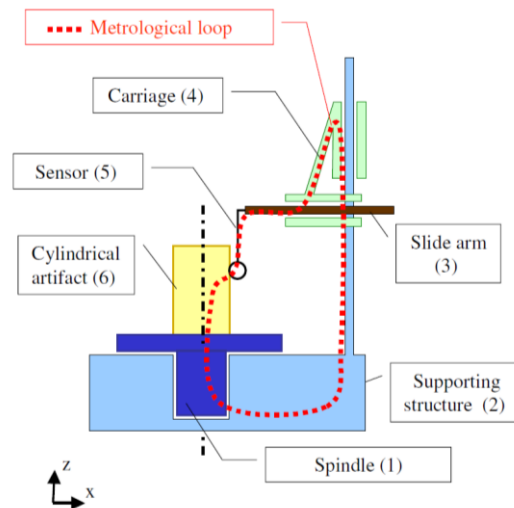


Figure 2.21. Structure of a roundness tester. The metrology loop is highlighted with a red dashed line [104].

The stability of the metrology loop is an important aspect to consider in the design phase for ensuring high accuracy measuring results. Thermo-elastic properties influence the deformation and distortions of the structure. The design of the metrology frame can follow different approaches. A first one is the limitation of thermal deformation by choosing low thermal expansion materials. This approach is however limited by the higher costs of these materials and can be applied only to structures with limited dimensions. Moreover it is an effective approach only in case of uniform temperature fields. Temperature gradients arise in transient conditions and are influenced by the thermal conductivity and the thermal inertia of the frame elements. For high thermal inertia and low conductivity components temperature gradients are maximized. Distortions due to these differential temperature distributions create high amplitude errors and are often not easy to predict. [35]. A design approach consists of using materials with high thermal conductivity, such

as aluminium, to reduce temperature gradients and consequently machine distortions [105]. The choice of the proper frame material is therefore not a straightforward decision [106]. Other solutions optimize the design shape of the frame to limit deformations or temperature gradients. Symmetric and closed shapes, such as full bridge, are less affected by temperature than open shape, i.e. cantilever beam. In accurate measuring systems the structure used to obtain information about the position of the measuring sensor is decoupled from the structural frame and constitutes an independent component of the measuring system. It is therefore possible to design it using more stable and expensive material (Invar, Zerodur). Using kinematic coupling it is possible to mechanically and thermally disengage the metrology frame from the main structure [107]–[109].

Numerical simulation can be used to understand the thermal deformation of the system structure under different thermal conditions and together with temperature measurements can provide an on-line compensation model for thermal deformations [34], [110], [111].

The positioning fixture is a series of components that supports the measuring object and provides an unambiguous location with fixed points. The eventual clamping of the part can be effectuated with elastic elements (springs), friction elements (vice), pneumatic systems (vacuum) or simply by passive forces, such as gravity. Fixtures (and more generally measuring equipment) can be designed for a single workpiece or for multi-workpiece measurements; this last case comprises batch and assembly measurement systems [112]. Positioning fixtures can be designed for a specific component or can be composed by modular elements that can be combined to accommodate workpieces with different shape and dimensions [113], [114]. The unambiguous location, where the position in the space, three coordinates and the three rotations are uniquely defined, can be achieved with six fixed points without over constraining the measuring object. For prismatic parts the 3-2-1 principle is often used: three mutual orthogonal planes representing a local reference system are defined by three, two and one points respectively. Cylindrical workpieces are often supported by a V-block which represents four fixed points and define the orientation of the cylinder axis. Two further fixed points define the axial displacement and the axial rotation of the part [115]. Some measuring systems, like optical scanners, do not require the exact positioning of the workpiece that have a floating positioning. Repeatability of the positioning is influenced by the geometrical errors and surface texture of both fixture and measuring object. To assess the repeatability and reproducibility of the positioning fixture, considering also the influence of the operator and of different workpieces, industrial practice suggests application of a Gauge Repeatability and Reproducibility (GRR) analysis [116].

2.6 Temperature sensors

The interest in measuring temperature in dimensional metrology is linked to the need of limiting the effect of thermal expansion on measuring object and equipment. An important distinction has to be made between contact and remote sensing since they involve different aspects and problematics. Both contact and non-contact technologies are suitable

for surface temperature measurements hence in the case of non-uniform temperature conditions, such as in the case of DLM, modelling and simulation are important tools for assessing the temperature in relevant locations of a part.

2.6.1 Contact sensors

These are usually composed of three main elements: a sensing element, terminals to connect the sensing element to the external electronic circuit and a shield to protect and support the sensing element [117]. Contact sensors always detect their own temperature [118]. Establishing a connection with the interest body leads to a change in their temperature that reaches a value constituting an approximation of the temperature to be measured. Thus the thermal coupling between these two bodies has a major influence in the measurement accuracy. More specifically the heat transfer coefficient must be maximized to ensure a proper coupling. The thermal inertia of the sensor, considered as the product of mass and specific heat, has to be limited to reduce the sensor reaction time in the case of dynamic measurements and to limit the load effect consisting of a disturbance in the temperature field due to heat flow from object to sensor [119]. In a realistic case temperature sensors are also thermally coupled with other objects, for example the terminal wires and air, introducing a further error source [117]. The sensing element has to be isolated to limit the heat flow towards external bodies. **Figure 2.22** represents the realistic case where a sensor is connected to an object to measure its temperature T_B . The measurement can be performed after an initial period where the sensor temperature changes to reach the object temperature. Due to heat dissipation towards external bodies the sensor can never reach the object temperature. A disturbance is visible in the object temperature when the sensor is connected [117]. Another important aspect that affects the uncertainty of the measurement is the isolation from electromagnetic noise. In the case of sensors based on electrical principles, such as resistance sensors, their output is sensitive to electromagnetic interference and all the components must be protected, especially when they extend for a long distance. Electromagnetic noise picked up by wires can be limited using twisted or coaxial cable and grounded shields [120]. The wires are usually isolated and protected from external elements, like humidity, using polymeric (Teflon, polyvinyl chloride PVC) or composite (fibreglass) materials. The most used contact sensors in dimensional metrology consist of resistance temperature detectors, thermistors and thermocouples.

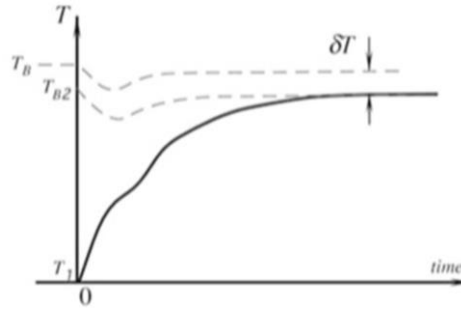


Figure 2.22 Temperature profiles during dynamic temperature measurement: T_B =object temperature, T_1 =measured temperature [117].

Resistance temperature detectors

Resistance temperature detectors, or RTD, are metallic elements where the electrical resistance changes with the temperature. They are among the most frequently used temperature sensor due to their high accuracy, linearity and long term stability. The most common material used of the sensing element is platinum due to its highly linear resistance variation as function of temperature; other materials used are copper, nickel and tungsten. Platinum made RTD are often called platinum resistance thermometer, PRT, or platinum thermometers followed by their nominal resistance value, for example PT100. Reference temperature are usually 10, 100, 500, 1000 Ω . In a range of temperature from 0 to 850 $^{\circ}\text{C}$ the resistance of PRTs can be expressed as [121]:

$$r_T = r_0 \cdot (1 + a \cdot T + b \cdot T^2) \quad 2.8$$

Where:

r_T is the resistance at the temperature T ;

r_0 is the resistance at 0 $^{\circ}\text{C}$;

$a = 3.9083 \cdot 10^{-3} \text{ } ^{\circ}\text{C}^{-1}$;

$b = -5.775 \cdot 10^{-7} \text{ } ^{\circ}\text{C}^{-2}$.

The sensing element can be composed by a coiled wire or by a thin film that is supported and protected by an element made of different materials, depending on the application [120]. They are divided into four tolerance classes (AA, A, B, C) depending on the tolerance on the measured temperature [121]. The measurement of the variation in the resistance is performed using a Wheatstone bridge circuit and then converted to a temperature value. The use of a three and four wire bridge type helps for removing the influence of the resistance of the lead wires which represent the most significant error in resistance thermometry. To measure the resistance of RTDs the sensing element must be powered with electrical current creating self-heating and introducing interference in the temperature field. To limit self-heating the current is limited, usually lower than 1 mA for a PT100.

Thermistor

Thermistors are elements similar to RTD where the resistance changes are related to temperature variations. However they are made with non-metallic material, such as ceramic (metal oxide) and semiconductor materials. Their response to temperature is highly nonlinear and can be both positive (positive temperature coefficient PTC) or negative (negative temperature coefficient NTC) depending on the material of the sensing element. The high sensitivity allows reducing the size of the sensor and consequently its thermal inertia. Similarly to RTDs they are affected by self-heating issues.

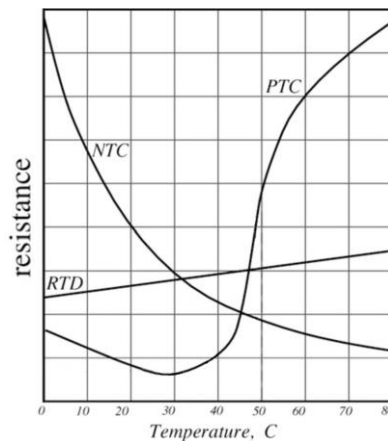


Figure 2.23 Thermistors (NTC,PTC) response compared to RTDs [117].

Thermocouple

Thermocouples, also called thermoelectric sensors, exploit the thermoelectric property called Seebeck effect. When two conductive elements of different materials are connected at two points to create a closed circuit and the two junctions are exposed to different temperatures a differential voltage generates between the junctions causing the flow of current. The voltage produced is proportional to the difference in temperature of the two junctions. Thermocouples are composed by two conducting wires of different materials connected at one end and connected to a voltage meter on the other **Figure 2.24**. The connection to the voltage meter must be at a uniform temperature; it is often referred as cold junction or reference junction. It must stay at a constant temperature to ensure that the voltage measured is directly proportional to the measurement junction temperature. In modern systems the temperature of the cold junction is not fixed, nevertheless it is measured with an absolute temperature sensor (i.e. RTD) and its influence compensated [117]. Thermocouples are classified according to the materials of the two wires; the most used types are listed in **Table 2.7**. They are divided into three tolerance classes (Class 1,2 and 3) [122]. Thermocouples are the most diffused temperature sensors [120] due to the simplicity, reliability and costs. They are less stable than RTDs but they have a wider measuring range, useful especially for process control application.

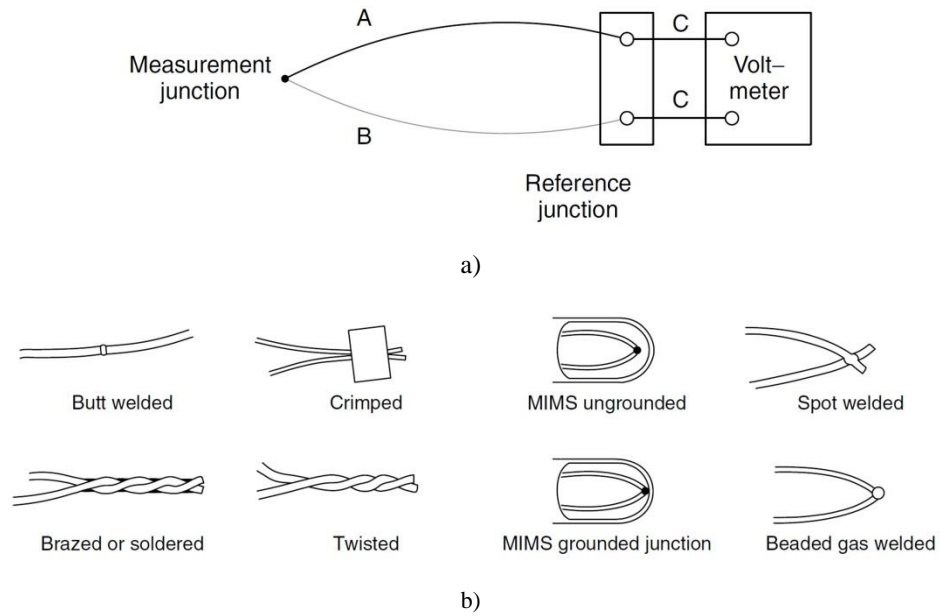


Figure 2.24 Thermocouples: a) basic measuring circuit; b) type of junctions [120].

Table 2.7: Types of thermocouples [118].

<i>Type</i>	<i>Materials</i>	<i>Max. temperature °C</i>	<i>Sensitivity at 20 °C /μmV/°C</i>
B	Pt 30% Rh / Pt 6% Rh	1700	0
E	Ni-Cr alloy / Cu-Ni alloy	870	60.5
J	Fe / Cu-Ni alloy	760	51.5
K	Ni-Cr alloy / Ni-Al alloy	1260	40.3
N	Ni-Cr alloy / Ni-Si alloy	1300	26.6
R	Pt 13% Rh / Pt	1400	5.9
S	Pt 10% Rh / Pt	1400	5.9
T	Cu / Cu-Ni alloy	370	40.3

2.6.2 Infrared sensors

All bodies at temperatures above absolute zero absorb and emit electromagnetic radiation. For an ideal body, referred as blackbody, the incident radiation is completely absorbed and emitted. For a real body the incident radiation is partially absorbed, reflected and transmitted. The radiation emitted by a real body can be related to the ideal case with the parameter of emissivity ε :

$$\varepsilon = \frac{M(T)}{M^B(T)} \quad 2.9$$

Where:

M is the radiant emittance of a generic body at the temperature T ;

M^B is the radiant emittance of a blackbody at the temperature T .

The emissivity represents also the percentage of the incident radiance that is absorbed. Similarly the concept of transmissivity τ and reflectivity ρ can be introduced as the percentage of radiation transmitted and reflected. Emissivity, transmissivity and reflectivity are always lower than 1, while their sum is always equal to 1, as they represent a portion of the total incident radiation. Emitted radiations of non-ideal bodies depend on the body features like material and surface appearance, on the entity of the radiation, wavelength and direction of radiation. Thus for a defined body emissivity can assume different definitions depending on the considered wavelength and direction. For practical engineering applications the hemispherical total emissivity is considered. The entity of the thermal radiation of a blackbody, intensity and wavelength, depends on the temperature of the body according to Planck's law. For a generic body the emitted radiance at the absolute temperature T is:

$$M = \varepsilon \cdot \sigma \cdot T^4 \quad 2.10$$

Where:

σ is the Stefan-Boltzmann constant, equal to $5.67051 \times 10^{-8} \text{ Wm}^{-2}\text{K}^{-4}$;

ε is the hemispherical total emissivity.

Hence a directly traceable temperature measurement can be created correlating the radiance of a body to its temperature using thermodynamic laws. Nevertheless the measurement must consider correction due to reflected and absorbed radiation (proportional to $1-\varepsilon$) and other error source [118], [120].

Below 500 °C all radiations are in the infrared spectrum thus the measurement of temperature using radiation is referred to as infrared measurement. Calibration of infrared sensors is performed using high emissivity reference objects which are considered as blackbody. These artefacts are constructed with materials with high emissivity (often it is sufficient to use coatings) and with particular geometries to trap incident radiations.

Infrared temperature detectors can be divided in two main groups: photon (or quantum) detectors and thermal detectors. Photon detectors are composed of elements, such as photodiodes or photoconductors, which create an electrical voltage when excited with electromagnetic radiation. Elements of thermal detectors have properties sensitive to tem-

perature; initially the electromagnetic radiation is converted into thermal energy that changes temperature and properties of the sensor elements, i.e. as resistance in a bolometer. In single spot sensors the detector is composed of a single sensing element while in thermal cameras an array of elements is placed in the focal plane of the lenses [123]. Another important element of infrared sensors is represented by the lenses; they define the field of view and the working distance of the system. A relevant parameter used to describe the performance of an infrared measurement system is the noise equivalent temperature difference (NETD) that is defined as the temperature difference between ambient and object that generates a signal level equal to the noise. It represents the resolution of the detector [124]. Other quantities relevant to define the sensor are wavelength band range, temperature range, field of view and spatial resolution in the case of array detectors. Most thermal cameras nowadays are equipped with micro bolometer arrays. They are cheaper than photon sensors yet they have a slower response, lower sensitivity and strong dependency on the temperature of the detector. Photon detectors are used for more challenging applications since they have smaller NETD and higher acquisition frequency. Photon detectors must be cooled to reduce the signal noise while the temperature of thermal detectors must be stabilized [123].

The total radiance P_m of an opaque target object measured by an infrared sensor can be described as:

$$M_m = \varepsilon \cdot M(T_t) + (1 - \varepsilon) \cdot M(T_b) \quad 2.11$$

Where

ε is the emissivity of the target object;

$M(T_t)$, $M(T_b)$ refers to the radiance emitted from the target and the background respectively.

The temperature of the target body can then be extracted knowing the other quantities and the relationship between measured radiance and temperature.

Infrared temperature measurements rely on the knowledge of the emissivity of the measuring body. Accurate measurements of emissivity are performed with radiometers and are also capable of detecting the influence of wavelength and directionality [125], [126]. Thermal cameras however detect radiations within a defined wavelength band. Therefore objects are considered as grey bodies that are defined as objects having constant emission for the entire wavelength band of interest. Hence for practical applications the hemispherical total emissivity is of interest and can be estimated directly with an infrared temperature sensor. Three techniques can be exploited [127]. The first one requires the use of a well-known emissivity coating or tape to put on a partial area of the measuring object that must be at a different temperature than the background. If the temperature of the object is homogenous the target emissivity ε_t can be estimated as:

$$\varepsilon_t = \frac{M_t - M_b}{M_r - M_b} \cdot \varepsilon_r \quad 2.12$$

Where

ε is the emissivity;

M is the total radiance measured with the infrared sensor;

t, r, b refers to the target, reference and background respectively.

The second method requires the use of a reference temperature measurement, for instance performed with a contact sensor. The target emissivity is:

$$\varepsilon_t = \frac{T_t - T_b}{T_c - T_b} \quad 2.13$$

Where T_c is the temperature measured with the reference sensor.

If the target object is at the same temperature as the background the emissivity estimation is not possible since the emitted radiation can not be properly separated from the reflected one.

A third method requires the target to be at two different temperatures levels. The estimated emissivity is:

$$\varepsilon_t = \frac{T_{t1} - T_{t2}}{T_{c1} - T_{c2}} \quad 2.14$$

Where

T_{t1} and T_{t2} are the temperatures measured with the infrared sensors for the two thermal conditions;

T_{c1} and T_{c2} are the reference temperatures for the two thermal conditions.

Typical applications of infrared thermography (using thermal camera) are in civil engineering as building diagnostics [128], in material science for detecting defects in non-destructive testing and to measure temperature fields during material testing and in general applications to detect failure in components [129]. All these applications require a relative temperature measurement, since they are mostly focused on temperature differences in the target component. Other applications requiring absolute temperature measurements are in metal cutting [130] and material testing [131]. In a DLM application an absolute temperature measurement is necessary and can be achieved with thermography accepting an increase of the measurement uncertainty.

A complete and yet simplified model describing an infrared temperature measurement is depicted in **Figure 2.25**. Two main sources of errors can be identified, namely internal and external errors. The first class includes all the errors due to the measuring instrument such as detector sensitivity, noise, resolution error, drift, lens distortion, non-uniformity of the detector (especially in the case of thermal cameras). To cope with non-uniformity and drift thermal cameras have an internal calibration system known as non-uniformity correction, or NUC [123], [132]. External errors include the uncertainty on the emissivity of the target object, effect of the radiation emitted by the surroundings and reflected by

the target and radiation absorbed and emitted by the atmosphere. Absorption is mainly caused by molecules of water, carbon dioxide and ozone [124]. The surroundings can be considered as a blackbody at the ambient temperature. Another source of error is represented by the detector radiance that is reflected either by the atmosphere or by the target object. Depending on the detector temperature a warmer or colder reflection is visible at the detector output. This effect is also known as Narcissus effect [123]. The most influent source is represented by the uncertainty of the object emissivity that results in being dominant over the influence of ambient temperature and humidity and distance between object and detector [133], [134].

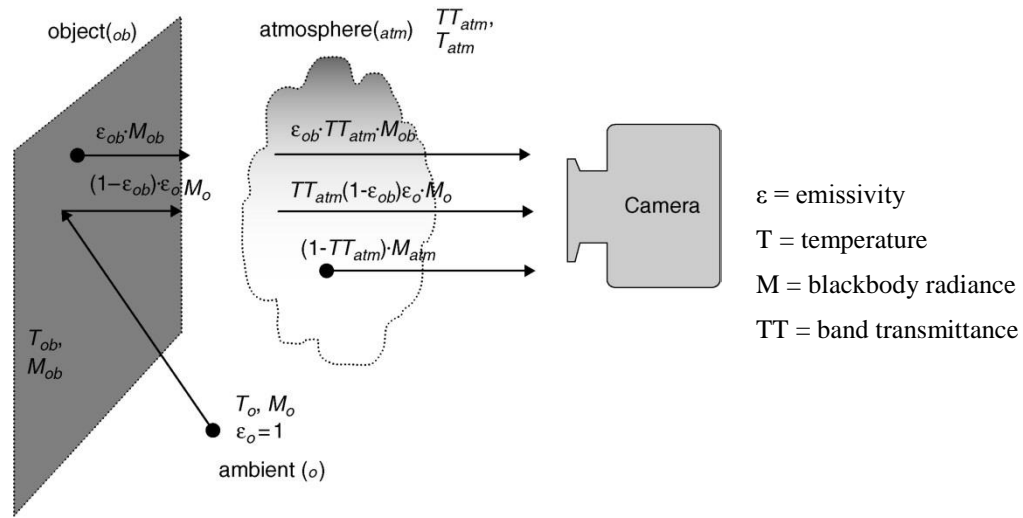


Figure 2.25 Infrared temperature measurement: radiation model [124].

2.7 Conclusion

The topic of dimensional measurements in production environment is initially discussed.

The influence factors that affect dimensional stability and dimensional measurements are presented. A comprehensive list of these factors is already available in ISO 14253-2. The focus of the discussion is however oriented on quantities that cause workpiece dimensional instability in the post production period more than the one causing constant systematic variations. The focus is oriented to instabilities affecting polymers. Three main categories of contributions are defined, namely temperature, humidity and stress driven instability. Temperature causes thermal expansion of any components, which can be quantified with the thermal expansion coefficient. As the measuring equipment is also influenced by temperature a systematic variation on the measured length value which

does not correspond to an actual change in the workpiece dimension can arise. The humidity effect, more specifically the swelling due to moisture absorption, is problematic typical of polymers. It can be described similarly as the thermal expansion with a coefficient of moisture expansion. In equilibrium conditions the moisture uptake is proportional to the ambient humidity and consequently the hygroscopic swelling is a function of ambient conditions. For pure elastic materials the effect of force causes a static elastic deformation. In the case of viscoelastic materials, like polymers, probing forces also causes time dependent creep. Post production shrinkage due to residual stress relaxation is once more an instability affecting viscoelastic materials. It is typical of polymer parts produced by injection moulding. In case of more stable materials (metals and ceramics) only thermal effects and elastic deformations due to probing force are to be considered.

A state of the art on technologies for dimensional metrology is discussed. Sensors for dimensional measurements are categorized in two main groups: contact and optical sensors. All dimensional sensors, and specifically contact sensors, can be classified according to the number of working dimensions as they can measure 1, 2, 3 dimensional quantities. Manual one-dimensional sensors are often used in industrial context due to the limited cost and versatility. The accuracy is however limited to tens of microns and is largely affected by the operator. Another diffused category of one-dimensional sensors is represented by inductive probes. They can be implemented in single point measurements or in more complex fixtures for measuring several dimensions in a single component. The MPE of these devices can be as low as $0.4\text{ }\mu\text{m}$. As an alternative to inductive probes encoder-based sensors offer larger working ranges with slightly lower accuracies. CMM are considered three-dimensional measuring devices. They can perform a vast range of measuring tasks with different type of probes. General values of measuring accuracies can be estimated with calibration and reverification procedures; however task specific uncertainty can be calculated to consider the effect of the measuring procedure.

The main advantage of optical sensors is the absence of contact with the workpiece. On the other hand optical measurements are affected by the surface appearance of the workpiece. The different techniques can be subdivided according to the working principle. Intensity based sensors record the distance from a reflecting plane comparing it with the intensity of the light reflected. Interferometric systems usually provide distance measurements with the highest accuracy. They are directly traceable as they rely on wave properties of light. The disadvantage of having a narrow absolute measuring range can be solved introducing a multi wavelength system. Triangulation systems are very frequently used in industry. This class encompasses techniques such as focus techniques, laser scanners, structured light scanners and photogrammetry systems. Triangulation systems can consist of independent measuring devices, such as laser scanners, or as sensors to be included in a more complex device. Optical CMMs in fact are often equipped with different triangulation sensors, such as autofocus or laser point sensors. Image processing, such as digital image correlation, is included in triangulation technique category as a dimensional measurement of displacement or absolute length which can be performed by analysing picture acquired with a vision probe or a camera. The comparison of optical techniques features with the requirements for DLM reveal that the main limitation is represented by the acquisition time and costs, especially of standalone technologies.

Reference artefacts are a necessary tool to transfer traceability. To limit the uncertainty of the traceability chain ideal objects should be selected as reference objects. In the case of contact measurements low roughness and low form error artefacts are required while for optical measurements it is important to ensure a collaborative surface on the artefacts.

Metrology frame and positioning fixtures are important components of a measuring device. Metrology frame ensures the correct definition of relative position of the measuring object referred to the probing system. The crucial aspect of metrology frame is the thermal stability, which can be achieved with low thermal expansion materials or with particular designs to have a predictable temperature field, coupled with compensation systems. Positioning fixture ensures support and an unambiguous workpiece location. The 6-points principle allows achieving uniquely defined positioning. GRR is a diffuse methodology to analyse repeatability and reproducibility of the positioning fixture.

The measurement of temperature is a crucial aspect of a DLM system. This type of sensor can be divided in contact and non-contact sensors. Contact sensors exploit the property of certain material to produce an electrical output that can be related to temperature variations. They must have a limited thermal inertia to reduce the load effect when they are applied to the surface to measure and to ensure a fast response. Resistance temperature detectors (RTDs), often made of platinum, change their resistance when subjected to temperature variations; they have a highly linear response and they produce a stable and accurate temperature measurement. Thermistors are made with non-metallic materials. The working principle is similar to RTDs; yet they do not reach high level of linearity and accuracy. The working principle of thermocouples is based on the Seebeck effect. Their performance is less efficient than RTDs but they offer a higher measuring range and they are generally cheaper. Non-contact temperature measurements are based on the measurement of the infrared radiance produced by an object. It is a traceable technique since it can be related directly to thermodynamic constants. Nonetheless infrared measurements are largely affected by many error sources. The uncertainty on the emissivity value of the object is one of the principal contributors to the measurement uncertainty. The principal contributors are the uncertainty on the material emissivity, which can be measured with a comparison procedure against a reference surface at the same temperature or with a reference contact temperature measurement. Other contributors are represented by the radiations not directly related to the object emission, due to reflection and absorption. Infrared measurement devices can consist of single spot measurement sensors (pyrometer) or thermal imagers.

3

Experimental investigation on probing systems for DLM

The application of DLM in dimensional measurements introduces new challenges for the probing systems involved. The time variant state requires the simultaneous and fast measurements of different quantities, such as length and temperature. Moreover without previous knowledge of material properties the measurement device has to provide a series of information to extract these properties. For example in the case of contact dimensional measurement, the length at the reference condition of zero contact force can be found with a traditional static compensation of the elastic deformation or with a extrapolation of dynamic measurement performed applying a variable probing force. The dynamic non-uniform thermal state requires measurements of temperature directly on the workpiece and potentially in multiple locations which can be performed with a single thermal imager. Hence unconventional probing systems must be examined to assess the applicability to DLM.

3.1 A measuring device with active force control

The contact displacement sensor selected is a commercial linear actuator equipped with an encoder for a feedback control of the position. The system has been tested using reference artefacts and the uncertainty has been assessed using a statistical method compliant to the “*Guide to the expression of Uncertainty in Measurement*” (*GUM*) [135]. The main contributions to the uncertainty were identified using the *Procedure for Uncertainty Management (PUMa method)* described by ISO 14253-2 [10]. These statistical tools have already been effectively employed in uncertainty estimations of measuring equipment

[82], [136]. The study aims to the determination of the metrological characteristics of the measuring device (described in detail in section below). Random and systematic effects are investigated under different conditions (measuring force and position of the actuator stem). The use of statistical tools allows for the separation of random and systematic contributions of the measurement errors.

3.1.1 Measuring process

Measuring system

The linear actuator is produced by SMAC Corporation (US). The main characteristics are listed in **Table 3.1**. The specific model has been selected as its encoder resolution and small probing force make it a valid alternative to inductive probes. The system is provided with a linear encoder, with a glass measuring scale, to feed a closed loop control. Thus it can move controlling the force, the position, the speed or the acceleration of the stem. A built in instruction package allows it to be used as a contact displacement sensor (the stem moves slowly and stops as soon as the contact with an object is detected).

Table 3.1: Nominal characteristics of the actuator under calibration (from catalogue).

Dimensions / mm	70×55×25
Stroke / mm	10
Voltage supply / V	24
Maximum current / A	1.6
Encoder resolution / μm	0.1
Nominal force / N	3

The reference artefacts consist of grade 0 steel gauge blocks (ISO 3650 [101]) and are used as reference object to be measured. The blocks are wrung together to cover 8 mm stroke with steps of 1 mm. The coefficient of thermal expansion (CTE) of the blocks is 11.5 ppm/°C, as reported in the calibration certificate.

Metrology frame: the main frame consists of a main plate and supports made in Invar, with a CTE equal to 1.6 ppm/°C. The actuator is fixed on the plate by means of two clamps. The gauge block is placed on a flat surface and the correct position on the plane is ensured by a three point contact.

Definition of the measuring task

The output signal of the system consists of the encoder counts. It can be transformed into length units applying a multiplicative factor to be defined from the measurements.

The contact force applied during the measurement is controlled by measuring the current consumption of the actuator. This force has been varied from 0 N to 3 N. The standard uncertainty of the force measurements is evaluated to be 0.015 N, from a preliminary investigation using a calibrated load cell.

The experiments are performed in a metrology laboratory with a controlled ambient temperature. Even if the temperature of the measuring system is not directly measured, a reasonable temperature range may be defined based on previous measurements.

The measurand is defined as the encoder output (i.e. the position of the actuator stem measured by the internal encoder) when the tip of the stem is in contact with the reference object.

The measuring setup is represented in a simplified form in **Figure 3.1**.

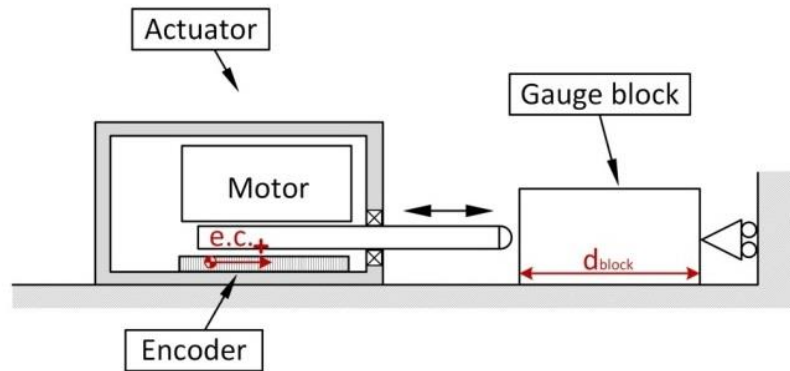


Figure 3.1 The measuring setup for actuator calibration (e.c. = encoder counts, d_{block} = dimension of gauge block).

From the particular orientation of the reference system, the smaller the gauge block under measurement the greater the output of the encoder. When performing the data analysis, the raw data values are rescaled as follows:

- The values are transformed from encoder counts into millimetres (1 e.c. = 10^{-4} mm).
- The values are then shifted of a constant value to make the output relative to the bigger gauge block to coincide to zero. Consequently, all the values are nominally positive and represent a relative variation of the encoder output.

Experimental procedure

The calibration procedure consists of measuring the length of gauge blocks of 9 different dimensions (from 20 mm to 12 mm, with a step of 1 mm) with 8 different contact forces (nominally 0.17 N, 0.33 N, 0.50 N, 0.66 N, 0.83 N, 1.00 N, 2.00 N, 3.00 N).

The test is performed in the following way:

- 1 The gauge block is positioned.
- 2 The actuator is programmed to measure the gauge block with each of the different force levels.
- 3 The gauge block is repositioned and step 2 is repeated. Step 3 is repeated 3 times.
- 4 The gauge block is replaced with another one of different dimension and steps 2 and 3 are repeated.
- 5 The whole procedure is repeated another time for a total of 6 repeated measurements for each combination of gauge block and measuring force.

Definition of the mathematical model

The mathematical model for the measured length L may be expressed by three additive terms, i.e.:

$$L = L_{scale} - \Delta L_{force} - \Delta L_{gauge} \quad 3.1$$

where L_{scale} is the component of the measured length taking into account the thermal expansion of the glass measuring scale, ΔL_{force} is the deformation due to the contact force and ΔL_{gauge} is the thermal expansion of the measured gauge blocks.

The first term of the mathematical model (L_{scale}) may be expressed as follows:

$$L_{scale} = (er - er_0) \cdot \alpha \cdot [1 + CTE_{scale} \cdot (T - 20)] \quad 3.2$$

where er is the raw encoder output, er_0 is the reference for zeroing the encoder output, α is the transformation factor (from encoder counts to millimetres), CTE_{scale} is the thermal expansion coefficient of the glass measuring scale and T is the temperature of the whole system. Considering now directly the lengths of the blocks, equation 3.2 becomes:

$$L_{scale} = (L_{20} - L_{block}) \cdot [1 + CTE_{scale} \cdot (T - 20)] \quad 3.3$$

where L_{20} is the length of the 20 mm gauge block used to zeroing and L_{block} is the length of the measured block. Since some measured lengths are obtained by wringing two blocks of lengths L_1 and L_2 , equation 3.3 becomes:

$$L_{scale} = [L_{20} - (L_1 + L_2)] \cdot [1 + CTE_{scale} \cdot (T - 20)] \quad 3.4$$

The second term of the mathematical model (ΔL_{force}) may be expressed with equation 2.5 in agreement to Hertz formulas in case of contact between a rigid sphere and a plane.

The third term of the mathematical model (ΔL_{gauge}) may be expressed as follows:

$$\Delta L_{gauge} = L_{block} \cdot [1 + CTE_{block} \cdot (T - 20)] \quad 3.5$$

where CTE_{block} is the thermal expansion coefficient of the blocks, and L_{block} and T are defined above. When the measured length is obtained by wringing two blocks of lengths L_1 and L_2 , equation 3.3 becomes:

$$\Delta L_{gauge} = (L_1 + L_2) \cdot [1 + CTE_{block} \cdot (T - 20)] \quad 3.6$$

So, according to equation 3.1, i.e. putting together the three additive terms of the mathematical model, it results:

$$L = [L_{20} - (L_1 + L_2)] \cdot [1 + CTE_{scale} \cdot (T - 20)] - \left[\frac{3 \cdot (1 - \nu^2)}{4 \cdot ra^{\frac{1}{2}} \cdot E} \right]^{\frac{2}{3}} F^{\frac{2}{3}} + (L_1 + L_2) \cdot [1 + CTE_{block} \cdot (T - 20)] \quad 3.7$$

This complete model allows a thorough comparison among the effects of all the factors affecting the uncertainty of the measured length L .

3.1.2 A priori uncertainty evaluation

The uncertainty of the measured length L was evaluated before performing the measurements in order to identify the most significant factors. This is called *a priori* uncertainty evaluation.

Estimating the a priori contributions

In order to have an a priori estimate of the measured length L and its uncertainty, an estimate of the values of the independent variables of the mathematical model, shown in equation 3.7, and their variabilities is required. According to GUM [135], the latter contributions may be evaluated as variability ranges (Type B evaluation) when standard uncertainties, obtained from repeated observations (Type A evaluation), are not available. By way of example, the working condition with a measured length L of approximately 6 mm and a nominal contact force of 0.17 N is considered. **Table 3.2** shows the estimated values of the independent variables. The nominal lengths of gauge blocks L_1 , L_2 and L_{20} are reported in the calibration certificate, as well as the value of the thermal expansion coefficient CTE_{block} . Instead, the value of the thermal expansion coefficient CTE_{scale} is taken from literature, since it is not available from the technical specifications of the encoder. The temperature of the whole system T is estimated based on the prior experience. The Poisson ratio ν is taken from literature, as well as the Young modulus E . The radius of the probe tip ra is given in the technical specifications of the actuator, while F is the nominal value of the contact force.

Table 3.3 shows the estimated variability of the independent variables. Only the variability of contact force F is known a priori as standard uncertainty (Type A evaluation). For the other independent variables, the variability range is exploited (Type B evaluation). By assuming rectangular distributions of width equal to the range, the corresponding variances may be calculated for each contribution by dividing the square of the range by the factor 12, as indicated by GUM. Then, the standard uncertainties are, of course, obtained by taking the square root of the corresponding variances.

The ranges for the lengths of the gauge blocks L_1 , L_2 and L_{20} are derived from the limit deviations given in ISO 3650. As shown in the next session, these contributions are criti-

cal for the overall uncertainty of the measured length L , therefore grade 0 gauge blocks were adopted. In ISO 3650, the limit deviations are defined per length intervals, i.e. [0.5 mm, 10 mm], (10 mm, 25 mm], and so on. The measurement resolution of the encoder which also influences the length measurements has, however, a negligible effect.

Table 3.2: Estimated values of the independent variables of the actuator model.

<i>Variable</i>	<i>Value</i>
L_{20} / mm	20.0003
L_1 / mm	9.0003
L_2 / mm	5.0000
$CTE_{scale} / ppm/^{\circ}C^{-1}$	8.0
$T / ^{\circ}C$	21
ν	0.30
ra / mm	1.50
$E / N \cdot mm^{-2}$	2.05×10^5
F / N	0.17
$CTE_{block} / ppm/^{\circ}C^{-1}$	11.5

Instead, the effect of measurement repeatability is certainly significant, but it cannot be evaluated a priori. The range for the thermal expansion coefficient CTE_{block} is given in the calibration certificate. Instead, the range for the thermal expansion coefficient CTE_{scale} is taken from literature, being not available from the technical specifications. The range for the temperature T is estimated basing on the prior experience. The ranges for the Poisson ratio ν and Young modulus E are taken from literature. The range for the radius of the probe tip ra is given in the technical specifications of the actuator. Finally, for the contact force F the standard uncertainty is known from preliminary investigations by means of a load cell.

Uncertainty table

The uncertainty evaluation according to GUM and PUMa methods may be properly organized in a tabular format, with reference to EA-4/02 M [137]. A small modification from this format has been introduced by substituting standard deviations with variances

[138] thus managing additive quantities which can be compared more easily. **Table 3.3** shows the individual contributions to variance of output quantity L for the working condition considered in the section above (i.e. measured length L of approximately 6 mm and nominal contact force of 0.17 N).

Table 3.3: Estimated variability of the independent variables of the actuator model. The variability range is given for Type B evaluations, while the standard uncertainty is given for Type A evaluations.

<i>Variable</i>	<i>Range</i>	<i>Standard uncertainty</i>
$L_{20} / \mu m$	0.28	
$L_1 / \mu m$	0.24	
$L_2 / \mu m$	0.24	
$CTE_{scale} / ppm/^{\circ}C^{-1}$	2.0	
$T / ^{\circ}C$	1	
ν	0.04	
ra / mm	0.1	
$E / N \cdot mm^{-2}$	2.10×10^4	
F / N		0.015
$CTE_{block} / ppm/^{\circ}C^{-1}$	2.0	

Symbols of independent variables appearing in the mathematical model and their values are written down in column x_j . Entries in column $u(x_j)$ are the standard uncertainties for each contribution, while values in column df_j represent the relevant degrees of freedom, which are set to 100 in absence of specific information. Coefficients of sensitivity c_j may be evaluated either by partial derivation, or numerically, and eventually contributions $u_j^2(L)$ of variance of dependent variable L can be calculated. By taking into account all this information, it is possible to get the expanded uncertainty $U(L)$.

By examining the values of the column $u_j^2(L)$ in **Table 3.4**, the weights of the different uncertainty contributions are determined. The ranges for the lengths of the gauge blocks L_1 , L_2 and L_{20} are the major contributions. Indeed, passing from the adopted grade 0 gauge blocks to grade 2 gauge blocks, the expanded uncertainty (at 95% confidence

level) increases from 0.28 μm to 1.0 μm . Instead, the expanded uncertainty does not change significantly when considering other combinations of contact force and measured length.

Table 3.4: Uncertainty table for the length L (expressed in millimetres) measured with the actuator for a specific working condition.

x_j		$u(x_j)$	c_j	$u_j^2(L)$	df_j	$u_j^4(L)/df_j$
Symbol	Value					
L_{20}	20.0003	8.1×10^{-5}	1.0	6.5×10^{-9}	100	4.3×10^{-19}
L_1	9.0003	6.9×10^{-5}	-1.0	4.8×10^{-9}	100	2.3×10^{-19}
L_2	5.0000	6.9×10^{-5}	-1.0	4.8×10^{-9}	100	2.3×10^{-19}
CTE_{scale}	8.0×10^{-6}	5.8×10^{-7}	6.0	1.2×10^{-11}	100	1.4×10^{-24}
T	21	5.8×10^{-1}	-1.1×10^{-4}	4.3×10^{-9}	100	1.8×10^{-19}
ν	0.30	1.2×10^{-2}	2.6×10^{-5}	9.2×10^{-14}	100	8.5×10^{-29}
ra	1.50	2.9×10^{-2}	1.3×10^{-5}	1.5×10^{-13}	100	2.2×10^{-28}
E	2.05×10^5	6.1×10^3	1.9×10^{-10}	1.4×10^{-12}	100	1.9×10^{-26}
F	0.17	1.5×10^{-2}	-2.3×10^{-4}	1.2×10^{-11}	100	1.5×10^{-24}
CTE_{block}	1.15×10^{-5}	5.8×10^{-7}	-1.4×10^1	6.5×10^{-11}	100	4.3×10^{-23}
L	5.9999		$u^2(L)$	2.0×10^{-8}	Σ	1.1×10^{-18}
			$u(L)$	1.4×10^{-4}	df_L	392
			p	95%		
			$t_p(df_L)$	2.0		
			$U(L)$	2.8×10^{-4}		

3.1.3 A posteriori uncertainty evaluation

The experimental data are composed of 72 series of 12 data points for every combination of gauge block and measuring force. Their values represent the raw output of the encoder. Given the experimental data, it is possible to obtain an a posteriori estimate of measurement uncertainty.

Firstly the Chauvenet criterion is used to identify suspected outliers (i.e. measurement accidents). The method is applied within each single series in order to consider only the variability relevant to each set of measuring conditions. The method considers the residuals of each repetition from the average value of all repetitions. Outliers are then replaced by the median value of the series.

Experimental data are then rescaled according to Section 2.2, the transformation factor being 10^{-4} mm/count. The shift is defined as the average of all measurements for the 20 mm gauge block. Systematic effects linked to rescaling are identified and compensated later in the analysis. The differences between measured values and the reference value (i.e. residuals R) are calculated for each data point. For each series the average and the standard deviation of the residuals are calculated and used in the subsequent analysis.

Before evaluating measurement uncertainty, systematic effects are corrected [135]. The influence of measuring force is calculated as elastic deformation according to equation 2.5. The calculated values (listed in **Table 3.5**) are then subtracted from residuals R .

Table 3.5: Systematic effects (deformation) due to measuring force.

<i>Nominal Force / N</i>	<i>Deformation / μm</i>
0.17	0.06
0.33	0.09
0.50	0.12
0.66	0.15
0.83	0.17
1.00	0.19
2.00	0.31
3.00	0.41

Box-plots in **Figure 3.2** show the scatter of the residuals corrected for the force effect ($R_{corr,F}$) as a function of measuring length, underlining a clear trend. The latter represents

the metrological characteristic of the actuator, showing a sensitivity error with a negligible nonlinearity.

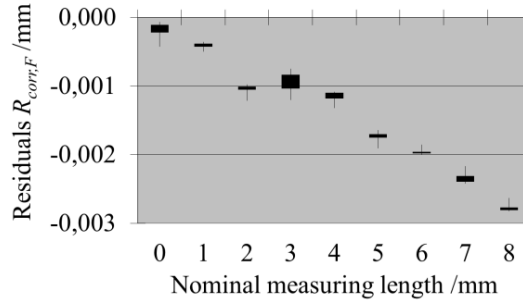


Figure 3.2 Box-plots of residuals $R_{corr,F}$ vs. measuring length.

Therefore, linear regression between nominal measuring length and residuals is performed to quantify the influence of length, according to the model:

$$R_{corr,F} = a_L \cdot L + b_L \quad 3.8$$

where L is the nominal measuring length, a_L and b_L are the coefficients of the model.

Residuals corrected from the systematic influence of the measuring length ($R_{corr,FL}$) are calculated as:

$$R_{corr,FL} = R_{corr,F} - (a_L \cdot L + b_L) \quad 3.9$$

According to GUM, the correction of the sensitivity error results should have, in the worst case, a standard uncertainty of about $0.06 \mu\text{m}$. Box-plots of residuals corrected for systematic effects of measuring length and force ($R_{corr,FL}$) are shown in Fig. 3.

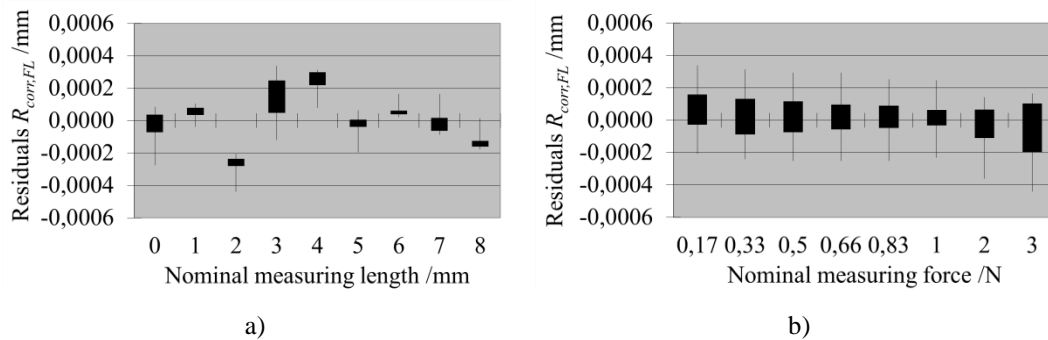


Figure 3.3 Box-plots of residuals $R_{corr,FL}$ vs. measuring length (a) and measuring force (b).

Residuals $R_{corr,FL}$ appear to be almost unaffected by the two factors considered. This is confirmed by the normal probability plot, shown in Fig. 4, which does not highlight substantial discrepancies from normality. So, the standard deviation of the residuals $R_{corr,FL}$, is equal to $0.17\text{ }\mu\text{m}$, is taken as measurement repeatability. Combining the latter contribution with the standard uncertainty relevant to the previous correction (equation 3.9) and the standard uncertainty relevant to all the factors considered in the a priori evaluation (**Table 3.4**), a combined standard uncertainty equal to $0.23\text{ }\mu\text{m}$ is obtained. In this way, the a posteriori estimate of expanded uncertainty (at 95% confidence level) of measured length L is $0.46\text{ }\mu\text{m}$.

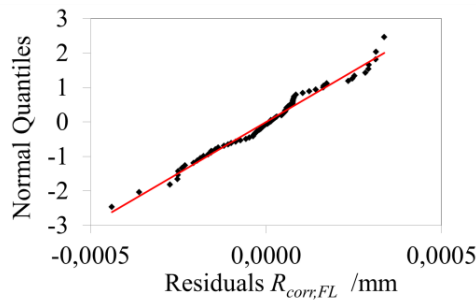


Figure 3.4 Normal probability plot for residuals $R_{corr,FL}$.

3.2 Multi-wavelength interferometer

The commercial interferometer produced by Lumphos GmbH is a multi-wavelength interferometric system capable of absolute measurements with accuracies lower than $0.05\text{ }\mu\text{m}$ (3σ) [50]. It can be employed as profilometer, roundness tester or simple displacement probe. As an optical technique it provides measurements without thermomechanical interaction with the workpiece. On the other hand the measurement accuracy is influenced by the surface texture of the target and can get as high as $1\text{ }\mu\text{m}$ for rough surfaces [139]. Hence an adequate application to exploit the potential of the instrument is length measurement with sub-micrometre accuracy on low roughness parts, such as ground or polished metal parts. In the next section the applicability as length measurement device is tested on step gauges with step height of the order of $1\text{ }\mu\text{m}$ and $100\text{ }\mu\text{m}$.

3.2.1 Procedure description

The tests consist of repeated measurements of two calibrated step gauges. The step gauges consist of a set of gauge blocks wrung on an optical flat. The artefacts are composed as follow:

- Step gauge 1 (SG1):
 - 3 gauge blocks with nominal length of 1.3, 1.5, 1.6 mm
 - Step heights achievable: 100, 200, 300 μm
 - Grade 0 (ISO3650) with calibration certificate
- Step gauge 2 (SG2):
 - 5 gauge blocks with nominal length of 1.010, 1.007, 1.003, 1.010
 - Step height achievable: 3, 4, 7, 10 μm
 - Grade 1 (ISO3560) without calibration certificate

The first and the last steps have nominally the same height to help during the data processing for removing the profile orientation. In SG1 these areas are represented by the optical flat, while in SG2 they consist of two gauge block of the same nominal height.

The measurements of the step height are performed in a scan mode (**Figure 3.5**): the interferometric beam is positioned approximately in the middle area of the gauge blocks and it is moved across the artefact (x direction). The height (z direction) is measured continuously every 10 μm of step in x direction. The scan cycle (forth and back) is repeated 15 times consecutively, thus a total of 30 replicated measurements are available. The tests are performed in an uncontrolled temperature room, however the temperature is assumed constant during the scanning process.

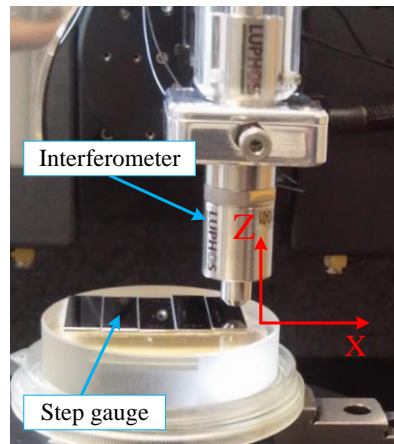


Figure 3.5 Step gauge measurement with a MWLI system.

3.2.2 Data analysis

Each single profile (of the step gauge) measurement must be processed as follows to estimate the amplitude of the step heights:

- The main orientation of the profile (coming from a non-perfect horizontal alignment of the sample) can be removed by subtracting the linear trend calculated from the interpolation of the first and last segment (**Figure 3.6**).

- The height of the steps is estimated in a central position of the gauge blocks. It is calculated as the average z coordinate of 20 consecutive data points (**Figure 3.7**). This averaging reduces the influence of the noise.
- The difference between the heights is calculated and compared with the reference value from the calibration certificate for the gauge block.

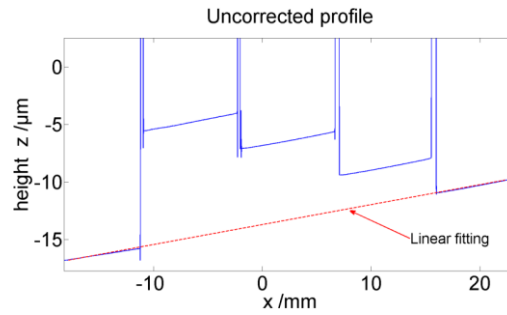


Figure 3.6 Levelling of main orientation of MWLI measurement.

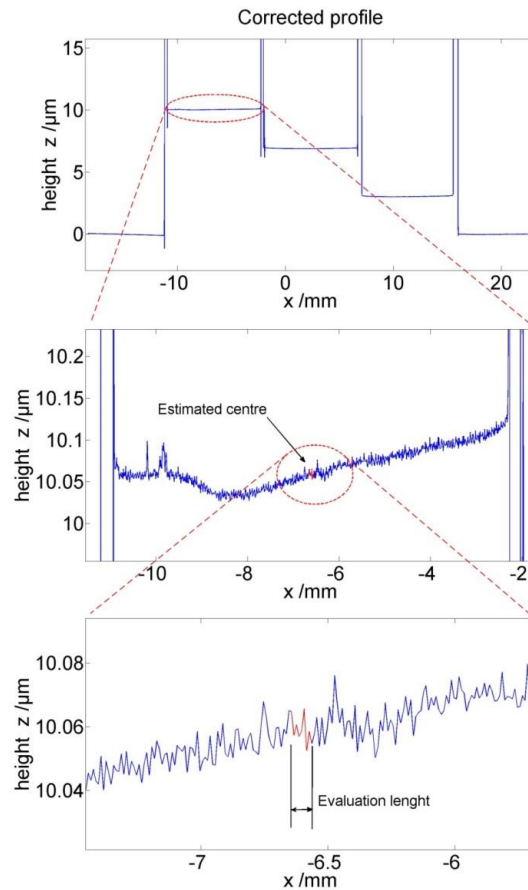


Figure 3.7 Data processing: definition of measuring point on the step gauge.

The comparison between the measured values L_m of SG1 and the reference values L_{ref} shows a residual bias with a visible linear behaviour. After the correction of this linear component the results $L_{m,c}$ are improved and become consistent with the calibration certificate (**Figure 3.8**). The measured step heights of SG2 do not show the same linear trend and are in agreement with ISO 3650 nominal values (**Figure 3.9**).

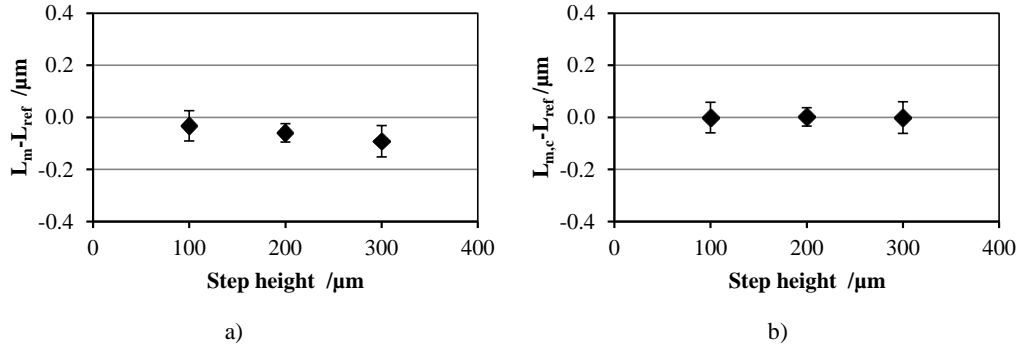


Figure 3.8 Comparison of measurement results with reference lengths for SG1 before (a) and after (b) compensation of systematic linear trend (error bars represent the expanded uncertainty).

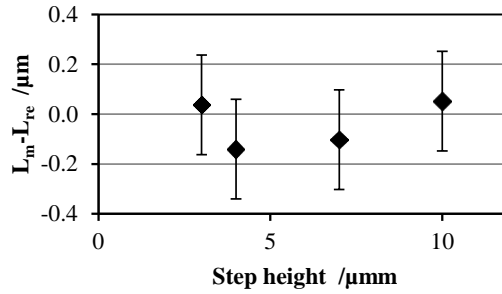


Figure 3.9 Comparison of measurement results with reference lengths for SG2 (error bars represent the expanded uncertainty).

The main contributor to the measurement uncertainty is represented by the uncertainty on the reference value of the step gauges. Other contributors, for instance related to the diffractive index of air, are ignored as the beam path is considered sufficiently short. Expanded uncertainties in the order of $0.06 \mu\text{m}$ and $0.2 \mu\text{m}$ are achieved for Grade 0 and Grade 1 artefacts respectively. For rougher surfaces the measurement uncertainty is expected to increase up to $1 \mu\text{m}$.

3.3 Infrared temperature sensors

Temperature measurements with infrared techniques represent a convenient alternative if a contact sensor cannot be installed on the measured part. Moreover using a thermal imager a complex temperature field measurement can be obtained. In section 2.6.2 it has already been mentioned how the measurements are connected to the knowledge of the emissivity of the target and the surrounding conditions.

The tests presented below concern:

- accuracy estimation on high emissivity parts (matt black);
- testing the suitability for temperature field calculation.

3.3.1 Accuracy of temperature measurement

The test deals with the comparison of the temperatures measured with a thermal imager and with contact sensors with the purpose of evaluating the measurement uncertainty for a specific measuring condition (indoor climate, distance from the target, type of target) as it is believed to be lower than the generic uncertainty state by the producer. The experimental setup (see **Figure 3.10**) is composed of a thermal camera positioned vertically over an aluminium heating plate. The plate contains a retroactive heating circuit, with two resistors and a thermocouple. The surface is ideally divided in four quadrants with one target area each. The radiation emitted by the camera is partially detected by the sensor as they are reflected by the surface orthogonally aligned to the camera. Hence the targets are positioned in a peripheral position to avoid biased measurements. Three areas consist of elements with high emissivity, namely a black matt label and the backing material of two contact temperature sensors. The fourth is used to acquire the temperature from the bare metallic surface.

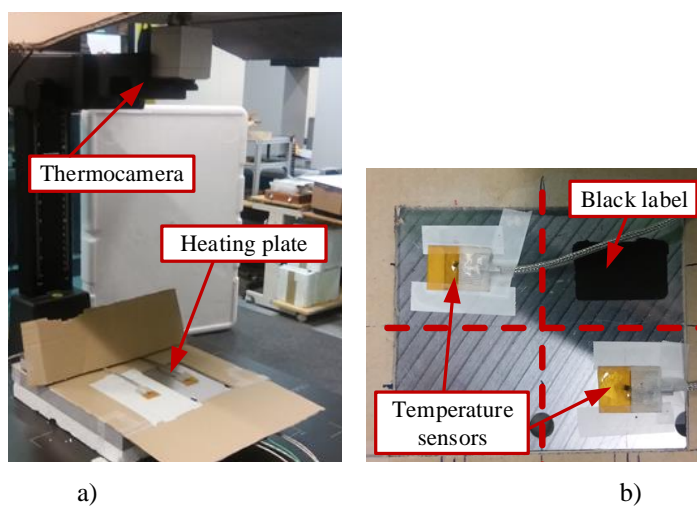


Figure 3.10 Experimental set up for infrared temperature measurements: a) thermal camera position; b) heating plate with targets.

The thermocamera characteristics are listed in **Table 1.2**. The measuring software provides direct temperature measurements through a correction of the radiation energy from the influence of factors like ambient and sensor temperature. In the software routine any object in the field of view of the camera can be selected and its emissivity adjusted. The contact sensors consist of two RTD sensors (PT100) with a measurement uncertainty of 0.02 °C.

Table 3.7: Thermal camera characteristics.

Optical resolution	160×200 pixels
Spectral range	7.5÷13 μm
System accuracy	±2 °C
Resolution	0.1 °C
Temperature range	0÷250 °C

Procedure

The test is performed in a laboratory at constant temperature. Great care has been taken to reduce the infrared radiations originating in the surroundings, especially by lighting and operators. Initially the emissivity of each target must be adjusted in the camera software. Therefore the heating plate is warmed up to a temperature of 30 °C. Four measuring areas are selected on the field of view of the camera to match the position of the two sensors, the black label and the metallic area, and their average temperature is acquired by the camera. As the temperature reaches a stable value the emissivity on the different areas is adjusted to match the output of the thermocamera with the one coming from the contact sensors. Fluctuations and noise in the infrared signal reduce the accuracy in the determination of the emissivity.

A warm body considered as an ideal black body causes an underestimation of the extracted temperature since the emissivity is overestimated. Nevertheless, in the case of the black matt label the temperature measured with the camera always results higher than the one measured, even using the maximum value of emissivity. In the case of the metallic surface the emissivity is fixed at a minimum value.

A complete cycle of heating up and cooling (from 20 to 30 °C) is performed and temperature is measured both with the thermocamera and by the contact sensors. The signals are then directly compared since they refer to the same location. Even though they do not relate to a contact measurement the temperature information of the black label and the metallic surface are useful information for the analysis of the camera behaviour.

The temperature of the heating plate cannot be considered uniform even if aluminium ensures high heat conductivity. To cope with the influence of the position on the plate four complete cycles are performed interchanging the location of the measured elements.

Results

As an example the results for one cycle for infrared and contact measurements are shown in **Figure 3.11**. The metallic surface leads to a noisy and unreliable signal. A practical solution is the application of a coating or a tape to change the surface appearance without modifying the thermal properties of the component, similar to the experimental case with a black matt label. It is however not suitable for the task of production quality control. The differences between infrared measurements and contact measurement for the two areas involving the RTD sensors are depicted in **Figure 3.12** showing compatibility within an interval of ± 0.5 °C. The initial section of **Figure 3.12** is ignored since it refers to the warm up phase characterized with fast temperature changes and non-uniform temperature fields.

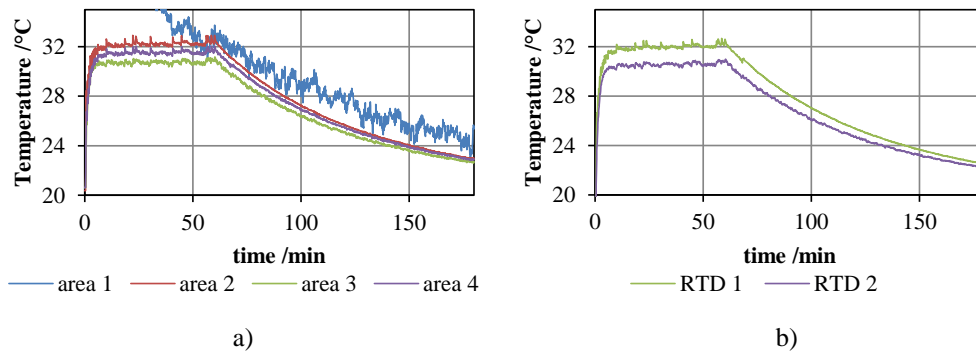


Figure 3.11 Measured temperatures on heating plate: a) with thermocamera, area 1=metallic surface, area 2=black matt label, area 3= contact sensor RTD 1, area 4= contact sensor RTD 2; b) with contact sensors.

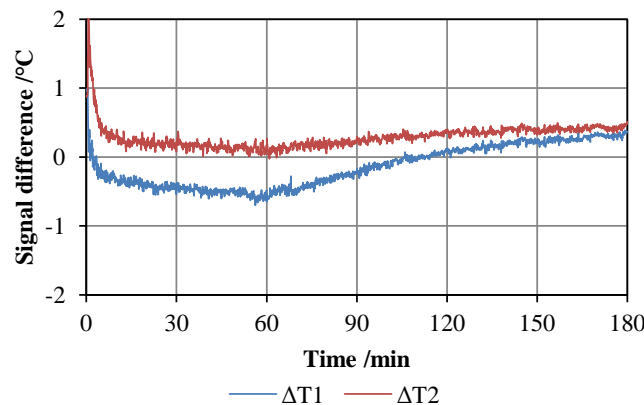


Figure 3.12 Difference between infrared and contact temperature measurements of the heating plate: $\Delta T1$ refers to RTD 1 while $\Delta T2$ to RTD 2.

3.3.2 Temperature field on polymeric parts

One main advantage of thermal cameras is the possibility to obtain in one single shot the temperature in different locations of a part. This feature is exploited in the measurements of the temperature field of polymer parts during a cooling phase. The selected part is made in ABS and presents a prismatic hollow shape. It is warmed up on a heating device and then positioned on a metallic support in front of the camera. Repeated measurements are performed with different orientations of the component. The temperature field estimated from the infrared measurements reveals useful information both regarding the distortions involved during the cooling phase and the extent of the transfer in different locations.

A quantitative analysis is performed comparing the temperature in three selected locations on the part (**Figure 3.13**). The temperature profile is decreasing towards the support plane where the temperature undergoes a more drastic drop in the first period of cooling.

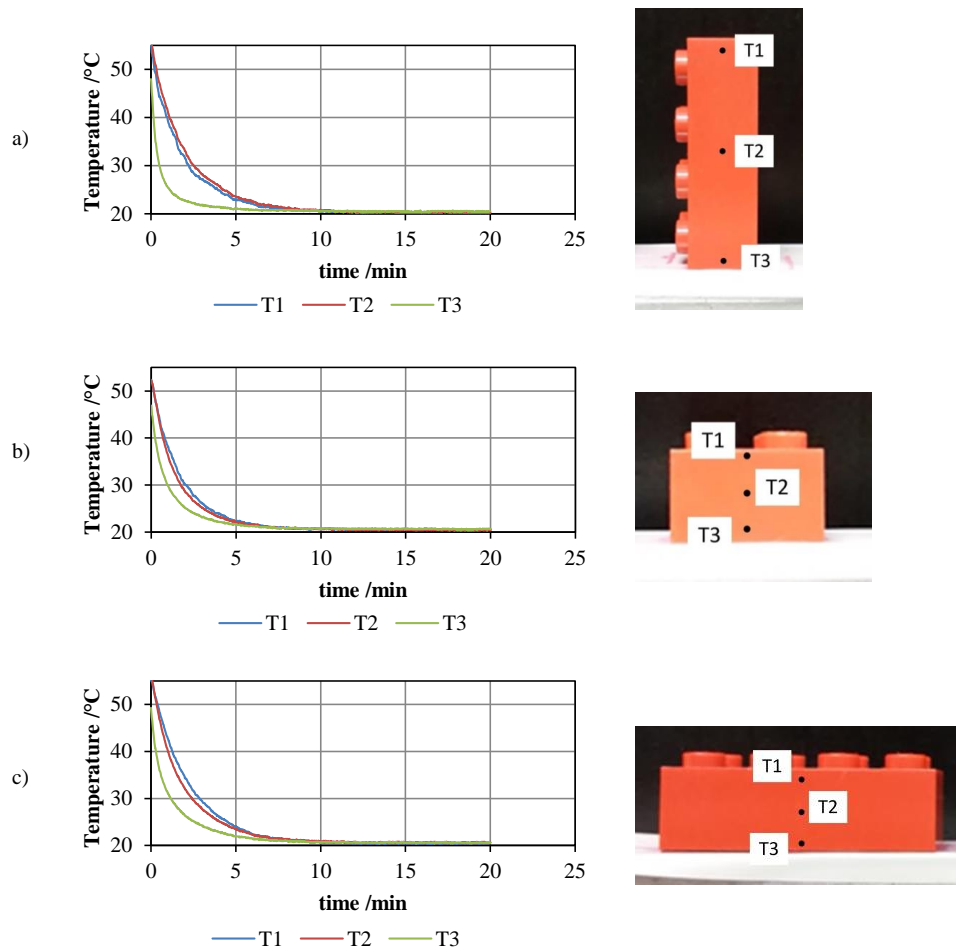


Figure 3.13 Infrared temperature measurements: temperature profiles in three locations for three different orientations of an ABS workpiece during cooling.

Figure 3.14 shows the output of the thermal camera for the three orientations selected for three time instants during the test. A qualitative analysis of the temperature fields reveals that:

- The temperature gradient in the part appears very steep in the area in contact with the support due to the large heat exchanged by conduction through solids than the one transmitted by air convection.
- The drop in temperature in the contact area is almost instantaneous while it is slower in the rest of the component. After one minute the temperature drops about 15 °C in all sections of the component and after two minutes the drop is higher than 20 °C.
- If the boundary conditions are symmetrical (position 2 and 3) the temperature field is inclined to be symmetric as well.

Outcome of such an analysis are useful in different stages of a DLM measurement. In the first place the thermocamera can be installed in the multisensory measuring device to give direct inputs to the extrapolation of the length at reference condition. It can also be implemented in a design stage where it is necessary to develop the proper sensing strategy, i.e. the position of the temperature sensors, and as tool for validation of finite element model simulations.

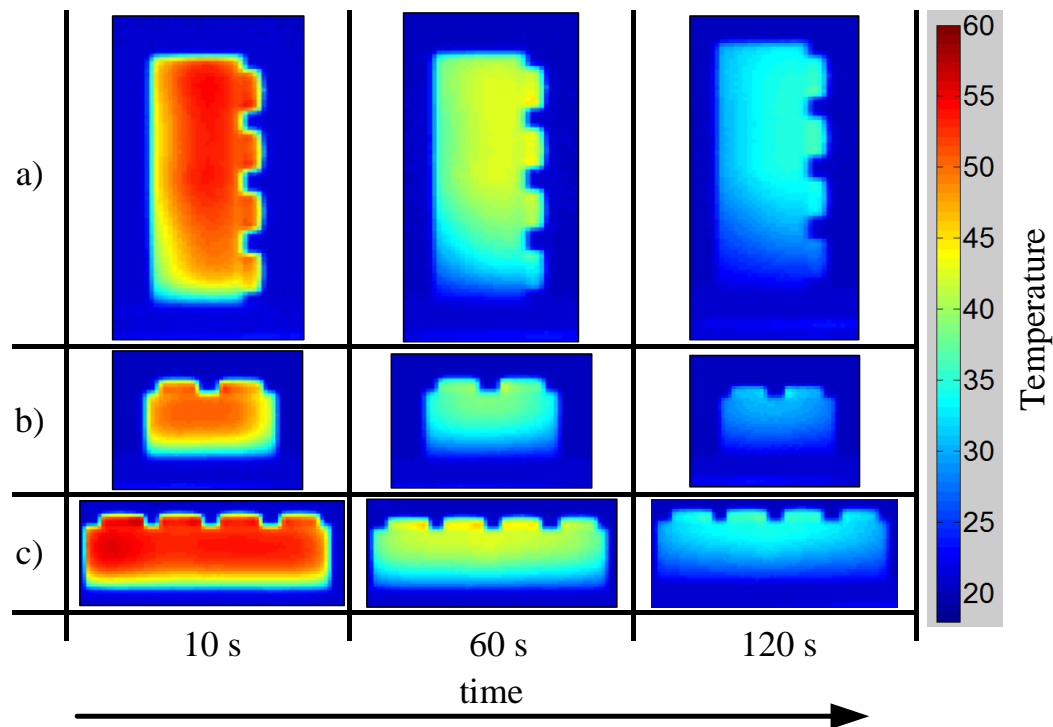


Figure 3.14 Infrared temperature measurements: temperature fields of an ABS workpiece during cooling positioned at different orientations.

3.3.3 Conclusions on thermal camera

The introduction of a thermal camera in DLM applications leads to potential benefits though with many limitations. It represents a convenient non-contact method that does not require any sensor installation and is suitable for measurements in multiple locations. It can also be used to measure several components at the same time, such as workpiece and equipment. However it is suitable only of high emissivity materials hence excluding all machined metallic parts, unless the surface appearance is previously modified with paint or tape. It is also sensitive to the surrounding radiations. The measuring device can be placed in a shielded cabinet to exclude any external radiation source; nevertheless the infrared measurement is sensitive also to radiation emitted by the camera itself and by any other equipment at the environment temperature. The measurement accuracy is higher compared to conventional RTD or thermocouple. Finally the high costs must be mentioned as a downside of thermal cameras. A cheaper alternative to thermal cameras are pyrometers. They work using the identical measuring principle, thus with same advantages and disadvantages, but they provide a single point measurement.

3.4 Conclusion

To comply with the description of dynamic length metrology the elastic deformation has to be compensated using only knowledge from direct measurements on the workpiece. A solution is represented by a contact sensor with controllable contact force. A linear industrial actuator featuring a position and force control loop is identified as suitable equipment for performing this particular task. The measuring accuracy of length measurement with variable contact force is estimated using a test rig and gauge blocks as reference artefacts. The uncertainty budget follows the guideline of the GUM, hence input factors are initially defined and a mathematical model is introduced to describe the system and to define the sensitivity of the input factors. A measuring expanded uncertainty of 0.5 μm has been documented.

Multi-wavelength interferometric systems have been recently introduced on the market as probing devices for profilometers. A commercial MWLI is tested using a metallic step gauge to assess the applicability in high accurate DLM application. Two sets of step gauges, with step height intervals of 100 μm and 3 μm are used during the test. After a short data processing, necessary to level the measured profiles, a measurement uncertainty of 0.06 μm is estimated for a grade 0 gauge block artefact. The main uncertainty contributor is represented by the uncertainty of the gauge block reference length while repeatability and noise of the interferometric measurement are limited. Nonetheless for rougher surfaces (machined and ground) a more substantial influence of the instrument is expected.

Infrared temperature measurements are not widespread in dimensional metrology application as contact measurements. Although they provide less accurate measurement the use of thermal imager allows the measurement of complex temperature fields. Therefore they cover the needs of a DLM system to cope with non-uniform temperature state. The

measurement accuracy of a commercial thermocamera is investigated on a heated metallic plate. Infrared measurements are compared with reference contact measurements performed with RTD sensors positioned in the field of view of the thermal imager. Several regions with different emissivity are considered using labels on the metallic surface. Measurements on bare metallic surface lead to noisy and unreliable results. The use of high emissivity labels improves the accuracy which is still not comparable with the one from contact measurements. A discrepancy of 0.5 °C between contact and infrared measurements is documented in a range of temperatures from 12 to 2 °C from ambient temperature. Even though infrared sensors provide low measurement accuracy they still can be used to obtain an estimation of the temperature field of the workpiece under investigation. A polymer part has been monitored during a cooling phase providing a satisfactory estimation of the temperature field useful for the definition of more specific measuring strategies.

4

Probing strategies for DLM

4.1 The need for novel probing strategies

The innovative DLM approach requires the study and the development of novel probing strategies as it differs in many aspects from standard dimensional metrology. The strategies to be developed require the implementation of measurements of several quantities and the proper fusion of the gathered data. **Figure 4.1** depicts a schematic DLM measuring system for a cylindrical metallic component, representing a common industrial case, such as the measurement of a shaft or a ring. Displacements of workpiece and temperature variations are simultaneously measured in time. The length at reference condition and the apparent material properties are calculated with analytical and numerical tool.

The absolute length measurement is ensured by the comparison between the length sensor (probe) readings of workpiece and reference artefact, which should be followed by a traceable calibration certificate.

The measuring methodology followed by DLM is represented in **Figure 4.2**. The final length at reference condition is estimated after a sequence of calculations using information from dynamic measurements of length and other relevant quantities. Numerical simulations, such as finite element model (FEM) simulations, can be implemented to support the calculations. At a first step, the DLM method provides condition specific material properties, defined as apparent properties. Hence the development of probing strategies concerns the definition the measuring quantities necessary for the length prediction, the selection of the proper measuring parameters, including measuring time, sampling rate and resolution of the equipment, and the formulation of an efficient prediction algorithm.

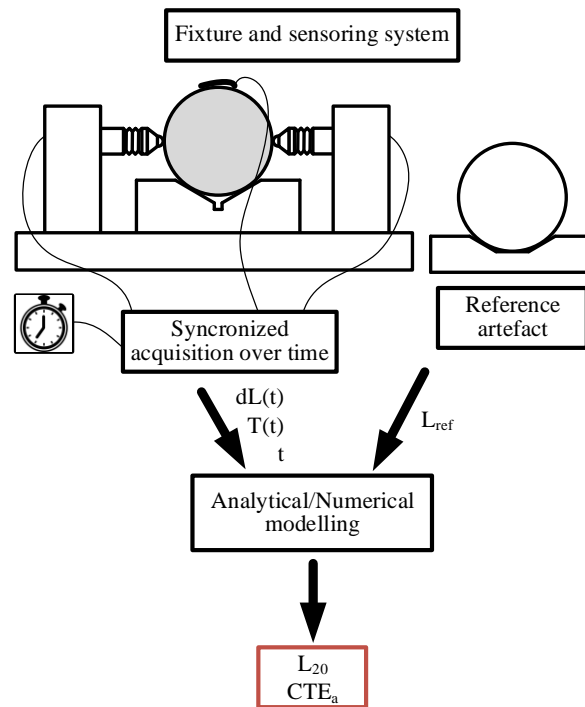


Figure 4.1 Schematic DLM measuring system showing the main elements of the method.

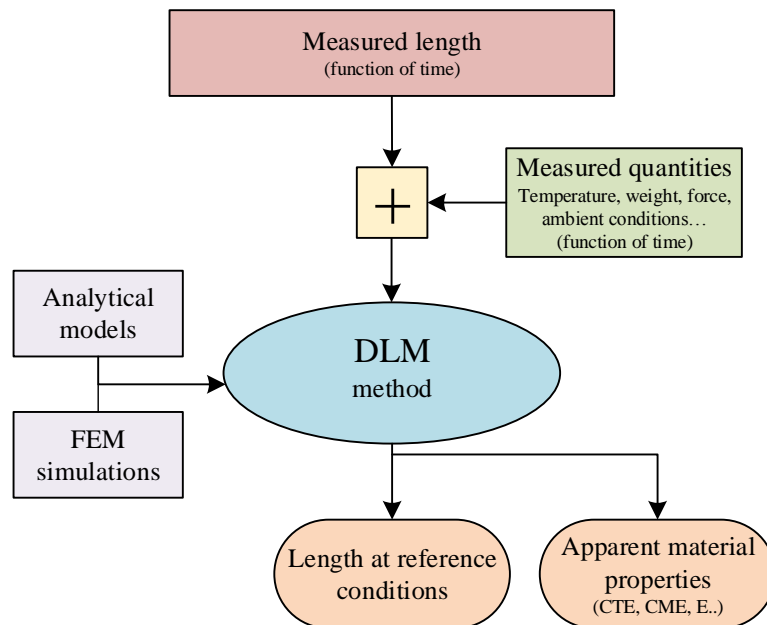


Figure 4.2 DLM method: from dimensional measurements to length prediction.

The concept of apparent material properties is introduced to describe the sensitivity of a dimension on an external parameter during a time transient stabilization period (**Figure 4.3**). A distinction from the traditional definition of material properties is necessary since the measurements performed in DLM refer to specific geometries and are performed with a non-standardized procedure. Apparent properties must therefore be referred to a particular combination of measured dimension, workpiece geometry and material, measuring conditions (e.g. temperature field) and measuring strategy. Although apparent properties appear to assume arbitrary values, they can be used as a comparison parameter between different measuring strategies and they provide an indication on the success of the measurement.

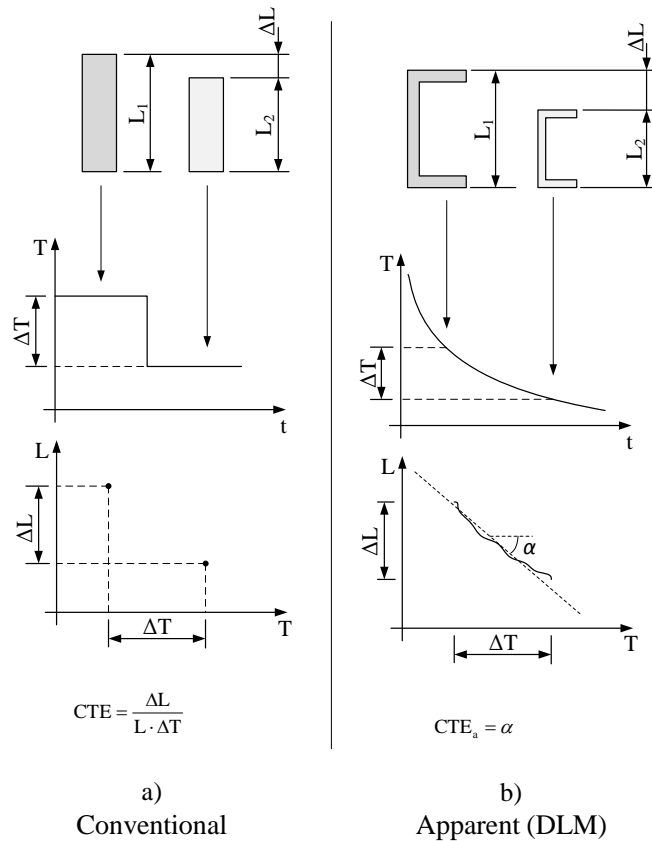


Figure 4.3 Comparison between conventional and apparent coefficient of thermal expansion. Conventional CTE is calculated from measurements of a standardized specimen under stationary condition. Apparent CTE is defined for a specific part of any shape and for specific measurement procedure in transitory condition.

Different approaches must be developed for measuring components made of metal and ceramic material or polymer. Metals and ceramics are generally influenced only by temperature and the probing force effect is often neglected due to the high stiffness of these materials and relatively low contact forces: a deformation of 0.2 μm occurs during the

measurement of a steel component with a probe with 3 mm spherical tip applying a force of 0.6 N. In the case of polymers many other sources of dimensional instability arise, such as moisture uptake and residual stresses. On the other hand in conventional metrology applications, metal parts are often measured with sub-micrometre accuracy which becomes some micrometres in the case of polymer parts. To provide a suitable replacement for conventional metrology the target uncertainty for DLM measurements should resemble the one already obtainable with traditional methods; hence measurements on metal parts must provide a lower uncertainty than the case of polymer parts.

The implementation of a DLM measuring system requires the presence of time variant quantities. It is therefore important to consider in the definition of the probing strategy the magnitude of the influence on dimensional stability but also the variation rate of these quantities. For rapid variations a manual arrangement of the measurement, e.g. manual positioning and alignment, is inconvenient since a short delay causes a major change in the workpiece condition. In such situations an elaborate automated system is advisable. Moreover measurements of fast variant quantities require the introduction of a more complex model to cope with the dynamics of the measuring system, such as the sensors' response time. Slow changes can instead be easily measured even with manual operations but require long measuring times to obtain a signal with a sufficient amplitude, in respect to the noise, to be useful for the prediction algorithm. Short measuring time is necessary for the competitiveness of DLM therefore slow changes may not be suitable for dynamic measurements and must be considered as systematic effects as in traditional metrology. Another aspect to consider is the superposition of several influence factors. The length variation must be related to the variation of these factors. If they have similar variation rates they affect the part dimensions in parallel and it is then challenging to separate their effects in an efficient way. Instead, if their variations happen with different speeds it is possible to consider them separately, as they are combined in series and one factor becomes influent when the effect of the other has already ceased.

The outcome of the probing strategy development is the definition of the three main elements of a DLM measuring system, namely the workpiece and measuring structure (positioning fixture and metrology frame), the FEM simulations and the sensory elements. The designs of these three elements are closely connected and each of them influences the other two (**Figure 4.4**). The strategy development starts from the description of the measuring task that specifies the workpiece and the dimension to be determined. While the workpiece properties are fixed, its state, e.g. the temperature field, depends on the positioning fixture. The sensory system has to be defined accordingly to the workpiece state and properties. FEM simulations are developed for the specific workpiece and fixture system and must be tailored to the type of information collected by the sensors. **Figure 4.4** describes a bidirectional connection among the elements of a DLM system as variations in one of them have to be followed by adjustments in the others. The development of appropriate probing strategies is therefore an iterative procedure.

A set of general guidelines is sought through several experimental works both dealing with investigations on (apparent) material properties, to gain experience on the behaviour of workpieces under different conditions, and with investigation into different measuring strategies. In the experimental work the influence of relevant quantities (chapter 2) are

treated separately to isolate their influence on dimensions and the resulting outcomes merged together in the formulation of the measuring guidelines. The chapter focuses especially on measurements of polymer parts.

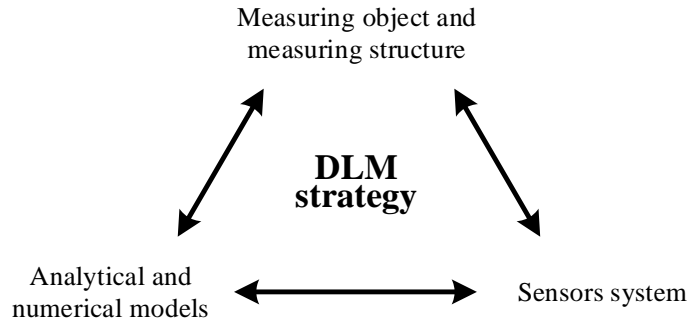


Figure 4.4 The DLM measuring strategy is defined by three main elements mutually connected.

4.2 Effect of forces

In contact dimensional measurements the probe exerts a force on the workpiece causing an elastic deformation localized in the contact area. Deformations occur in both workpiece and measuring devices, as in the case of long stem probes in CMMs [24]. It is conventional practice to compensate this systematic effect using information about the geometry and the elastic properties of the bodies involved in the contact. However it is adequate when measuring polymers in DLM to consider the measuring device ideally rigid and the deformation occurring only to the workpiece. Especially in the case of polymer workpieces this assumption correctly describes the measuring complex, as the workpiece has low rigidity compare to metallic components of the measuring equipment. To consider the effect elasticity in DLM measurements two solutions can be adopted. The first one resembles the conventional approach: the force applied by the length measuring device is calibrated (chapter 3) and the elastic deformation is then compensated with a static procedure using predetermined workpiece properties. A second solution better follows the definition of DLM. Using a device able to apply different measuring forces, such as the actuator studied in chapter 2, the workpiece is measured using progressively decreasing (or increasing) probing forces. The dimension at reference condition (corresponding to zero contact force) can then be extrapolated from the measurement at variable contact force. This second option does not require particular knowledge about the workpiece behaviour, yet it needs a complex sensor system able to measure both displacement and force. A series of tests are performed using the mentioned actuator to vali-

date the applicability of length measurements with variable force. The measuring equipment, depicted in **Figure 4.5** consists of the actuator (able to measure both displacements and contact force) installed on a thermally stable positioning fixture.

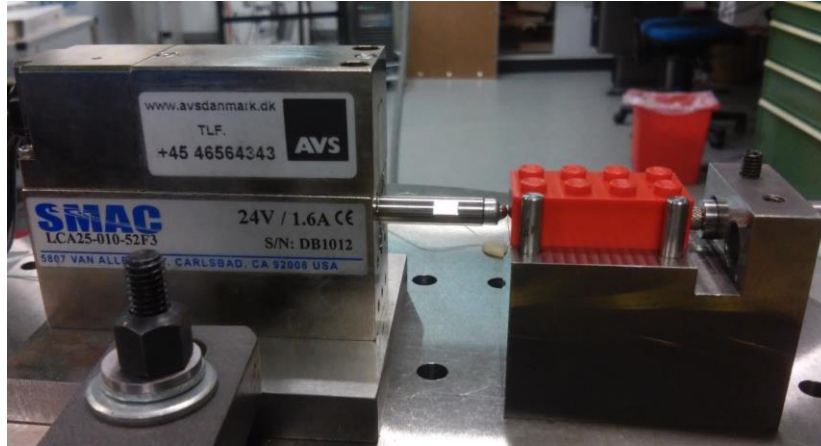


Figure 4.5 Experimental setup for length measurements at variable contact force.

The selected workpieces are ABS prismatic hollow parts. The probing head is composed of a steel sphere with a diameter of 3 mm. The test procedure is inspired by tensile tests. The workpiece is initially positioned on the fixture; then the actuator establishes the contact with the part and successively applies a continuously increasing contact force, from 0.1 to 1.0 N with an increase rate of 0.1 N/s. The short contact time ensures a limited viscoelastic effect. The procedure is then repeated for another 10 nominally identical parts. The length at zero force can be calculated with an extrapolation of the experimental data. **Figure 4.6** shows the experimental results of deformation as function of contact force. Three different models are used to describe the elastic behaviour: a linear and a quadratic model and a model developed from the contact mechanics formulations. The linear model provides the best fitting of the experimental data although it is not supported by a formal theoretical formulation. Yet all the models considered provide a satisfactory description of the data visible in **Figure 4.6 b**. Nonetheless the extrapolation at zero force produces different results among the models. In the specific case a systematic difference of 2 μm occurs. The choice of the right model is therefore important in order to properly compensate for the measuring force.

In case of a prolonged measurement on a polymer part, the contact force applied by the instrument causes the activation of viscoelastic deformations which are not easily recognizable post production measurements as they are superimposed to other instabilities occurring in the polymer part. Viscoelastic deformations can be limited using an automatic retraction mechanism to avoid continuous contact. A test has been performed on the ABS part in **Figure 4.5** to assess the amplitude of a viscoelastic deformation. The length of the polymer part has been continuously measured for several days using a con-

tact inductive displacement sensor with nominal force of 0.5 N while keeping the ambient temperature controlled to limit the thermal expansion. **Figure 4.7** shows the time variant viscoelastic deformation. For continuous measurements performed within 1 hour the viscoelastic deformation is of the order of 0.5 μm .

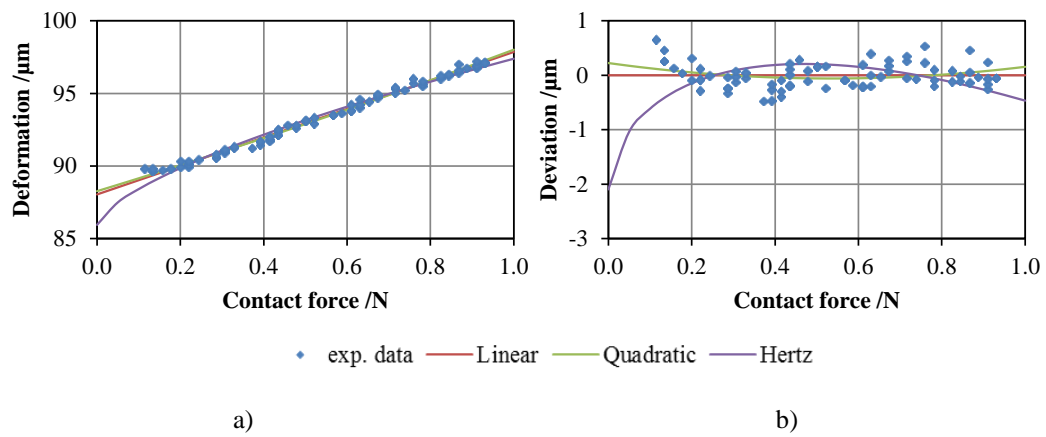


Figure 4.6 Elastic deformation due to probing force: a) absolute values; b) residual from linear trend. Blue points correspond to the experimental data while the continuous line to the fitting curves uses different models.

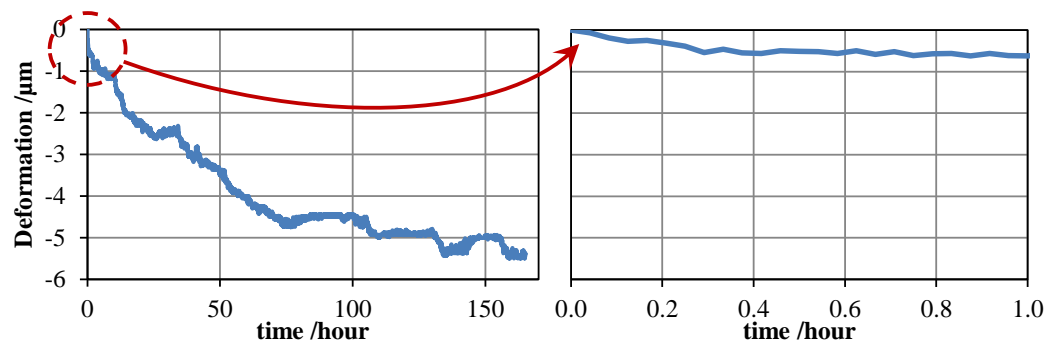


Figure 4.7 Creep effect for a prolonged measurement contact.

4.3 The influence of temperature

4.3.1 Calculation of apparent CTE

The effect of temperature concerns both the measuring object and the measuring equipment. While the measuring workpiece is affected by thermal expansion the measuring equipment can undergo other thermal effects especially if electrical components are involved in the measurement. The effect of temperature changes on the complex equipment, considered as fixture, frame and sensors, can be classified in two contributions: the change of the position of the zero point and the change of the sensor sensitivity. While the first one is typical of thermal expansion of the frame components, the second one is usually assigned to the sensing part, for instance in the case of the expansion of the scale of an encoder or the change in the electrical properties of a transducer. The zero drift can be tackled with a frequent verification of the instrument with a reference artefact and an eventual compensation. The changes in sensitivity can instead be considered in a compensation routine of the sensor output using a temperature effect coefficient.

Traditionally the effect of thermal expansion is compensated using knowledge of temperature, coefficient of thermal expansion (CTE) and geometry [25] through the equation 2.1. The value of CTE refers to a material property and is usually recovered from a data sheet or previous knowledge. It can be measured in a separate test using a dilatometer or a thermomechanical analysers (TMA) [140], [141] which is composed by a temperature controlled chamber and a displacement sensor. LVDT sensors are widely used even though for very precise applications it is substituted with an interferometer system [142]–[144]. For the estimation of the CTE a material curve is defined by several measurements of length at different, but constant and homogenous, temperature level. Two main definitions of CTE can be deduced from the unique formulation of thermal expansion and the experimental curve (see **Figure 4.8**).

A first one is determined as the angular slope of the chord between two points in the temperature length diagram. It represents the mean value for the temperature interval considered [140], [141]. The instantaneous CTE instead is described as the local slope of the curve at a defined temperature (analytical derivate) [145]. The more the material behaves linearly the more the two definitions of CTEs agree. For more stable materials, like metals and ceramics, the CTE value is usually considered constant unless very high measurement accuracy is required. For polymeric materials instead this condition is not always met. The instantaneous CTE formulation is used in DLM measurements since it better resamples the concept of apparent property as generic sensitivity.

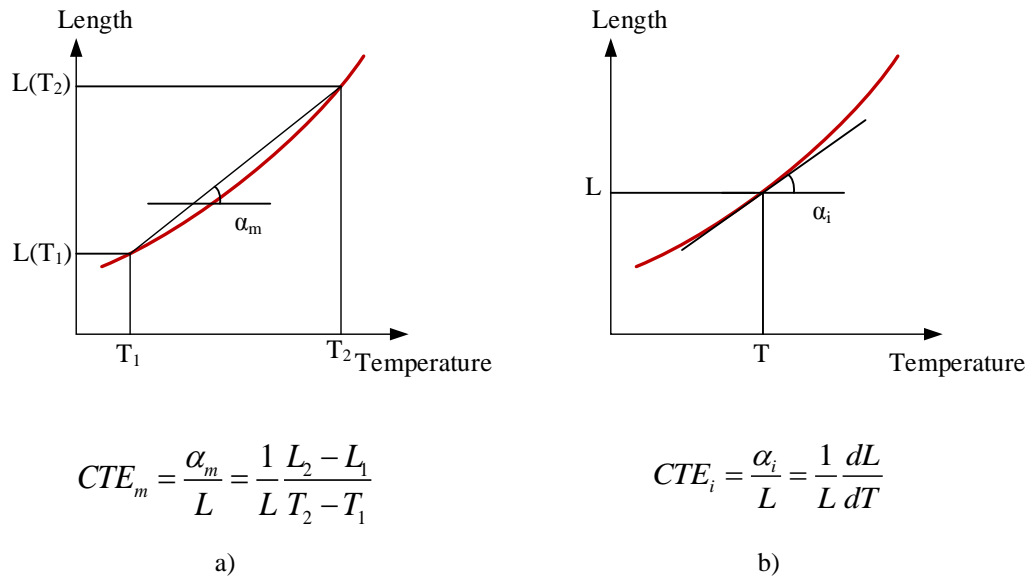


Figure 4.8 Definitions of the coefficient of thermal expansion: a) mean value; b) instantaneous value.

In an industrial environment, temperature conditions do not correspond to the reference state both because the environment is not at 20 °C and because the requirements of steady-state and homogeneity are not fulfilled. In a typical situation where DLM has to be applied environmental changes can be considered to be slow and the ambient temperature between 18 and 30 °C (in a working environment the condition must guarantee a certain degree of comfort for operators). The manufacturing process usually involves thermal inputs applied to the workpiece, as in the case of metal cutting processes or injection moulding of polymers. Hence the initial thermal state of the workpiece is considered to be at a higher temperature than the ambient and the measurement is partially performed during the cooling. The equipment can be considered in equilibrium with the ambient unless the amount of heat energy dissipated by the measuring object is not negligible. In that case the equipment temperature progressively increases with the working time. In the following chapter this last eventuality is not considered since the workpieces involved are polymer components with a mass considerably smaller than for the measuring equipment.

Considering the situation described above, the cooling phase can be exploited for achieving simultaneous measurements of length and temperature in order to define a cooling curve similar to the one achievable with a dilatometer. The curve so defined represents the behaviour of the workpiece that evolves from a non-uniform warm condition to a homogenous thermal state in equilibrium with the ambient. The registered dimensional trend can be extrapolated to define in the first place the dimensions at complete equilibrium with the ambient and further to extract the dimensions at the reference state. The extraction of length at reference conditions is more accurate as the cooling curve better resembles the one calculated according to the standard procedure. This condition is partially met if the temperature used in the definition of the cooling curve is representa-

tive of the cooling process and therefore the proper choice of the position and number of temperature sensors together with results from thermomechanical simulations necessary for the success of the length extraction. **Figure 4.9** represents simple example of cooling of a one dimensional object (block) to better describe this concept. The length of the beam and its temperature in the middle (x_1) are measured during the cooling phase. The apparent CTE_a useful for the extraction of the length at reference condition is better approximated using the average temperature of the beam (T_{mean}). Two solutions can be introduced to improve the probing system: the sensor can be placed in a different position (x_2) or a correction coefficient obtained from complex analysis, such as FEM simulations, can be applied to the measured temperature.

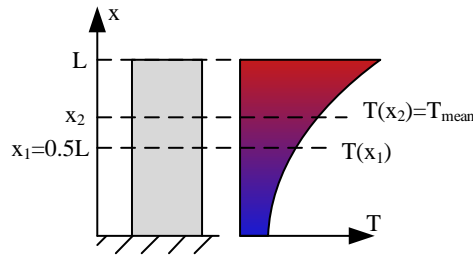


Figure 4.9 Considerations of DLM measurement during cooling of a mono dimensional beam.

4.3.2 The influence of the measurement time

This section concerns investigations on the influence of the measurement time on the accuracy of the length extraction presented above. Dynamic measurements are performed in a simulated industrial condition; only temperature is taken into account and the effect of the other influence factors is neglected. Then the dimension at reference conditions is estimated using sections of the measured data vectors with different length and starting point. The uncertainty of the estimated lengths is used to compare the different cases to address the matter of the choice of the measuring time. The material CTE is considered linear and every departure from the linearity is attributed to the probing strategy.

The experimental work

The experiments involve the measurement of the length of the industrial part made of ABS used in the previous section. To emulate the typical thermal conditions of the part after the production process (injection moulding), the workpiece heated up on a temperature controlled heating plate prior to the measurements (**Figure 4.10**). The measuring set up is depicted in **Figure 4.11**. It is composed by a highly stable frame, made from low expansion material components, namely Zerodur and Invar, and by an inductive displacement probe - MPE of $(0.07 + 0.4 \cdot L) \mu\text{m}$ (L in mm) - as measuring device. The frame holds the inductive probe and a fixed stainless steel rod both provided with a spherical

tip. During the measurement the polymer part is placed horizontally in between these two components. The temperature of the workpiece is measured with a calibrated contact resistance sensor positioned in the centre of the top surface. The test is performed in a laboratory at 20 °C, hence the extrapolation process to obtain the reference length results in more accuracy than in a generic environment. Nevertheless the outcome is still of general interest.

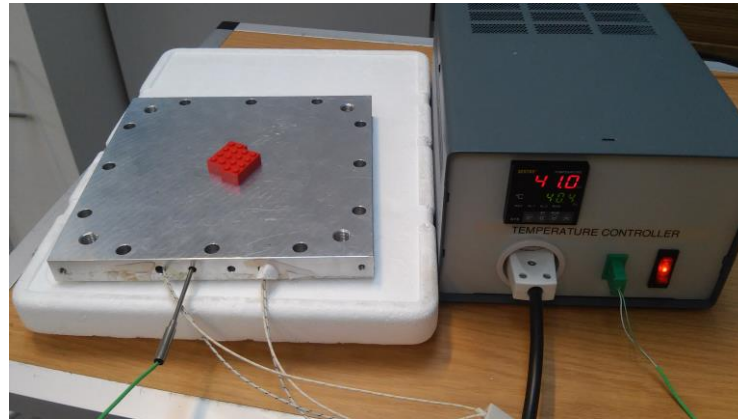


Figure 4.10 Heating device: the adjustable temperature is achieved with a closed loop temperature control.

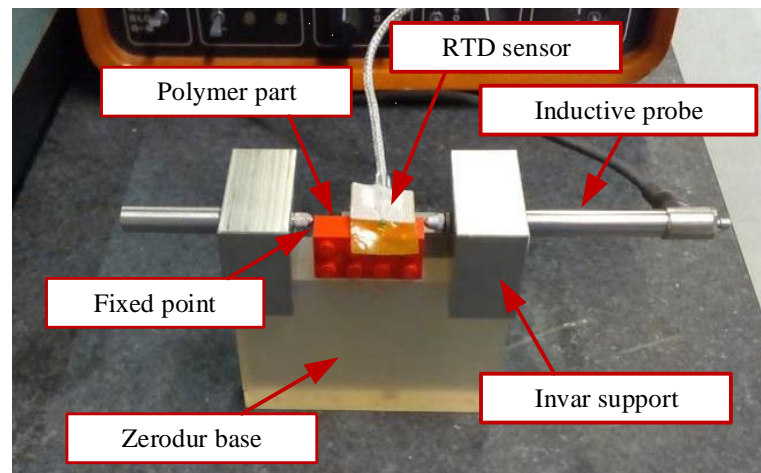


Figure 4.11 Experimental set up for investigation on influence of measuring time on DLM results.

The workpiece is initially heated up uniformly to a temperature higher than 30 °C. Then the temperature sensor is placed on the surface and the part positioned on the fixture. Length variation and temperature are acquired simultaneously with a sampling rate of 1 Hz as soon as the measured temperature decreases below 27 °C. This step is meant

for minimizing temperature gradients in the component due to the drastic change in the boundary conditions passing from heating plate to measuring fixture.

The procedure is reproduced several times for the same item and repeated for another 5 nominally identical parts. **Figure 4.12 a** shows the measured quantities (temperature and length) variations over time for one single repetition while **Figure 4.12 b** depicts the dependency of length variation from measured temperature for all the repetition performed. The length variation is already referred to the reference length calculated according to the analysis described below.

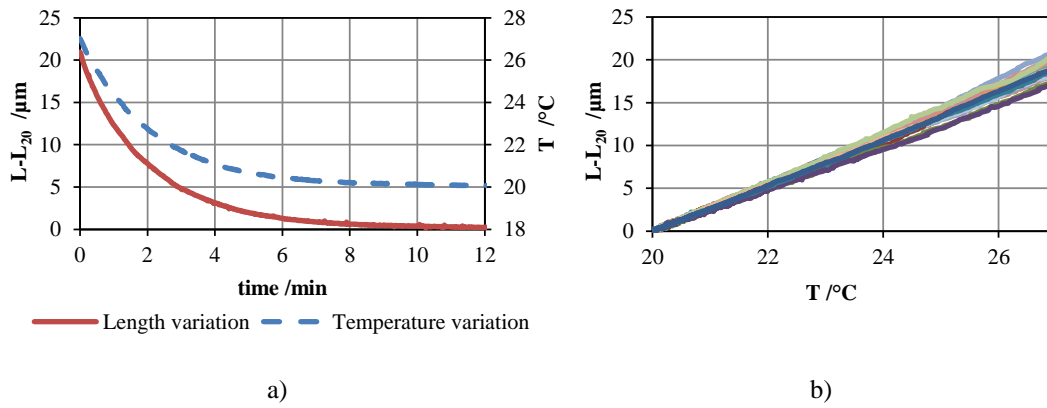


Figure 4.12 Measurements of cooling of an ABS workpiece: a) length and temperature variation vs time; b) length variations vs temperature.

Data analysis

The first step of the data analysis is the extraction of the length at reference temperature. For each repetition the length at 20 °C (L_{20}) is calculated as a regression parameter from a linear regression of measured length L_m over temperature T . A linear and a quadratic regression model, following equation 4.1, are compared considering the entire cooling curve. The resulting reference lengths show good agreement between the two models chosen, indicating that the simpler model (linear) is sufficiently accurate. The mean value of the results of the two models is considered as reference length L_{20} used to zeroing the experimental data.

$$\begin{aligned}
 \text{linear} \quad L_{20} &= L_m \cdot [1 - a \cdot (T - 20)] \\
 \text{quadratic} \quad L_{20} &= L_m \cdot [1 - a \cdot (T - 20) - b \cdot (T - 20)^2]
 \end{aligned} \tag{4.1}$$

Portions of the experimental curve with different time spans (30, 60, 90, 120, 240, 300 s) and different starting points are then considered individually in the second step of the data analysis. It is more pertinent to assign the different starting points according to the initial measured temperature instead of to the measuring time in order to obtain more

general results. An estimation of the reference length, indicated as $L_{20,est}$, is obtained performing a regression with a linear model on the segmented experimental data. All the estimated lengths are then grouped depending on the segment size and the starting temperature to assess the influence of the measurement time and the deviation from the reference case. The average error (difference between L_{20} and $L_{20,est}$) and its standard deviation are calculated for each group with same segment size and starting temperature. The average error value represents the systematic error committed by the using the particular set of probing parameters and its standard deviation can be explained as the variability of the experimental procedure and length extraction method.

Uncertainty budget

The expanded uncertainty of $L_{20,est}$ is evaluated according to equation 4.2.

$$U(L_{20,est}) = k \cdot \sqrt{(2 \cdot u_L)^2 + (2 \cdot CTE_T \cdot u_T)^2 + u_m^2 + u_{rep}^2} \quad 4.2$$

Where:

u_L is the uncertainty on the length measurement calculated from the MPE value of the probes;

u_T is the uncertainty on the temperature measurement calculated from the uncertainty of the temperature sensor stated in the calibration certificate;

CTE_T is the average coefficient of thermal expansion calculated from the regression of experimental data representing the sensitivity factor of the temperature uncertainty;

u_m is the uncertainty of the estimation model, i.e. the average systematic error $L_{20} - L_{20,est}$ of all 5 workpieces;

u_{rep} is the uncertainty due to the repeatability of the calculation of $L_{20,est}$, i.e. the standard deviation of the average error $L_{20} - L_{20,est}$;

k is the coverage factor, set equal to 2.

The components u_L and u_T are multiplied by 2 since they influence both the values of L_{20} and $L_{20,est}$. The numerical results of the uncertainty budget are listed in **Table 4.1** for the different cases. The uncertainty decreases for temperatures closer to 20 °C and for longer data sets. For measuring times longer than one minute an uncertainty lower than 2 µm has been achieved. The starting temperature influences the uncertainty, both because it quantifies the distance from the reference condition and because for higher temperatures the part has more irregular temperature fields. Hence the determination of the optimal sampling time that balances accuracy improvement and measuring time require knowledge of the thermal state of the part since the uncertainty depends on both temperature and time of the measurement (as shown in **Table 4.1**). A marked temperature variation during the measurements ensures a solid identification of the length-temperature relationship and therefore a better prediction of the length at 20 °C. If small temperature variations occur the background noise may lead to higher uncertainty.

Table 4.1: Expanded uncertainty of the estimated reference lengths of the ABS workpiece using a DLM approach and following formula 4.2 (values in μm).

		<i>Length of data segment /s</i>						
		30	60	90	120	180	240	300
<i>Starting temperature /°C</i>	21	0.73	0.57	0.48	0.43	0.40	0.38	0.38
	22	1.05	0.66	0.55	0.48	0.42	0.39	0.37
	23	0.99	0.64	0.60	0.55	0.45	0.40	0.38
	24	1.24	0.68	0.52	0.50	0.45	0.40	0.38
	25	2.40	0.99	0.59	0.53	0.50	0.44	0.40
	26	2.02	1.67	1.01	0.67	0.54	0.48	0.43
	27	2.93	1.97	1.56	1.18	0.74	0.59	0.50

4.3.3 Non-uniform temperature field with contact sensors and simulations

In the previous section the temperature in the workpiece during the measurement has been considered reasonably homogenous and the temperature in a central position of the part representative of the overall thermal condition. The linear behaviour found between length and temperature supports this hypothesis. In different situations the temperature field can be less homogenous causing the need for a more advanced analysis of the thermal state (see the example in section 4.3.1). The next study case has been developed to demonstrate the close relationship described in **Figure 4.4** between the three contributors to the measuring strategy.

Experimental work

The experimental setup is depicted in **Figure 4.13**. The workpiece and the measured dimension are nominally identical to the ones in the previous section. However the positioning fixture and metrology frame are different. Two inductive displacement probes are used to measure the workpiece length to a specific position in the bottom area of the component. The frame is composed of Invar components. The workpiece positioning is similar to one layout used in section 3.3.2 to evaluate the potential of a thermocamera implementation in DLM. Already at that stage the temperature field of the part has been qualitatively assessed having a primary gradient in the vertical direction due to the heat exchange with the bottom metallic support. The temperature field therefore cannot be

considered homogeneous. Three thermocouples type K are applied to the surface of the workpiece to measure the temperature in different locations: two of them are approximately aligned at the same height of the displacement probes while the third one is located in the top section of the sample surface. The part is heated on the device depicted in **Figure 4.10** and successively placed in the measuring fixture till complete cooling, happening within the first 10 minutes of measurement. Several nominally identical samples are considered for the repetition and the replication of the procedure. A total of 25 repetitions have been performed. The test is performed in a non-controlled environment therefore the ambient and the frame temperature are measured as well and the stability of the fixture is controlled regularly using a reference Invar artefact with same nominal dimensions as the polymeric workpiece. The measured ambient temperature is 22.4 ± 0.2 C. Both temperature and dimensions of the metrology frame were stable during the tests.

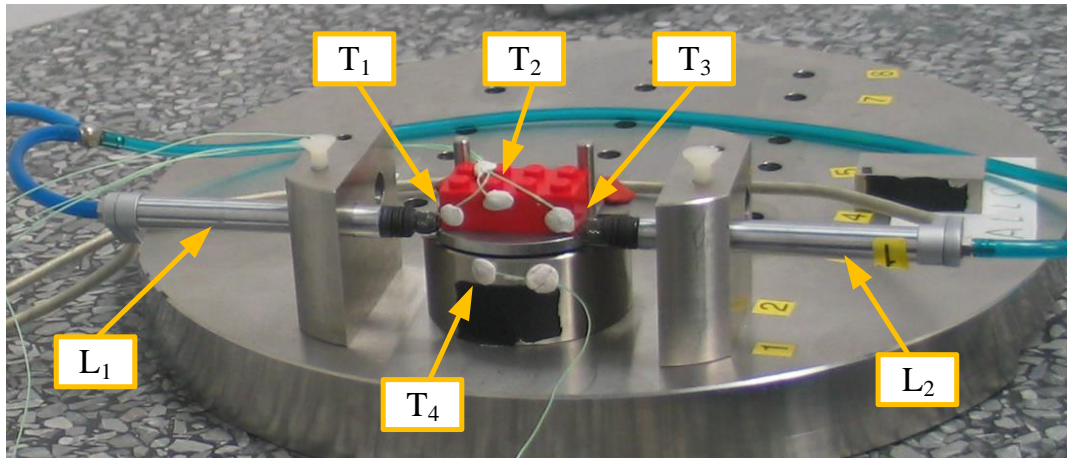


Figure 4.13 Set-up for multipoint temperature measurements on a ABS workpiece: L_i = inductive probes, T_i = thermocouples.

Analysis of different probing strategies

The material properties are considered constant in the temperature range investigated. Moreover the mono dimensional length measurement does not allow addressing the issue of distortions and second order deformations. For those two reasons a linear relationship between length and temperature is sought. The three measured temperature are then combined in different way to provide a more appropriate temperature value that better matches the hypothesis of linearity between length and temperature. Three models are defined using weighted averages of the measured temperature. The models can be described as follows:

$$L_{20} = L_m \left[1 - CTE \cdot (T_{a,i} - 20) \right] \quad 4.3$$

$$T_{a,i} = \frac{k_{i,1} \cdot T_{m,1} + k_{i,2} \cdot T_{m,2} + k_{i,3} \cdot T_{m,3}}{3} \quad 4.4$$

Where

L_{20} is the estimated length at 20 °C;

L_m is the measured length;

CTE is the estimated apparent coefficient of thermal expansion;

$T_{a,i}$ is the average temperature for the considered model I ;

$T_{m,j}$ is the measured temperature at the location j on the workpiece (according to **Figure 4.13**);

k_{ij} is the weight applied in the average model i to temperature $T_{m,j}$; they are listed in **Table 4.2**.

Table 4.2: Weights used in the averaging of the temperature measured in three location of the ABS workpiece.

		<i>Temperature location</i>		
		1	2	3
<i>model n.</i>	1	1	1	1
	2	1.2	0.6	1.2
	3	1.5	0	1.5

Model 1 considers a simple averaged temperature, while in model 3 the temperature in position 2, and therefore the one furthest from the length measuring location, is neglected. Temperatures in location 1 and 3 are considered equivalently in all the three models as they are placed in equivalent locations, according to the assumed temperature field.

A linear regression is performed to fit the experimental data with the analytical model described in equation 4.3. The agreement between analytical model and experimental results is appraised considering the sum of squares of the regression residual. The results for all the repetitions performed (5 workpieces measured 5 times) are depicted in **Figure 4.14**. Model 3 leads to the smallest residuals in all the cases considered. Moreover the initial assumption of a vertical temperature gradient confirms that in this specific condition the more appropriate temperature to assign to the workpiece is measured in the location at the same height as the measured length.

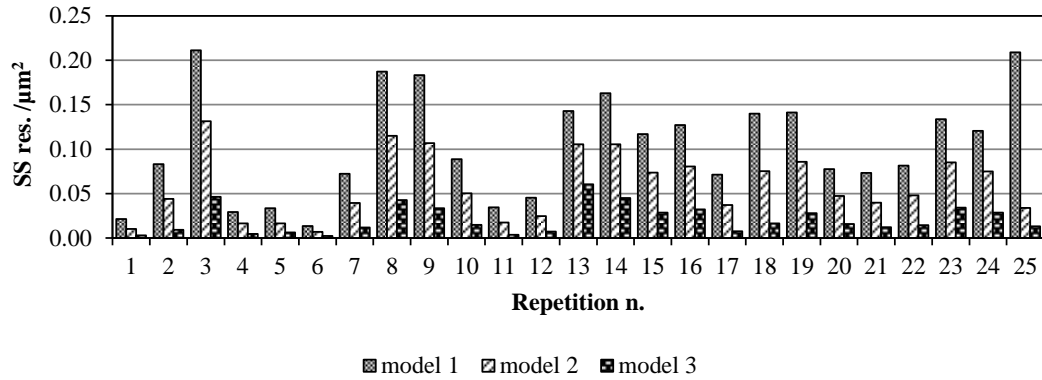


Figure 4.14 Sum of square of residuals of the regression of cooling curve.

FEM simulations

A finite element thermomechanical model of the polymeric workpiece has been developed using the commercially available software ABAQUS (Dassault Systèmes). The measuring process is simulated modifying initial and boundary conditions. The initial temperature has been considered uniformly distributed. The boundary conditions are adjusted to match the thermal coupling with the support plane and the convection of air. The material properties regarding thermal expansion and thermal conductivity have been tailored to best match the simulated behaviour with the measured temperature and length variation of each run. The low variability of the heat transfer coefficient ensures that the problem is well formulated. The performed simulation provides more information about temperature and displacement in all the locations of the workpiece. Hence a broader understanding of the distortions occurring during the measurement is available together with a well-defined temperature field. **Figure 4.15** represents the temperature fields estimated with the FEM simulation at the beginning and at the end of the measurement. The formation of a vertical temperature gradient is visible. Moreover the FEM model provides intrinsic material properties uncorrelated from the geometry. The coefficient of thermal expansion calculated during the regression of the experimental data is compared with the CTE included in the FEM model (see **Figure 4.16**). On average the FEM model provides a CTE value higher than the analytical. This difference can be partially attributed to the underestimation of the relevant temperature in the analytical calculations. The smaller discrepancy is obtained from the comparison of the FEM result with the analytical model 3. The average values of the estimated CTEs and the standard deviation over all the repeated measurement runs are listed in **Table 4.3** showing a good agreement between analytical model 3 and FEM model.

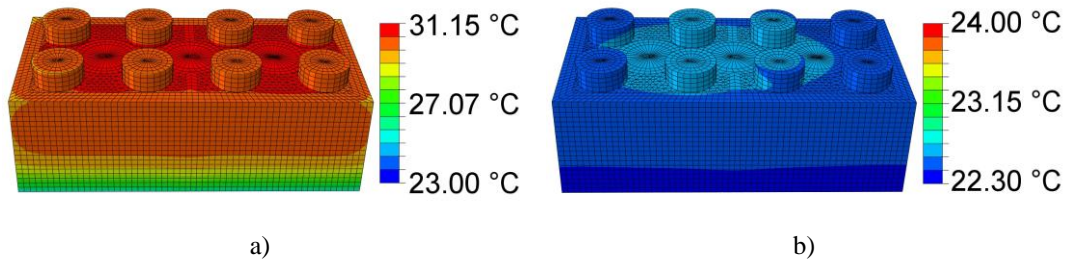


Figure 4.15 Temperature fields estimated from numerical model after 30 s (a) and 600 s (b) after the beginning of the measurement.

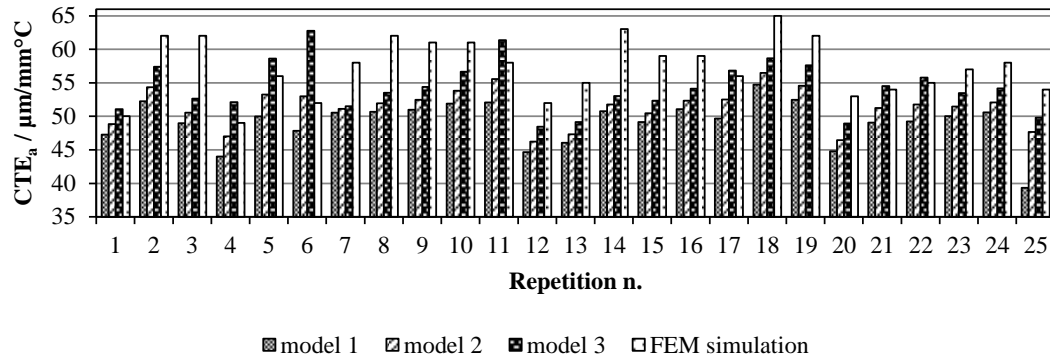


Figure 4.16 Apparent CTEs estimated with analytical and numerical tools.

Table 4.3: Estimated average CTEs for analytical and FEM models. Values in $\mu\text{m}/\text{mm}^\circ\text{C}$.

<i>Model type</i>	<i>Average CTE</i>	<i>Standard deviation</i>
Analytical 1	49.1	3.3
Analytical 2	51.4	2.8
Analytical 3	54.3	3.7
FEM	57.3	4.3

4.3.4 Discussion

Temperature in a DLM typical application is neither constant nor uniform, especially in the measuring workpiece. The choice of the location where the temperature measurements are performed is crucial to obtain good results. A first analysis is performed to address the definition of the proper measuring time in a cooling phase of the measuring part for obtaining a reliable output. The temperature range plays a more important role in the definition of the measuring strategy. A certain amount of time must pass from the instant of the part positioning on the fixture and the measurement trigger to avoid steep temperature gradients and fast temperature variation as they are difficult to model and cause unstable measurements. At the same time it is necessary to ensure a sufficient temperature variation for a solid fitting result. Hence the definition of the measuring time concerning the thermal aspect is a trade-off between reducing the time of measurements and ensures sufficient measurement accuracy. The cooling phase of metallic parts is much longer than for polymer parts, in fact a metallic gauge block can take more than one hour to cool from 25 to 20 °C [9] while in the case presented above the polymer parts need less than 15 minutes to undergo the same cooling. Therefore for polymer parts the main issue is represented by the limitation of the time gap between production and measurement to avoid excessive cooling while for metallic part it is important to reduce the measuring time to the minimum still providing an accurate length estimation.

The same polymer part is measured in a different fixture and (**Figure 4.13**) showing different problematics. The differential cooling is now dominant as the heat exchange occurs in a preferential direction and it is evident by measuring the temperature in a different location. The optimal location for the temperature measurement is determined based on the best agreement of the experimental results with a linear thermal expansion. The temperature measurements in multiple points are useful as input for a FEM simulation of the cooling phase which can lead to improvements of the calculations for length extraction. A further study exploiting the results of the simulation is represented by the analysis of the sensitivity of the length extraction to the position of the temperature sensors. As output the uncertainty contribution due to the misplacing of the temperature sensors can be calculated. This is however not discussed in the thesis.

4.4 Influence of humidity

The effect of humidity does not have the same consideration as temperature in dimensional metrology. Nevertheless it constitutes a main contributor to the dimensional instability of polymers. Chapter 2 has already introduced the concept of hygroscopic swelling and coefficient of moisture expansion. However the measurement of the moisture uptake is not a direct task and presents different issues than the thermal case. The measurement of the moisture uptake in a component can be performed with a gravimetric method. It consists of measuring the weight of the part before and after the moisture absorption occurs [146]. Despite its simplicity this measuring technique provides measurements of the sole relative changes in the workpiece weight and not the absolute moisture content.

Hence it is insufficient in a DLM application unless the measurement occurs in a well-known and stabilized condition that can be referred to the reference conditions or to the complete dry condition. Nonetheless in many manufacturing processes, like injection moulding, the raw material is dried prior to the moulding process and therefore it is potentially possible to assume a dry condition of the components in the early stage after production. Moreover the gravimetric method provides only information on the moisture uptake of the whole part that can be related to the change of the overall workpiece volume. Thus the relationship between increase of weight and increase of one specific dimension depends on the geometry of the part and its entity must be demonstrated experimentally or with simulations.

For a component in equilibrium with the ambient the change in dimensions due to water absorption can be related directly to the relative ambient humidity RH , instead of to the change in weight:

$$L_{RH} = L_{50} + L_{50} \cdot CME_{RH} \cdot (RH - 50) \quad 4.5$$

Where:

L_{RH} is the length of the object at ambient humidity RH ;

L_{50} is the length of the object at 50% ambient humidity.

CME_{RH} is the coefficient of moisture expansion relative to ambient humidity

In both cases if the coefficient of moisture expansion is constant and the hygroscopic swelling and the moisture uptake follow a linear relationship. To generalize for non-linear behaviour the coefficient of moisture expansion can be considered a function of the humidity uptake for more complex models.

The manufacturing industry of polymer goods mostly uses the process of injection moulding that produces in most cases parts with initial low level of water content. The freshly produced parts therefore need an acclimatization period to absorb water and reach equilibrium with the ambient. As DLM must provide a result in an early stage after production, the measurement must be performed during this transitory period. Hence equation 2.4 is applicable directly using the gravimetric method. An extra computational step must be introduced to correlate the results to the condition at reference ambient humidity.

The investigations on water absorption of polymers described below have the double objective to get a better understanding of the phenomena and to analyse possible probing solution to propose for a DLM application. The tests performed can be divided into two types. The first one concerns measurements of water absorption and hygroscopic swelling in equilibrium conditions. The second one instead concerns the study of the transitory period occurring after the production of a plastic component.

4.4.1 Hygroscopy and swelling

To have a better understanding of the moisture absorption in polymer parts and to confirm the assumption described above a series of tests are performed on a commercial ABS part to assess the water absorption and the hygroscopic swelling in equilibrium conditions with the ambient at different relative humidity levels. Two series of tests have been per-

formed, namely test 1 and test 2, dealing with measurement in controlled and uncontrolled humidity conditions respectively.

Measurements on a climate chamber

The experiments referred to as test 1 are performed using a humidity chamber capable of maintaining a stable level of temperature and humidity (**Figure 4.17**). The length of the part is measured using a setup made of Invar with 8 measuring stations, each one equipped with a displacement inductive probe with resolution of $0.1\text{ }\mu\text{m}$ (**Figure 4.18**).

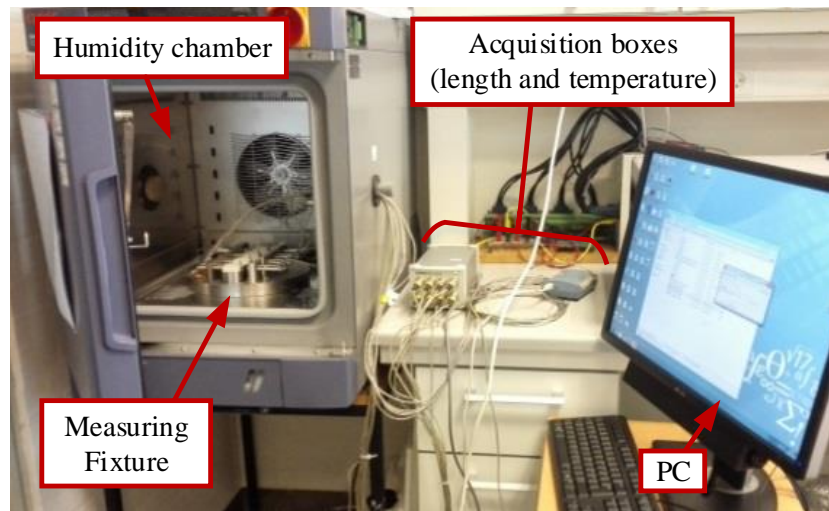


Figure 4.17 Experimental set-up for moisture uptake and moisture expansion measurements.

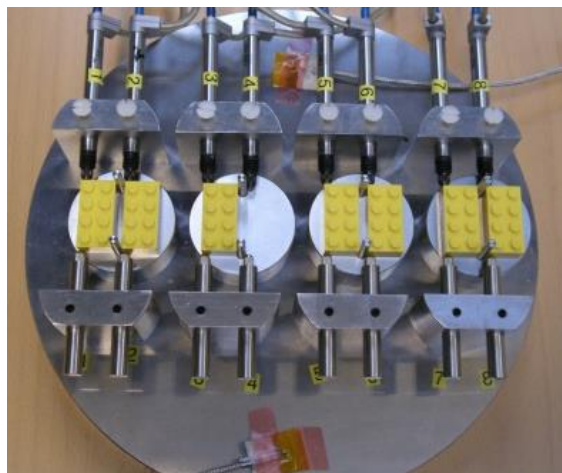


Figure 4.18 Fixture for simultaneous length measurements of 8 parts.

An electronic scale, with a resolution of 0.1 mg, is used for checking the weight of the samples. A preliminary test needs to be performed to assess the time necessary for the workpiece to reach saturation after changes in the ambient condition. The polymer parts are soaked in water for several days and the weight variation is measured regularly. According to the increase in weight, the water absorption is considered concluded after 24 hours. Even though the absorption of liquid water (soaking condition) and vapour water (due to ambient moisture) are slightly different diffusion mechanisms, the result of the preliminary test is considered a valid estimation of the saturation time to use in the moisture absorption experiment. Consequently the tests performed consist of the measurement of weight and length of the selected ABS parts that have been conditioned at constant humidity and temperature in the humidity chamber for a time of about 24 hours. The temperature in the chamber is fixed at 20 °C to comply with the reference temperature condition and leaves only the ambient humidity as the only variable parameter. Several levels of relative ambient humidity (RH) are contemplated from 50 % to 90 %.

A set of absorption curves, length and weight variation, is obtained for 8 nominally identical parts. To allow the comparison among all the workpieces only relative length and weight variations are considered in the data analysis. Therefore the initial step in the data processing consists of subtracting the average value of length and weight for the experimental curves of each workpiece. After this step all the data points converge to a similar trend and can be analysed jointly. Length and weight variations are also referred to the reference condition; therefore a regression using a linear model is performed to find the value corresponding to 50 % relative humidity which is then subtracted from the experimental data. The relative length and weight variations are plotted in **Figure 4.19**; as they are referred to the reference condition they have zero value in correspondence to relative humidity of 50 %.

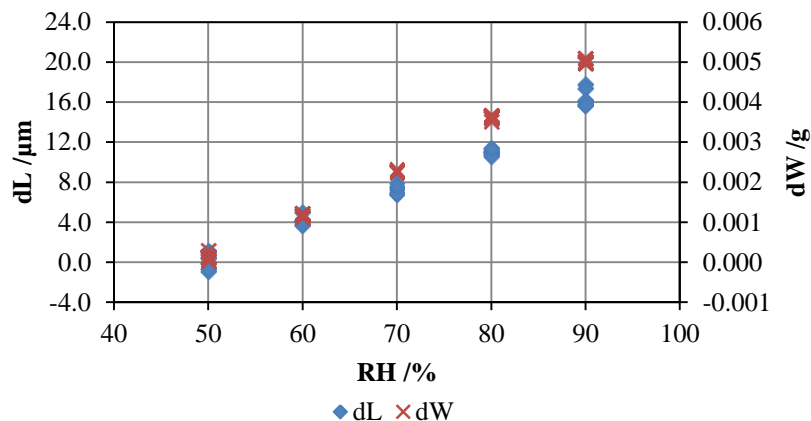


Figure 4.19 Test 1 on hygroscopy: relative length (dL) and water content (dW) variations for 8 parts. The values are zeroed at the 50 % relative humidity condition.

Both length and weight variations present a linear increasing trend with the increase of the ambient humidity. In **Figure 4.20** the length variation dL is plotted against the weight variation dW , corresponding to the water content increment from the reference condition.

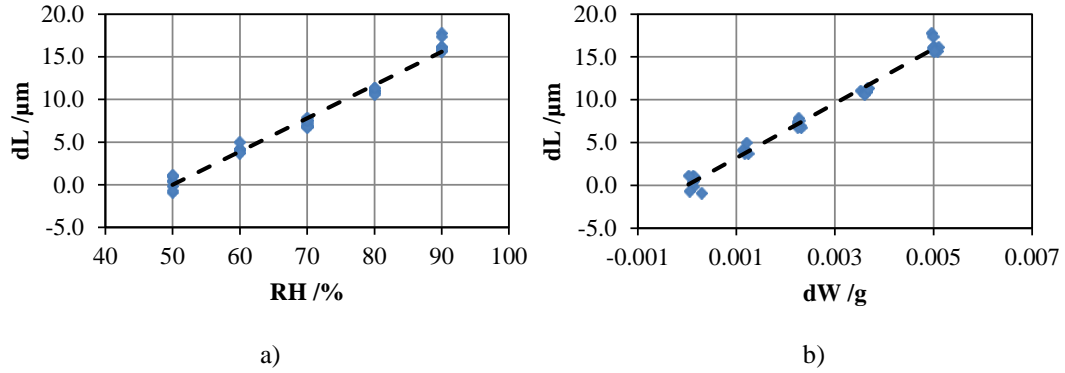


Figure 4.20 Test 1 on hygroscopy: relative length dL vs relative ambient humidity RH (a) and relative water content dW (b). The dashed line represents the linear regression of the data.

A linear regression is then performed to find the value of the apparent coefficient of moisture expansion, considering the ambient humidity $CME_{RH,a}$ and the moisture uptake $CME_{W,a}$ defined according to the formula:

$$CME_{RH,a} = \frac{dL}{dRH} \quad 4.6$$

$$CME_{W,a} = \frac{dL}{dW}$$

The standard uncertainty of the calculated apparent CME is estimated considering the standard error of the regression coefficient, which is considered as the contribution of the experimental repeatability. The expanded uncertainty is then calculated applying a coverage factor corresponding to a confidence level of 95 %.

Measurement in non-controlled humidity environment

A similar test, referred as test 2, is successively performed on parts with same characteristics (material and geometry) in non-controlled humidity conditions. Four parts are stored in a room at 20 ± 0.5 °C and their dimension and weight are measured daily for a period of time of 50 days allowing the ambient relative humidity to vary approximately from 20 to 50 %. Ambient humidity variations are gradual hence the workpieces are considered always in quasi-equilibrium with the ambient. The length is measured using a contact CMM with MPE of $0.4 + L/900$ μm , with L =measured length, in mm. The alignment and the procedure of the CMM measurements resemble the one employed in the previous test. The weight is measured using an electronic scale. The experimental

values are again considered as relative variation therefore for each workpiece data set the average values are subtracted from the original data. To evaluate the influence of possible unsaturated condition the length variation is compared against both weight variation and ambient relative humidity. In the case of severe non-equilibrium the influence of the weight in the length variation is more dominant than the influence of ambient conditions according to that stated in chapter 2. Furthermore length variations contain the influence of time, probably due to an aging process of the polymeric material. Therefore time is considered as a second input parameter in the data analysis. Two linear regression models with two input variables are analysed in the study of length variation dL to consider the effect of time t combined with ambient humidity RH and moisture uptake dW respectively. The regression models can be described as:

$$dL = a_1 + b_1 \cdot t + CME_{RH,a} \cdot RH \quad 4.7$$

$$dL = a_2 + b_2 \cdot t + CME_{W,a} \cdot dW \quad 4.8$$

Higher grade polynomial models are not considered since they do not provide any sensible improvement in the results. **Figure 4.21** shows the experimental data after the removal of the time influence. Both the models appear valid to represent the length variation behaviour indicating that saturation is achieved throughout the measurement. The regression also provides the values for the apparent coefficient of moisture expansion CME_a . Its uncertainty is estimated equal to the standard error coming from the regression. The values of the experimental CMEs are compared in **Figure 4.24**; there is not a good agreement between the results of the two separated tests.

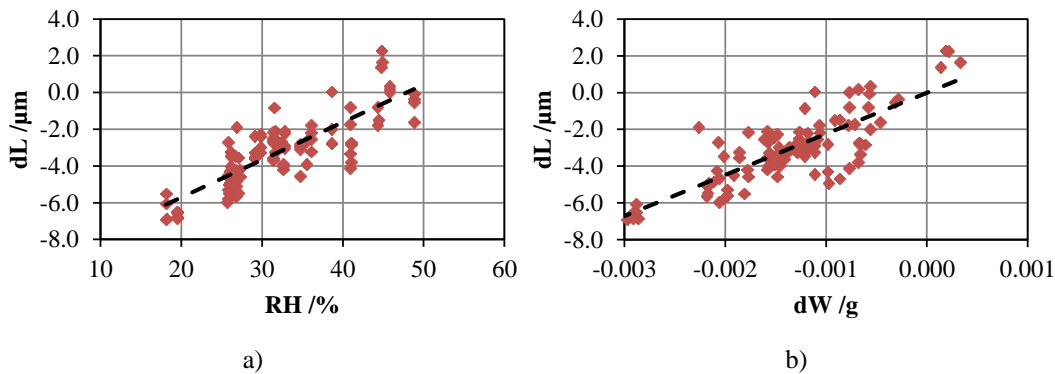


Figure 4.21 Test 2 on hygroscopy: relative length dL vs relative ambient humidity RH (a) and relative water content dW (b). The dashed line represents the linear regression of the data.

Merged results

A further step is performed to investigate the compatibility of the two experiments. The two sets of values of relative length and weight variation are merged together.

Figure 4.22 depicts the merged values together with the linear model describing the separated data set. The consideration of one model over the other introduces an error in the whole humidity range (0-100 %) When ambient relative humidity is considered as input parameter a larger error occurs. Even though the calculated CMEs are not compatible the merged data appear consistent. A new regression with a linear and quadratic model is performed to fit the data, see **Figure 4.23**. The quadratic model better characterizes the length variation trend and addresses the issue of the different CME values. However the difference between the two regression models is minimal, especially regarding the calculation with the weight variation, and the linear model can be considered instead. The apparent CMEs calculated for the merged data set consists in an averaged value between test 1 and test 2.

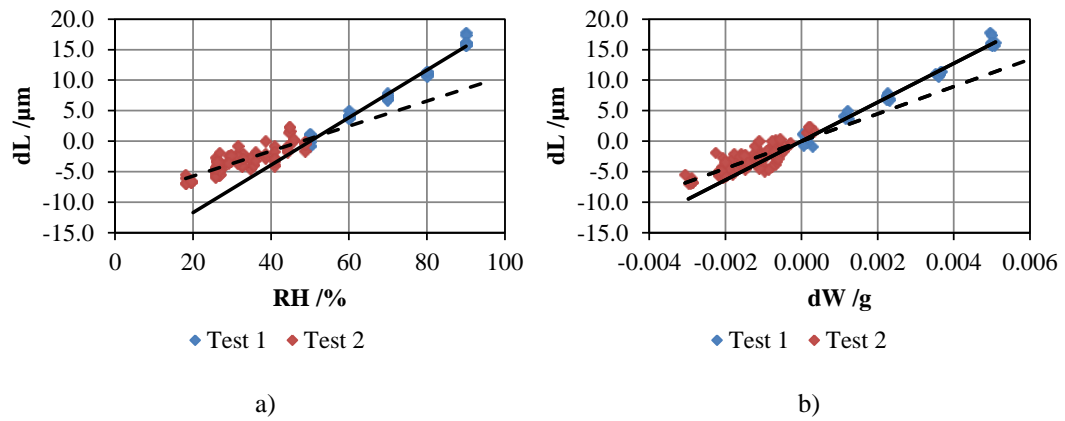


Figure 4.22 Merged data sets of length variations at different ambient humidity. The continuous and dashed line represent the regression line performed with data sets of test 1 and test 2 respectively.

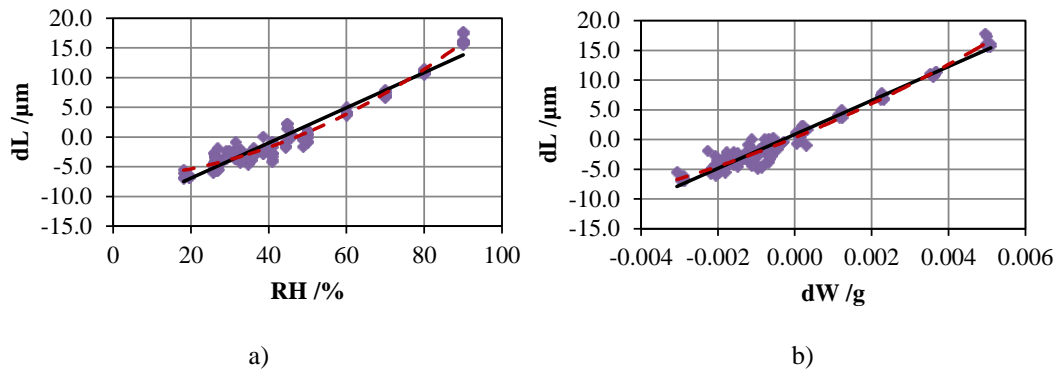


Figure 4.23 Linear (continuous black line) and quadratic (dashed red line) regression of the merged data set of two tests on hygroscopy.

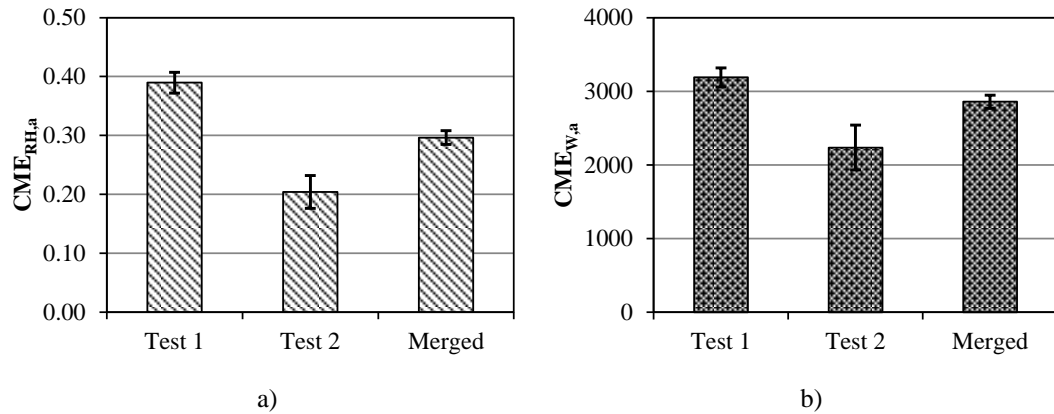


Figure 4.24 Calculated apparent CMEs for two separated tests and for the merged data set considering: a) relative humidity RH; b) relative water content dW . The error bars represent the estimated expanded uncertainties.

4.4.2 Transitory period

Length and weight at variable ambient humidity

After the investigations of moisture uptake in saturated conditions it is necessary to study the transitory period occurring after the production of polymer parts. A first test involves ABS aged parts that have already been subjected to the post-moulding moisture uptake. The measuring equipment, depicted in **Figure 4.25**, is similar to the one used for test 1 described in the previous section.

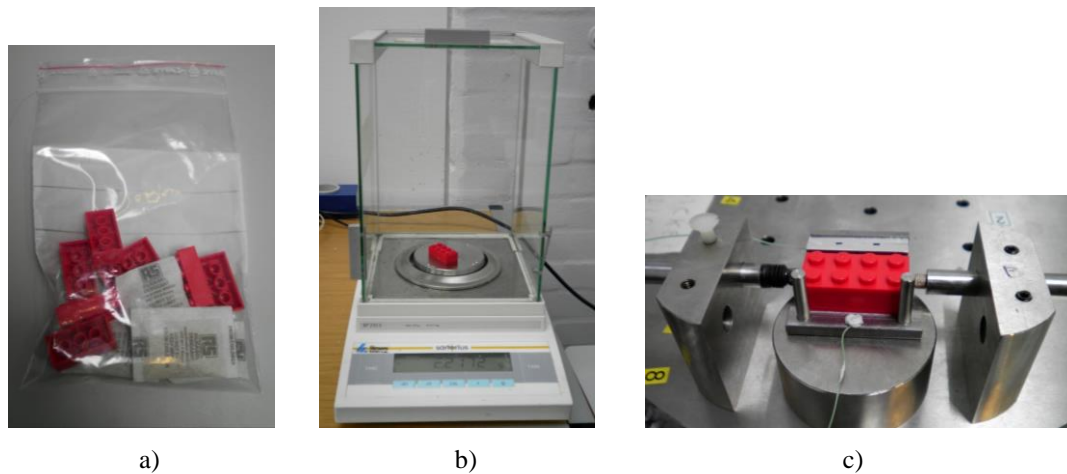


Figure 4.25 Equipment for moisture absorption measurements: a) sealed bags with desiccant; b) electronic scale; c) length measurement fixture.

The experiments are performed in a non-controlled environment; throughout the tests the ambient temperature fluctuates between 23.58 °C and 25.8 °C while the ambient relative humidity between 23 % and 34 %. Ambient humidity is not considered as an influent parameter due to its limited variation, instead the temperature of the workpiece is measured using a thermocouple type K, with resolution of 0.1 °C and measurement accuracy of 0.2 °C. The workpiece temperature is also influenced by the operator handling hence it is always equal to or greater than the ambient one. A batch of 40 parts produced from 8 different cavities in 5 shots is considered. The workpieces are initially dried to emulate the post moulding conditions employing a dryer for polymeric raw material (pellet) and using drying parameters (time, temperature, air flow) similar to the ones suggested for pellets of the same material. The parts are then stored in sealed plastic bags together with sachets of desiccant and acclimatized to the ambient temperature. Weight, length and temperature are then measured every hour for the first 8 hours and one more time after about 24 hours.

For each workpiece length and weight outputs are normalized subtracting the average value to allow the comparison among the batches. **Figure 4.26** shows the values of weight variation as function of time and length variation as function of time, temperature and weight variation.

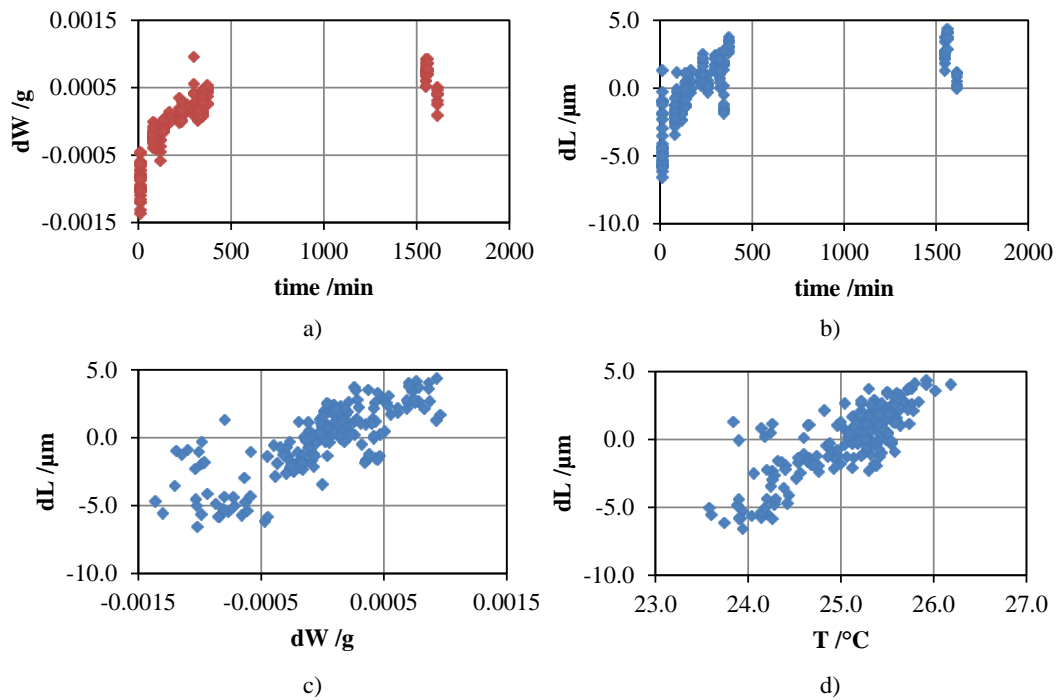


Figure 4.26 Experimental results on moisture uptake: a) weight variation dW vs time t ; b) length variation dL vs time t ; c) length variation dL vs weight variation dW ; d) length variation dL vs temperature T .

The complete saturation appears to occur within the test time. A non-linear regression, using the model described by equation 4.9, is performed on the whole dataset to consider the effect of time t and the effect of the temperature, considered as the difference of the measured value T from the reference temperature value, on length variation dL .

$$dL = a \cdot e^{bt} + c \cdot T + d \quad 4.9$$

An exponential trend is chosen to describe the evolution in time of the moisture absorption in agreement with a gradient driven process and to consider the stabilization at infinite time. The regression residuals appear flat, without any particular remaining trend; the residual standard deviation is 0.78 μm .

The influence of the temperature can now be removed from the experimental data, and the length at the reference temperature $dL_{T=20}$ calculated according to equation 4.9.

$$dL_{T=20^\circ\text{C}} = dL - c \cdot (T - 20) \quad 4.10$$

A regression following equation 4.8 can be performed to define the influence of the dimension on the absorbed moisture. The resulting $CME_{W,a}$ is 2655 $\mu\text{m/g}$ with an expanded uncertainty of 255 $\mu\text{m/g}$, estimated considering only the regression error. This value is compatible with the result from the pooled analysis in section 4.4.1.

After production weight measurements

A second investigation is performed at the production site to measure the actual effect of moisture absorption after injection moulding. Only the weight variations are considered and measured using an electronic scale with a resolution of 1 mg. Three batches are produced on different days and the weight progression is monitored during working hours for the following days. During the whole test the ambient temperature is $22.5 \pm 0.4^\circ\text{C}$. Ambient humidity for the first two batches is $53.2 \pm 2.4\%$ while for the third batch is slightly lower, equal to $45.4 \pm 1.2\%$. To reduce the variability introduced by the low resolution, the measured weight value consists of the average values over three replications. Two batches are composed of 4 elements and the third one from 8 elements; the elements within each batch are produced from the same mould cavity. Similarly to above the average weight of each part value is subtracted from the measured weight variation data. The experimental values are depicted in **Figure 4.27**. The weight variation dW over time t appears to follow a negative exponential increment hence a non-linear regression is performed according to the equation:

$$dW = a \cdot e^{bt} + c \quad 4.11$$

The overall moisture uptake dW after moulding can be found by subtracting the coefficients a to c . The numerical results of the regression performed on the three batches are listed in **Table 4.4**. The regression coefficients can be considered compatible. In **Figure 4.27** a comparison is performed between the results of batch 1 and the information on weight variation acquired in the previous test of this section. The two data sets suggest different trends, probably caused by an incomplete drying occurring in the conditioning of the samples in the dryer. Nonetheless the results of the previous investigation remain

valid as they describe the direct connection between length and weight variation represented by the apparent coefficient of moisture expansion. Moreover the moisture uptakes are compatible with the hypothesis of initial dry condition. According to the results of section 4.4.1 the ABS parts absorb 0.005 g of water passing from a dry condition to an ambient with humidity of 50 %.

Table 4.4: Coefficients of the non-linear regression of the post moulding moisture uptake. The uncertainty U is referred at 95 % level of confidence.

<i>Batch n.</i>	<i>a</i>	<i>U(a)</i>	<i>b</i>	<i>U(b)</i>	<i>c</i>	<i>U(c)</i>	<i>dW/g</i>
1	-0.0049	0.0002	-1.96	0.19	0.0007	0.0001	0.0056
2	-0.0048	0.0004	-2.34	0.77	0.0014	0.0003	0.0062
3	-0.0043	0.0001	-2.10	0.21	0.0010	0.0001	0.0052

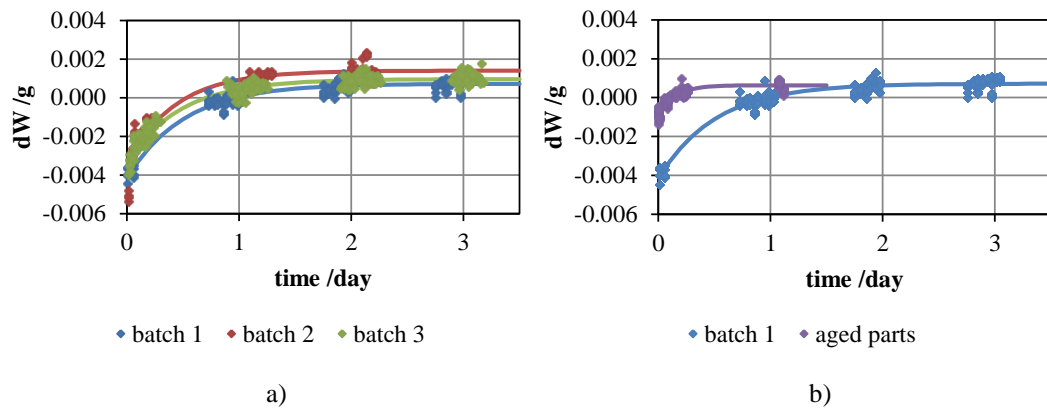


Figure 4.27 Weight variation due to moisture uptake (continuous line represents the exponential regression model): a) three batches measured after production; b) batch from production compared with a dried aged batch.

Weight measurements on dummy parts

Two main issues arose during the investigation of moisture uptake. The first one is represented by the limited resolution of the electronic scale. In the study performed at the production site described above the resolution constitutes approximately the 20 % of the total weight variation measured. Scales with higher sensitivity are available on the market but they are affected by disturbances occurring in production environment, such as vibrations and dust. The second issue consists of the inconvenient measuring procedure to be

executed when both length and weight are simultaneously measured. In fact, to acquire both quantities in a dynamic mode the sample has to be repeatedly shifted from the length measuring equipment to the scale and any sensor attached to the sample, such as temperature sensors, removed before the weight measurement. This procedure is particularly unsuitable if the sample undergoes to rapid cooling as in the study cases described in section 4.3. A strategy to solve this issue is the introduction of an indirect measurement of the sample weight. If the behaviour of parts produced with injection moulding is considered similar among samples produced from the same shot, the measured weight variation of any item can be generalized to all the parts of the same shot. This allows the fulfilment of the weight variation measurements on a secondary workpiece and transfer the information to the main one. Moreover the secondary workpiece can consist of multiple parts. The relevant weight variation is then calculated as a fraction of the measured one with a consequent reduction of the variability due to the resolution of the scale. To support the described methodology the measurements in the previous section are also performed for groups on multiple elements, named dummy parts, produced concurrently to batch 1 and batch 2 respectively, but not considered in first place since they come from different mould cavity. The exponential regression described in equation 4.11 is performed on the average behaviour of the dummy parts. The regression coefficients are compared with the one calculated for each single element of batch 1 and 2 in **Figure 4.28**, showing an adequate agreement between the behaviour of the principal samples and the dummy parts. Besides, the use of groups of dummy samples reduces the experimental variability, as expected.

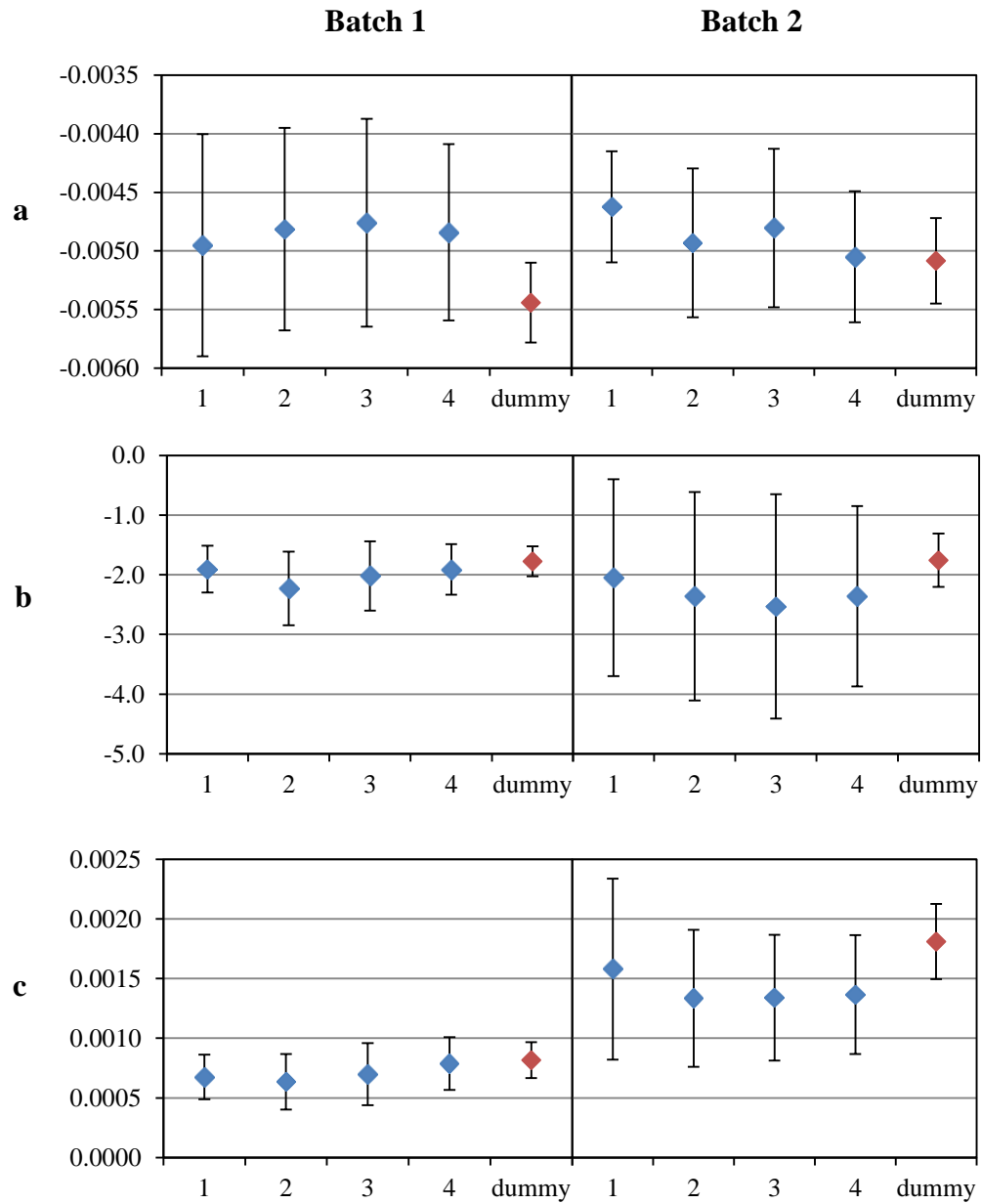


Figure 4.28 Parameters of the exponential regression models of moisture absorption: comparison between principal measured samples and dummy parts.

4.4.3 A proposed method for considering humidity uptake

Considering the knowledge acquired in the experimental work a suggested strategy for extraction of length at reference ambient humidity is presented. In the study case the length variations due to moisture uptake appear much slower than the one caused by temperature variations. This specific outcome can be considered of general validity therefore

when considering moisture uptake it is necessary to formulate a solution that predicts the final length using early stage information.

The proposed solution employs measurements of weight and length and requires a minimum of information on the component behaviour. An initial measurement of length and weight is performed as soon as possible to obtain a data point at low moisture content to be considered as a fully dry condition. More data points (length and weight) are then collected in a period of time of some hours. Length and weight variations are then fitted with a linear or polynomial curve to define the apparent moisture expansion coefficient. The same data points of length and weight can be considered as a function of time and fitted with an exponential model and information about the saturation condition at the average ambient relative humidity occurring during the measurements can be extrapolated from the model. By considering the increase in weight and length from the dry condition to saturation linearly proportional to the ambient humidity, the conditions referred at relative humidity of 50 % can be calculated. The proposed solution presents many downsides starting from the assumption of the initial condition of perfectly dry parts. Moreover many regressions and extrapolations are required whose performance have not been demonstrated. Alternatively the length at relative humidity of 50 % can be calculated using a more conventional calculation employing a priori knowledge. By knowing the length just after production and assuming specific moisture content, in any case close to zero, a systematic compensation can be applied to calculate the length at reference condition. This approach is necessary if the measurement has to be performed within few minutes after production.

4.5 Conclusions

This chapter gives an insight into the problematics faced during the definition of probing strategies for a DLM application. The main scope is to produce some practical study to support the definition of a set of guidelines for the development of a DLM application. The behaviour of a measurement workpiece in an industrial environment depends on material properties, geometry of the part and boundary conditions. It is therefore necessary to develop an iterative designing process to obtain the optimal measuring solution. Preliminary studies, focused on the characteristics of the measuring part and on the thermomechanical coupling between part and fixture, have to be performed to give a wider understanding of the measuring system and provide more accurate alternatives. The outputs from numerical FEM simulation are useful as an alternative to experimental work and to improve the prediction algorithm.

A study on the effect of contact force on ABS parts shows how the choice of the analytical model for the description of the experimental results affects the reference length determination. Models with different complexity, more or less supported by theoretical bases (linear, quadratic, hertzian model), are likewise compatible with the experimental data, due to the limited amplitude of the forces involved. A deviation of about 2 μm occurs when considering a simple linear model or a complex hertzian model. The applica-

tion of a prolonged contact causes creep in viscoelastic materials. The experiments show that for short time contact measurements the creep effect is of the order of one tenth of a micrometre and can be ignored when dealing with overall uncertainties of the order of 5–10 μm .

The effect of temperature is studied by heating up the polymer parts to simulate the thermal condition just after the injection moulding process. A first test is performed to investigate the cooling time of prismatic hollow ABS parts and how it influences the choice of the proper measured time. The cooling time required to pass from 30 to 20 °C is of the order of 10 minutes. Higher starting temperatures slightly increase the cooling time due to fast initial heat exchange. Hence the measurement must start within the first minute after the ejection from the moulding machine. This implies a certain vicinity of the measuring equipment to the production line or an automated handling of the moulded parts. By measuring temperature and length over time and performing a regression between the two quantities, the length at reference condition (uniform temperature of 20 °C) can be extrapolated. Uncertainties lower than 2 μm are achieved when considering data vectors corresponding to measuring time longer than 1 minute. A second test is performed on the same component using a different positioning fixture where the measuring length is oriented horizontally. The highly directional (vertical) temperature field, caused by a preferential direction of heat flow towards the support plane, allows the study of different strategies for measuring the temperature. The temperature in three different locations is measured simultaneously to the predefined length. Three different models, considering the weighted average of temperature data are compared. The most suitable model is identified as the one with the more linear behaviour. It considers only the temperature at the same vertical coordinate as the measured length. The data from length and temperature variations are used for producing a FEM thermomechanical model. The results of the numerical solution are compared with the analytical one showing a good agreement between the analytical apparent CTE, which contains the influence of the part geometry, and the numerical one, closer to the definition of material property. The tests show the importance of the analysis of the temperature field during the definition of the measuring strategies. The same components can be measured using different fixtures and the measuring strategies must be adapted consequently. FEM simulations provide an overall complete understanding of the measuring complex.

Two main aspects of influence of humidity on dimensional stability are identified and investigated. The first aspect regards the definition and the study of the relationship between ambient humidity, moisture uptake, and swelling in saturated conditions. The tests are divided into two steps. One is performed in a controlled environment using a humidity chamber to obtain a variation of ambient RH from 50 to 90 % at constant temperature of 20 °C. The dimensions of the ABS components are measured using a dedicated fixture with inductive probes. The second part of the test is performed measuring the polymer component with a CMM in a room with controlled temperature, fixed at 20 °C, and humidity variable from 20 to 50 %. A slight discrepancy between the results of the two tests appears and is attributed to the quasi-saturated conditions obtained in the second tests. A sensitivity of 0.30 $\mu\text{m}/\%$ and $2.9 \cdot 10^{-3} \mu\text{m}/\text{g}$ is obtained in this initial investigation.

A second investigation is performed to study the transitory period occurring after injection moulding when the ABS part absorbs humidity to reach the equilibrium with the ambient. Initially the test involves some polymer parts already stabilized after production which are dried to simulate the production condition and are measured in length and weight during the following 24 hours. The weight follows an exponential trend that can be considered concluded within the measuring time. The dimension has a similar trend with a further systematic effect due to the effective workpiece. After the correction of the thermal systematic effect the length variation due to moisture uptake exhibits behaviour comparable to the one found in the first investigations. The next step involves measurements of moisture uptake just after injection moulding. The tests are performed at the industrial site and the weight of freshly moulded ABS parts is measured for several days. The moisture uptake does not comply with the one found previously on artificially dried parts, which means that the drying process cannot be considered completed.

A method to measure with higher precision of the weight variation is proposed. Assuming a similar behaviour among the elements produced from the same cavity in the same shot the weight variation on the principal part can be estimated from weight measurement on a group of dummy elements. A study on two batches of ABS parts supports this indirect measurement as the behaviour among elements from the same shot is compatible.

Finally two solutions are proposed to obtain measurements at reference ambient humidity. One considers concurrent measurements of weight and length during a period of time of some hours. It requires extrapolations and assumptions therefore it requires a validation investigation. The second one applies a more conventional systematic compensation.

5

Optical solution for DLM using a vision system and digital image correlation

5.1 Optical solution for profile measurements

Optical metrology usually employs general purpose measurement systems, like laser scanners and optical CMM. The possibility of performing different measuring tasks makes these systems very versatile yet it increases their costs. On the contrary, in contact dimensional metrology general purpose solutions are often substituted with dedicated devices and fixtures designed for a specific application. An innovative solution is therefore conceived to address the implementation of optical instruments in customized measurement apparatus.

5.1.1 Method

Considering the case of an optical CMM equipped with a video probe, a 2D profile of an object can be measured taking pictures of the edges of the object and performing an edge detection routine. Movements of the camera ensure coverage of large profiles with an acceptable magnification and resolution. Traceability is usually established with calibration of the optics and often with previous measurements of a reference artefact. By including a traceable reference artefact in the field of view of the video probe the measurements of a profile becomes immediately traceable and insensitive to systematic errors, for example due to temperature or camera movements. For measurements of 2D profiles on objects with a planar surface the reference artefact can be represented by a grid, a scale

or a series of marks on a flat plate. The design developed in this work consists of a flat transparent plate with reference marks on the top surface. The plate works as support plane for the measuring object and as a traceable reference. The camera is placed below the plate and focused on the top surface. The measuring object can be placed on top of the plate leaning on the surface to be measured. Consequently the reference marks and the object profile share the same focus plane making it possible to take a picture containing both the measuring and the reference objects.

For some types of measurands (two point length and diameters, small features, thicknesses) the information necessary for the measurements are the position of the edges at the extremity of the workpiece. Hence the camera can focus only in these areas discarding the rest of the profile. This innovative measuring principle can be applied to different practical solutions designed for a specific measuring task or for a more flexible application:

- Using a series of mirrors two or more profile details are projected in the field of view (FOV) of the camera (**Figure 5.1**). The FOV is therefore split in several sections each containing a portion of the profile and the reference marks. In one single shot it is possible to acquire all the information necessary for the measurement. It is a fast and cheap implementation of the measuring principle however the presence of several mirrors introduces image distortions that have to be addressed with a proper calibration. Moreover the dimensions of the profile details observed by the camera are limited since only a portion of the FOV is allocated for each of them. It is possible to create a modular design with a single frame and camera where the reference glass and mirror elements can be replaced to measure different parts and features.

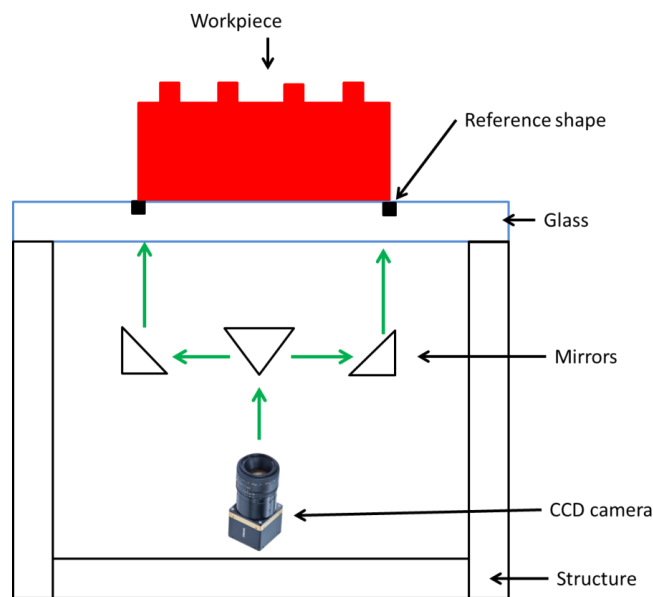


Figure 5.1 Methodology for directly traceable profiles measurements with a vision system.

- Several cameras can be implemented in a system where each camera catches only one detail. It is easy to design and more expensive than the first case. However it can only be implemented to measure relatively big parts due to the size of the optics.
- Introducing a movement to the camera allow viewing of details in different positions of the profile. The movement repeatability does not influence the measurements since the measurement is always performed by comparison with the reference artefact. However the image acquisition of several details does not happen simultaneously and may create problems if fast measurements are needed.
- The measuring concept can be implemented in optical CMMs or already existing systems. For optical CMMs the implementation can be less intuitive since the design described above should be flipped to account for the fact that on CMMs the camera is usually above the measuring object. Similarly to above also in this case the movements do not affect the measurement accuracy.

In an optical set up a variation of the distance from the focal plane causes different magnification values. This effect must be minimized when performing 2D measurements using a single camera because the system is not able to detect axial displacements. Using telecentric lenses differential magnification effects are minimized since all planes in the focus distance of the camera have the same magnification. Telecentric lenses are thus necessary in the case of non-ideal objects where the presence of small chamfers and corner radii causes the measuring edge to be in a different plane than the reference mask. Telecentric lenses also are useful in non-controlled environment applications to reduce the effects of thermal displacements.

The measuring strategy consists of the comparison of the object profile with a reference plate. Differently from optical CMMs an eventual movement of the camera is not involved in the measurement strategy leading to a measurement accuracy independent from the measured feature dimensions. On the other hand the measurement accuracy depends on the reliability of the object edges that are often far from ideal with irregularities such as burrs and uneven chamfers. In the presence of extensive chamfers the measurement is still possible however the depth of focus of the lenses must ensure a focused picture on both the reference and measuring profile. This leads to an upper limit of the magnification applicable. Another limitation of this method is the possibility to measure only features on 2D profiles, such as point to point distances or diameters. As with any optical measurements, the comparison with more established contact measurement is difficult. In particular the measurement of the position of the edge of a profile is not easy to replicate with a contact instrument.

Table 5.1: Advantages and disadvantages of the proposed profile optical measurement solution.

<i>Pros</i>	<i>Cons</i>
Simple and fast measurements	Only profiles
Traceable because of the reference plate	Profiles are often not ideal (chamfer, corner radius, burrs)
Uncertainty not influenced by size to be measured	Influenced by light setting
Can be used for several workpieces with interchangeable mirrors and references	Difficult to compare to contact measurements due to measurements on the edge
Shop floor measurements	

5.1.2 Edge detection algorithm

Edge detection implementations are diffused in image processing and metrology applications. Although edge detection is very commonly used in commercial optical CMM with video probes, the source algorithm is not available and therefore a new edge detection routine must be developed from scratch.

In a generic application two main issues arise. The first one is the recognition of only, and all, the real edges. An ideal edge consists of a sharp colour (or grey level) transition between pixels, similar to a step function. In reality this transition is gradual, with small amplitude and disturbed by noise. The detection algorithm therefore may not recognize an effective edge and, at the same time, may consider an intensity transitions on an continuous surface as an edge (false positive and false negative) [147]. In a metrological application, such as in an optical CMM, edge appearance can be sharpened through a proper light setting to improve the performance of the edge detection. The second main issue regards the accurate definition of the edge position principally for two reasons: the presence of a wide intensity transition zone requires a decision rule to set the edge position in a specific location and the pixel spatial resolution of digital pictures that is not always sufficiently dense. The limited resolution subpixel registration technique can be introduced to refine the resolution to a fraction of a pixel. In the specific application studied the first problem mentioned is not considered as critical since a searching area can be defined manually over the approximate location of the edge. Moreover the use of a back light helps to create a clear and sharp transition between the object (dark areas) and the background (bright areas). The second matter is more relevant in the application. Thus the development of the algorithm has been focused on the optimization of the subpixel edge registration with a fixed edge detection method.

Several edge detection methods are available in literature. They are usually categorized accordingly to their principle. An exhaustive description can be found in [147]. Algorithms based on intensity gradient and template matching are easy to implement and require low computational time while they are less efficient than Gaussian and Laplacian based algorithms [148]. The conceived solution employs an edge detection algorithm

based on the Sobel method due to its simplicity and low computational requirements. It consists in a template based method exploiting intensity gradient properties.

An edge represented in a picture can be described as a ramp intensity function. The edge position can be fixed as the position of the flex point of the ramp, corresponding to the maximum of the 1st order derivative and the zero crossing of the 2nd order derivative (**Figure 5.2**). Hence by computing the picture gradient, the detection of edges is converted to a maximum search problem. An alternative to the gradient operator is represented by the Sobel method (template-based) since it produces an approximated gradient result. The output of any template-based method consists in the convolution of the image with a defined mask as in the case of the application of discrete filters. Sobel method firstly computes the directional convolutions with a horizontal and a vertical mask (**Figure 5.3**) that are successively used to calculate the amplitude of the global convolution. The convoluted image has high intensities in pixels corresponding with steep intensity variation in the original image, i.e. edge locations. Therefore the Sobel convolution is often referred as an edge enhancement filter. The next step in the method is the application of a threshold to the convoluted image that allows the recognition of edges.

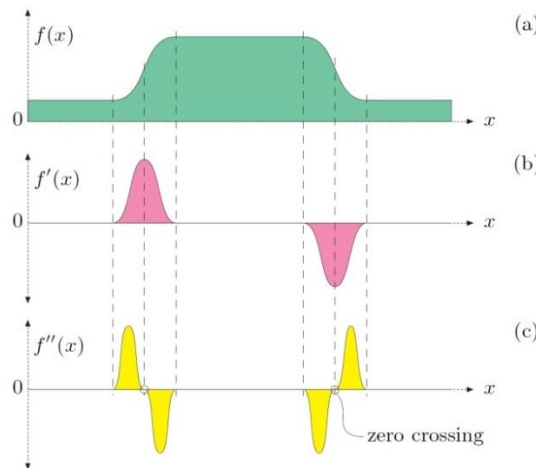


Figure 5.2 Gradient based edge detection: position of the edge (a) corresponds to the maximum of the first derivative (b) and to the zero crossing of the second derivative (c) [149].

-1	0	1
-2	0	2
-1	0	1

a

-1	-2	-1
0	0	0
1	2	1

b

Figure 5.3 Horizontal (a) and vertical (b) Sobel convolution masks.

In the specific application a procedure involving the Sobel edge detection method and a subpixel registration is developed. Firstly a searching area is selected. It must contain only two main portions with different intensity levels that are separated by the edge to be found. The Sobel convolution is then applied to the searching area. Depending on the direction, horizontal or vertical, of the edge the following elaboration is performed along pixel columns or row. For a horizontal (or vertical) edge each column (or row) is analysed singularly. It can be described with a bell shape function in the proximity of the dark/bright transition and with near zero value elsewhere. The position of the maximum of this function identifies the position of the edge for that particular column with a lateral resolution of 1 pixel. The found edge position can be refined with a subpixel registration method. Hence a regression of the neighbourhood pixels is performed considering a bell shape model, i.e. polynomial or Gaussian functions. The maximum position of the bell shaped curve is determined with a higher resolution. Once all the edge points in the searching window are determined a regression using a linear model is performed to remove noise and waviness. The result of the regression, i.e. straight line, is considered as the detected edge (**Figure 5.4**).

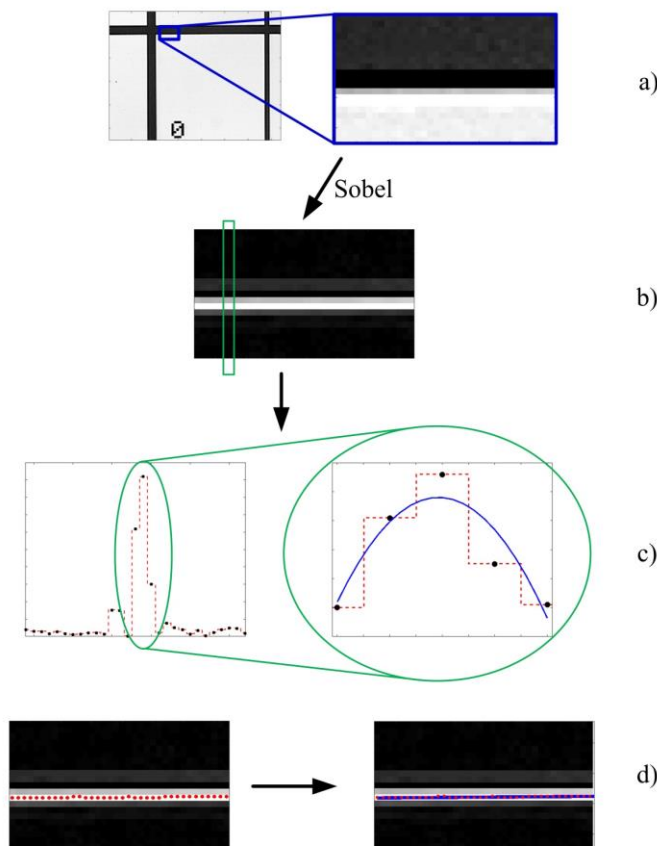


Figure 5.4 Edge detection algorithm: a) searching window selection; b) Sobel edge enhancement; c) column analysis, regression of maximum neighbourhood for subpixel detection; d) linear fitting of calculated data point.

Inclined profiles can be measured in the same way accepting a slight reduction of the performance due to the fact that the maximum search procedure cannot be performed along the edge orthogonal direction. In the case of non-straight profiles, such as holes or corner radii, a similar procedure can be applied. The whole edge must be segmented in portions to best match a horizontal or vertical behaviour that are then recombined to perform a final circular regression instead of a linear one.

5.1.3 Investigation set up

For practical reasons the design and development of a new measuring system from scratch has been avoided and a solution with already available equipment has been developed. Hence an optical CMM is used as imaging device since it already offers an easy alignment of the camera as well as adjustable light conditions. As already mentioned, in this solution the camera is placed above the measuring workpiece, therefore also the reference glass must be placed on top of the workpiece. The CMM design allows the camera to be already aligned vertically while the measuring plane offers a horizontal support for the workpiece.

The vision system involved is composed by a CCD camera equipped with telecentric lenses. The camera has a resolution of 764×572 pixels. The lenses are characterized by a fixed 2x magnification and narrow field of view, about 3×2 mm, and limited depth of focus. Three types of illuminations are available: axial light, ring light and back light.

An optical grid, with cell dimension of 1 mm, has been chosen as reference glass.

5.1.4 Camera calibration

Dimensional measurements from pictures require an initial calibration of the imaging device. The procedure of camera calibration produces a series of parameters necessary for the conversion of the measurement result from image coordinates, quantified in pixels, to world coordinates in length units. Extrinsic parameters consider position and orientation of the camera in the space while intrinsic parameters refer to the camera properties, such as magnification and lens distortions. Intrinsic parameters characterize the behaviour of the camera and are often considered Invariant.

These lenses provide orthographic projection of the scene contrary to conventional lenses with perspective projection. This means that for telecentric lenses the field of view is cylindrical and constant at any distance from the camera and the parallax error, defined as the change in the magnification due to changes of the distance object-camera, is eliminated. The measurement accuracy is then improved since the distance of the object from the focal plane is irrelevant during the measurements and can fluctuate as long as the focus is maintained (see **Figure 5.5**).

Many different calibration procedures are available in literature. However most of them use the pinhole camera model as they refer to conventional lenses and they cannot be applied to telecentric lenses. Nevertheless specific calibration procedures for telecentric lenses have been studied, both considering ideal lenses [150][151] and introducing distortions [3] [4].

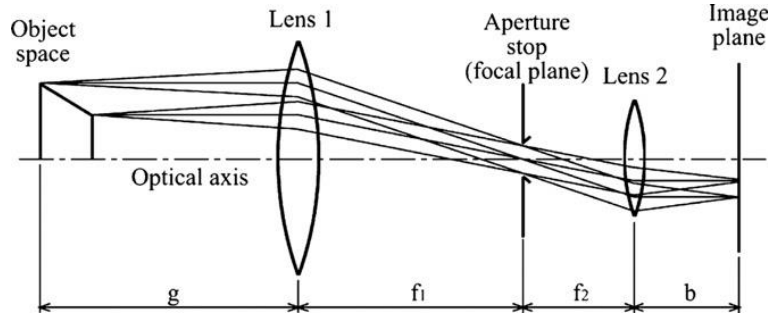


Figure 5.5 Bilateral telecentric lenses model [152].

Image distortions are considered as deviations from the ideal modelled camera due to imperfections in the optical components. Generally they are divided into three additive contributions which can be described as a function of the point position in the image coordinate plane (u, v) [154]:

- Radial distortions

$$\begin{aligned}\delta_{u,r} &= k_1 \cdot u \cdot (u^2 + v^2) + O[(u, v)^5] \\ \delta_{v,r} &= k_1 \cdot v \cdot (u^2 + v^2) + O[(u, v)^5]\end{aligned}\tag{5.1}$$

- Decentering distortions

$$\begin{aligned}\delta_{u,d} &= p_1 \cdot (3u^2 + v^2) + 2p_2 uv + O[(u, v)^4] \\ \delta_{v,d} &= 2p_1 uv + p_2 \cdot (u^2 + 3v^2) + O[(u, v)^4]\end{aligned}\tag{5.2}$$

- Thin prism distortion

$$\begin{aligned}\delta_{u,p} &= s_1 \cdot (u^2 + v^2) + O[(u, v)^4] \\ \delta_{v,p} &= s_2 \cdot (u^2 + v^2) + O[(u, v)^4]\end{aligned}\tag{5.3}$$

Usually the main contribution to image aberration is brought on by radial distortion [155], therefore it can be considered with an higher grade of approximation as[153]:

$$\begin{aligned}\delta_{u,r} &= u \cdot (k_1 \cdot (u^2 + v^2) + k_2 \cdot (u^2 + v^2)^2) + O[(u, v)^7] \\ \delta_{v,r} &= v \cdot (k_1 \cdot (u^2 + v^2) + k_2 \cdot (u^2 + v^2)^2) + O[(u, v)^7]\end{aligned}\tag{5.4}$$

Pixel size estimation

A simple calibration procedure is performed to quickly calculate the average pixel size of pictures. As the lenses introduce a magnification in the image the pixel size does not correspond to the size of the pixels in the CCD chip. It is instead the dimension of the area that occupies one pixel once it is projected into the camera sensor. A glass artefact for calibration of microscopes is used as reference object. It consists of a chessboard pattern with a calibrated value of the pitch (**Figure 5.6**). The vision system is considered ideal without distortion and the grid surface oriented orthogonal to the optical axis. Therefore the calibration can be performed just by counting the number of pixels constituting a pitch and comparing with the reference calibrated length. To enhance the grid edges the picture is processed with a Sobel filter. A subpixel routine is not necessary since the effect of limited resolution can be minimized by considering a multiple pitch length. The uncertainty of the pixel size is assessed considering the artefact calibration uncertainty and the resolution uncertainty on the definition of the edge position as follows:

$$s_{px} = \frac{L_p \cdot n_p}{\Delta p}$$

$$u_{s_{px}} = \sqrt{\left(\frac{n_p}{\Delta p}\right)^2 \cdot u_{l_p}^2 + \left(-\frac{L_p \cdot n_p}{\Delta p^2}\right)^2 \cdot u_{\Delta p}^2} \quad 5.5$$

Where:

- s_{px} is the calculated pixel size;
- L_p is the calibrated pitch length;
- n_p is the number of pitches considered;
- Δp is the pixel count over considered length;
- $u_{s_{px}}$ is the standard uncertainty of the calculated pixel size;
- u_{l_p} is the calibration uncertainty of pitch length;
- $u_{\Delta p}$ is the uncertainty contribution due to the pixel resolution.

The procedure is performed in several locations and orientations on the picture according to **Figure 2.2b** for accounting for non-uniformities and the average values computed. The uncertainty on the average pixel size considers the average uncertainty of the single calculated value $u_{s_{px}}^*$ and the variability over the contribution from the variability due to different locations on the picture u_{std} .

$$U_{s_{px}} = k \cdot \sqrt{u_{s_{px}}^{*2} + u_{std}^2} \quad 5.6$$

Where:

- k = coverage factor
- $u_{s_{px}}^*$ = standard uncertainty of the calculated pixel size
- u_{std} = standard deviation of pixel size over repeated measurements in different picture location

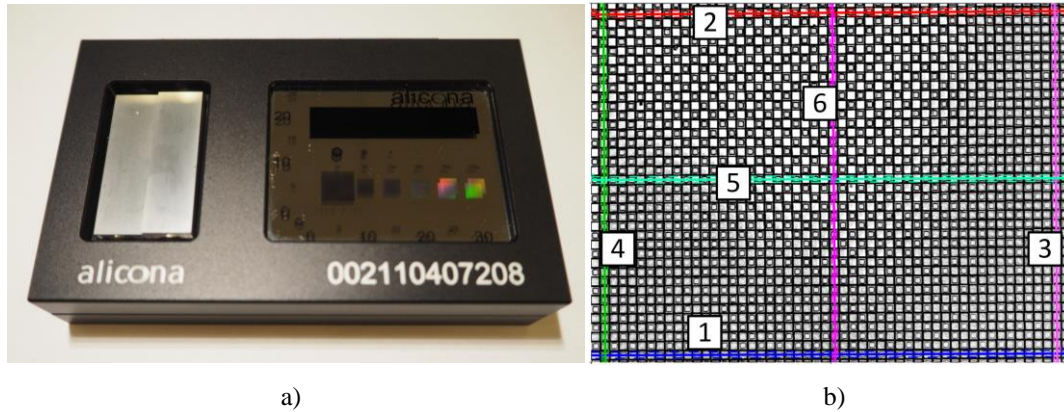


Figure 5.6 Reference chessboard: a) calibration artefact; b) 6 locations used for pixel size estimation, indicated with coloured lines (appearance of the chessboard after Sobel filter application).

Formal calibration

A more refined calibration procedure has been performed following the work of Li [152]. It is necessary to take a picture of the reference object (chessboard) with defined control points and determine the position of these points on the picture. The intersections in the chessboard are therefore determined with the edge detection routine described above. **Figure 5.7** shows the points along the edges determined after the application of Sobel filter and with subpixel resolution, and their regression line representing the edge position. The intersection of horizontal and vertical lines defines the control point.

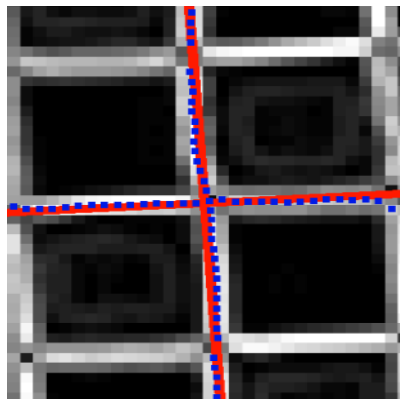


Figure 5.7 Detection of control points on the picture of the chessboard after Sobel filter.

The calibration method consists of a closed-form calculation followed by a non-linear iterative adjustment. Initially lens distortions are neglected allowing the calculation of approximated values of pixel size and external parameters. Since telecentric lenses are unaffected by axial displacements the external parameters consist of two coordinates and

three angles. The model is adjusted to consider only the rotation around the optical axes as the other two rotations are negligible. In the second step distortions are introduced in the model formulation. For the specific case only 5th order radial and decentring distortion are considered.

A single picture of the chessboard is sufficient to perform the calibration procedure. However the routine has been performed for 12 pictures, each with a different rotation of the chessboard, to consider the variability of the calibration method. The outcome values of pixel size and distortions are averaged over the 12 repetitions. The pixel size value appears consistent for all repetitions with narrow variability, as depicted in **Figure 5.8**. The uncertainty relative to the pixel size is estimated considering only the contribution from the uncertainty of the calibrated chessboard since the variability over the repeated runs is negligible. This contribution is computed by considering the uncertainty of the upper and lower limit of l_p in the calibration calculations.

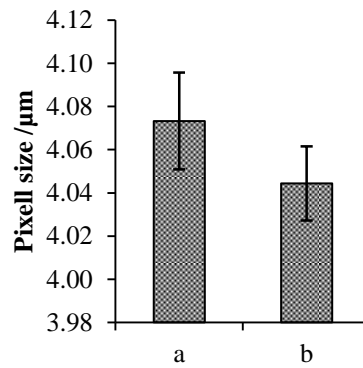


Figure 5.8 Pixel size calculated with pixel size estimation (a) and with the formal calibration (b). The error bars represent the expanded uncertainty.

Average distortion coefficients are implemented in the correction of the distortions of the control points. The amplitude of distortions is then computed as the difference between the projection of the chessboard control points (according to the ideal model) and the position of the control points in the picture before and after the correction. In **Table 5.2** the maximum values and the root mean squares RMS of distortions before and after correction are compared. The imaging equipment produces pictures with minimal distortions that are only partially compensated using the calibration parameters. The slight improvement after the distortion correction uncovers the limitations of the performed calibration in very precise applications. The limited performance of the calibration can be attributed to several aspects, such as the inaccurate detection of the control points or the simplification introduced in the model. Nevertheless the distortions are considered sufficiently limited for the specific application therefore a further compensation routine to be applied to every picture is not developed.

Table 5.2: Maximum value and root mean square value of image distortions calculated during the camera calibration (values in μm).

	<i>Max</i>	<i>RMS</i>
Before correction	0.70	0.29
After correction	0.43	0.20

5.1.5 Measurement strategy

For a two point length measurement a set of two pictures, namely left and right side, is necessary for perform a measurement. A strategy for the extraction of the length from position of edges must be defined. Three sets of coordinate systems are then introduced (**Figure 5.9**). The first one is the image coordinate system already mentioned above. The second one, called relative reference coordinate system has the axis coincident with the edges of the reference grid. These two systems are defined separately for the left and right side edges. The third system, namely absolute reference system is defined only with the position of the grid on the left side picture.

Firstly the edges found must be converted from image coordinate to relative reference coordinates. Thus a translation and a rotation, based on the position and orientation of the grid edges, are applied independently to the left and side pictures. The next step consists in merging the two pictures to a single absolute reference coordinate system. Assuming that the grid marks are straight enough to ensure the same orientation for the two relative reference systems then the remaining operation consists of adding the calibrated reference length to the right picture relative reference system. At this point the two pictures are aligned to the same coordinate system and the dimension extraction requires simple Euclidean geometric calculation. In order to perform the alignment described a grid horizontal and vertical edge must be defined on each picture.

The measurement requires then the definition of the measurand and rules for establishment of the alignment between reference grid and workpiece. **Figure 5.9** refers to the length measurements of a prismatic part (see section 5.1.7) and can be considered as an example. The length to be measured is defined as the distance between two points on the vertical edge at 1 mm from the horizontal edge. Hence vertical and horizontal edges are detected. The horizontal edge is used in the first place to define the rotation of the workpiece compared to the reference system. The measuring point is determined as the intersection of the vertical edge with the parallel line to the horizontal edge at 1 mm distance, see **Figure 5.10**. The definition of the measuring point can vary from case to case. It can be a single point on the object edge at a defined coordinate, as in the example, or the average over a small portion of the edge.

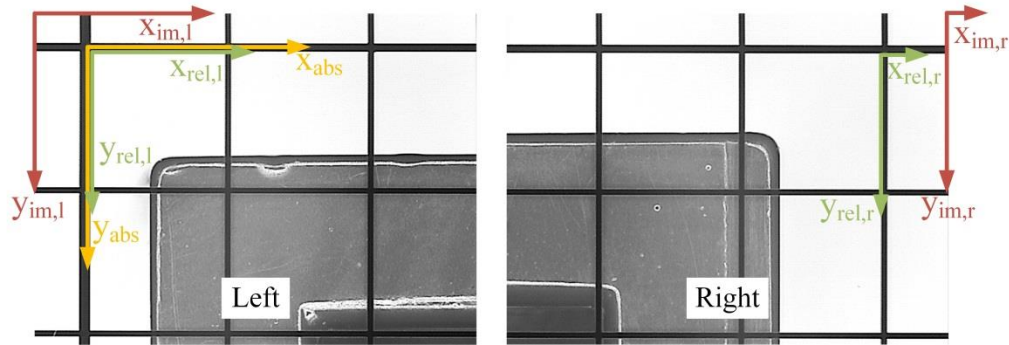


Figure 5.9 Difference coordinate systems defined for a two points length measurement of the optical method under development: (x_{im}, y_{im}) = image coordinate systems, (x_{rel}, y_{rel}) = relative reference systems, (x_{abs}, y_{abs}) = absolute reference system, l, r =left or right picture.

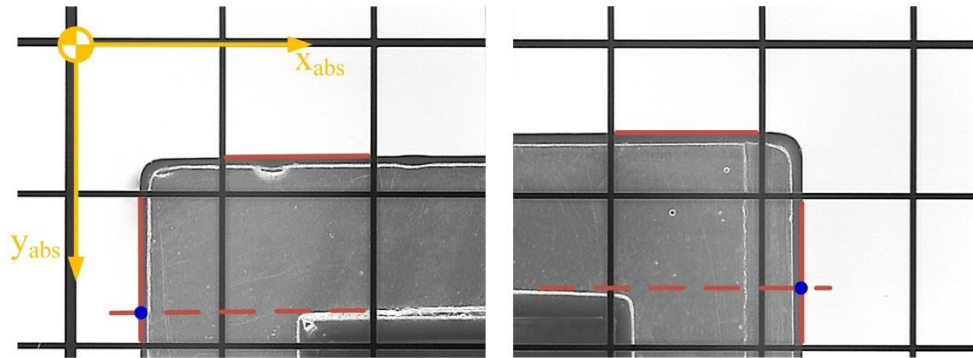


Figure 5.10 Example of measuring strategy of the optical method under development: red continuous line= detected edges, blue dots= measuring points.

5.1.6 A preliminary investigation on a calibrated scale

To verify the performance of the measuring method combined with the conceived edge detection algorithm a series of tests is performed using an optical scale as workpiece with ideal edges. The measuring strategy is similar to the one described above where a horizontal line is defined to identify a single measuring point on the workpiece edge. The interest is focused on estimating the repeatability to assign to the measurement apparatus and assess the sensitivity of the measurement to different algorithm versions. Hence 25 replicated measurements are performed for different versions of the edge detection code, where the variations regard the subpixel analysis along columns (or rows) after the application of the Sobel operator, namely the function and the size of the interval adjacent to the maximum used for the regression and the resolution with which the function maximum is computed. The repeatability of the measurement apparatus is evaluated considering the standard deviation over replicated measurements while the influence of the algo-

rithm is computed calculating the difference between the overall average and each factor combination considered.

At first the influence of the bell shaped function used in the regression is investigated. Three models are considered:

- Gaussian $f_{gauss}(x) = a \cdot e^{-\frac{(x-x_0)^2}{2b^2}}$
- 2nd order polynomial $f_{poly2}(x) = a + b \cdot x + c \cdot x^2$
- 4th order polynomial $f_{poly4}(x) = a + b \cdot x + c \cdot x^2 + d \cdot x^3 + 3 \cdot x^4$

The regression interval size is fixed as 5 data points for the first two models and to 7 data points for the last one to keep the same degree of freedom (DOF) in the regression. The resolution is fixed at 0.2 pixels, equal to 0.8 μm . The repeatability is unaffected from the choice of the regression model while the systematic variation slightly increases in the case of the Gaussian model (**Figure 5.11**). Nevertheless the Gaussian model requires a computational time as high as 4 times the one required for the polynomial ones.

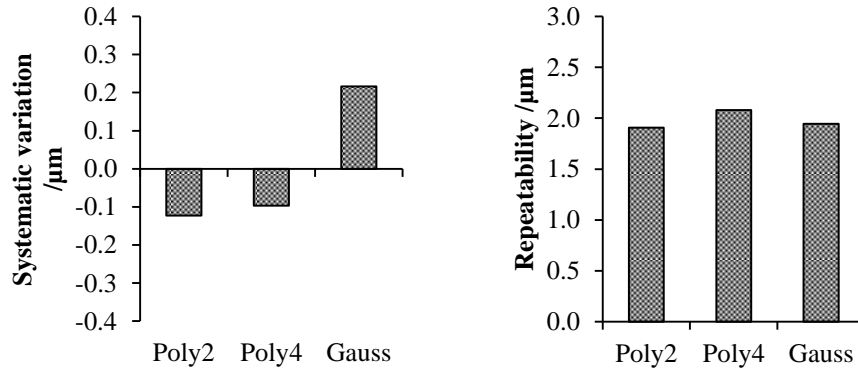


Figure 5.11 Influence of the regression model on performance of the optical method.

The second parameter investigated consists of the amplitude of the interval to be used in the regression. The resolution remains unchanged as before and only the polynomial models are employed in considering the results just achieved. To compare the results from the two models in **Figure 5.12** the regression DOF are considered instead of the interval amplitude. The results in **Figure 5.12** show that the data points fitting (0 DOF regression) leads to inferior results than when considering a proper regression. However an increment of the dataset size causes a reduction of the performances of the method since more less-relevant data points are considered in the regression.

Lastly the influence of the resolution is considered (**Figure 5.13**). Three resolution levels, 0.5, 0.2, 0.05 pixels (equal to 2.0, 0.8, 0.2 μm), are investigated for two levels of DOF and a single regression model (4th order polynomial). The resolution influences

mostly the systematic effect while it does not significantly affect the repeatability of the measurement.

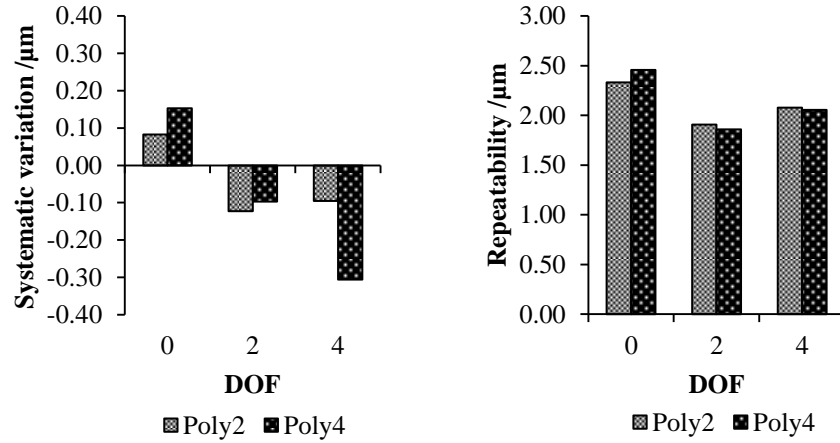


Figure 5.12 Influence of the regression DOF on measurement performance of the optical method.

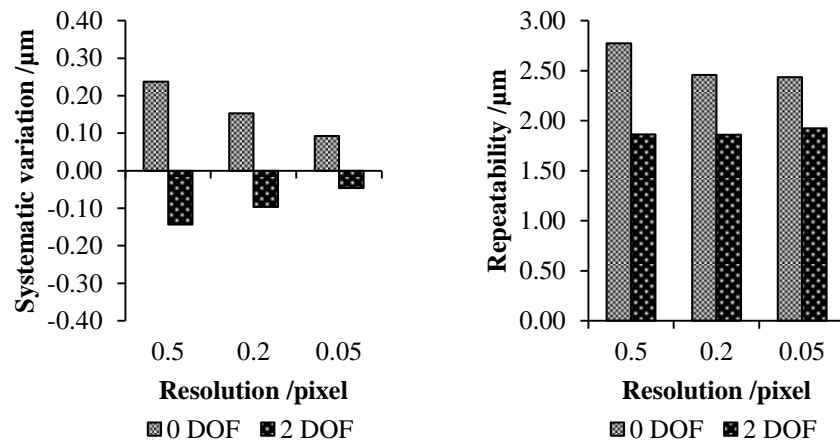


Figure 5.13 Influence of the subpixel resolution on measurement performance of the optical method.

The performance analysis shows an overall systematic variation less than $0.5 \mu\text{m}$ and a repeatability fluctuating around $2 \mu\text{m}$. This confirms the solidity of the algorithm conceived since the measurement results are moderately influenced by changes in the edge computation as well as a limitation in the accuracy achievable. The insensitivity of the repeatability to the image processing, especially to the subpixel resolution adopted, and its large magnitude compared to the resolution suggests that it is influenced by other factors than the edge detection algorithm.

5.1.7 Measurements of polymer parts

The case has already been introduced as an example in section 5.1.5. Measurements of polymeric prismatic parts are performed with the optical solution developed to assess the performance on non-ideal geometries typical of injection moulded components. The edge detection algorithm is defined with a subpixel routine using a regression with a 2nd order polynomial model over 7 data points and with a resolution of 0.2 pixel. The accuracy assigned to the measurement device is potentially independent from the dimension due to the direct comparison with the dimensions of the reference grid. In order to validate it two workpieces with different nominal lengths of 32 and 64 mm are selected for the test. The standard deviation of 25 replicated measurements is listed in **Table 5.3** showing the independence of the measurement uncertainty from the nominal length considered. Moreover measurements on industrial workpieces with non-ideal edges cause an increment of the variability of the results.

Table 5.3: Standard deviation of optical measurements on two polymeric components.

<i>Nominal length /mm</i>	<i>Standard deviation /μm</i>
32	3.0
64	2.5

5.2 Optical solution for displacement measurements

5.2.1 Motivation

In a Dynamic Length Metrology application the measurement of displacement as relative length variation of a workpiece is important as much as the measurement of absolute length since it is necessary to achieve a reliable estimation of the dimensions at reference conditions. Moreover the knowledge of dimension evolution in many positions on the part is useful in the case of complex estimation algorithms supported by simulations. A solution for having more information about dimension changes is represented by the use of several contact probes. Nevertheless this alternative can be limited by size problems when measuring small parts and creates an overconstrained condition on the measuring part that can cause unexpected behaviour. A remote optical solution is therefore advisable if displacements of several points are required. Among all optical solutions a vision system represents a cheap alternative, easy to combine with other devices.

Many applications of vision systems in dimensional metrology consist of the measurements of edge absolute position using edge detection algorithms. In the particular case absolute measurements are not required nevertheless the edge detection can be applied to recognize a feature and follow its development through time. The recognition of an edge is anyhow bonded to the quality of the image, i.e. there must be a sharp transition between a dark and white area, and provide information only of a local surface feature. Digital Image Correlation is not widely used in dimensional metrology as edge detection. However it does not require the presence of a well-defined edge but only a rough surface allowing more freedom in the choice of the measuring spot. The independence from surface details permits measurement of displacements in several position in the field of view of the camera and the definition of a local field of displacements.

5.2.2 Digital Image Correlation

Digital Image Correlation has been already introduced in Chapter 2. It is a measuring method used especially in experimental mechanics to measure surface displacement and strain field of a loaded specimen.

The mathematical tool of cross-correlation is used in signal processing to compare two sets of signals and estimate similarities. Cross-correlation is used in many application of image processing. The most relevant consist of the measurement of the translation of a subject depicted before and after the transformation. If image processing images are considered as two-dimensional discrete signals then a 2D cross-correlation operation can be applied to a set of two images $x(m,n)$ and $y(m,n)$ as:

$$r_{xy}(k,l) = \sum_{k=-\infty}^{+\infty} \sum_{l=-\infty}^{+\infty} x(m,n) \cdot y(m+k,n+l) \quad 5.7$$

Cross-correlation gives as output a third function $r_{xy}(k,l)$ consisting of the sum of the punctual product between the input functions while one is being translated by an amount equal to (k,l) . It can be easily visualized considering a fixed image and another floating image that slides over the first one. The correlation function is the sum of the punctual product of the overlapped area. The correlation function reflects similarities of the two input signals and its maximum is located in the coordinate corresponding to the translation that maximises the likeness of the signals. In the case of equal input signals, i.e. $x(m,n)$, the operation is called auto-correlation; the maximum of $r_{xx}(k,l)$ is located in correspondence to the origin.

In practical applications the two pictures are divided into smaller subsets (regions of interests) usually following a grid pattern. The correlation algorithm tracks similar features in the reference and deformed images and returns a correlation coefficient as a function of the shift between two related subsets. The position of the maximum of the correlation coefficient function corresponds to the displacement occurring during the test and necessary to create the maximum overlap of the two subsets. For small deformations and small subset size a rigid translation of the subsets can be assumed. Otherwise higher-order shape functions have to be introduced in the correlation calculation to cope with the

deformation of the subsets. Two analytical tools can be used to in the correlation method: the cross-correlation and the sum-squared difference criterion [67]. Both criteria can be normalized by the amplitude and the mean to get results insensitive to the light exposure and lighting variations.

The correlation tool mentioned above returns the displacement value with pixel resolution. To better improve the result a subpixel registration tool has to be introduced in the image processing. Resolutions of 0.01 pixel can be achieved [94]. Some of the most used subpixel registration methods are the interpolation of the correlation coefficient function, the Newton-Rapson iteration method and the gradient-based method. The Newton-Rapson method gives better results than the others; however it requires much more computational time and it may not be suitable for real time application [94].

The image processing influence the accuracy of the calculated displacement, First of all the subset size must be chosen adequately and mostly based on the dimension of the speckle pattern. Bigger subsets contain more features therefore are less sensitive to noise and lead to more accurate results. On the other hand adopting a small subset increases the spatial resolution of the resulting displacement field [96]. Moreover the accuracy of DIC can be increased by choosing normalized correlation criteria and more precise subpixel registration methods.

5.2.3 Algorithm development

The image processing is performed using the commercial software MATLAB. The code performs DIC between two images, a reference image related to the reference state and an inspection image related to the final state. The calculation can be divided into two steps:

- Image cross-correlation (normalized);
- Displacement definition with subpixel resolution.

The first step involves calculations based on formula 5.7. Cross-correlation can be applied directly to the whole images to get a single displacement value. However dividing the inspection image in subsets and the reference image in searching windows is more efficient. The analysis is performed on homologues subsets and searching windows independently. The image subdivision yields an output value for each subset that is then assigned to the position of the centre of the subset in the inspection image. With this further image subdivision a displacement field can be defined instead of a single displacement value. The output of the cross-correlation calculation is the discrete normalized correlation function of each subset.

A displacement value is already available as the position of the maximum of the correlation function. However it is defined only with a pixel resolution that can be reduced with a further analysis. A neighbourhood of the maximum with dimensions 5×5 is selected from the correlation function. A regression with a continuous two dimensional function, such as a polynomial function, is then performed using the least square method. The position of the maximum of the fitted function is detected with a higher resolution, fixed equal to $0.05 \mu\text{m}$. The output of this step represents the displacement assigned to the considered subset with subpixel resolution.

The inspection subset must be completely engaged in the correlation (i.e. it completely overlaps the searching windows) to obtaining a correct cross-correlation function otherwise the output function will suffer from the degree of engagement. Therefore the searching window must be oversized to a degree greater than the displacement value to ensure the reliability of the cross-correlation function, at least in the proximity of its maximum. If a previous knowledge of the expected displacement is available it is possible to tune the searching window dimensions and limit the calculation time.

5.2.4 Experimental setup

To investigate DIC as a tool for Dynamic Length Metrology an experimental campaign has been performed. The equipment used to take pictures is composed by a camera equipped with telecentric lenses (see section 5.1). The camera allows photographing details as big as 3×2 mm with a resolution of $4.04 \mu\text{m}$ according to the calibration. An axial illumination is used to enhance the contrast of the surface texture. As workpiece a commercial polymer part made of ABS with a prismatic hollow shape has been selected. It presents a visible surface texture, from the machining process of the mould production, and some high relief characters, such as the company logo, that creates a differentiated surface appearance. Such a surface does not completely fulfil the requirement of DIC for an optimal displacement and strain measurement, i.e. randomness and isotropy. However it is not feasible to create an artificial speckle pattern in the surface with a process like painting considering the application in in-process dimensional control. A loss in the DIC performance is then expected and accepted since the thermal strain is predicted to be limited and with limited gradients.

To create a displacement as a simulation of the change in dimensions after the production process the part is heated up on a heating device and subsequently placed on a positioning fixture under the camera during the cooling period (see **Figure 5.14**). The fixture, realized in Invar, is composed by a support plane and three other fixed pins for the univocal definition of the position. In the direction of the bigger dimension of the workpiece and opposite to the fixed point a floating point applying a spring force is added to the fixture. The camera is then focused in a region close to the floating point. The supplementary floating element enables the part to shrink freely, but forces the deformations along the direction of the force to be always directed towards the fixed point. Consequently the area detected by the camera undergoes local deformations together with a displacement equal to the integral of all the local strain along the direction of the force. The displacements measured are related to the change in size along the main dimension of the workpiece. Since only displacements in one direction are guided, displacements in the other direction are neglected. The analysis involves therefore only one-dimensional measurements. Nevertheless the investigation is valid also for 2D applications.

Several pictures are taken during the cooling phase. The algorithm is then applied to each picture considering the first one of the series as the reference one.

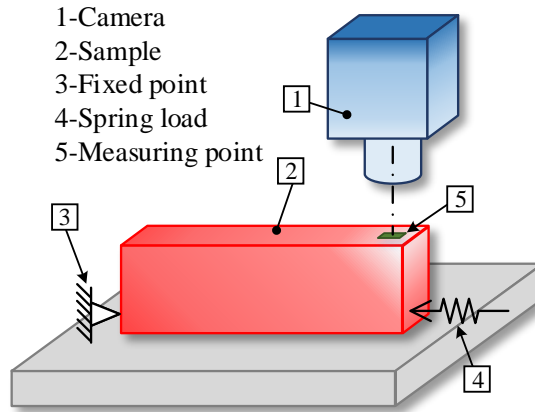


Figure 5.14 Experimental set-up for DIC experimental test campaign.

5.2.5 Performance assessment

A series of tests are carried out to evaluate the variability of the algorithm developed and the applicability of DIC to the specific case, principally considering the non-ideal workpiece regarding geometry and surface appearance. They concern mainly calculation time and estimation of the reliability of the calculated displacements.

The DIC algorithm has been modified to assess the influence of the subset size and the type of regression model used during the subpixel calculation. Subsets are placed following a matrix $n \times m$ to cover the entire surface caught in the pictures. To avoid overlapping of the subset area that will cause redundancy of the results, the number of subsets $n \times m$ is reduced as the subset size increases.

In the second step of the algorithm a Gaussian (5.8) and a polynomial (5.9) regression model are selected to obtain a subpixel resolution. In 5.8 and 5.9 x, y represent the coordinate axis of the functions and a, b, c, d, x_0, y_0 the regression parameters. The orientation of the axis x, y does not correspond to the image axes orientation but is defined case by case to maximize the fitting.

$$f_{gauss}(x, y) = a \cdot e^{-\left(\frac{(x-x_0)^2}{2 \cdot b^2} + \frac{(y-y_0)^2}{2 \cdot c^2}\right)} \quad 5.8$$

$$f_{poly}(x, y) = a + b \cdot x + c \cdot y + d \cdot x^2 + e \cdot y^2 \quad 5.9$$

A first analysis is performed to evaluate the calculation time of the different version of the correlation algorithm. The interest can be focused separately on the pure cross-correlation calculation time and in the following subpixel extraction time. The analysis is performed considering subset sizes from 30 up to 440 pixels. **Figure 5.15** depicts the time necessary to perform the calculations described above for a single subset. Results are

averaged over several repetitions to reduce the variability. The cross-correlation time increases non-linearly with the subset dimension as expected considering the increasing of the number of simple calculations (sums and products). On the other hand the fitting for the subpixel analysis is always performed from a set of data with a defined size (5×5) leading to a computational time independent from the subset size. Moreover the polynomial fitting requires approximately half the computational time than the Gaussian fitting.

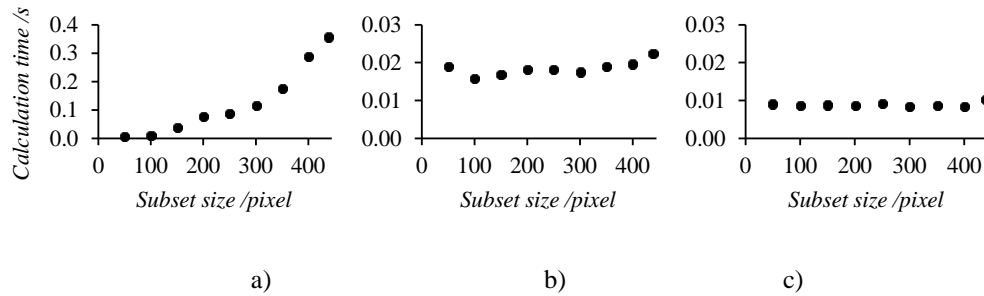


Figure 5.15 Average calculation times for a DIC algorithm: a) pure cross-correlation; b) regression of correlation function with Gaussian model; c) regression of correlation function with polynomial model.

A second analysis is performed to evaluate and compare the results from cases with different algorithm and surface appearance. Analysing results from different surface types provides an assessment of the influence of non-ideal surfaces in a DIC application. From the same workpiece two areas, marked with A and B in **Figure 5.16**, have been selected.

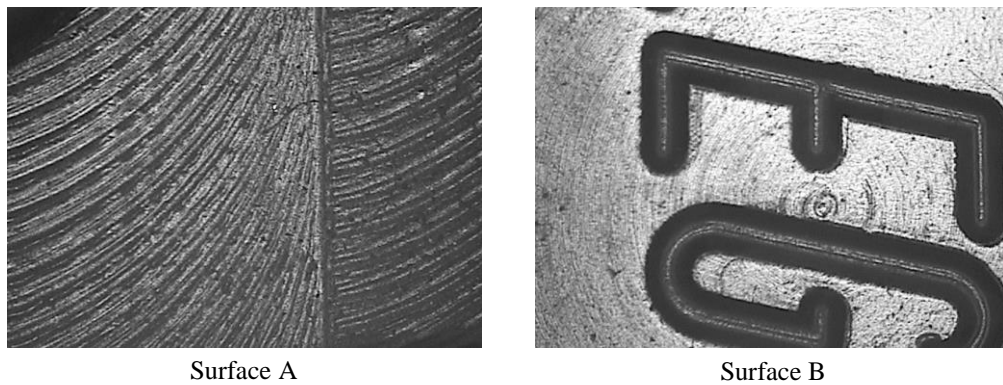


Figure 5.16 Surfaces used during DIC performance assessment of a DIC algorithm.

Both surfaces present machining marks characterized by high directionality and periodicity. Moreover area B contains an alphanumeric logo that interrupts the periodicity. On an overall scale both surfaces are considered sufficiently random and isotropic, how-

ever a subset subdivision amplifies the non-ideality due to a more local analysis. Four values of subset size are considered in this second study (see **Table 5.4**). As mentioned in the previous section the number of subsets is reduced with the increase in the subset size to avoid redundant results. A set of pictures relative to each of the two selected areas is obtained according to the procedure described above. Each set is analysed with a different subset size and subpixel algorithm for a total of 8 cases. The output of the application of DIC is the time-variant thermal displacement field. A reference displacement value is determined performing the DIC without subset subdivision.

Table 5.4: Subset sizes (in pixels) considered in the performance assessment of DIC algorithm.

<i>Subset size</i>	<i>matrix of subset $n \times m$</i>
31×31	12×10
61×61	7×9
91×91	5×7
121×121	4×5

Accounting for the condition of natural cooling together with the low heat conduction of ABS and the narrow area analysed, the temperature of the considered portion is assumed uniformly decreasing during time. This hypothesis implies that the displacements vary in space and time always maintaining a linear spatial pattern. Consequently the displacement field can be described using only the average displacement value and the spatial gradient.

A comparison of the average and reference displacements is obtained analysing their difference averaged over time (see **Figure 5.17**). The subset size slightly influences the average displacement value however the subpixel calculation affects the DIC outputs especially for the case of surface A.

Further investigations can be realized analysing the distribution of the displacements. A linear regression is performed between the displacements values and their location to comply with the hypothesis of homogenous cooling. The residuals of the regressions are analysed considering their standard deviation averaged over time. A comparison of the linearity of the displacement field between surface A and B is meaningless since the relative displacement fields can be more or less linear due to the different location on the workpiece or simply due to experimental variability (measurements of the two surfaces performed in two different runs). **Figure 5.18** depicts the residuals' standard deviations. Small subset sizes lead to more noisy results with higher variability. Nevertheless the performance of DIC appears independent from the subset size for larger subsets. The subpixel calculation appears to influence the quality of the results. Once more the Gaussian models works better than the polynomial one.

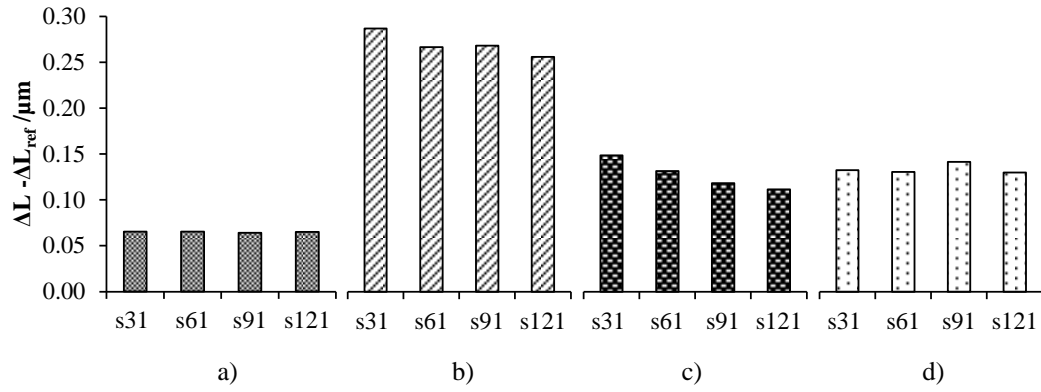


Figure 5.17 Comparison between average displacement ΔL and reference displacement ΔL_{ref} as function of subset size (s31÷s121): a) surface A Gaussian regression; b) surface A polynomial regression; a) surface B Gaussian regression; d) surface B polynomial regression.

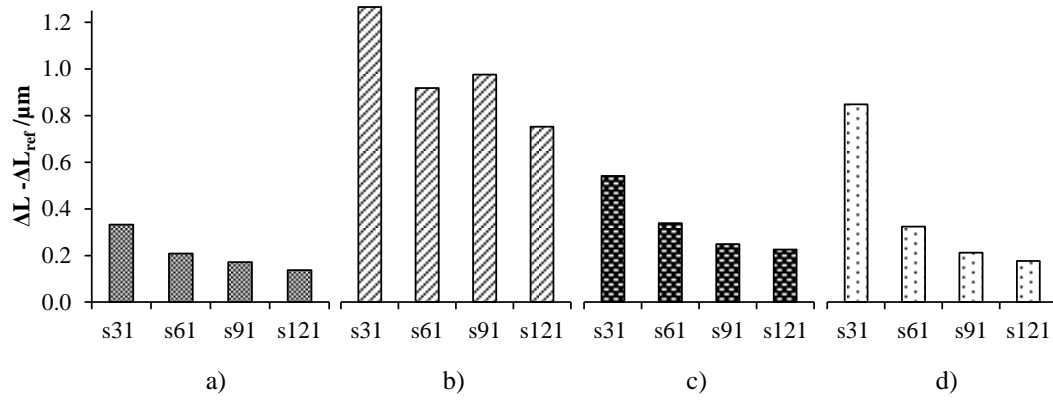


Figure 5.18 Residuals of the spatial linear regression of the displacements as function of subset size (s31÷s121): a) surface A Gaussian regression; b) surface A polynomial regression; a) surface B Gaussian regression; d) surface B polynomial regression.

A quantitative output of the performance verification is the determination of a measurement uncertainty relative to the DIC method developed. The variability of the results and the deviation from the reference displacement value are considered two main contributors to the measuring uncertainty. As outcome from the camera calibration also the uncertainty on the pixel size is considered in the final measurement uncertainty. An uncertainty model is defined just considering the conversion of the calculated displacement from pixels to length unit.

$$\delta_{\mu m} = s_{px} \times \delta_{px} \quad 5.10$$

Where:

$\delta_{\mu m}$ is the displacement in micrometres;

s_{px} represents calibrated value of the pixel size in micrometres;

δ_{px} is the displacement expressed in pixels.

Consequently the standard uncertainty $u_{d\mu m}$ of the measured displacement as defined above is:

$$u_{\delta_{\mu m}} = \sqrt{s_{px}^2 \times (u_{rep}^2 + u_{sist}^2) + \delta_{px}^2 \times u_{spx}^2} \quad 5.11$$

Where:

u_{spx} is the standard uncertainty of the calibrated pixel size;

u_{rep} is the contributor due to the variability of the DIC output;

u_{sist} is the systematic effect of the calculation, i.e. the difference from the reference displacement.

The expanded uncertainties for an average displacement of 30 μm are shown in **Figure 5.19**. Measurement uncertainties lower than 0.6 μm can be achieved for subset sizes bigger than 90 \times 90 pixels with a Gaussian regression model.

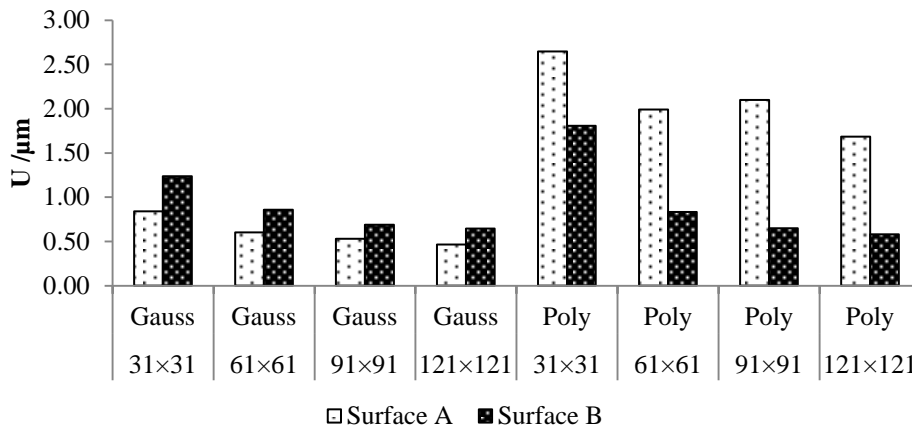


Figure 5.19 Expanded uncertainty of displacement measurement with the developed DIC method.

The outcome of this section can be summarized as:

- Small subsets require less calculation time. However they produce less accurate results. On the other hand it is not advisable to oversize the subset as the variability reaches a stable result and does not improve further, while time of calculation increases and the spatial resolution of the displacement field decreases.
- The polynomial regression model reduces the computational time of the sub-pixel analysis and leads to less accurate results than the Gaussian model.
- Surface B appears more reliable than surface A since it produces results less dependent on the type of calculation.

5.2.6 Applicability to DLM

A further series of tests is carried out similar to the performance assessment to evaluate the applicability of the DIC method in Dynamic Length Metrology. The purpose of this study is to compare and merge outputs from displacement measurement with the newly developed DIC method and measurement performed with a traditional contact method. According to the DLM concept temperatures are also measured to produce a concurrent material characterization useful for the prediction of the length at reference conditions.

Considering the outcome from the previous analysis the investigations concern thermal displacements of the surface B analysed with a 90×90 subset division cross-correlation and subpixel resolution analysis with Gaussian model.

The equipment and the experimental procedure remain the same with the addition of temperature sensors on the workpiece (**Figure 5.20**) and the implementation of an inductive probe as floating point. The inductive probe applies a pushing force to the workpiece and at the same time performs a displacement measurement. Considering the thermal boundary conditions the heat flux is considered primarily directed towards the bottom of the part since the coupling with the metallic surface is characterized with a high heat conduction coefficient compared to the natural convection present in the rest of the workpiece boundaries. Consequently the temperature gradient in the part can be approximated to a vertical gradient and position, at the same height and similar temperature. This allows placing the temperature sensors in any location at a defined height to measure a relevant temperature for that height. The first temperature sensor T_1 is placed close to the measuring area while T_2 is intended to measure a temperature relevant for the contact sensor displacement measurements and it is placed in a location approximately at the same height as the probe. The outcome of the experimental work is two series of data regarding length and temperature during cooling phase in two distinct locations on the workpiece.

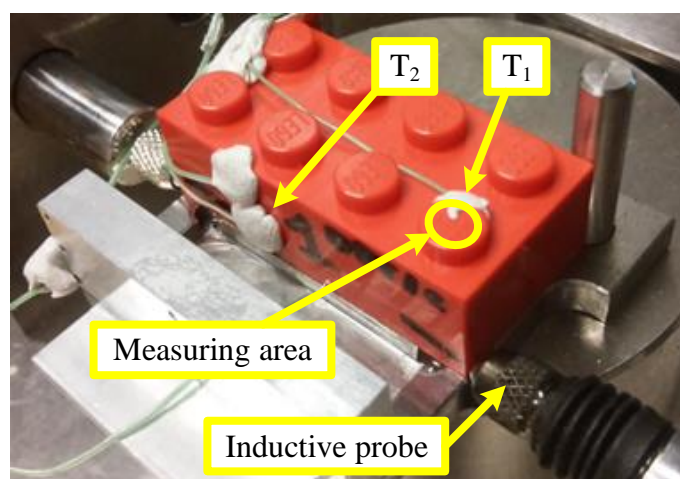


Figure 5.20 Experimental layout for a DLM application of the DIC method.

CTE estimation

The apparent coefficient of thermal expansion can be calculated from a regression of the displacement value against temperatures for both series of data. It can be considered as a global analysis and the CTE value being influenced by the temperature distribution along the workpiece. Nevertheless for the DIC measurement a further apparent CTE can be computed considering surface differential displacements, in particular exploiting the evolution of the spatial gradient during the cooling phase according to the linear expansion model depicted in **Figure 5.21** and described by formula 5.12.

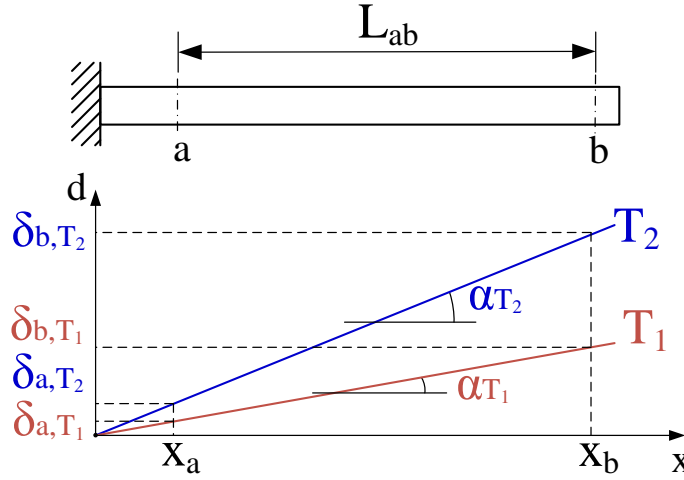


Figure 5.21 Displacement distribution of a linear thermal expansion model.

These calculations involve local quantities, therefore the outcome apparent CTE value can be considered closer to the traditional concept of material property. The value of the three CTE calculated are listed in **Table 5.5**: CTE_1 refers to the contact displacement measurement, CTE_2 to the DIC measurement using the global approach and CTE_3 using the local approach. The values are consistently different however a marked difference is expected as they refer to different measurement procedures and different data analyses.

$$CTE = \frac{1}{L_{ab}} \cdot \frac{L_{ab,T_2} - L_{ab,T_1}}{T_2 - T_1} = \frac{1}{L_{ab}} \cdot \frac{(\delta_{b,T_2} - \delta_{a,T_2}) - (\delta_{b,T_1} - \delta_{a,T_1})}{T_2 - T_1} = \frac{\alpha_{T_2} - \alpha_{T_1}}{T_2 - T_1} \quad 5.12$$

Where:

L_{ab,T_i} is the distance between the points a and b at the temperature T_i ;

δ_{k,T_i} is the displacement (from a generic reference state) of the points k at the temperature T_i ;

α_{T_i} is the spatial gradient of displacements at the temperature T_i .

Table 5.5: Apparent CTE calculated from contact displacement measurement (CTE_1) and DIC optical measurements using a global approach (CTE_2) and a local approach (CTE_3).

	$CTE / ppm/^{\circ}C$
CTE_1	65.5
CTE_2	43.2
CTE_3	83.1

Displacement distribution

Measurements performed using DIC are not sufficient for an independent measuring station since they do not provide information about absolute length value. However DIC is a useful tool to generate additional information about the three-dimensional behaviour of the measuring part. In the experimental case for example the inductive contact probe leads to the determination of a stand-alone absolute length measurement. In a DLM application however it must be supported by other source of information to account for the 3D time-variant state, for instance with the addition of temperature or displacement sensor. The combination of contact sensor and DIC provides sufficient information to describe the distortions occurring during the cooling phase due to non-uniform temperature variations. Differential deformations are detected in the experimental investigation, proving that the workpiece cools down and shrinks faster in the area in contact with the support plane see **Figure 5.22**.

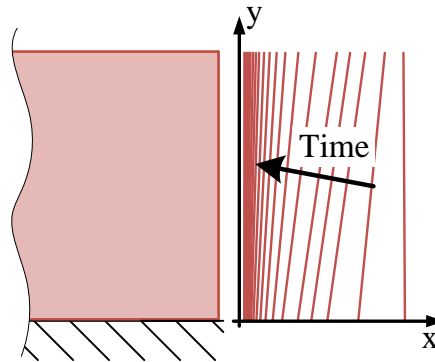


Figure 5.22 Differential thermal expansions: the vertical red lines represent the workpiece edge progression during cooling.

The DIC measuring method proves to be a valid alternative to implement in a DLM applications for measurements of relative surface displacements. They can be implement-

ed in a unit for measurements of small parts to solve the issue of limited space. At the same time DIC is relevant also for measurements of bigger parts since they provide information from local measurements that are less influenced by geometry and thermal state and therefore closer to the definition of material properties, like in the case of the CTE.

5.3 Conclusion

Two optical methodologies have been developed to obtain absolute traceable dimensional measurements and relative displacement measurements. Both are based on vision systems with similar requirements hence they can be implemented independently or together in a combined solution.

The absolute length measurement method is based on edge detection. The measurement is performed on objects with flat surfaces where the positions of the edges of the surface are identified. The workpiece and a reference artefact with calibrated marks, such as a grid or a scale, are placed in the measuring work plane. The measurement consists of the comparison of the position of the workpiece edges with the one of the reference marks. The method can be applied on a newly designed system as well as a generic vision device, such as optical CMMs. The concept developed makes use of a split field of view of the imaging device through a series of mirrors to obtain images only of the desired details, i.e. the edge of the workpiece in two particular locations, enabling increasing the measured part dimension without worsening the resolution.

An edge detection algorithm is newly defined to obtain subpixel resolution results. After the identification of the area of interest a Sobel filter is applied to the image to enhance the borders. The edge position, along columns for horizontal edges and along rows for vertical edges, is located as the position of the pixel with maximum intensity. A subpixel routine is then performed to locate the maximum with an improved resolution by fitting the neighbouring pixels with a bell shaped curve. The final straight edge is defined with a linear regression of the found points.

The experimental work is performed on an optical CMM with a videoprobe with 2x magnification used as an imaging device. Initially the imaging system is calibrated using a microscope calibration artefact. Two calibration methodologies are applied. A simple one consists of counting the pixels occupied by a known calibrated length. A more complex one considers lens distortion. The estimations of the average pixel dimension in the two cases are in agreement. Lens distortions appear limited so they are not considered further.

A methodology is developed to obtain two point length measurements from the information of the positions of two opposite edges of an object. Two pictures, each one containing one edge of the measuring object and the reference grid, are considered. The methodology consists to an initial alignment of the coordinate system to the grid directions and a further comparison of the position of the object edges with the grid edges. In

the case presented the workpiece does not have to be aligned to the grid as the relative orientation can be determined and considered in the length calculation.

Prior to investigations on industrial parts, some tests are performed to validate the edge detection algorithm and the measuring strategy. An optical calibrated scale with ideal sharp edges is used as measuring object. Several trials are performed by changing the setting in the algorithm mainly regarding the routine for subpixel edge definition. Results, considering 25 replicated acquisitions, show a limited influence on the different algorithm versions studied. A standard deviation of about 2 μm is obtained among the replications.

Investigations on industrial polymer parts are performed exploiting the results from the preliminary tests. Two workpieces with different lengths are measured according to the procedure previously defined. The comparison is performed on the standard deviation over 25 replicated acquisitions. The performances of the method are reduced by the lower quality of the edges of industrial objects and are not influenced by the dimensions of the parts.

The second optical solution studied allows the measurements of surface displacement field. In a DLM implementation surface displacements are useful information for the calculation of the length in reference condition. It is however necessary to couple displacements results with an absolute dimensional measurement. The method is based on the technique of digital image correlation. It consists of comparing a picture of a deformed state with the picture of the original state. A correlation tool provides a function in which amplitude is proportional to the degree of matching of the two pictures. The displacement of the subject in the pictures corresponds to the position of the maximum of the correlation function, which can be defined with a subpixel resolution with a regression of the maximum region. A requirement for the success of the method is the presence of surface features, which ideally should be random and equally distributed without periodicity.

Once again an optical CMM is used as imaging device. To perform the experiments commercial polymer parts are initially warmed up and then placed under the camera. Several pictures are acquired during the cooling phase. The first picture is considered as the reference one. The developed algorithm considers a subdivision of the field of view of the camera in several subsets in order to obtain a displacement field composed by several displacements value.

A performance assessment investigation is carried out to identify the influence of different algorithm versions on the correlation results. The parameters investigated are the size and number of the subsets, the regression model used in the subpixel resolution routine and the type of surface appearance. Four subset sizes are considered while the number of subsets is decreases with the subset dimensions to cover the entire pictures without useless overlapping. The regression models consist of a Gaussian and a 2nd order polynomial model. The imaging is performed on two locations of the workpiece to consider two different surface appearances. An uncertainty budget is formulated considering the contribution from the uncertainty of the pixel size, the contribution from the repeatability of the measurement and the systematic difference from a reference measurement. The reference value is estimated with the DIC procedure considering the whole picture (without

the subset division). Gaussian model is considered better than the polynomial since it produces results independent from the surface appearance. Bigger subset size leads to lower uncertainties, yet the displacement field produced has a lower spatial resolution.

To evaluate the applicability in DLM a series of tests is performed adding temperature and displacement sensors in the measuring set up. The concurrent measurement of length and temperature in different locations on the part allows the definition of several apparent coefficients of thermal expansion. A differential displacement field is defined using the information from the measurements of thermal displacement performed in two locations with contact and optical methods.

6

Industrial case

6.1 Introduction

This chapter involves dimensional measurements of polymer parts with the DLM approach in industrial environment exploiting the experience gained from the experimental work described in the previous chapters. The item selected for the investigation is a component for a medical device (**Figure 6.1**).



Figure 6.1 The POM component selected as industrial case.

It consists of a polymer part made of POM (polyoxymethylene) and produced by injection moulding. The component has a complex shape geometry that can be roughly described as a thin wall tube with constant diameter. It is therefore defined as a tube. **Table 6.1** lists the approximated object properties while in **Table 6.2** the generic properties of POM are listed. The measurand is length of the tube, defined as the plane to plane distance between the end faces. The experiments are designed to be performed at the production site in a non-controlled environment (next to the moulding machine) however for practical reasons they are mainly performed in a temperature controlled environment, with ambient temperature of 20 ± 1 °C. The last measurement points are performed in different ambient temperature and humidity condition. The controlled ambient conditions do

not comply with the description (and the potentiality) of DLM yet the results of the investigation are still of interest as an attempt to combine all the aspects addressed separately in the previous work. The investigation is performed during one full week (7 days) in which several parts are collected from production on different days and measured over time. The measurements are always referred to the production day and hour hence the length of the data vector acquired differs from batch to batch depending on the day in which the part is produced.

Table 6.1: Characteristics of the selected POM workpiece.

Length	59 mm
Diameter	8.0 mm
Thickness	1.0 mm
Weight	1.5 g

Table 6.2: Generic properties of POM [17].

Elastic modulus	2.7 GPa
CTE	110 ppm/°C
Density	1.4 g/cm ³
Moisture absorption (ISO 62)	0.2 %

6.2 Experimental work

The measuring equipment is depicted in **Figure 6.2**. It consists mainly of two stations for measuring length and weight respectively. The weight measurement is performed using an electronic scale with a resolution of 0.1 mg. The station for length measurements is composed of a thermally stable frame made from Invar and steel components. An Invar column holds a displacement inductive probe orthogonally to the base surface. On top of the base plate a further flat plate is added to ensure a smooth support surface. The probe, model TESA GT 21 HP, has a digital resolution of 0.2 μm and a MPE of $(0.07+0.4 L) \mu\text{m}$ (L in mm) and is equipped with a flat disc tip. The measuring force is 0.6 ± 0.2 N. Three thermocouples type K (MPE of 0.2 °C) are used to measure the temper-

ature in two positions on the workpiece and on the base plate. Temperature and displacement signals are acquired simultaneously using Marposs Easybox acquisition devices. The system is zeroed using a 70 mm long grade 1 gauge block.

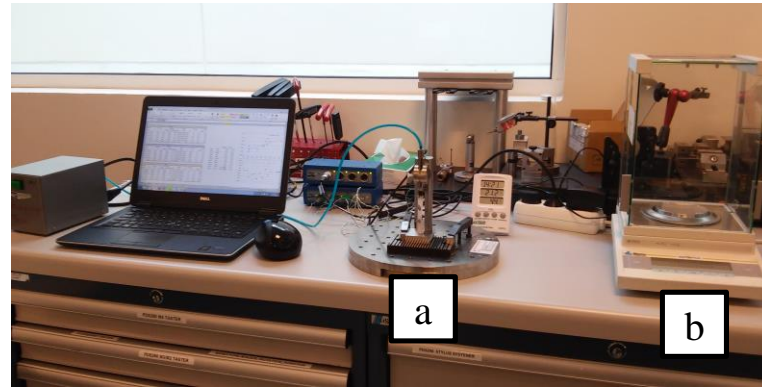


Figure 6.2 Measuring setup of the industrial case: a) station for length (and temperature) measurements; b) scale for weight measurements.

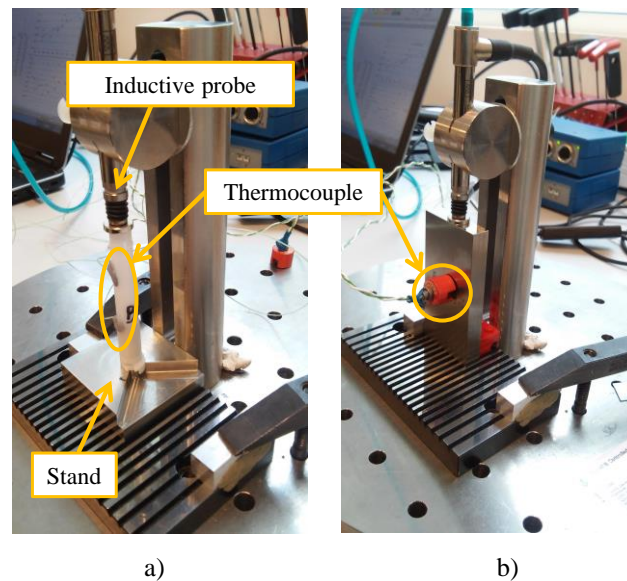


Figure 6.3 Station for length measurement: a) measurement on polymer tube; b) zeroing using reference gauge block.

The positioning of the workpiece is performed using a stand composed of a square base and a vertical pin. Under the effect of the probing force the measured component adjusts the vertical position to align its top and bottom surfaces parallel to the stand and probe end surfaces. The vertical pin has the task of ensuring the alignment without introducing any constraint. The horizontal alignment is ensured by a repeatable position of the

stand against fixed components of the main frame (**Figure 6.3 a**). The rotation of the workpiece around the vertical axis is fixed as well. Hence the positioning and the alignment of the measuring object are considered well defined and repeatable. Ambient relative humidity and temperature are monitored using a dedicated hygro-thermometer clock, with accuracy of 1 °C on temperature measurements and 6 % on relative humidity accuracy. A calibration consisting in a comparison with a more accurate instrument allows the improvement of the accuracy of the relative humidity measurements; a systematic deviation of 5 % is identified and removed from the instrument reading.

Two types of test are performed. A first one consists of an extensive measurement of length and other quantities (temperature, ambient humidity, weight) lasting for several days to obtain and collect information on the dimensional behaviour of the component. The in-depth knowledge acquired provides the definition of a measuring procedure and data analysis to be used in a second set of tests where the length in stabilized condition is extrapolated from measurements performed in a limited time.

The polymer part is considered subjected to four main dimensional instabilities due to temperature, moisture absorption, relaxation of residual stresses and probing force. The measuring procedure aims to assess the first three causes of length variation. The effect of the probing force is considered as a systematic effect to be statically compensated. The influence of temperature occurs in the first minutes after moulding during the fast cooling of the part. It is therefore of primary importance to measure length and temperature at an early stage for assessing the temperature influence on dimensions. The influence of moisture uptake is considered slower compared to the effect of temperature. Finally the residual stress relaxation usually happens in the following days after production.

The length of the polymer parts is calculated as a comparison between the output of the inductive probe measuring the part and the reference gauge block (**Figure 6.4**). Hence the length value is the result of an algebraic sum of the dimensions of the component involved in the measurements. The estimated length at reference condition is then calculated adding the contributions due to the influence factors to the formulation of length as described in equation 6.1.

$$\begin{aligned} L_{tube}(T, W, t) &= L_{gb} - L_{stand} - \Delta x_{probe} \\ L_{tube, 20, W_{ref}, t_{ref}} &= L_{tube}(T, W, t) + \Delta L_p \end{aligned} \quad 6.1$$

Where

$L_{tube}(T, W, t)$ is the measured workpiece length at any condition, of temperature and moisture uptake and time;

$L_{tube, 20, W_{ref}, t_{ref}}$ is the predicted length of the workpiece at reference condition and reference time;

L_{gb} is the length of the gauge block from the calibration certificate;

L_{stand} is the calibrated thickness of the stand plate;

Δx_{probe} is the difference in the inductive probe reading between the zeroing using the gauge block and the measurement of the workpiece;

ΔL_p is the estimated systematic variation to obtain $L_{tube}(T, W, t)$, composed of the contributions of thermal expansion, moisture expansion, shrinkage and elastic deformation.

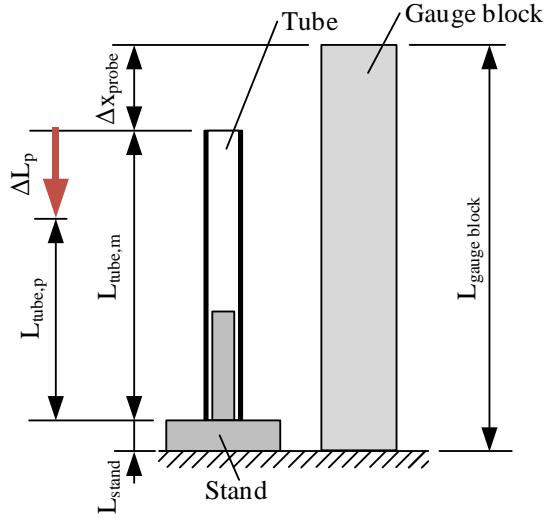


Figure 6.4 Length measurement of the POM tube using the comparator method.

The uncertainty budget for $L_{tube,20,W_{ref},t_{ref}}$ follows equation 6.2, which is developed by the formulation in equation 4.1 where all the uncertainty contributions are considered uncorrelated. The coverage factor k is set equal to 2. The contributors u_i are described in detail in **Table 6.3**.

$$U_{L_{tube,20,W_{ref},t_{ref}}} = k \cdot \sqrt{\sum_i u_i^2} \quad 6.2$$

The length measuring station is designed to minimize the instability due to temperature. The thermal expansion of the system in the direction of the measuring length can be described from the two contributions from the Invar column and the steel support plane. Their dimensions are sketched in **Figure 6.5**. Considering a CTE of 1.6 and 11.0·ppm/°C for Invar and steel respectively the total thermal error in the measurement of the length L consequent to a uniform temperature variation is lower than 0.05 μm/°C. As first step of the data processing the thermal drift of the fixture and the thermal drift of the inductive probe, equal to 0.15 μm/°Cn are removed from the raw instrument reading.

Table 6.3: Uncertainty contributors for the predicted length at reference conditions of the POM tube.

<i>Contributor</i>	<i>symbol</i>	<i>Source of uncertainty</i>
Reference gauge block	$u_{gb,1}$	Calibration certificate
	$u_{gb,2}$	Thermal expansion – uncertainty on CTE value
	$u_{gb,3}$	Thermal expansion – uncertainty on temperature
	$u_{gb,4}$	Repeatability of measurement (due to positioning errors)
Stand	$u_{stand,1}$	Calibration certificate
	$u_{stand,2}$	Thermal expansion – uncertainty on CTE value
	$u_{stand,3}$	Thermal expansion – uncertainty on temperature
Fixture	$u_{f,1}$	Thermal expansion – uncertainty on CTE value
	$u_{f,2}$	Thermal expansion – uncertainty on temperature
Equipment	$u_{eq,1}$	Probe reading
Workpiece	u_{rep}	Repeatability of measurement (due to positioning)
Prediction	$u_{p,1}$	Thermal expansion
	$u_{p,2}$	Moisture expansion
	$u_{p,3}$	Residual stresses shrinkage
	$u_{p,4}$	Elastic deformation

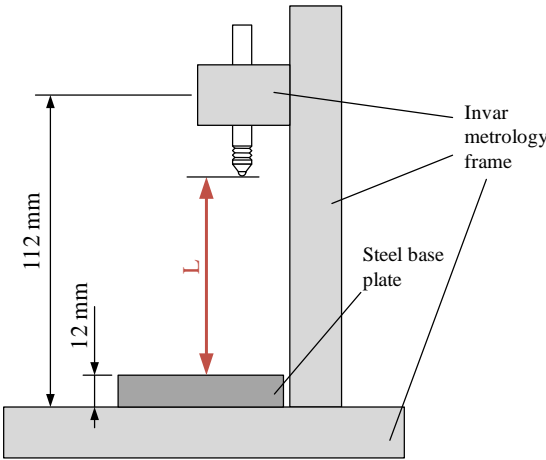


Figure 6.5 The “column type” metrology frame of the length measuring station. Thermal expansion is limited by the use of a combination of Invar and steel components.

Nevertheless the stability of the length measuring station is monitored at least twice a day using the reference gauge block. **Figure 6.3b** depicts the process of zeroing; both length and temperature are measured to address the thermal expansion due to small temperature variations caused by manual handling and ambient temperature fluctuation. Each data point collected consists of the average value over five repeated measurements. The values of the probe output acquired for the stability check through the test are plotted in **Figure 6.6** as a function of the block temperature. The effect of the thermal expansion is visible. A linear regression allows a rough calculation of the coefficient of thermal expansion of the gauge block. The estimated CTE for the gauge block is $16.4 \text{ ppm}/^{\circ}\text{C}$ and it is not compatible with the usual certificate value of $10.6 \pm 1 \text{ ppm}/^{\circ}\text{C}$. Nonetheless the regression analysis provides the probe reading corresponding to the length of the gauge block at 20°C . The standard deviation of the regression residuals is considered as the uncertainty due to the contributions $u_{gb,2}$, $u_{gb,3}$, $u_{gb,4}$.

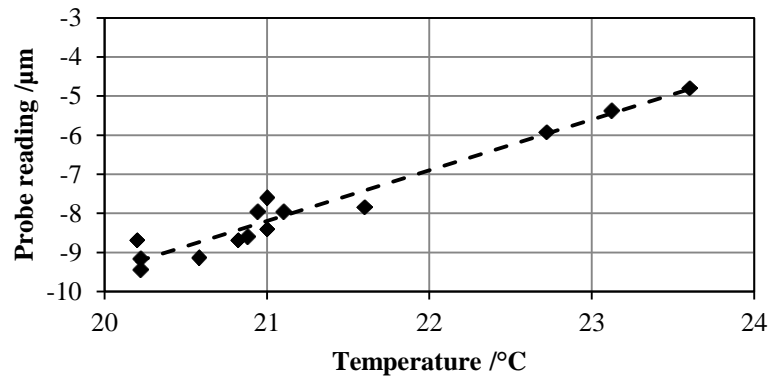


Figure 6.6 Zeroing of measuring equipment using a gauge block: probe reading vs temperature.

A batch composed of tubes from a single shot (total of 20 elements) is taken directly from the injection moulding machine. One single element and a group of 10 elements, both from random cavities, are selected for the measurement. The single sample is firstly weighed, then two temperature sensors are applied using fixing wax and the part is positioned on the measuring fixture. This allows an early weight measurement to be used as a reference in the following calculation. The time necessary to perform all the operation from the mould ejection to the starting of the length measurement acquisition corresponds approximately to 3 minutes. Length and temperature of the tube are then measured simultaneously and continuously for 30 minutes. A relatively high acquisition rate of 0.2 Hz is used. The information acquired concerns the cooling of the workpiece and can be used for the identification of the temperature influence. Successively weight, length and temperature of the part are monitored approximately every hour for the following days to assess the influence of moisture uptake and shrinkage due to stress relaxation. The overall weight of the 10 element group is measured using an analogue method to reduce the error due to the scale resolution according to the statement in section 4.4.2. A total of 7 batches

produced in the first 4 days are considered in this extensive measurement procedure. The described measurement procedure provides information to use in the investigation of the behaviour of the selected item and the definition of a prediction strategy to be applied in short time measurements. Hence to validate the prediction algorithm, measurements in a similar, but shorter, fashion are performed on other 4 batches. A randomly selected single part is initially weighted then length and temperature are measured continuously for 10 minutes. Successively the weight, length and temperature are monitored once every 10 minutes for the following hour for a total of 5 repeated single measurements. The duration of the test is considered a reasonable measuring time to compromise between fast measurement and reliability of the length prediction. A final measurement of length and weight is performed after several weeks to obtain a data point to compare with the prediction performed. All the batches are progressively numbered from 1 to 11: the first 7 refer to the first step of the experimental analysis (extensive measurements) while the last four are used in the validation procedure.

6.3 Data analysis

This section involves data analysis on the experimental results obtained with extensive measurements on batches from 1 to 7. The scope of the analysis is the definition of a DLM prediction algorithm for the specific case of the POM tubes.

6.3.1 The effect of probing force

In contrast to the case studied in section 4.2 the contact between the polymer and the inductive probe is extended on a ring shaped area. Stress and strain are consequently limited. Only the effect of the static elastic deformation is considered relevant and it is taken into account in a systematic compensation in the post processing of the experimental data. A deformation δ of 1.3 μm is expected according to equation 6.3

$$\delta = \frac{F \cdot L}{A \cdot E} \quad 6.3$$

Where:

F is the measuring force, equal to 0.6 N;

L is the length of the workpiece;

A is the contact area, estimated equal to 9 mm^2 ;

E is the elastic modulus of the POM.

The uncertainty on the elastic deformation is composed of two contributions, one assigned to the uncertainty on the measuring force and one to the uncertainty on the elastic modulus of the polymer material.

6.3.2 The effect of temperature

Temperature and length variations are collected during the cooling phase after the injection moulding as the acquisition starts when the polymer component is still warm. An example of cooling curve is depicted in **Figure 6.7**; the average temperature, measured with two thermocouples, and probe reading are plotted as a function of the elapsed time from the production (corresponding to the ejection of the parts from the mould).

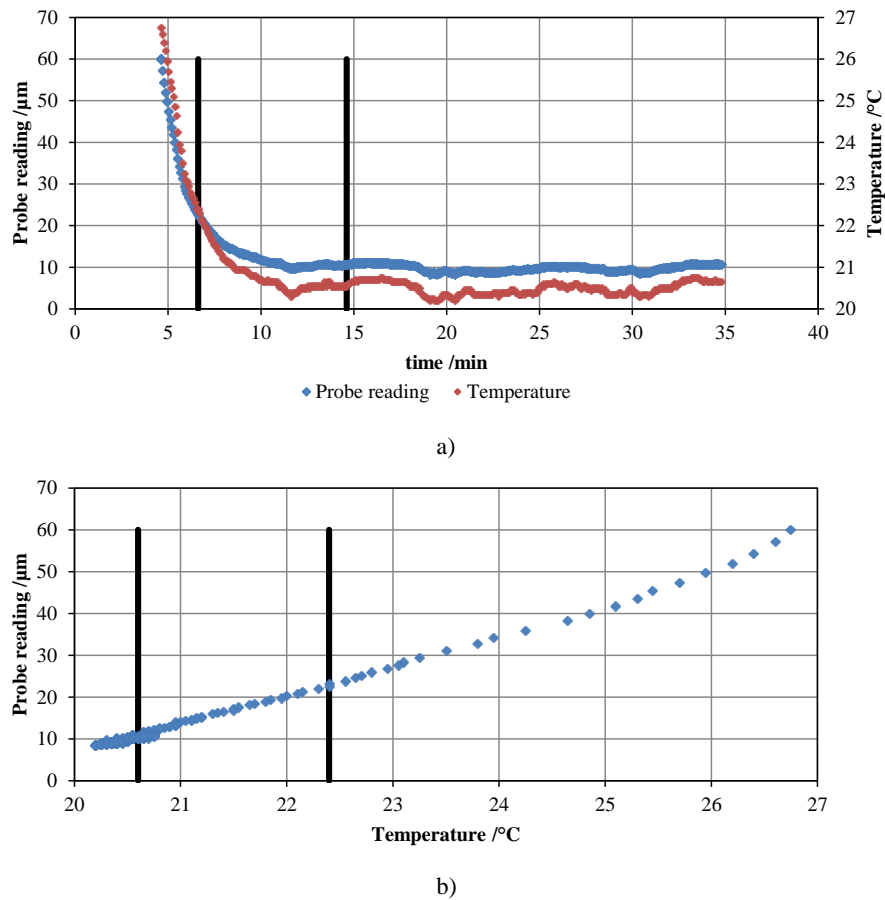


Figure 6.7 Post moulding cooling of POM tube: a) length and temperature measurements over time; b) length variation vs temperature variation. The black continuous line delimits the dataset used in the data processing.

When observing the length variations as a function of temperature, the initial portion of data points, corresponding to the higher temperature, appears non-linear due to high temperature gradients generated by the fast cooling and the change in boundary conditions. The cooling can be considered completed about 15 minutes after moulding. Hence only the measured data from 3 to 10 minutes after the triggering are used in the calculation procedure. Displacements corresponding to temperature variation of about 4 $^{\circ}\text{C}$ are therefore considered representing a sufficient temperature span to obtain a reliable result

for the reference length extraction. The temperature distribution in the part is unknown since no thermographic analysis or FEM simulation has been performed. Nevertheless the temperature gradients can be assumed vertical due to the axial symmetry of the part and with limited amplitude due to the low heat exchange towards the support plane and probe as the contact area is restricted. The average value over the temperature measured on two points at different heights is considered sufficiently representative of the part temperature. The value of the apparent CTE is calculated from the linear regression of the data intervals defined above according to equation 2.1. The data process is performed separately for each single workpiece to obtain a CTE value specific for each part in order to include the variability on material properties due to the production process. The different apparent CTE values are depicted in **Figure 6.8**. The error bars represent the estimated expanded uncertainty considering the standard error of the regression calculations, the uncertainty on the measured length and the uncertainty on the defined temperature, including the measurement uncertainty and influence on errors on the positioning of the sensors. An influence on the production day is visible. The uncertainty of the average value contains a contribution from the uncertainty of the single CTEs and one from the variability over the 7 samples. The average CTE, equal to $109.7 \pm 14 \text{ ppm/}^\circ\text{C}$, is used in the following section, during the validation procedure, to compensate the thermal influence on reference measurements.

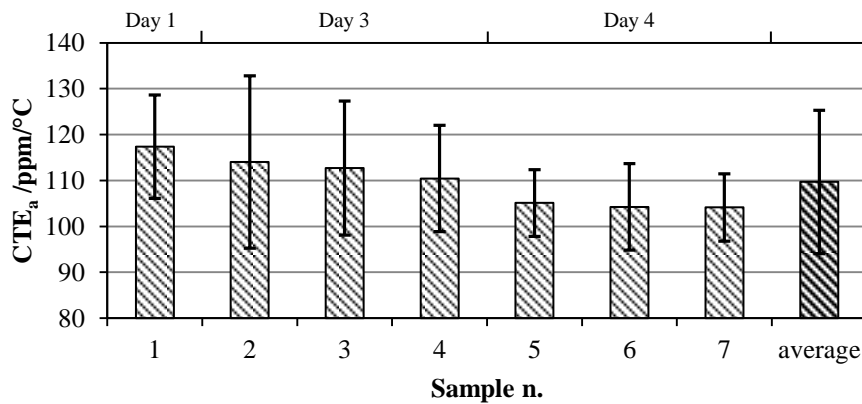


Figure 6.8 Calculated apparent CTE of 7 POM tubes. In the upper horizontal scale the production day is indicated. The error bar represents the expanded uncertainty.

The procedure presented for the estimation of the CTE suits the requirements of fast stage post moulding measurements hence it can be applied in the validation of the prediction algorithm. Using the thermal expansion formula all the measured lengths can then be referred to the reference temperature condition. A limited error is expected since all the measurements are performed close to 20°C .

6.3.3 The effect of moisture uptake

The moisture uptake is measured weighing the single elements and the corresponding 10 dummy parts. Among batches the weight varies because parts from random cavities are selected, nonetheless weight variations can be compared. The tests (lasting for several days) are performed at constant relative ambient humidity of 50 % except for one day where the relative humidity was 60 %. The weight variations are computed as the difference between the single measured values and the weight measured on the third day after production, when the post moulding moisture uptake is considered concluded. The values of weight variations for the single elements and the dummy group are depicted in **Figure 6.9** showing a good agreement between the two series of measurements. Moreover the use of dummy parts leads to a reduction of the experimental variability as showed in section 4.4.2. The post moulding moisture uptake appears to be repeatable among batches and it can be considered concluded within the first 24 hours after moulding. A regression analysis is performed to determine the trend of the weight variation over time. The experimental values of the 7 samples are merged together and the initial post moulding variation is fitted using a power law model according to equation 6.4.

$$W = -0.0059 \times t^{-0.1} + k \quad 6.4$$

The saturation time is considered as the point when the analytical model reaches the value corresponding to the average weight measured after 24 hours (when stabilization already occurred). A saturation time equal to 9 hours is found. The power law curve describing the initial weight variation is valid until this time. Successively the weight is considered following the fluctuations of the ambient humidity.

The analytical model just found can be applied in a fitting analysis of short post moulding measurements to determine the saturation weight, i.e. the weight at 9 hours after moulding.

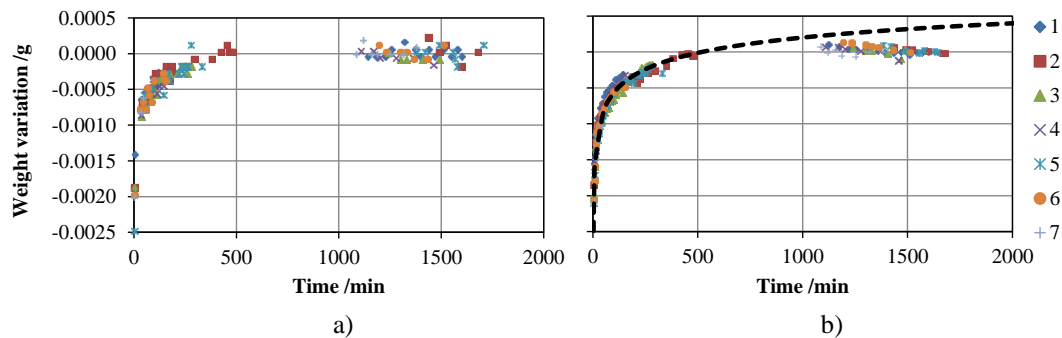


Figure 6.9 Weight variation measured on: a) single parts; b) groups of dummy parts, the black dashed line correspond to the fitting model (equation 6.4). The different batches are indicated with progressive numbers.

Figure 6.10 compares the weight variations of the first day with the length variations measured in the same period. A correlation between moisture uptake and length variation

is not visible despite the previous findings and can be explained by the fact that other mechanisms concurrently affect the dimensions in an opposite way resulting in a balancing of all instabilities. Alternatively the negligible post moulding hygroscopic swelling can be justified as the moisture absorption occurs at the surface of a part and for a tubular shaped workpiece causing an increase of thickness more than an increase of length. Following this explanation the length of the tube should not be affected by moisture uptake and ambient humidity. Nonetheless a dimensional variation due to moisture absorption is observed during the test as explained below and this second hypothesis is rejected.

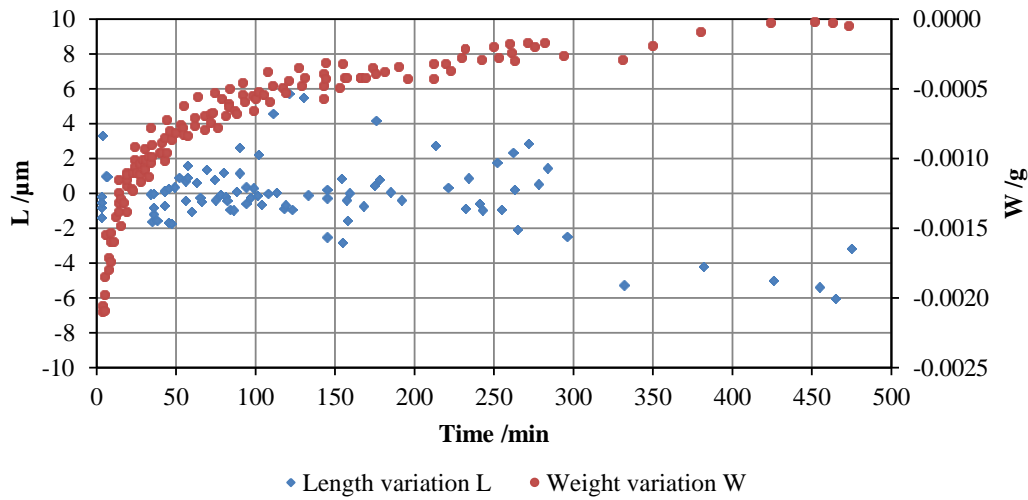


Figure 6.10 Post moulding length and weight variation for 7 samples of POM tubes. A clear correlation is not visible.

During the test campaign the ambient humidity is constant except for one day (day 6). Dimensions and weight of the parts are consequently affected (**Figure 6.11**). In particular the length of all the tubes measured in that particular day shows a systematic variation of about 25 μm from the overall trend. With reference to **Figure 6.11** the value of the coefficient of moisture expansion ($CME_{w,a}$) defined according to equation 4.6, is calculated using the variations occurring in the period from day 4 to day 6. Length and weight variations are calculated as the difference between average values of measurements on day 5 and average values of measurements on day 4 and 6. The values of the apparent CME calculated separately for all the tubes are compared in **Figure 6.12**; the error bars correspond to the estimated expanded uncertainty which considers the measurement uncertainty coming from the resolution of probe and scale. Since the moisture effect is hardly recognizable from short post moulding measurements, it is necessary to estimate coefficient of the moisture expansion to use in the prediction formulation prior the measuring process. Therefore the average value of the CMEs calculated for the 7 tubes is used as estimation of $CME_{w,a}$ in the validation procedure; its value is equal to $26692 \pm 2992 \mu\text{m/g}$ (2σ),

where the uncertainty considers contributions from the uncertainties of the single CMEs and from the variability over the 7 samples.

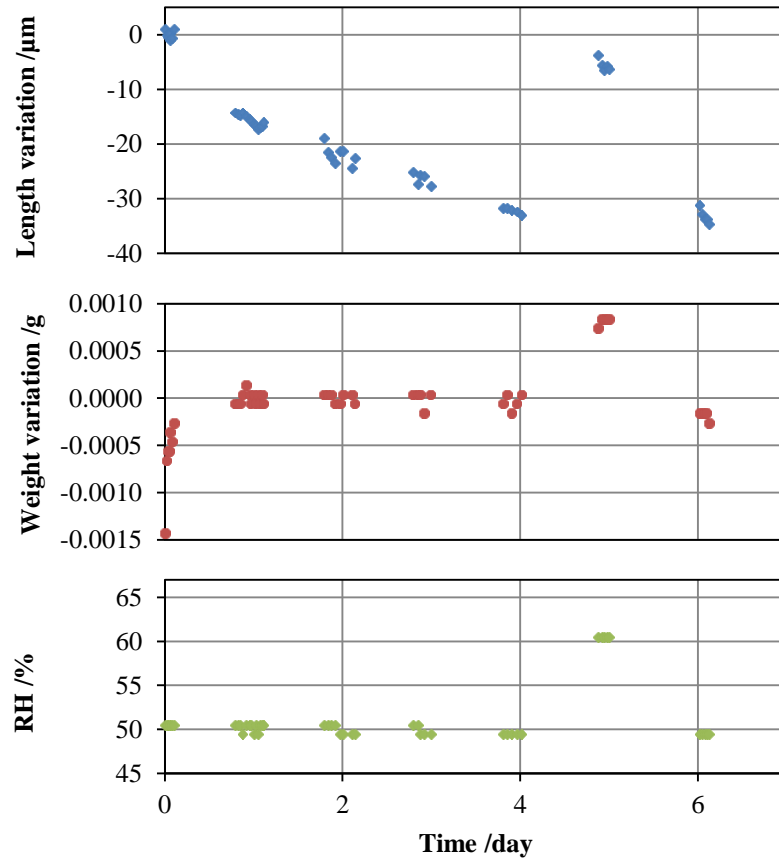


Figure 6.11 Post moulding length variation (blue), weight variation (red) and ambient humidity (green) referred to the measurements on sample n. 1. A change in ambient humidity in the fifth day after moulding causes a change in dimensions and weight of the part.

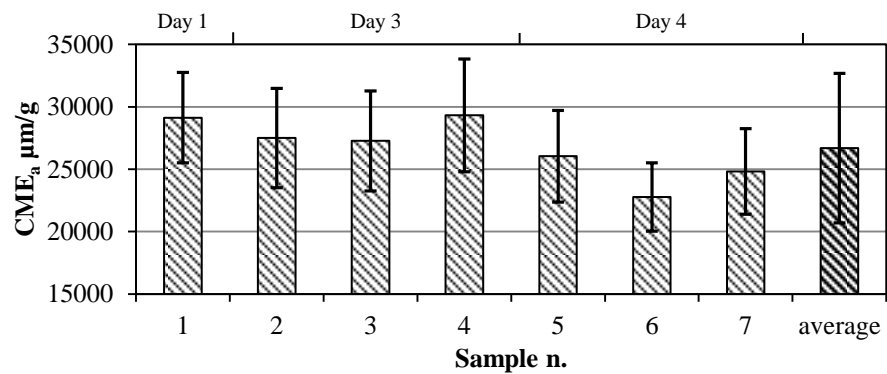


Figure 6.12 Calculated apparent CME of 7 POM tubes. In the upper horizontal scale the production day is indicated. The error bars represent the expanded uncertainty.

After the estimation of the coefficient of moisture expansion all the length measurements can be compensated for the hygroscopic swelling and referred to the reference condition, i.e. the weight in saturation conditions at ambient relative humidity of 50 %. The reference weight is therefore estimated as the average among the measured weight in day 4 and 6.

6.3.4 The effect of residual stresses

After the compensation of temperature and moisture effects (**Figure 6.13**) the length of the POM tubes have a residual decreasing trend (shrinkage) due to stress relaxation. A logarithmic model (equation 6.5) can be applied to fit the dataset of each single tube. The logarithmic trend is confirmed by further measurements performed 6 and 12 weeks after production (about 40 and 80 days respectively). The logarithmic model does not reach stabilization, however the length decrement slows dramatically after some weeks. From the measurement performed the logarithmic decay is still active after two months from production.

$$L(t) = a \cdot \ln(t) + b \quad 6.5$$

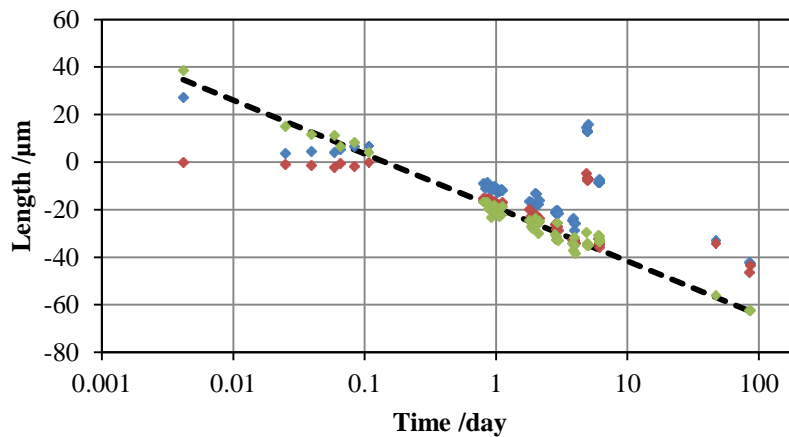


Figure 6.13 Post moulding length measurement of POM tube: probe reading of tube n.1 (blue); after thermal expansion correction (red); after moisture expansion correction (green). The logarithmic fitting is represented by the dashed black line. The measurements after several weeks are also indicated.

As the post moulding shrinkage is a long lasting effect, it cannot be predicted from short measurements after production. Hence it is considered as a systematic effect, constant among all parts. The data sets of length variations of the 7 samples are referred to the last measured point (12 weeks after production) and merged together, see **Figure 6.14**, to perform a regression using the model described in equation 6.5. The standard deviation of the residuals of the regression is equal to 4.1 μm and it is considered the

uncertainty assigned to the compensation of the stress-driven shrinkage. The fitting model is described by equation 6.6.

$$L(t) = -9.23 \cdot \ln(t) + b \quad 6.6$$

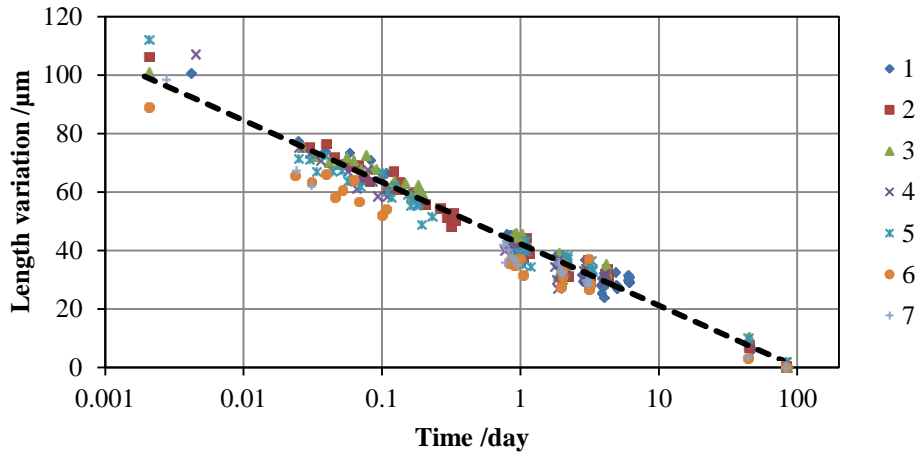


Figure 6.14 Shrinkage during a week after production for 7 parts. The black dashed line corresponds to the logarithmic model fitting all the data points.

6.4 Validation

The validation is performed on 4 elements (progressively numbered from 8 to 11) which have been measured shortly after production in an ambient at 20 ± 1 °C and constant relative humidity. The measuring procedure has been described in section 6.2, and provide length measurements that must be referred to a specific temperature, weight and time after production, indicated as $L(T, W, t)$. According to the previous analysis the main contributors of length variation are handled as follows:

- Probing force effect: constant elastic deformation is compensated according to equation 6.3.
- Thermal effect: the apparent CTE, CTE_a , is calculated similarly to section 6.3.2. Successively all the length measured the measured at time t after moulding, at temperature T and when the part has weight W , $L_{meas}(T, W, t)$, are compensated from the thermal expansion and referred to 20 °C (reference temperature condition) following equation 6.7. The temperature compensated length are indicated as $L_{20}(W, t)$.

$$L_{20}(W, t) = L_{meas}(T, W, t) - L_n \cdot CTE_a \cdot (T - 20) \quad 6.7$$

- Hygroscopic swelling: weight measurements over time in the first hour after injection moulding are fitted using equation 6.4. The fitting model is used to extrapolate the weight in saturated conditions W_{ref} , i.e. 9 hours after production. Since the test is performed at ambient humidity of 50 % the estimated weight in saturated state already refers to the standard stabilized conditions. The length values $L_{20}(W, t)$ are then compensated for the hygroscopic swelling and referred to W_{ref} according to equation 6.8, using the average coefficient of moisture expansion, $CME_{W,a}$, calculated before and the weight measurements W performed concurrently to length measurements. The resulting length are indicated as $L_{20, Wref}(t)$.

$$L_{20, Wref}(t) = L_{20}(W, t) - CME_{W,a} \cdot (W - W_{ref}) \quad 6.8$$

- Residual stresses shrinkage: after compensation of temperature and humidity effects, the length of the tubes can be fitted using the model described by equation 6.6; the variable b allows fitting the logarithmic decay to parts with different length. The resulting model equation represents the predictive model to use in the estimation of the length of the parts at any time after production, $L_{20, Wref, t}$.

The estimation of the length $L_{20, Wref, t}$ includes DLM elements, characterized by direct definition of coefficient and material properties (thermal expansion), combined with conventional compensation elements, which uses coefficient established in advance (residual stresses).

The validation procedure requires the comparison of the predicted length with reference measurements. Hence after the initial post moulding measurement the four tubes are stored in a controlled temperature environment, with ambient temperature of 20 ± 0.5 °C. 6 and 12 weeks after production, at time indicated as t_1 and t_2 , length measurements are performed using the same equipment; the measured length are indicated as $L(T, W, t_1)$ and $L(T, W, t_2)$ and are referred to temperature, weight and time concurrently measured. It is necessary to refer the measurement to the actual conditions as it do not match the reference conditions; in fact the temperature of the workpieces during these measurements is on average 20.3 ± 0.1 °C while the ambient relative humidity is 60 %. A successive compensation following equation 6.7 and 6.8 is performed to obtain the value of length in reference conditions, $L_{20, Wref}(t_1)$ and $L_{20, Wref}(t_2)$. In this particular case the compensation should resemble a traditional methodology using predetermine information in opposition to the DLM methodology. Therefore the CTE and CME values consist of the average value of the CTEs and CMEs calculated in the previous section.

The reference measurements contain uncertainty contributors shared with the post production measurements, such as the elastic deformation due to the probing force, the length of the gauge block and the length of the stand. These elements influence the estimation (value and uncertainty) of the absolute length of the workpiece and not the estimation of the length variation after production, i.e. ΔL_p in equation 6.1 as they are constant for all performed measurements. They are therefore not considered in the procedure for the validation of the prediction algorithm and in the uncertainty budget.

The uncertainty budget of $L_{20,Wref}(t_1)$ and $L_{20,Wref}(t_2)$ is performed according to [10]; as an example the budget regarding the $L_{20,Wref}(t_1)$ of tube n.8 is presented in **Table 6.4**. It considers a contribution due to the instrument (digital resolution), a contribution due to the repeatability of the measurement, calculated as standard deviation of 5 replications of the measurement (with repositioning of the part), a contribution due to the uncertainty of the measured temperature and estimated CTE and contributions due to moisture uptake, as measurement uncertainty of the weight measurement and uncertainty on the value of the CME. The main contributors are related to the weight measurement and CME estimation.

The uncertainty of the estimated length $L_{20,Wref,t1}$ (**Table 6.5**) considers contributions coming from the implementation of equations 6.6, 6.7 and 6.8. The value of the CTE has been defined with the direct DLM method; therefore it has a lower variation limit than the case presented in **Table 6.4**. The values of temperate and weight used to calculate the sensitivity factor of the CTE and CME contributors are estimated as average value of the measurements performed during one hour after injection moulding. As the weight is still far from the reference value the length variation limit is deeply affected by the CME uncertainty. The contribution due to the shrinkage compensation is added as standard deviation of the residuals of the fitting performed in section 6.3.4. The compensation of long term shrinkage and the uncertainty on the CME represent the main contributions to the uncertainty of the predicted length.

Table 6.4: Uncertainty budget according to [10] for reference measurement $L_{20,Wref}(t_1)$ of POM tube n.8.

	Contributor	Evaluation type	df	Variation limit	Length variation / μm	Distribution divisor	Standard uncertainty / μm
L	Probe (resolution)	B		0.2 μm	0.20	1.7	0.12
u_{CTE}	CTE	B	14	$ppm/^{\circ}C$	0.25	1.0	0.25
u_{temp}	Temperature	B	0.15	$^{\circ}C$	1.29	1.7	0.57
u_W	W (resolution)	B	0.0001	g	2.67	1.7	1.57
u_{CME}	CME	B	2992	$\mu m/g$	0.92	1.0	0.92
u_p	Repeatability	A	5	0.6 μm	0.64	1.0	0.64
u_c	combined uncertainty / μm						2.02
U	expanded uncertainty (k=2) / μm						4.0

Table 6.5: Uncertainty budget according to [10] for estimated length measurement $L_{20,Wref,t1}$ of POM tube n.8.

	<i>Contributor</i>	<i>Evaluation type</i>	<i>df</i>	<i>Variation limit</i>	<i>Length variation /μm</i>	<i>Distribution divisor</i>	<i>Standard uncertainty /μm</i>
L	Probe (resolution)	B		0.2 μm	0.20	1.7	0.12
u_{CTE}	CTE	B	4	$\text{ppm}/^{\circ}\text{C}$	0.24	1.0	0.24
u_{temp}	Temperature	B	0.15	$^{\circ}\text{C}$	0.93	1.7	0.55
u_W	W (resolution)	B		0.0001 g	2.67	1.7	1.57
u_{CME}	CME	B	2992	$\mu\text{m}/\text{g}$	3.49	1.0	3.49
u_s	Shrinkage	b	4.1	μm	4.06	1.0	4.06
u_c	combined uncertainty / μm						5.62
U	expanded uncertainty (k=2) / μm						11.2

In **Figure 6.15** the predicted length $L_{20,Wref,t1}$ and $L_{20,Wref,t2}$ are compared with the measured (and compensated) one; the error bars represent the expanded uncertainties estimated according to the procedure abovementioned. A general level of expanded uncertainty better than 5 μm is obtained for the reference measurements, while the uncertainty of the predicted length is in the order of 11 μm . In all cases the estimated length is compatible with the reference one. The prediction methodology estimates more efficiently the length at time t_1 (six weeks after production) with a lower systematic error than the case at t_2 .

The successful comparison and the relative low level of calculated uncertainty are related to the fact that the ambient temperature and humidity during the validation measurement (just after production) are close to the reference value of 20 $^{\circ}\text{C}$ and 50 %. This reduces the impact of an error in the definition of the CTE and CME. Unfortunately for practical reasons it was not possible to perform the validation measurements in a different environment.

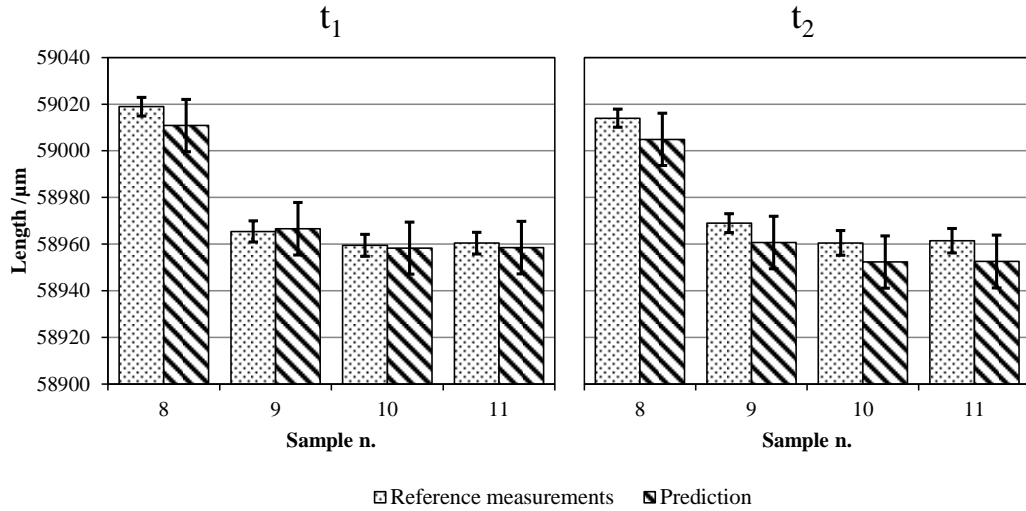


Figure 6.15 Predicted length $L_{20,Wref,t}$ for 4 workpieces compared to reference measured values $L_{20,Wref}(t)$. The error bars represent the expanded uncertainties according to table 6.4 and 6.5.

6.5 Conclusion

The DLM methodology and the guideline defined in chapter 4 are implemented in a practical industrial case. A component made of POM with a tubular shape has been selected for the investigations. The measuring equipment consists of a set-up to measure concurrently length and temperature on two points of the component and an electronic scale for measuring weight variations. Measurements are carried out on components few minutes after injection moulding for the prediction of the parts length at standard condition after stabilization. The procedure starts with an initial continuous measurement of length and temperature to get the information from the cooling phase. Then the procedure involves static single measurements of weight, length and temperature approximately every hour for the following days. 7 samples, produced in 3 different days are considered in the investigation.

The viscous deformation due to the probing force is not accounted and the force effect is considered as a static systematic contribution due to elastic deformation. The temperature effect can be analysed from the length and temperature data set measured during the cooling phase. The linear regression of length variation over temperature provides the value of the apparent CTE. After the definition of the apparent CTE all the length values can be compensated for the thermal effect and referred to the reference temperature. The analysis of the weight variation gives information about the moisture uptake. The method of using dummy samples presented in section 4.4 appears a valid solution for reducing the variability of the measurements. Weight variations of the 7 parts are merged to define a

common model equation, useful to predict the weight corresponding to full saturation after production using only short post moulding measurements. The length variation just after moulding, during the transitory period to reach saturation, appears uncorrelated to the moisture uptake. However a change of the ambient relative humidity produces a change in length and weight which allow for the calculation of an average value of CME to use in case of short post moulding measurements. After the compensation for thermal and moisture expansion the measurements show a logarithmic decreasing trend lasting for several days that can be assigned to the shrinkage due to residual stresses. Measurements performed after 6 and 12 weeks from production confirm the logarithmic decay. The data sets of all the samples are zeroed on the final length value (corresponding to 12 weeks after production) and pooled together to define a shrinkage curve valid for all the parts. The shrinkage is then compensated as a systematic effect since it cannot be estimated from short time measurements. Therefore the effect of temperature is compensated exploiting dynamic measurements (calculation of CTE); the compensation of moisture uptake and hygroscopic swelling uses a combination of dynamic measurements (to define the saturated weight) and predetermined information (CME), as well as the compensation of residual stresses.

The developed methodology is applied to short time post moulding measurement of four samples. Continuous length and temperature measurements during the cooling phase (first 10 minutes after injection moulding) and 5 static measurements of length, weight and temperature performed during the first hour after production are used to predict the length at reference conditions at any time after production. Further measurements, performed 6 and 12 weeks after production, are used to validate the prediction model. After compensation of thermal expansion and hygroscopic swelling of the reference measurements, a comparison between the estimated length and the measured length is performed. The expanded uncertainty for the measured reference length is assessed equal to 5 μm while for the estimated length is assessed equal to 11 μm . The two sets of data are in agreement showing the validity of the method.

7

Summary and conclusions

7.1 Summary

Dimensional measurements in production environments are sought by manufacturing companies for anticipating the measuring process and to produce data for the process control. To address the unstable and time transient state of measuring components the methodology of Dynamic Length Metrology has been introduced. DLM aims to obtain an accurate estimation of the dimensions at reference conditions from measurements performed right after the production process. The method requires the simultaneous measurements of multiple quantities, besides dimensions, which are combined in a series of calculations to predict the length at reference conditions. DLM can be applied on measurements of metal or polymer components. The work here focused on the implementation of DLM in injection moulded polymer parts.

A state of the art review on the topic of dimensional measurements in production has been presented. Production environment and early stage measurements introduce instabilities on the component. In the case of metallic or ceramic components the main instabilities are represented by thermal effects. In the case of components made of polymer these instabilities have been identified caused by temperature, moisture absorption and mechanical stresses.

Dimensional measurements can be performed with contact and optical techniques. Contact one-dimensional techniques allow fast punctual measurements of simple geometries. More complex 3D measuring systems, such as CMM, allow simple measurements as well as complex scanning of freeform parts. Similarly optical techniques can be implemented in simple measurements or complex 3D scans depending on the working principle. Contact methods are affected by the interaction between probe and workpiece. Elastic deformation is relevant to consider especially in the case of workpieces made of less rigid materials, like polymers. Optical methods on the other hand are affected by the

surface appearance of the workpiece and by the interaction of the workpiece with the light.

Traceability of the measurements is ensured with calibration procedures. Generic calibration and performance verification procedures provide an overall assessment of the instrument accuracy, often represented by the MPE. In the case of well determined applications, task specific calibration routines using reference artefacts, which resemble the measuring object, lead to more detailed uncertainty estimation as more error sources are considered, such as positioning repeatability. Metrology frame and positioning fixture are two crucial components in the measurement instrument to minimize the measurement uncertainty. Metrology frames should be as stable as possible concerning thermal deformations and should be designed to reduce temperature gradients and distortions. Positioning fixtures must ensure a unambiguous location of the workpiece without over constraining it.

The implementation of Dynamic Length Metrology requires the use of equipment in unconventional ways to comply with transient conditions and unknown material properties. Three different pieces of equipment, two for dimensional measurements and one for temperature measurements have been analysed and tested.

A commercial linear actuator, equipped with an encoder for a feedback control of the position, was used as a contact displacement sensor. Thanks to the adjustable measuring force, the systematic effect of the contact force during the measurement was taken into account. In order to determine the metrological characteristics of the measuring system, the calibration consisted of length measurements of steel gauge blocks with different contact forces. A complete mathematical model for the measured length was defined, taking into account the thermal expansion of the glass measuring scale, the deformation due to the contact force and the thermal expansion of the measured gauge blocks. An a priori uncertainty evaluation, performed according to GUM, enabled identification of the most significant factors affecting uncertainty of the measured length. The limit deviations for the lengths of the gauge blocks were found to be the major contributions. Accordingly, grade 0 gauge blocks were selected. Then, considering experimental data, a systematic sensitivity error was identified and modelled. Subsequently the measurement repeatability was evaluated. In this way, an expanded uncertainty (at 95% confidence level) of measured length of about 0.5 μm was obtained.

Multi-wavelength interferometry offers the advantage of an absolute range of several millimetres in contrast to conventional laser interferometry where incremental measurements are necessary due to the narrow absolute range. A commercial MWLI system intended for profilometer application has been tested as a potential method for very accurate measurements in production. The interferometric system has been tested using two step gauges made with gauge blocks on an optical flat with step heights of 100 μm and 3 μm respectively. The measurements have been performed in a non-controlled environment in a short time span to ensure reproducibility conditions. The step gauges were measured in a scanning mode producing a profile of the artefact; only the centre position of the gauge blocks is considered in the analysis. The uncertainty of the measured step height has been estimated following the guidelines of ISO 14253 and considering repeat-

ability and noise of the interferometer. Uncertainties as low as $0.06\text{ }\mu\text{m}$ and $0.2\text{ }\mu\text{m}$ have been achieved for the two step gauges respectively. Nonetheless the main contributor in the uncertainty budget was represented by the uncertainty of the reference value of the step height showing that MWLI is suitable for absolute length measurements of workpieces with fine surfaces. The applicability on injection moulded polymer parts was not tested. However these components normally have fine surfaces (originated by a replication process on polished moulds) that do not cause worsening of the uncertainty. On the other hand, only measurements on metallic components require very low uncertainties, indicatively lower than $1\text{ }\mu\text{m}$, which can justify the high cost of this interferometric technology.

Temperature infrared sensors provide non-contact measurements which do not require the installation of the sensor directly on the surface of the workpiece. Moreover thermal imagers give extensive information on the temperature field in the case of transient non-uniform thermal conditions, typical of DLM applications. On the other hand the accuracy of infrared measurement is higher than the one obtained with contact sensors. An infrared thermocamera has been selected for testing its applicability in DLM measurements, concerning accuracy achievable in the specific application and the possibility of obtaining solid information about temperature fields. A first series of tests was performed measuring the temperature of a metallic plate during a thermal cycle of heating from $20\text{ }^{\circ}\text{C}$ (ambient temperature) to $30\text{ }^{\circ}\text{C}$ and following natural cooling. Four targets have been placed on the surface of the plate: two targets corresponded to two reference contact sensors (RTDs) with a backing material with high emissivity, one target corresponded to a high emissivity label and the last one is left as bare metallic surface as a case of low emissivity. This arrangement allowed the comparison of infrared and contact measurements as well as a comparison of infrared measurements on material with different emissivity. The measurements on the low emissivity surface were strongly affected by noise and could not be considered reliable. Measurements on high emissivity surfaces on the other hand presented less variability and departed from the reference contact measurements of about $\pm 0.5\text{ }^{\circ}\text{C}$. This systematic error was affected by the definition of the surface emissivity and by the influence of the background radiation. A second test has been performed to address the possibility to use thermal imagers for measurements of temperature fields. A polymer component, made of ABS with a prismatic hollow shape, was measured during a cooling phase considering different boundary conditions, namely placing the part with different orientations on a support plane. The infrared measurements led to a qualitative estimation of the temperature field, useful to study the cooling process for the design of the measurement strategy (number and location of the temperature measurements). An implementation of the thermocamera in the final DLM measurement set up is possible if the high cost of the device is accepted.

DLM requires the study of innovative probing strategies as the length measurements occur in non-stable conditions and must be coupled with measurements of other quantities for the calculation of material properties and the extraction of dimensional values at reference conditions. The experimental work carried out focused on components made out of polymer, which are less stable than metal, and involved the study on dimensional

instabilities, caused by probing forces, temperature changes and moisture absorption, and on the definition of novel probing strategies. To connect dimensional variation with influence factors the concept of apparent properties was introduced. They represent the sensitivity of a dimension with respect to a particular input, for instance the dimensional sensitivity on temperature variations (apparent CTE). Apparent properties are influenced by geometry and measurement procedure as well as material properties.

Force effect has been investigated using the industrial actuator previously introduced. The equipment allowed dimensional measurements with a resolution of $0.1\text{ }\mu\text{m}$ similar to a set up using inductive probes with the further possibility of adjusting the probing force. The test procedure consisted of measuring a polymer part, i.e. the same element (material and shape) used in the thermal imager investigation, using increasing force to assess the elastic deformation and define a compensation method. Three analytical models - linear, quadratic and a model following the hertz contact mechanic formulation - have been used to fit the measured deflection as a function of measured force. Although the hertzian case is supported by a formal theoretical modelling the linear formulation provided a better description of the experimental results, namely with smaller regression residuals. Nonetheless in all cases the regression led to a satisfactory result. The main consequence of choosing a different regression model arose during the calculation of the workpiece length after removing the elastic deformation contribution. A systematic variation of about $2\text{ }\mu\text{m}$ occurred between the extrapolation using the linear model and the hertzian model. Another series of tests has been performed to assess the viscoelastic deformation of prolonged probing contact on the same polymer components. A contact force of 0.5 N caused a deformation of $5\text{ }\mu\text{m}$ after a contact lasting 150 hours. For shorter periods, less than 1 hour, the viscoelastic deformation could be neglected as it was limited to one tenth of a micrometre.

The temperature state of an injection moulded polymer part after the production process consists of a cooling phase from the ejection temperature to the ambient temperature. Hence the experimental work has been carried out by heating up polymer workpieces, consisting of the ABS element already used in previous measurements, to emulate the post moulding condition and measure length and temperature over time. A first series of tests has been performed to address the issue of the measuring time. The heated workpiece was positioned in a measuring fixture, made with thermally stable materials (Zerodur and Invar). A two point length was measured with an inductive probe, and a RTD contact temperature sensor. The length of the workpiece at reference temperature has been extrapolated using a linear regression of the data acquired during cooling with an estimated uncertainty that considered the contribution due to the sensors, contribution due to the measurement procedure, namely the starting temperature and the duration of the measurement, and the repeatability of replicated measurements. Measuring times longer than one minute led to uncertainties lower than $1\text{ }\mu\text{m}$. Excessive extension of the measurement time did not lead to major improvement. The cooling of the component considered (with a mass of less than 2 g) was completed within the first 15 min after moulding hence in order to obtain information of the transient phase, as in the test reported, the manufacturing facilities must allow a rapid transition between production and measurement operations. In a completely automated production line the measuring task can be

implemented by an automated device or a robotic arm. A second investigation has been performed on the same ABS elements using the same procedure of emulating the post moulding condition but on a different measuring set-up. In this second case the workpiece had a marked directional (vertical) temperature field due to the preferential heat exchange towards the support plane which allowed for the study of different strategies for measuring the temperature. The measured dimension corresponded to the horizontal length of the prismatic component. Two temperature sensors (thermocouple type K) have been positioned on two locations at the same vertical coordinate of the measured length and a third one on a different location. Three apparent CTEs were calculated from the regression of the length variation with temperature defined using three different weighted averages of the measured values. The best results (with the lowest regression residual) were obtained using only temperature information from the sensors at the same height of the measured length. The position of the temperature sensors must therefore be related to the temperature field generated on the workpiece after the positioning in the measuring fixture. At the same time the temperature field can be modified using a different orientation of the workpiece or a different positioning fixture if the location of the temperature sensor is fixed. The experimental data of length and temperature variation were used as input for a thermomechanical FEM simulation of the workpiece. The results of the simulation complied with the initial hypothesis of vertical temperature gradient and with thermocamera measurements. In a development stage the number of temperature sensors can be large for providing a better understanding of the measuring condition and can be reduced with proper analysis (analytical and numerical).

The influence of ambient humidity and moisture absorption on dimensions of the usual polymer component has been investigated in two steps. The first one involved measurements of length and weight at different ambient humidity and temperature of 20 °C in quasi-saturated conditions. The interval from 50 to 90 % of relative humidity has been investigated using a humidity chamber. The workpieces were kept in the chamber for 24 hours (which is considered sufficient to reach saturation) at stable humidity level and measured in a dedicated fixture with inductive probes. For measurement in relative ambient humidity lower than 50 % the workpieces were kept in a metrology room with controlled ambient temperature and measured on a CMM using a procedure to replicate the alignment of the first fixture. In both cases the weight is measured with an electronic scale with resolution of 0.1 mg. The data of relative length and weight variation could be merged for defining an apparent CME valid for a wide range of ambient humidity. The measurement procedure just described could be implemented only during the design and development of a DLM application as it does not reflect the post production condition of injection moulded components which are usually ejected from the mould with a very low level of absorbed moisture and subsequently absorb water to reach equilibrium with the ambient. In the second step of the moisture related investigation the post moulding transient state has been investigated. Initially the ABS parts were dried out in a dryer designed for raw material (pellet) and length, temperature and weight were measured simultaneously for a period of 24 hours. The absorption and the hygroscopic swelling occurred with an exponential increment and reached stability within the measuring period. Successively the weight of the polymer parts has been monitored after the moulding process for

a period of time of 3 days showing once again an exponential increase but with higher amplitude and longer stabilization time. This discrepancy has been caused by an incomplete drying of the workpieces when using the pellet dryer. The results were still of interest and valid as the apparent CME calculated from the transitory absorption was compatible with the one calculated in the first step of the investigation. Difficulties encountered in the analysis of hygroscopic swelling were related to the extrapolation of the length at reference conditions. In fact the part dimensions with a moisture content corresponding to a saturated state at the reference ambient condition can be estimated from a generic state by measuring the absolute moisture content. This value cannot be obtained exclusively from measurement in production as only the relative moisture uptake after moulding can be assessed. A solution has been proposed but not validated; it involves both dynamic measurements and predetermined apparent properties and requires many assumptions and extrapolations. Alternatively hygroscopic swelling can be compensated with a more traditional way as a systematic effect.

The implementation of optical solutions in the context of DLM, and more in general in metrology in production, leads to many advantages. A main one is related to the removal of the probing contact. Moreover in many applications using optical devices the workpiece positioning can be a floating type without a fixed datum which makes the measurement procedure easier as positioning errors are eliminated. Two optical solutions based on a vision system have been developed to provide traceable and fast dimensional measurements in dynamic conditions.

The first solution involved absolute dimensional measurements using an edge detection algorithm. The method applies specifically to length measurements the distance between two edges of a plane surface of a workpiece. By including in the field of view of the camera reference marks, for instance using a calibrated grid or scale, the edge position can always be referred to the position of the marks, providing the necessary traceability. Several relevant edges can be caught simultaneously by the camera by splitting the field of view with a set of mirrors, using multiple cameras or introducing a relative movement. In this last case the positioning accuracy of the moving device does not affect the accuracy of the measurement as it is always based on the position of the reference marks. An optical CMM equipped with a video probe has been used in the validation of the method, as it represents a system with a movable camera. An edge detection algorithm has been developed. It is based on the Sobel filter for edge enhancement. Furthermore, the subpixel resolution has been achieved with a routine using intensity fitting around the edge position. Two methods for camera calibration have been proposed. They are based on the comparison of the pixel size with the dimensions of a reference chessboard. The first method consists of a comparison while the second one, formally more correct, considers also lens distortions. The calculated pixel sizes using the two methods were consistent thanks to the very low amplitude of image distortions. The method has been validated using an optical scale as workpiece and an optical grid as reference to ensure a limited effect due to non-ideal edges. A strategy for alignment of the coordinate system along the reference grid marks has been established as well as the specification of the length calculation from the edge position information. A standard deviation of 2 μm has been

achieved on 25 replicated acquisitions. Several versions of subpixel registration, involving different intensity fitting parameters, have been investigated. The output was slightly influenced by the variations of the algorithm, less than $0.5\text{ }\mu\text{m}$, indicating a robust and stable measuring method. Further, the methodology has been tested on polymer parts with different lengths. The repeatability of replicated measurements was not affected by the amplitude of the measured length; consequently also the accuracy related to the measurement device can be considered independent, or only moderately influenced, by the measured dimension.

The second optical solution has been developed in order to measure surface displacements, for instance due to thermal expansion. The methodology is based on digital image correlation (DIC). A routine based on intensity interpolation of the correlation function enables reaching subpixel resolutions. The correlation calculation can be performed in the whole image giving as output the overall displacement of the surface captured in the pictures, or in several smaller subsets for the definition of a displacement field with finer spatial resolution. The performance of the DIC methodology has been verified on measurements of thermal displacement of a polymer part considering two surface details with different appearance, four subset sizes (30, 60, 90 and 120 pixels) and two models (Gaussian and polynomial) for the intensity fitting in the subpixel resolution routine. The measurement uncertainty has been estimated considering contributions due to the accuracy of the calibration and due to the correlation algorithm. Measurement uncertainties lower than $0.6\text{ }\mu\text{m}$ could be achieved for subset sizes bigger than 90×90 pixels with a Gaussian regression model. Finally the DIC methodology has been implemented in a multisensory set-up to address the applicability to DLM. Thermal displacements have been measured in two locations using DIC and contact inductive probes while temperatures have been measured with thermocouples. The data from all the sensors were fused to provide three apparent CTEs and a displacement field. The apparent CTEs were not compatible showing that they are affected by the measuring strategy.

The final chapter of this work deals with the development and validation of a DLM measuring methodology applied to a specific industrial case. The selected component was a tubular shape part made of POM; it was different in material and shape from the one considered in the rest of the investigations. In a first stage, extensive measurements of length, temperature and weight lasting up to 5 days allowed the study of the post moulding dimensional behaviour of the part. Measurements of length and temperature in the initial minutes after moulding were performed to estimate the apparent CTE to be used in the compensation of thermal effects. Measurements of weight variation showed a power law increment not followed by a dimensional increment; possible cause was identified in the superposition of opposite factors. The hygroscopic swelling could be investigated only from variation due to ambient humidity changes occurring during the tests. A further instability due to residual stresses relaxation was recognized only by long term (several days) length measurements and its amplitude summarized by a logarithmic decreasing curve. After these initial tests a customized DLM methodology for post moulding dimensional control has been proposed: thermal effect could be compensated after the calculation of an apparent CTE from measurement of length and temperature in the first 15

minutes after moulding; post moulding moisture uptake could be predicted using a power law model and hygroscopic swelling was considered with a predetermined CME; residual stresses could be compensated using the logarithmic trends previously defined.

The methodology proposed has been validated on newly produced parts. The measurements performed within one hour from moulding were used for the extrapolation of the length at reference conditions at any time after production, achieving accuracies in the order of 11 μm . The extrapolated length was successfully compared with measurements performed 6 and 12 weeks after production.

7.2 Conclusions

This PhD project had the purpose of investigating the experimental aspects of the newly conceived methodology of Dynamic Length Metrology. The main results achieved with this work can be summarized as:

- Three unconventional pieces of equipment have been tested focusing on the possibility to be implemented in DLM. The measurement accuracy of a linear actuator, intended for dimensional measurements with adjustable force, has been estimated equal to 0.5 μm . A MLWI system for absolute interferometric measurements provided measurement accuracies better than 0.06 μm . A thermal imager proved to be useful for investigation of temperature fields in time transient conditions with an error of about 0.5 $^{\circ}\text{C}$.
- The main sources of dimensional instability in polymer components have been investigated to propose a series of general guidelines for their compensation. Elastic deformation due to contact force can be compensated with a DLM approach with the adjustable force system investigated above, providing a correct local contact model. CTE can be successfully estimated with measurements of the post moulding cooling, namely in the first 10 minutes after moulding. The strategy for measuring the temperature must take into consideration the temperature field present in the workpiece. Moisture absorption emerged to be the most difficult aspect to consider. Moisture uptake can be measured via a gravimetric method and compensated using DLM if a specific condition is known, i.e. completely dry condition as in the case of a part after injection moulding. Moreover as the absorption takes more than one day a DLM approach with a fast post moulding measurement may be insufficiently accurate.
- Two optical solutions employing a vision system have been proposed and validated. A method for absolute and directly traceable length measurement based on edge detection has been investigated using an ideal workpiece (optical scale) and industrial injection moulded parts; measurement repeatability of 2 and 3 μm respectively has been achieved. A method based on DIC for displacement measurements provided uncertainties lower than 0.6 μm when measuring thermal displacements on polymer parts.

- DLM method has been applied to post moulding measurements of an industrial component. Thermal effects and hygroscopic swelling have been successfully considered in a DLM length prediction. Shrinkage due to residual stresses lasted for several weeks and has been addressed using a conventional compensation method. A hybrid DLM/conventional prediction algorithm provided 11 μm result accuracies.
- The DLM methodology for length prediction from measurement in non-stable conditions showed both strengths and weaknesses. Two crucial aspects to consider are the time necessary for a particular instability source to expire and the necessity to have information on a specific state to perform the prediction. The first aspect is important for the definition of the measuring time necessary to obtain an accurate prediction model. If an instability source undergoes to excessively rapid changes the measurement result will be inaccurate, such as in the case of very fast and non-uniform cooling. In contrast, several days long shrinking of the workpiece requires the measuring time to be inconveniently long for detecting such change. The second aspect is crucial especially in the treatment of hygroscopic swelling. Temperature and time after production can be measured directly on the workpiece for defining the workpiece state in relation to thermal expansion and shrinkage. Instead, the absolute moisture content cannot be measured directly on the part. A hybrid solution, similar to the one developed for an industrial case, is therefore a valid alternative, especially in the case of injection moulded polymer parts.
- Based on the results achieved in this work the following methodology is proposed for dimensional control of injection moulded parts using a DLM approach:
 - Few minutes after production the length and temperature of a component is measured. Based on the thermal boundary and initial conditions the measuring time varies indicatively between 2 and 10 minutes. The apparent CTE is successively estimated and thermal expansion can be compensated.
 - Elastic deformation in the case of contact measurement can be tackled in two different ways: static conventional compensation using nominal values of force and Young modulus or extrapolation of unreformed length from measurement at different contact forces.
 - The post moulding measurements consist of length and weight measurements for indicatively one hour. The data collected is fitted with an exponential regression model and the saturation condition can be extrapolated from the regression. An important assumption is that the injection moulding produces completely dry components, which must absorb a negligible quantity of moisture before the measurement; consequently the first data point refers to the dry condition. The length in saturated condition at 50 % ambient humidity is estimated considering a fraction of the hygroscopic swelling occurring between initial dry condition and saturated state at the measuring ambient condition. Alternatively a conventional

compensation can be applied by knowing the hygroscopic swelling occurring between dry state and saturated state at RH 50 %.

- Shrinkage, as it is a slow mechanism, can be compensated only using conventional methods. Hence a preliminary test is necessary to determine dimensional instability during several days after production (indicatively one week). The data can be fitted to determine a trend model line which can be used to compensate any measurement performed in an early stage after production.

In any case the design of a new DLM platform employing the described methodology requires some preliminary studies to identify the overall behaviour of the component, concerning apparent material properties and time constants of the different instability mechanisms, necessary to tune the various regressions in the data processing.

- In the case of metallic workpieces the DLM methodology can be applied directly since it considers only the first two bullet points of the methodology described above. The measuring time may differ as the initial thermal state in metallic parts and its evolution over time is different compared to polymer parts.

7.3 Outlook

This work and the experimental investigations reported contributed to the development of dimensional metrology in industrial environments, with particular focus on the injection moulding industry. Further research, involving experimental work and simulations, should be carried out as described as follow.

- Thermomechanical simulations have briefly been introduced as a valid alternative to preliminary investigations. The design of measuring equipment and the definition of measuring strategies can benefit from results from numerical simulations. Hence simulations, involving 3D thermal, mechanical, hygroscopic models should be studied for complex or simple geometries. A database containing general guidelines for probing strategies as a function of workpiece geometry and material properties can be created based on simulated results.
- Even though workpieces made out of metal have less sources of instability (i.e. thermal effect), different problems arise, such as the difficulties of estimating the volumetric temperature field from surface temperature measurements due to generally thicker components (compared to polymer parts), the much higher thermal input to the measuring equipment due to the greater amount heat exchanged and the necessity of obtaining lower measurement uncertainties. Studies on metallic parts should be performed with attention to thermal issues. Different probing strategies (position and number of temperature sensors) should be investigated in order to reduce the prediction uncertainty. The field of thermal error compensa-

tion in CMM and machine tools can provide suggestion and inspiration for both experimental work and data processing.

- Temperature influences on polymer workpieces have been investigated with successful results; in fact thermal deformations can be measured and compensated if a sufficiently slow cooling occurs (i.e. cooling time longer than 10 minutes). Slower instabilities, like stress relaxation deformations could not be addressed with a DLM methodology. Experimental work on hygroscopic effects and shrinkage should be performed to further investigate the applicability of a DLM compensation (i.e. without previous knowledge of material behaviour).
- The potential of infrared temperature measurements is vast since they do not require stitching of any sensor on the part surface and the study described in this work does not provide promising performance regarding measurement accuracy. However a deeper investigation should be performed in order to investigate different error sources (ambient temperature, different material emissivity) and to develop a complete characterization of the technology and eventually propose an error compensation algorithm.
- From an industrial point of view it may be relevant to study the applicability of DLM to existing measuring solutions like CMM. A study case should be developed using a CMM instead of inductive probes as length measuring systems. The possibility of having a measuring strategy with several measuring points should be investigated as well as the possibility of performing batch measurements. The issue of non-synchronous multipoint measurements must be studied.

Bibliography

- [1] H. Kunzmann, T. Pfeifer, and R. Schmitt, Productive metrology-Adding value to manufacture, *CIRP Ann. - Manuf. Technol.*, vol. 54, no. 2, pp. 155–168, 2005.
- [2] L. De Chiffre, The role of metrology in modern manufacturing, in *Annals of MTeM for 2007 & Proceedings of the 8th International MTeM Conference*, 2007, pp. 1–6.
- [3] E. Savio, L. De Chiffre, S. Carmignato, and J. Meinertz, Economic benefits of metrology in manufacturing, *CIRP Ann. - Manuf. Technol.*, vol. 65, no. 1, pp. 495–498, 2016.
- [4] ISO 1:2016 Geometrical product specifications (GPS) - Standard reference temperature for the specification of geometrical and dimensional properties. 2016.
- [5] ISO 291:2008 Plastics – Standard atmospheres for conditioning and testing. 2008.
- [6] Mahr solution - Our vision - Mahr metrology. [Online]. Available: <https://www.mahr.com/en-us/Services/Production-metrology/Products/MarSolution---Our-Visions/#DownloadBox>. [Accessed: 21-Aug-2017].
- [7] A. Weckenmann, X. Jiang, K. D. Sommer, U. Neuschaefer-Rube, J. Seewig, L. Shaw, and T. Estler, Multisensor data fusion in dimensional metrology, *CIRP Ann. - Manuf. Technol.*, vol. 58, no. 2, pp. 701–721, 2009.
- [8] L. De Chiffre, H. N. Hansen, J. H. Hattel, D. González-Madruga, G. Dalla Costa, M. R. Sonne, and A. Mohammadi, Dynamic Length Metrology (DLM) for measurements with sub-micrometre uncertainty in a production environment, in *Proceedings of euspen's 16th International Conference & Exhibition*, 2016.
- [9] L. De Chiffre, M. M. Gudnason, and D. Gonzalez-Madruga, Dimensional measurements with submicrometres uncertainty in production environment, in *Proceedings of euspen's 16th International Conference & Exhibition*, 2015.
- [10] ISO 14253-2:2011 Geometrical product specifications (GPS) – Inspection by measurement of workpieces and measuring equipment – Part 2: Guidance for the estimation of uncertainty in GPS measurement, in calibration of measuring equipment and in product verif. 2011.
- [11] ISO 8015:2011 Geometrical product specifications (GPS) – Fundamentals – Concepts, principles and rules. 2011.
- [12] ISO 62:2008 Plastics - Determination of water absorption, 2008.
- [13] W. R. Vieth, *Diffusion in and through polymers: principles and applications*. Hanser Publishers, 1991.
- [14] D. A. Bond and P. A. Smith, Modeling the Transport of Low-Molecular-Weight Penetrants Within Polymer Matrix Composites, *Appl. Mech. Rev.*, vol. 59, no. 5, p. 249, 2006.
- [15] W. D. Callister and D. G. Rethwisch, *Materials science and engineering*. NY:

- John Wiley & Sons, 2011.
- [16] T. Doiron and J. Beers, The gauge block handbook, *NIST Monogr.*, vol. 180, 2005.
 - [17] D. Bashford, *Thermoplastics*. Springer Science & Business Media, 1997.
 - [18] J. Zhou and J. S. Law, Effect of non-uniform moisture distribution on the hygroscopic swelling coefficient, *IEEE Trans. Components Packag. Technol.*, vol. 31, no. 2, pp. 269–276, Jun. 2008.
 - [19] E. Stellrecht, B. Han, and M. G. Pecht, Characterization of Hygroscopic Swelling Behavior of Mold Compounds and Plastic Packages, *IEEE Trans. components Packag. Technol.*, vol. 27, no. 3, pp. 499–506, 2004.
 - [20] K. L. Johnson, *Contact mechanics*. Cambridge University Press, 1987.
 - [21] J. C. Gerdeen and R. A. L. Rorrer, *Engineering design with polymers and composites*. CRC press, 2011.
 - [22] D. Annicchiarico and J. R. Alcock, Review of Factors that Affect Shrinkage of Molded Part in Injection Molding, *Mater. Manuf. Process.*, vol. 29, no. 6, pp. 662–682, Jun. 2014.
 - [23] B. Ozcelik and T. Erzurumlu, Comparison of the warpage optimization in the plastic injection molding using ANOVA, neural network model and genetic algorithm, *J. Mater. Process. Technol.*, vol. 171, no. 3, pp. 437–445, Feb. 2006.
 - [24] A. Weckenmann, T. Estler, G. Peggs, and D. McMurtry, Probing Systems in Dimensional Metrology, *CIRP Ann. - Manuf. Technol.*, vol. 53, no. 2, pp. 657–684, 2004.
 - [25] ISO 15530-3:2011 Geometrical product specifications (GPS) - Coordinate measuring machines (CMM): Technique for determining the uncertainty of measurement - Part 3: Use of calibrated workpieces or measurement standards, 2011.
 - [26] Brown & Sharpe TESA Catalog. [Online]. Available: <http://go.hexagonmi.com/1/49752/2016-06-06/39djby>. [Accessed: 29-Aug-2017].
 - [27] LVDT AND HBT MINIATURE MEASURING CELLS. [Online]. Available: http://www.marposs.com/product.php/eng/small_gauging_cell. [Accessed: 29-Aug-2017].
 - [28] H. Kunzmann, T. Pfeifer, and J. Flügge, Scales vs. Laser Interferometers Performance and Comparison of Two Measuring Systems, *CIRP Ann. - Manuf. Technol.*, vol. 42, no. 2, pp. 753–767, 1993.
 - [29] Length gauges. [Online]. Available: https://www.heidenhain.com/en_US/products/length-gauges/. [Accessed: 29-Aug-2017].
 - [30] Linear actuator. [Online]. Available: <http://www.smac-mca.com/products/linear-actuators>. [Accessed: 29-Aug-2017].
 - [31] ISO 10360-1:2000 Geometrical Product Specifications (GPS) - Acceptance and reverification tests for coordinate measuring machines (CMM) - Part 1: Vocabulary, 2000.
 - [32] R. K. Leach, *Fundamental principles of engineering nanometrology*. Elsevier, 2014.
 - [33] E. Savio, L. De Chiffre, and R. Schmitt, Metrology of freeform shaped parts, *CIRP Ann. - Manuf. Technol.*, vol. 56, no. 2, pp. 810–835, 2007.
 - [34] A. Balsamo, D. Marques, and S. Sartori, Method for thermal-deformation correction of CMMs, *CIRP Ann. - Manuf. Technol.*, vol. 39, no. 1, pp. 557–560, 1990.
 - [35] J. P. Kruth, P. Vanherck, C. Van Den Bergh, and B. Schacht, Interaction between

- workpiece and CMM during geometrical quality control in non-standard thermal conditions, *Precis. Eng.*, vol. 26, no. 1, pp. 93–98, 2002.
- [36] R. G. Wilhelm, R. Hocken, and H. Schwenke, Task specific uncertainty in coordinate measurement, *CIRP Ann. - Manuf. Technol.*, vol. 50, no. 2, pp. 553–563, 2001.
- [37] J. Śladek, *Coordinate metrology: accuracy of systems and measurements*. Springer, 2015.
- [38] H. Schwenke, U. Neuschaefer-Rube, T. Pfeifer, and H. Kunzmann, Optical Methods for Dimensional Metrology in Production Engineering, *CIRP Ann. - Manuf. Technol.*, vol. 51, no. 2, pp. 685–699, 2002.
- [39] A. Weckenmann, G. Peggs, and J. Hoffmann, Probing systems for dimensional micro- and nano-metrology, *Meas. Sci. Technol.*, vol. 17, no. 3, pp. 504–509, 2006.
- [40] J. Beraldin, M. Rioux, L. Cournoyer, F. Blais, M. Picard, and J. Pekelsky, Traceable 3D Imaging Metrology, *Proc. SPIE*, vol. 6491, no. October, 2007.
- [41] G. Berkovic and E. Shafir, Optical methods for distance and displacement measurements, *Adv. Opt. Photonics*, vol. 4, pp. 441–471, 2012.
- [42] Optical sensor for non-contact linear measurements. [Online]. Available: http://www.marposs.com/product.php/eng/optical_probing_system. [Accessed: 29-Aug-2017].
- [43] B. Edlén, The Refractive Index of Air, *Metrologia*, vol. 2, no. 2, p. 71, 1966.
- [44] D. J. Whitehouse, *Handbook of Surface and Nanometrology*, vol. 49, no. 5. CRC press, 2010.
- [45] H. J. Tiziani and G. Pedrini, From speckle pattern photography to digital holographic interferometry, *Appl. Opt.*, vol. 52, no. 1, pp. 30–44, 2013.
- [46] G. Pedrini, W. Osten, and M. E. Gusev, High-speed digital holographic interferometry for vibration measurement, *Appl. Opt.*, vol. 45, no. 15, pp. 3456–3462, 2006.
- [47] J. a Leendertz, Interferometric displacement measurement on scattering surfaces utilizing speckle effect, *J. Phys. E.*, vol. 3, no. 3, pp. 214–218, 2002.
- [48] R. Leach, *Optical measurement of surface topography*. Springer, 2011.
- [49] K. Meiners-Hagen, R. Schödel, F. Pollinger, and A. Abou-Zeid, Multi-Wavelength Interferometry for Length Measurements Using Diode Lasers, *Meas. Sci. Rev.*, vol. 9, no. 1, pp. 16–26, 2009.
- [50] Non-contact 3D Optical Profilers, 2016. [Online]. Available: <http://www.taylor-hobson.com/products/34/109.html>. [Accessed: 28-Aug-2017].
- [51] XL-80 Laser system. [Online]. Available: <http://www.renishaw.com/en/xl-80-laser-system--8268>. [Accessed: 28-Aug-2017].
- [52] Length and angle measurement systems - SIOS Messtechnik. [Online]. Available: <http://www.sios-de.com/products/length-and-angle-measurement-systems/>.
- [53] W. T. Estler, K. L. Edmundson, G. N. Peggs, and D. H. Parker, Large-Scale Metrology – An Update, *CIRP Ann. - Manuf. Technol.*, vol. 51, no. 2, pp. 587–609, 2002.
- [54] H. Schwenke, M. Franke, J. Hannaford, and H. Kunzmann, Error mapping of CMMs and machine tools by a single tracking interferometer, *CIRP Ann. - Manuf. Technol.*, vol. 54, no. 1, pp. 475–478, 2005.
- [55] G. N. Peggs, P. G. Maropoulos, E. B. Hughes, A. B. Forbes, S. Robson, M. Ziebart, and B. Muralikrishnan, Recent developments in large-scale dimensional metrology, *Proc. Inst. Mech. Eng. Part B J. Eng. Manuf.*, vol. 223, pp. 571–595, 2009.

- [56] H. N. Hansen, K. Carneiro, H. Haitjema, and L. De Chiffre, Dimensional micro and nano metrology, *CIRP Ann. - Manuf. Technol.*, vol. 55, no. 2, pp. 721–743, 2006.
- [57] G. Y. Sirat, Conoscopic holography. I. Basic principles and physical basis, *J. Opt. Soc. Am. A*, vol. 9, no. 1, p. 70, 1992.
- [58] 3D Non contact measurements - Optimet. [Online]. Available: <http://www.optimet.com/>. [Accessed: 28-Aug-2017].
- [59] L. M. Galantucci, E. Piperi, F. Lavecchia, and A. Zhavo, Semi-automatic Low Cost 3D Laser Scanning Systems for Reverse Engineering, *Procedia CIRP*, vol. 28, pp. 94–99, 2015.
- [60] S. Martinez, E. Cuesta, J. Barreiro, and B. Alvarez, Analysis of laser scanning and strategies for dimensional and geometrical control, *Int. J. Adv. Manuf. Technol.*, vol. 46, no. 5–8, pp. 621–629, 2010.
- [61] 3shape - Digital Solutions for Orthodontic Labs. [Online]. Available: <http://www.3shape.com/>. [Accessed: 21-Aug-2017].
- [62] Precise Industrial 3D Metrology. [Online]. Available: <http://www.gom.com/>. [Accessed: 01-Jan-2017].
- [63] L. M. Galantucci, M. Pesce, and F. Lavecchia, A powerful scanning methodology for 3D measurements of small parts with complex surfaces and sub millimeter-sized features, based on close range photogrammetry, *Precis. Eng.*, vol. 43, pp. 211–219, 2016.
- [64] J. Shmueli, M. A. Eder, and A. Tesauero, A versatile stereo photogrammetry based technique for measuring fracture mode displacements in structures, *Precis. Eng.*, vol. 39, pp. 38–46, 2015.
- [65] L. M. Galantucci, M. Pesce, and F. Lavecchia, A stereo photogrammetry scanning methodology, for precise and accurate 3D digitization of small parts with sub-millimeter sized features, *CIRP Ann. - Manuf. Technol.*, vol. 64, no. 1, pp. 507–510, 2015.
- [66] T. Luhmann, Close range photogrammetry for industrial applications, *ISPRS J. Photogramm. Remote Sens.*, vol. 65, no. 6, pp. 558–569, 2010.
- [67] B. Pan, K. Qian, H. Xie, and A. Asundi, Two-dimensional digital image correlation for in-plane displacement and strain measurement: a review, *Meas. Sci. Technol.*, vol. 20, pp. 1–17, 2009.
- [68] P.-C. Hung and a. S. Voloshin, In-plane strain measurement by digital image correlation, *J. Brazilian Soc. Mech. Sci. Eng.*, vol. 25, no. 3, pp. 215–221, 2003.
- [69] R. Montanini and F. Freni, Non-contact measurement of linear thermal expansion coefficients of solid materials by infrared image correlation, *Meas. Sci. Technol.*, vol. 25, no. 1, p. 15013, 2014.
- [70] M. Pesce, L. M. Galantucci, G. Percoco, and F. Lavecchia, A Low-cost Multi Camera 3D Scanning System for Quality Measurement of Non-static Subjects, in *Procedia CIRP*, 2015, vol. 28, pp. 88–93.
- [71] D. C. Brown, Close-range camera calibration, *Photogrammetric Engineering*, vol. 37, no. 8, pp. 855–866, 1971.
- [72] Z. Zhang, A Flexible New Technique for Camera Calibration (Technical Report), *IEEE Trans. Pattern Anal. Mach. Intell.*, vol. 22, no. 11, pp. 1330–1334, 2002.
- [73] J. Angelo Beraldin, D. Mackinnon, and L. Cournoyer, Metrological characterization of 3D imaging systems: progress report on standards developments, in *17th International Congress of Metrology*, 2015.
- [74] B. Jahne, *Computer vision and applications: a guide for students and practitioners*. Academic Press, 2000.

- [75] Orbit - Digital measuring network - catalogue. [Online]. Available: <http://online.pubhtml5.com/mnpj/vfjo/index.html>. [Accessed: 21-Aug-2017].
- [76] Laser displacement sensors (triangulation). [Online]. Available: <http://www.micro-epsilon.com/displacement-position-sensors/laser-sensor/>. [Accessed: 21-Aug-2017].
- [77] ISO 25178-602:2010 Geometrical product specifications (GPS) – Surface texture: Areal – Part 602: Nominal characteristics of non-contact (confocal chromatic probe) instruments, 2010.
- [78] H. Nouira, N. El-Hayek, X. Yuan, and N. Anwer, Characterization of the main error sources of chromatic confocal probes for dimensional measurement, *Meas. Sci. Technol.*, vol. 25, no. 4, p. 44011, 2014.
- [79] G. Percoco, F. Lavecchia, and A. J. S. Salmerón, Preliminary study on the 3D digitization of millimeter scale products by means of photogrammetry, *Procedia CIRP*, vol. 33, pp. 257–262, 2015.
- [80] G. Percoco and A. J. Sánchez Salmerón, Photogrammetric measurement of 3D freeform millimetre-sized objects with micro features: an experimental validation of the close-range camera calibration model for narrow angles of view, *Meas. Sci. Technol.*, vol. 26, no. 9, p. 95203, 2015.
- [81] I. Toschi, E. Nocerino, M. Hess, F. Menna, B. Sargeant, L. MacDonald, F. Remondino, and S. Robson, Improving automated 3D reconstruction methods via vision metrology, in *Proc. of SPIE*, 2015, vol. 9528, p. 95280H.
- [82] L. Carli, G. Genta, a Cantatore, G. Barbato, L. De Chiffre, and R. Levi, Uncertainty evaluation for three-dimensional scanning electron microscope reconstructions based on the stereo-pair technique, *Meas. Sci. Technol.*, vol. 22, no. 3, p. 35103, 2011.
- [83] J. D. Barnfather, M. J. Goodfellow, and T. Abram, Photogrammetric measurement process capability for metrology assisted robotic machining, *Measurement*, vol. 78, pp. 29–41, 2016.
- [84] L. M. Galantucci, F. Lavecchia, G. Percoco, and S. Raspatelli, New method to calibrate and validate a high-resolution 3D scanner, based on photogrammetry, *Precis. Eng.*, vol. 38, no. 2, pp. 279–291, 2014.
- [85] J. Kaufman, A. E. W. Rennie, and M. Clement, Reverse Engineering Using Close Range Photogrammetry for Additive Manufactured Reproduction of Egyptian Artefacts and Other Objets d’art, *J. Comput. Inf. Sci. Eng.*, vol. 15, p. 11006, 2015.
- [86] T. Luhmann, S. Robson, S. Kyle, and I. Harley, *Close Range Photogrammetry Principles, techniques and applications*. Whittles Publishing, 2006.
- [87] M. J. Smith and E. Cope, The Effects of Temperature Variation on Single-Lens-Reflex Digital Camera Calibration Parameters, vol. 38, no. 5, pp. 554–559, 2010.
- [88] H. González-Jorge, B. Riveiro, J. Armesto, and P. Arias, Verification artifact for photogrammetric measurement systems, *Opt. Eng.*, vol. 50, no. 7, p. 73603, 2011.
- [89] L. Galantucci, G. Percoco, and R. Ferrandes, Accuracy Issues of Digital Photogrammetry for 3D Digitization of Industrial Products, *Rev. Int. Ing. Numer.*, vol. 2, no. 1–2, pp. 29–40, 2006.
- [90] B. Triggs, P. F. McLauchlan, R. I. Hartley, and A. W. Fitzgibbon, Bundle Adjustment — A Modern Synthesis, in *Vision Algorithms: Theory and Practice: International Workshop on Vision Algorithms*, 2000, vol. 1883, pp. 298–372.
- [91] L. M. Galantucci, F. Lavecchia, and G. Percoco, Multistack Close Range Photogrammetry for Low Cost Submillimeter Metrology, *J. Comput. Inf. Sci. Eng.*, vol. 13, no. 4, p. 44501, 2013.

- [92] M. Bornert, F. Bremand, P. Doumalin, J. C. Dupre, M. Fazzini, M. Grédiac, F. Hild, S. Mistou, J. Molimard, J. J. Orteu, L. Robert, Y. Surrel, P. Vacher, and B. Wattrisse, Assessment of digital image correlation measurement errors: Methodology and results, *Exp. Mech.*, vol. 49, no. 3, pp. 353–370, 2009.
- [93] B. Gorny, T. Niendorf, J. Lackmann, M. Thoene, T. Troester, and H. J. Maier, In situ characterization of the deformation and failure behavior of non-stochastic porous structures processed by selective laser melting, *Mater. Sci. Eng. A*, vol. 528, no. 27, pp. 7962–7967, 2011.
- [94] P. Bing, X. Hui-min, X. Bo-qin, and D. Fu-long, Performance of sub-pixel registration algorithms in digital image correlation, *Meas. Sci. Technol.*, vol. 17, no. 6, pp. 1615–1621, 2006.
- [95] S. Ma, J. Pang, and Q. Ma, The systematic error in digital image correlation induced by self-heating of a digital camera, *Meas. Sci. Technol.*, vol. 23, no. 2, p. 25403, 2012.
- [96] G. Crammond, S. W. Boyd, and J. M. Dulieu-Barton, Speckle pattern quality assessment for digital image correlation, *Opt. Lasers Eng.*, vol. 51, no. 12, pp. 1368–1378, 2013.
- [97] L. De Chiffre and H. N. Hansen, Metrological Limitations of Optical Probing Techniques, *CIRP Ann. - Manuf. Technol.*, vol. 44, no. 1, pp. 501–504, 1995.
- [98] Zeiss O-INSPECT - Multisensor CMM. [Online]. Available: <https://www.zeiss.com/metrology/products/systems/optical-systems/o-inspect.html>. [Accessed: 28-Aug-2017].
- [99] R. Christoph and H. J. Neumann, *Multisensor Coordinate Metrology: Measurement of Form, Size, and Location in Production and Quality Control*. Verlag Moderne Industrie, 2004.
- [100] DS/ISO/IEC Guide 99 - International vocabulary of metrology – Basic and general concepts and associated terms (VIM), 2008.
- [101] ISO 3650:1998. Geometrical Product Specifications (GPS) -- Length standards -- Gauge blocks.
- [102] E. Savio and L. De Chiffre, An artefact for traceable freeform measurements on coordinate measuring machines, *Precis. Eng.*, vol. 26, no. 1, pp. 58–68, 2002.
- [103] Optical Dimensional Standard. [Online]. Available: <http://www.npl.co.uk/measurement-services/dimensional/optical-dimensional-standard>. [Accessed: 07-Sep-2017].
- [104] A. Vissiere, H. Nouria, M. Damak, O. Gibaru, and J.-M. David, Concept and architecture of a new apparatus for cylindrical form measurement with a nanometric level of accuracy, *Meas. Sci. Technol.*, vol. 23, no. 9, p. 94014, 2012.
- [105] J. Bryan, International Status of Thermal Error Research (1990), *CIRP Ann. - Manuf. Technol.*, vol. 39, no. 2, pp. 645–656, 1990.
- [106] D. G. Chetwynd, Selection of structural materials for precision devices, *Precis. Eng.*, vol. 9, no. 1, pp. 3–6, 1987.
- [107] G. N. Peggs, a. J. Lewis, and S. Oldfield, Design for a Compact High-Accuracy CMM, *CIRP Ann. - Manuf. Technol.*, vol. 48, no. 1, pp. 417–420, 1999.
- [108] U. Brand and J. Kirchhoff, A micro-CMM with metrology frame for low uncertainty measurements, *Meas. Sci. Technol.*, vol. 16, no. 12, pp. 2489–2497, 2005.
- [109] J. Piot, J. Qian, and H. Pirée, Design of a thermally and mechanically stable metrological atomic force microscope at KULeuven, in *Proceedings of euspen's 9th International Conference & Exhibition*, 2009, pp. 2–5.
- [110] J. Mayr, J. Jedrzejewski, E. Uhlmann, M. Alkan Donmez, W. Knapp, F. Härtig, K.

- Wendt, T. Moriwaki, P. Shore, R. Schmitt, C. Brecher, T. Würz, and K. Wegener, Thermal issues in machine tools, *CIRP Ann. - Manuf. Technol.*, vol. 61, no. 2, pp. 771–791, 2012.
- [111] A. Jakstas, S. Kausinis, R. Barauskas, A. Kasparaitis, and A. Barakauskas, Thermal error analysis in precision length measurements, *Meas. J. Int. Meas. Confed.*, vol. 51, no. 1, pp. 133–146, 2014.
- [112] A. Gameros, S. Lowth, D. Axinte, A. Nagy-Sochacki, O. Craig, and H. R. Siller, State-of-the-art in fixture systems for the manufacture and assembly of rigid components: A review, *Int. J. Mach. Tools Manuf.*, vol. 123, pp. 1–21, 2017.
- [113] Metrology fixtures. [Online]. Available: <http://www.renishaw.com/en/metrology-fixtures--20748>. [Accessed: 20-Sep-2017].
- [114] Fixturing Systems. [Online]. Available: <https://www.zeiss.com/metrology/products/accessories/fixture-systems.html>. [Accessed: 20-Sep-2017].
- [115] G. Halevi and R. Weill, *Principles of process planning: a logical approach*. Springer Science & Business Media, 2012.
- [116] M. Down, F. Czubak, G. Gruska, S. Stahley, and D. Benham, *Measurements systems analysis reference manual*. General Motors Corporation, United States, Ford Motor Company, 2010.
- [117] J. Fraden, *Handbook of modern sensors: Physics, designs, and applications*. Springer, 2016.
- [118] D. R. Tobergte and S. Curtis, *Springer Handbook of Metrology and Testing*, vol. 53, no. 9. Springer, 2013.
- [119] L. Michalski, K. Eckersdorf, and J. McGhee, *Temperature Measurement*, vol. 9. John Wiley & Sons, 2001.
- [120] J. V. Nicholas and D. R. White, *Traceable Temperatures: An Introduction to Temperature Measurement and Calibration*. John Wiley & Sons, 2002.
- [121] IEC 60751 - Industrial platinum resistance thermometers and platinum temperature sensors, 2008.
- [122] DS/EN 60584-1 - Thermocouples – Part 1: EMF specifications and tolerances, 2014.
- [123] M. Vollmer and K.-P. Möllmann, *Infrared Thermal Imaging: Fundamentals, Research and Applications*. John Wiley & Sons, 2010.
- [124] W. Minkina and S. Dudzik, *Infrared Thermography*. John Wiley & Sons, 2009.
- [125] M. Honner and P. Honnerová, Survey of emissivity measurement by radiometric methods, *Appl. Opt.*, vol. 54, no. 4, p. 669, 2015.
- [126] L. del Campo, R. B. Pérez-Sáez, L. González-Fernández, X. Esquisabel, I. Fernández, P. González-Martín, and M. J. Tello, Emissivity measurements on aeronautical alloys, *J. Alloys Compd.*, vol. 489, no. 2, pp. 482–487, 2010.
- [127] R. P. Madding, Emissivity measurement and temperature correction accuracy considerations, in *Spie Conference on Thermosense XXI*, 1999, vol. 3700, pp. 393–401.
- [128] C. A. Balaras and A. A. Argiriou, Infrared thermography for building diagnostics, *Energy Build.*, vol. 34, no. 2, pp. 171–183, 2002.
- [129] S. Bagavathiappan, B. B. B. Lahiri, T. Saravanan, J. Philip, and T. Jayakumar, Infrared thermography for condition monitoring - A review, *Infrared Phys. Technol.*, vol. 60, pp. 35–55, 2013.
- [130] B. Lane, E. Whitenton, V. Madhavan, and A. Donmez, Uncertainty of temperature measurements by infrared thermography for metal cutting applications, *Metrologia*, vol. 50, no. 6, pp. 637–653, 2013.

- [131] M. San Juan, O. Martín, F. J. Santos, P. De Tiedra, F. Daroca, and R. López, Application of thermography to analyse the influence of the deformation speed in the forming process, in *Procedia Engineering*, 2013, vol. 63, pp. 821–828.
- [132] G. Grgić and I. Pušnik, Analysis of thermal imagers, *Int. J. Thermophys.*, vol. 32, no. 1–2, pp. 237–247, 2011.
- [133] P. R. Muniz, R. de Araújo Kalid, S. P. N. Cani, and R. da Silva Magalhães, Handy method to estimate uncertainty of temperature measurement by infrared thermography, *Opt. Eng.*, vol. 53, no. 7, p. 74101, 2014.
- [134] W. Minkina and S. Dudzik, Simulation analysis of uncertainty of infrared camera measurement and processing path, *Meas. J. Int. Meas. Confed.*, vol. 39, no. 8, pp. 758–763, 2006.
- [135] ISO/IEC Guide 98-3:2008. Uncertainty of measurement – Part 3: Guide to the expression of uncertainty in measurement, 2008.
- [136] G. Genta, A. Germak, G. Barbato, and R. Levi, Metrological characterization of an hexapod-shaped Multicomponent Force Transducer, *Meas. J. Int. Meas. Confed.*, vol. 78, pp. 202–206, 2016.
- [137] EA-4/02 M:2013. Evaluation of the uncertainty of measurement in calibration.
- [138] G. Barbato, A. Germak, and G. Genta, *Measurements for decision making*. Bologna: Società Editrice Esculapio, 2013.
- [139] J. Petter and G. Berger, Non-contact profiling for high precision fast asphere topology measurement, *Proc. SPIE*, vol. 8788, p. 878819, 2013.
- [140] ASTM E831 - 14 Standard Test Method for Linear Thermal Expansion of Solid Materials by Thermomechanical Analysis, 2014.
- [141] ASTM D696 - 16 Standard Test Method for Coefficient of Linear Thermal Expansion of Plastics Between -30°C and 30°C with a Vitreous Silica Dilatometer.
- [142] R. Schödel, Ultra-high accuracy thermal expansion measurements with PTB's precision interferometer, *Meas. Sci. Technol.*, vol. 19, no. 8, p. 84003, 2008.
- [143] V. G. Badami and M. Linder, Ultra-High Accuracy Measurement of the Coefficient of Thermal Expansion for Ultra-Low Expansion Materials, *SPIE Conf.*, vol. 4688, no. 585, pp. 469–480, 2002.
- [144] R. Jedamzik, T. Döhring, T. Johansson, P. Hartmann, and T. Westerhoff, CTE characterization of ZERODUR for the ELT century, *Proc. SPIE*, vol. 7425, p. 742504, 2009.
- [145] J. D. James, J. A. Spittle, S. G. R. Brown, and R. W. Evans, A review of measurement techniques for the thermal expansion coefficient of metals and alloys at elevated temperatures, *Meas. Sci. Technol.*, vol. 12, no. 3, pp. R1–R15, 2001.
- [146] H. Pranjoto and D. D. Denton, Gravimetric Measurements of Steady-State Moisture Uptake in Spin-Coated Polyimide Films, *J. Appl. Polym. Sci.*, vol. 42, no. 1, pp. 75–83, 1991.
- [147] J. R. Parker, *Algorithms for Image Processing and Computer Vision*. John Wiley & Sons, 2010.
- [148] M. Sharifi, M. Fathy, and M. T. Mahmoudi, A classified and comparative study of edge detection algorithms, *Proceedings. Int. Conf. Inf. Technol. Coding Comput.*, pp. 5–8, 2002.
- [149] W. Burger and M. Burge, *Digital image processing: an algorithmic introduction using Java*. Springer, 2016.
- [150] J. G. R. Espino, J.-J. Gonzalez-Barbosa, R. A. G. Loenzo, D. M. C. Esparza, and R. Gonzalez-Barbosa, Vision System for 3D Reconstruction with Telecentric Lens, in *MCPR*, 2012, pp. 127–136.

- [151] D. Lanman, D. C. Hauagge, and G. Taubin, Shape from depth discontinuities under orthographic projection, *Comput. Vis. Work. (ICCV Work. 2009 IEEE 12th Int. Conf.)*, pp. 1550–1557, 2009.
- [152] D. Li and J. Tian, An accurate calibration method for a camera with telecentric lenses, *Opt. Lasers Eng.*, vol. 51, no. 5, pp. 538–541, 2013.
- [153] L. Huiyang, C. Zhong, and Z. Xianmin, Calibration of camera with small FOV and DOF telecentric lens, in *IEEE International Conference on Robotics and Biomimetics*, 2013, pp. 498–503.
- [154] Juyang Weng, Camera calibration with distortion models and accuracy evaluation, *IEEE Trans. Pattern Anal. Mach. Intell.*, vol. 14, no. 10, pp. 965–980, 1992.
- [155] Z. Zhang, Flexible Camera Calibration By Viewing a Plane From Unknown Orientations, *Comput. Vision, 1999. Proc. 7th IEEE Int. Conf.*, vol. 1, pp. 666–673, 1999.

List of publications

- L. De Chiffre, D. Gonzalez-Madruga, G. Dalla Costa, L. C. Neves, and I. Jespersen, Accurate characterisation of post moulding shrinkage of polymer parts, in *Proceedings of euspen's 16th International Conference & Exhibition*, 2015.
- D. Gonzalez-Madruga, A. Alexiou, G. Dalla Costa, L. De Chiffre, and L. C. Neves, The influence of humidity on accuracy length measurement on polymer parts, in *Proceedings of euspen's 16th International Conference & Exhibition*, 2016.
- Mohammadi, M.R. Sonne, G. Dalla Costa, D. Gonzalez-Madruga, L. De Chiffre, and J.H. Hattel, Modelling the effect of probe force on length measurements on polymer parts, in *Proceedings of euspen's 16th International Conference & Exhibition*, 2016.
- G. Dalla Costa, D. Gonzalez-Madruga, L. De Chiffre, and H. N. Hansen, Length determination on industrial polymer parts from measurement performed under transient temperature conditions, in *Proceedings of euspen's 16th International Conference & Exhibition*, 2016.
- L. De Chiffre, H.N. Hansen, J.H. Hattel, D. Gonzalez-Madruga, G. Dalla Costa, M.R. Sonne, and A Mohammadi Dynamic Length Metrology (DLM) for measurements with sub-micrometre uncertainty in a production environment, in *Proceedings of euspen's 16th International Conference & Exhibition*, 2016.
- G. Dalla Costa, G. Genta, G. Barbato, L. De Chiffre, and H.N. Hansen, Accuracy assessment of an industrial actuator, in *Procedia CIRP*, Vol. 62, p. 417-422, 2016.
- G. Dalla Costa, D. Gonzalez-Madruga, and L. De Chiffre, Monitoring of the thermal deformations on polymer parts using a vision system, in *Proceedings of euspen's 17th International Conference & Exhibition*, 2017.
- M.R. Sonne, D. Gonzalez-Madruga, G. Dalla Costa, L. De Chiffre, A. Mohammadi, and J.H. Hattel, Inline temperature compensation for dimensional metrology of polymer parts in a production environment based on 3D thermomechanical analysis, *Precis. Eng.*, vol. 53, no. 1, pp. 46–53, 2018.
- G. Dalla Costa, D. Gonzalez-Madruga, and L. De Chiffre, Post moulding dimensional control of polymer components, in *Proceedings of euspen's 18th International Conference & Exhibition*, 2018.
- M.R. Sonne, A Mohammadi, G. Dalla Costa, D. Gonzalez-Madruga, L. De Chiffre, and J.H. Hattel, Considerations on numerical modelling for compensation of in-process metrology in manufacturing, in *Proceedings of euspen's 18th International Conference & Exhibition*, 2018.

Appendix A: Matlab codes

Camera calibration

```

%%%%%%%%%%%%%%%%%%%%%%%%%%%%%%%%%%%%%%%%%%%%%%%%%%%%%%%%%%%%%%%%%%%%%%%%%% Camera calibration from grid intersection
% Author= Giuseppe Dalla Costa
% date= 2017/02/01
% Description= finds the distortion of telecentric lenses using the points
%              from a calibrated grid. Method from:
%              Li Dong, and Jindong Tian
%              "An accurate calibration method for a camera with telecentric
lenses"
%              Optics and Lasers in Engineering 51.5 (2013): 538-541.
%              ONLY ROTATION AROUND Z IS CONSIDERED = grid normal to
%              optical axis
% Input: coordinates of grid intersections
% Output:  - axial rotation
%          - magnification
%          - decentering
%          - distortion correction coefficients
%          - maximum error from ideal grid considering/not considering
%          distortion correction
%%%%%%%%%%%%%%%%%%%%%%%%%%%%%%%%%%%%%%%%%%%%%%%%%%%%%%%%%%%%%%%%%%%%%%%%%%
clc
close all
clear all
%%
folder_name1 = uigetdir;
cd(folder_name1)
allFiles = dir( [folder_name1 '\*.mat']);
allNames = { allFiles.name };
n= length (allNames);
%%
calcoef1=zeros(16,n);
%%
for i=1:n
    clc
    %% Load calibration data
    FileName=char(allNames(i));
    load(FileName)
    %% Change picture coordinate system
    im=im(1:end-1,1:end-1);
    xx=xx(1:end-1,1:end-1)-381;
    yy=yy(1:end-1,1:end-1)-285;
    x_r=x_r-381;
    y_r=y_r-285;
    cx1=cx1-381;
    cy1=cy1-285;
    %% position of the points on the chessboard in the world coord. system (in µm)
    % first point on the board has coordinate (0,0)
    sq_dim=119.854; %dimensione chessboard element in µm from calibration certificate
    X=reshape(repmat((0:ncol-1),nrow,1),nrow*ncol,1)*sq_dim;
    Y=reshape(repmat((0:nrow-1)',1,ncol),nrow*ncol,1)*sq_dim;

    %% Firtst step of calibration: closed form solution
    % linear system
    M= [y_r.*X y_r.*Y y_r -x_r.*X -x_r.*Y];
    R= linsolve(M,x_r);
    format long
    %% Rotation angles and translations
    % non linear system
    u0 = [0,0,(y_r(nrow*(ncol-1)+1)-y_r(1))/(x_r(nrow*(ncol-1)+1)-
x_r(1)),x_r(1)*4,y_r(1)*4];
    RotMat = @(U) [ (R(1)+R(5))/2-cos(U(3))/U(5);
(R(2)-R(4))/2+sin(U(3))/U(5);
R(3)-U(4)/U(5)];
    options = optimoptions('fsolve','Algorithm','levenberg-marquardt');
    [u,fval]=fsolve(RotMat,u0,options);
    %% Rotation matrix
    r11=cos(u(3));
    r12=-sin(u(3));
    r21=sin(u(3));
    r22=cos(u(3));

```

```

%% Magnification
M1=[r11*X+r12*Y+u(4);...
r21*X+r22*Y+u(5)];
mag= linsolve(M1,[x_r;y_r]);

%% show found parameter
fprintf('first iteration\n');
fprintf('alfa:           %.4g \n',u(1))
fprintf('beta:           %.4g \n',u(2))
fprintf('gamma:          %.4g \n',u(3))
fprintf('translation x:    %.4g \n',u(4))
fprintf('translation y:    %.4g \n',u(5))
fprintf('magnification:     %.4g \n',mag)
fprintf('\n')
%% Distorsions Model:complete model, radial distorsion to higher order.decentering
and thin prism
%Description of model:
%xu = mag*(r11*X+r12*Y+tx);
% yu = mag*(r21*X+r22*Y+ty);
%
% deltax= xu.*(k1(5)*(xu.^2+yu.^2)+ k1(6)*(xu.^2+yu.^2).^2)+
k1(7)*(3*xu.^2+yu.^2) + 2*k1(8)*xu.*yu + k1(9)*(xu.^2+yu.^2);
% deltay= yu.*(k1(5)*(xu.^2+yu.^2)+ k1(6)*(xu.^2+yu.^2).^2)+ 2*k1(7)*xu.*yu
+ k1(8)*(xu.^2+3*yu.^2) + k1(10)*(xu.^2+yu.^2);
%
% k1(5) = radial distortion
% k1(6) = 4th order radial distortion
% k1(7), k1(8) = decentering distortion
% k1(9), k1(10) = thin prism distortion
%
% xg=xu+deltax;
% yg=yu+deltay;
%
% fun = sum((x_r-xg).^2+(y_r-yg).^2));
% %fun = function to minimize
%
fun = @(k)sum(...
(x_r-(
k(4)*((cos(k(1)))*X+(-sin(k(1)))*Y+k(2)))+...
k(4)*((cos(k(1)))*X+(-sin(k(1)))*Y+k(2)).*...
(k(5)*((k(4)*((cos(k(1)))*X+(-sin(k(1)))*Y+k(2))).^2+
(k(4)*((sin(k(1)))*X+(cos(k(1)))*Y+k(3))).^2)+...
k(6)*((k(4)*((cos(k(1)))*X+(-sin(k(1)))*Y+k(2))).^2+
(k(4)*((sin(k(1)))*X+(cos(k(1)))*Y+k(3))).^2).^2)+...
k(7)*(3*(k(4)*((cos(k(1)))*X+(-sin(k(1)))*Y+k(2))).^2+
(k(4)*((sin(k(1)))*X+(cos(k(1)))*Y+k(3))).^2)+...
2*k(8)*(k(4)*((cos(k(1)))*X+(-sin(k(1)))*Y+k(2)).*
(k(4)*((sin(k(1)))*X+(cos(k(1)))*Y+k(3)))+...
0*((k(4)*((cos(k(1)))*X+(-sin(k(1)))*Y+k(2))).^2+
(k(4)*((sin(k(1)))*X+(cos(k(1)))*Y+k(3))).^2)).^2+...
(y_r-(
k(4)*((sin(k(1)))*X+(cos(k(1)))*Y+k(3)))+...
k(4)*((sin(k(1)))*X+(cos(k(1)))*Y+k(3)).*...
(k(5)*((k(4)*((cos(k(1)))*X+(-sin(k(1)))*Y+k(2))).^2+
(k(4)*((sin(k(1)))*X+(cos(k(1)))*Y+k(3))).^2)+...
k(6)*((k(4)*((cos(k(1)))*X+(-sin(k(1)))*Y+k(2))).^2+
(k(4)*((sin(k(1)))*X+(cos(k(1)))*Y+k(3))).^2).^2)+...
2*k(7)*(k(4)*((cos(k(1)))*X+(-sin(k(1)))*Y+k(2)).*
(k(4)*((sin(k(1)))*X+(cos(k(1)))*Y+k(3)))+...
k(8)*((k(4)*((cos(k(1)))*X+(-
sin(k(1)))*Y+k(2))).^2+3*(k(4)*((sin(k(1)))*X+(cos(k(1)))*Y+k(3))).^2)+...
0*((k(4)*((cos(k(1)))*X+(-sin(k(1)))*Y+k(2))).^2+
(k(4)*((sin(k(1)))*X+(cos(k(1)))*Y+k(3))).^2)).^2);
k0=[ u(3:end) mag 0 0 0 0];% 0 0];
k1=fminsearch(fun,k0);
k1=[0 0 k1 0 0 ];
%% show found parameter
fprintf('Second iteration\n');
fprintf('alfa:\t\t\t%.4g \n',k1(1))
fprintf('beta:\t\t\t%.4g \n',k1(2))

```

```

fprintf('gamma:\t\t\t%.4g \n',k1(3))
fprintf('translation x:\t%.4g \n',k1(4))
fprintf('translation y:\t%.4g \n',k1(5))
fprintf('magnification:\t%.4g \n',k1(6))
fprintf('\n')
%% Calculation corrected grid intersection
r11=cos(k1(2))*cos(k1(3));
r12=sin(k1(1))*sin(k1(2))*cos(k1(3))-cos(k1(1))*sin(k1(3));
r21=cos(k1(2))*sin(k1(3));
r22=cos(k1(1))*cos(k1(3))+sin(k1(1))*sin(k1(2))*sin(k1(3));

xul = k1(6)*(r11*X+r12*Y+k1(4));%position of grid points WITHOUT distortions in
image coordinate system
yul = k1(6)*(r21*X+r22*Y+k1(5));

deltax1= xul.*(k1(7)*(xul.^2+yul.^2)+ k1(8)*(xul.^2+yul.^2).^2)+
k1(9)*(3*xul.^2+yul.^2) + 2*k1(10)*xul.*yul + k1(11)*(xul.^2+yul.^2);
deltay1= yul.*(k1(7)*(xul.^2+yul.^2)+ k1(8)*(xul.^2+yul.^2).^2)+ 2*k1(9)*xul.*yul
+ k1(10)*(xul.^2+3*yul.^2) + k1(12)*(xul.^2+yul.^2);

xg1=xul+deltax1;%position of grid points WITH distortions
yg1=yul+deltay1;

errorx01=reshape(x_r-xul,nrow,ncol);%errors without considering distortions
errory01=reshape(y_r-yul,nrow,ncol);
errorx1= reshape(x_r-xg1,nrow,ncol);%errors considering distortions
errory1= reshape(y_r-yg1,nrow,ncol);

sigma01= sqrt(1/(ncol*nrow)*sum((xul-x_r).^2+(yul-y_r).^2));
sigma1= sqrt(1/(ncol*nrow)*sum((xg1-x_r).^2+(yg1-y_r).^2));
maxDelta01= max(sqrt((xul-x_r).^2+(yul-y_r).^2));
maxDelta1= max(sqrt((xg1-x_r).^2+(yg1-y_r).^2));

%
%% Plot chessboard intersection, original and corrected
figure;imagesc(xx(1,:),yy(:,1),im)
colormap(gray);axis image
hold on
scatter(x_r,y_r,'*', 'b')
scatter(xg,yg,'o', 'r')
hold off
legend({'original','corrected'}, 'Location','south','Orientation','horizontal')
%% Plot distortions
deltax1=reshape(deltax1,nrow,ncol);
deltay1=reshape(deltay1,nrow,ncol);
deltax2=reshape(deltax2,nrow,ncol);
deltay2=reshape(deltay2,nrow,ncol);
figure
subplot(1,2,1)
imagesc(xx(1,:),yy(:,1),im)
colormap(gray);axis image;alpha(.5);
hold on
quiver(cx1,cyl,deltax1*100,deltay1*100,'AutoScale',
'off','LineWidth',2,'Color',[0 0.1 0.9]);
quiver(cx1,cyl,errorx01*100,errory01*100,'AutoScale',
'off','LineWidth',2,'Color',[1 0.1 0]);
quiver(cx1,cyl,errorx1*100,errory1*100,'AutoScale', 'off','LineWidth',2,'Color',[0
1 0]);
hold off
subplot(1,2,2)
imagesc(xx(1,:),yy(:,1),im)
colormap(gray);axis image;alpha(.5);
hold on
quiver(cx1,cyl,deltax2*100,deltay2*100,'AutoScale',
'off','LineWidth',2,'Color',[0 0.1 0.9]);
quiver(cx1,cyl,errorx02*100,errory02*100,'AutoScale',
'off','LineWidth',2,'Color',[1 0.1 0]);
quiver(cx1,cyl,errorx2*100,errory2*100,'AutoScale', 'off','LineWidth',2,'Color',[0
1 0]);
hold off

```

```

%% Output vector
calcoef1(:,i)=[k1 maxDelta01 maxDelta1 sigma01 sigma1];
%
%% Save calibration data
[~,name,~]=fileparts(FileName);
name1=[name,'CalibrationResult.ascii'];
name1=fullfile(folder_name1,name1);
save(name1,'k1','-ascii','-double');

name4=[name,'CalibrationResult.txt'];
name3=fullfile(folder_name1,name4);
fileID=fopen(name3,'at');
fprintf(fileID,'\n');
fprintf(fileID,'Method 1');
fprintf(fileID,'\n');
fprintf(fileID,'alfa:\t%.5g\n',k1(1));
fprintf(fileID,'beta:\t%.5g\n',k1(2));
fprintf(fileID,'gamma:\t%.5g\n',k1(3));
fprintf(fileID,'translation x:\t%.5g\n',k1(4));
fprintf(fileID,'translation y:\t%.5g\n',k1(5));
fprintf(fileID,'magnification:\t%.5g\n',k1(6));
fprintf(fileID,'k1:\t%.5g\n',k1(7));
fprintf(fileID,'k2:\t%.5g\n',k1(8));
fprintf(fileID,'k3:\t%.5g\n',k1(9));
fprintf(fileID,'k4:\t%.5g\n',k(10));
fprintf(fileID,'k5:\t%.5g\n',k(11));
fprintf(fileID,'k5:\t%.5g\n',k(12));
fprintf(fileID,'MaxDelta:\t%.5g\n',maxDelta01);
fprintf(fileID,'MaxDelta1:\t%.5g\n',maxDelta1);
fprintf(fileID,'Sigma:\t%.5g\n',sigma01);
fprintf(fileID,'Sigma1:\t%.5g\n',sigma1);
fprintf(fileID,'\n');

fprintf(fileID,'\n');
fclose(fileID);
end

```

```

%%%%%%%%%
% Author= Giuseppe Dalla Costa
% date= 01/02/2017
% Description= finds the intersection points on a chessboard pattern picture
%             Automatic or MANUAL inputs of coordinates of four corners of
interested window
%             !!!!!
%             MANUAL inputs of number of squares (column and row)
%             MANUAL input of window size for single edge detection
%             !!!!!
%%%%%%%%%
clc
close all
clearvars -except grid_coord

%% Select and open folder
folder_name = uigetdir;
cd(folder_name)
allFiles = dir( [folder_name '\*.bmp'] );
allNames = { allFiles.name };
n= length (allNames);
%%

for k=1:n
disp(k)
%%
FileName=char(allNames(k));
res=0.2;
pp=1/res;
im=imread(FileName);
im=im2double((im(:,:,1)));
[imy, imx]=size(im);
xx=repmat(0:imx-1,imy,1); % matrix x coord.
xxhr=repmat(0:res:imx-res,imy*pp,1); % matrix x coord. high resolution
yy=repmat((0:imy-1)',1,imx); % matrix y coord.
yyhr=repmat((0:res:imy-res)',1,imx*pp); % matrix y coord. high resolution

%% Automatic point selection
% figure;
% fig = gcf;
% set ( fig, 'Units', 'normalized', 'Position', [0,0,1,1]);
% imagesc(im);colorbar;colormap('gray');
% title(['Select point 1'], 'FontSize', 30, 'Color', 'r');
% axis image;
% [x, y] = getpts(fig);
% close
%% MANUAL point selection
% imagesc(xx(1,:),yy(:,1),im)
% colormap(gray);axis image
%%
%%
x=grid_coord(k,1:4);
y=grid_coord(k,5:8);
ncol=grid_coord(k,9);
nrow=grid_coord(k,10);

%% Aproximate calculation of corners of chessboard
a=0:ncol-1;
b=0:nrow-1;
%first iteration
cx = repmat(round( x(1) + (x(2)-x(1))/50*a),nrow,1);
cy = repmat(round( y(1) + (y(4)-y(1))/37*b)',1,ncol);
% second iteration, considers also distortions
cx1=zeros(nrow,ncol);
cy1=zeros(nrow,ncol);
for i=1:ncol
for j=1:nrow
cx1(j,i)=round((x(1) + (x(2)-x(1))/(ncol-1)*a(i)) * ((cy(nrow,1)-
cy(j,1))/(cy(nrow,1)-cy(1,1)))...

```

```

    +(x(4) + (x(3)-x(4))/(ncol-1)*a(i)) * (1-(cy(nrow,1)-cy(j,1))/(cy(nrow,1)-
    cy(1,1)))));
    cy1(j,i)=round((y(1) + (y(4)-y(1))/(nrow-1)*b(j)) * ((cx(1,ncol)-
    cx(1,i))/(cx(1,ncol)-cx(1,1)))...
    +(y(2) + (y(3)-y(2))/(nrow-1)*b(j)) * (1-(cx(1,ncol)-cx(1,i))/(cx(1,ncol)-
    cx(1,1)))));
    end
end

% % plot of aproximated corners
% figure
% imagesc(xx(1,:),yy(:,1),im)
% colormap(gray);axis image
% hold on
% for i=1:nrow
% for j=1:ncol
% plot(cx1 (i,j),cy1 (i,j),'o','MarkerSize',3,'LineWidth', 3,'Color',[0 0.1 0.9])
% end
% end
% hold off
%% Calculation of corners position after edges detection
% edge filter
h = [1 2 1;0 0 0 ;-1 -2 -1];
v = [1 0 -1; 2 0 -2;1 0 -1];
J = abs(imfilter(im,h)); % horizontal sobel
K = abs(imfilter(im,v)); %vertical sobel
sobel3 = (J.^2 + K.^2).^0.5;

% for each corner a vertical and horizontal line are defined from maximum
% points of filtered image. Corner is the intersection of the lines
x_result=zeros(nrow,ncol);
y_result=zeros(nrow,ncol);
d=23; %MANUAL INPUT of searching window size
xpos=zeros(d*2+1,1);
ypos=zeros(d*2+1,1);

for i=1:nrow
disp(i)
for j=1:ncol

%definition of searching windows
window = sobel3(cy1(i,j)-d:cy1(i,j)+d,cx1(i,j)-d:cx1(i,j)+d);
bv_x= xx(cy1(i,j)-d:cy1(i,j)+d,cx1(i,j)-d:cx1(i,j)+d);
bv_y= yy(cy1(i,j)-d:cy1(i,j)+d,cx1(i,j)-d:cx1(i,j)+d);
bv_xhr=xxhr((cy1(i,j)-d-1)*pp+1:(cy1(i,j)+d)*pp,(cx1(i,j)-d-
1)*pp+1:(cx1(i,j)+d)*pp);
bv_yhr=yyhr((cy1(i,j)-d-1)*pp+1:(cy1(i,j)+d)*pp,(cx1(i,j)-d-
1)*pp+1:(cx1(i,j)+d)*pp);
%searching window fo vertical edge
window1 = K(cy1(i,j)-d:cy1(i,j)+d,cx1(i,j)-floor(d/3):cx1(i,j)+floor(d/3));
bv_x1= xx(cy1(i,j)-d:cy1(i,j)+d,cx1(i,j)-floor(d/3):cx1(i,j)+floor(d/3));
bv_y1= yy(cy1(i,j)-d:cy1(i,j)+d,cx1(i,j)-floor(d/3):cx1(i,j)+floor(d/3));
bv_xhr1=xxhr((cy1(i,j)-d-1)*pp+1:(cy1(i,j)+d)*pp,(cx1(i,j)-floor(d/3)-
1)*pp+1:(cx1(i,j)+floor(d/3))*pp);
bv_yhr1=yyhr((cy1(i,j)-d-1)*pp+1:(cy1(i,j)+d)*pp,(cx1(i,j)-floor(d/3)-
1)*pp+1:(cx1(i,j)+floor(d/3))*pp);
%searching window fo horizontal edge
window2 = J(cy1(i,j)-floor(d/3):cy1(i,j)+floor(d/3),cx1(i,j)-d:cx1(i,j)+d);
bv_x2= xx(cy1(i,j)-floor(d/3):cy1(i,j)+floor(d/3),cx1(i,j)-d:cx1(i,j)+d);
bv_y2= yy(cy1(i,j)-floor(d/3):cy1(i,j)+floor(d/3),cx1(i,j)-d:cx1(i,j)+d);
bv_xhr2=xxhr((cy1(i,j)-floor(d/3)-1)*pp+1:(cy1(i,j)+floor(d/3))*pp,(cx1(i,j)-d-
1)*pp+1:(cx1(i,j)+d)*pp);
bv_yhr2=yyhr((cy1(i,j)-floor(d/3)-1)*pp+1:(cy1(i,j)+floor(d/3))*pp,(cx1(i,j)-d-
1)*pp+1:(cx1(i,j)+d)*pp);

[n1, m1]=size(window1);
[n2, m2]=size(window2);

% determination of vertical edge
for k=1:n1

```

```

sq=(window1(k,:));%mean(window1(k,:))/std(window1(k,:));%normalization
[maxlr,I] = max(sq); % max of sobel along rows
if maxlr>2 % if max is low it is not considered
if and(I>3,I<=length(sq)-3) % if max is in the border of the window fitting not
possible
int=sq(I-3:I+3); % select neighbour interval near to max value
dx=-mean(bv_x1(k,I-3:I+3));
x=bv_x1(k,I-3:I+3)+dx; %remove average value of ordinate to have a better
condition in fitting
xhrl=bv_xhrl(1+(k-1)*pp,1+((I-1)-3)*pp:1+((I-1)+3)*pp);
% polynomial fitting 4th order (fitting of 5 points, not regression!)
[xData, yData] = prepareCurveData( x, int );
ft = fittype( 'poly4' );
opts = fitoptions( 'Method', 'LinearLeastSquares' );
opts.Normalize = 'on';
opts.Robust = 'Bisquare';
[fitresult, ~] = fit( xData, yData, ft );
coe=coeffvalues(fitresult);
%change fitting coefficients to match initial coordinates
coel(1)= coe(1);
coel(2)=4*coe(1)*dx + coe(2);
coel(3)=6*coe(1)*dx^2+3*coe(2)*dx + coe(3);
coel(4)=4*coe(1)*dx^3+3*coe(2)*dx^2+2*coe(3)*dx +coe(4);
coel(5)= coe(1)*dx^4+ coe(2)*dx^3+ coe(3)*dx^2+coe(4)*dx +coe(5);
%search for max high resolution
ghr= coel(1)*xhrl.^4 + coel(2)*xhrl.^3 + coel(3)*xhrl.^2 + coel(4)*xhrl+coel(5);
[~, Ihr]= max(ghr);
xpos(k,1)=xhrl(Ihr); %in pixel
end
end
clear sq
end

data1=[bv_y1(:,1),xpos(:,1)];
data1( ~any(data1(:,2)>min(bv_x1(1,:))&data1(:,2)<max(bv_x1(1,:)),2), : ) = [];
%remove zero points
[xData, yData] = prepareCurveData( data1(:,1), data1(:,2)); %linear fitting of
edge points
ft = fittype( 'polyl' );
opts = fitoptions( 'Method', 'LinearLeastSquares' );
opts.Normalize = 'on';
opts.Robust = 'Bisquare';
[fity, ~] = fit( xData, yData, ft );
coey = coeffvalues(fity);
coey(2)=-(coey(2)/coey(1)); %rotate coordinate system
coey(1)=1/coey(1);

%determination of horizontal border
for k=1:m2
sq=((window2(:,k)-mean(window2(:,k)))/std(window2(:,k)))';%normalization
[maxlr,I] = max(sq); % max of sobel along rows
if maxlr>2
% if max is in the border of the window fitting not possible
if and(I>3,I<=length(sq)-3)
int=sq(I-3:I+3); % select neighbour interval
%remove average value of ordinate to have a better condition in fitting
dy=-mean(bv_y2(I-3:I+3,k));
y=(bv_y2(I-3:I+3,k)+dy)';
yhr2=(bv_yhr2(1+((I-1)-3)*pp:1+((I-1)+3)*pp,1+(k-1)*pp))';
% polynomial fitting 4th order (fitting of 5 points, not regression!)
[xData, yData] = prepareCurveData( y, int );
ft = fittype( 'poly4' );
opts = fitoptions( 'Method', 'LinearLeastSquares' );
opts.Normalize = 'on';
opts.Robust = 'Bisquare';
[fitresult, ~] = fit( xData, yData, ft );
coe=coeffvalues(fitresult);
%change fitting coefficients to match initial coordinates
coel(1)= coe(1);
coel(2)=4*coe(1)*dy + coe(2);

```

```

coel(3)=6*coe(1)*dy^2+3*coe(2)*dy + coe(3);
coel(4)=4*coe(1)*dy^3+3*coe(2)*dy^2+2*coe(3)*dy +coe(4);
coel(5)= coe(1)*dy^4+ coe(2)*dy^3+ coe(3)*dy^2+coe(4)*dy +coe(5);
%search for max high resolution
ghr= coel(1)*yhr2.^4 + coel(2)*yhr2.^3 + coel(3)*yhr2.^2 + coel(4)*yhr2+coe(5);
[~, Ihr]= max(ghr);
ypos(k,1)=yhr2(Ihr);%in pixel
end
end
clear sq
end
data2=[bv_x2(1,:)',ypos(:,1)];
data2( ~any(data2(:,2)> min(bv_y2(:,1))&data2(:,2)<max(bv_y2(:,1)),2), : ) = [];
[xData, yData] = prepareCurveData( data2(:,1), data2(:,2));
ft = fittype( 'polyl' );
opts = fitoptions( 'Method', 'LinearLeastSquares' );
opts.Normalize = 'on';
opts.Robust = 'Bisquare';
[fitx, ~] = fit( xData, yData, ft );
coex=coeffvalues(fitx);
%intersection
x_result(i,j)=(coex(2)-coey(2))/(coey(1)-coex(1));
y_result(i,j)= x_result(i,j)*coex(1)+coex(2);
end
end
% %% Definition of edges for plotting
% linea2=bv_xhr2(1,:)*coex(1)+coex(2);
% lineal=bv_xhr1(1,:)*coey(1)+coey(2);
% %%
% figure
% imagesc(bv_x(1,:),bv_y(:,1),window)
% colormap(gray);axis image
% hold on
% plot(bv_xhr1(1,:),lineal,'LineWidth', 3,'Color',[1 0.1 0])
% plot(bv_xhr2(1,:),linea2,'LineWidth', 3,'Color',[1 0.1 0])
% plot(bv_x2(1,:),ypos(:,1),'o','MarkerSize',3,'LineWidth', 3,'Color',[0 0.1 0.9])
% plot(xpos(:,1),bv_y1(:,1),'o','MarkerSize',3,'LineWidth', 3,'Color',[0 0.1 0.9])
% hold off
% Reshape corners coordinates from matrix to vector and remove zeros
x_r=reshape(x_result,nrow*ncol,1);
y_r=reshape(y_result,nrow*ncol,1);
x_r( ~any(x_r,2), : ) = [];
y_r( ~any(y_r,2), : ) = [];
% %% Plotting new corners
% figure
% imagesc(xx(1,:),yy(:,1),im)
% colormap(gray);axis image
% hold on
% for i=1:nrow
% for j=1:ncol
% plot(x_result(i,j),y_result
(i,j),'o','MarkerSize',3,'LineWidth', 3,'Color',[0 0.1 0.9])
% end
% end
% hold off
% Save relevant variable
[~,name,~]=fileparts(FileName);
name=[name, '.mat'];
name=fullfile(folder_name,name);
save(name,'im','xx','yy','ncol','nrow','x_r','y_r','cx1','cy1','-mat','-double')
%
end

```

Edge detection

```

%%%%%%%%%%%%%%%%%%%%%%%%%%%%%%%%%%%%%%%%%%%%%%%%%%%%%%%%%%%%%%%%%%%%%%%%
% Author:giucos
% date 2016/12/01
% Description: to calculate edges distance from reference grid and
%             measuring object. Images selected from a single folder.
%%%%%%%%%%%%%%%%%%%%%%%%%%%%%%%%%%%%%%%%%%%%%%%%%%%%%%%%%%%%%%%%%%%%%%%%
%%
clc
close all
% clear all
clearvars -except windows

%% Select and open folder
folder_name = uigetdir;
addpath(genpath(folder_name));
% cd(folder_name)
d = dir(folder_name);
allFiles = dir( [folder_name '\*.bmp'] );
allNames = { allFiles.name };
%% Parameters
res= 0.2;           %Subpixel resolution, values: 0.5 , 0.1 , 0.02
SoN=7;             %Size of Neighborhood of maximum, values: 3 , 5 , 7
mod='POLY4';       %Fitting model, POLY2 , POLY4 , GAUSS
modn=2;
%note: POLY4 doesn't work with SoN=3
%% call edge detection function
%initialization for cycle
output=zeros(length(allNames)+1,10);
windows=zeros(length(allNames),16); %comment if searching windows already exist
%%
tic
% call edge detection function
for i=1:length(allNames)
    filename=char(allNames(i));
    disp(i)
    w=windows(i,:);
    [ox,oy,alfax,alfay,x1,y1,alfal,x2,y2,alfa2,w]=Edge_brick_grid_fun(filename,i,w,res
    ,SoN,mod);
    output(i+1,:)=[ox,oy,alfax,alfay,x1,y1,alfal,x2,y2,alfa2];
    windows(i,:)=w; %uncomment to create a searching window matrix
    %%
    h(1)=figure(i);
    h(2)=figure(i+50);
    [~,name,~]=fileparts(filename);
    name1=[name,'.fig'];
    name2=[name,'.jpg'];
    savefig(h,name1)
    saveas(h(1),name2)
    % questdlg
    choice = questdlg('Close figure?', ...
    'Figure', ...
    'Yes','No','Yes');
    % Handle response
    switch choice
    case 'Yes'
        close (h(1))
        close (h(2))
    case 'No'
        end
    close all
end
%%
output(1,1:3)=[res SoN modn];
output(1,4)= toc;

```

```

%%%%%%%%%
% Author:giucos
% date 2016/12/01
% Description:function to calculate edges from images of a corner of a lego
% brick with a reference grid. Calculate vertical and horizontal edge of
% brick and grid. REference point of grid: intersection of two edges.
% Points on the brick at 1 mm from other edge
%
% input:      filename:    image file name
%            fig_num:     order number of image (from cycle for)
%            w:           edge searching window matrix (could be 0)
%            res:         subpixel resolution.
%            SoN:         size of the neighborhood of maximum to fit with
%                        model. MUST be even!
%            model:       type of model to use for fitting:POLY2, POLY4, GAUSS
%
% output:     ox:         grid origin x coordinate
%            oy:         grid origin y coordinate
%            alfax:       angle of horizontal grid
%            alfay:       angle of vertical grid
%            xh:          x coordinate of meas. point on horizontal brick edge
%            yh:          y coordinate of meas. point on horizontal brick edge
%            alfah:       angle of horizontal brick edge
%            xv:          x coordinate of meas. point on vertical brick edge
%            yv:          y coordinate of meas. point on vertical brick edge
%            alfav:       angle of vertical brick edge
%            w:           edge searching window matrix used
%
%%%%%%%%%
%%
function
[ox,oy,alfax,alfay,xh,yh,alfah,xv,yv,alfav,win]=Edge_brick_grid_fun(filename,fig_n
um,w,res,SoN,mod)
%% Open image and create x y matrix
im=imread(filename);
im=im2double((im(:,:,1)));
[imy, imx]=size(im);
xx=repmat(0:imx-1,imy,1);           % matrix x coord.
xxhr=repmat(0:res:imx-res,imy/res,1); % matrix x coord. high resolution
yy=repmat((0:imy-1)',1,imx);        % matrix y coord.
yyhr=repmat((0:res:imy-res)',1,imx/res); % matrix y coord. high resolution
%%
%% Sobel of full image
h = [1 2 1;0 0 0;-1 -2 -1];
v = [1 0 -1; 2 0 -2;1 0 -1];
J = imfilter(im,h);
K = imfilter(im,v);
sobel = (J.^2 + K.^2).^0.5;
%
%% Edge detection
edge_type1='GRID';
edge_type2='BRICK';
edge_dir1='horizontal';
edge_dir2='vertical';
%%
[a1, b1,
edge1,w1]=edgedetection_fun_param(im,xx,yy,xxhr,yyhr,edge_type1,edge_dir1,w(1:4),
res,SoN,mod);
[a3, b3,
edge3,w3]=edgedetection_fun_param(im,xx,yy,xxhr,yyhr,edge_type1,edge_dir2,w(9:12),
res,SoN,mod);

ox = (b1-b3)/(a3-a1); %grid origin x coordinate
oy = a1*ox+b1;       %grid origin y coordinate

%% Rough search for brick edge and definition of smaller windows
% Selection of area within a cell of the grid
flag=ox>imx/2;
switch flag
case 0

```

```

win1=[floor(ox)+260 floor(ox)+470 floor(oy)+10 floor(oy)+220];
win2=[floor(ox)+10 floor(ox)+220 floor(oy)+260 floor(oy)+470];
case 1
win1=[floor(ox)-480 floor(ox)-270 floor(oy)+10 floor(oy)+220];
win2=[floor(ox)-230 floor(ox)-20 floor(oy)+260 floor(oy)+470];
end
%%
window1=sobel(win1(3):win1(4),win1(1):win1(2));
window2=sobel(win2(3):win2(4),win2(1):win2(2));
[~, edge_pos1]=max(sum(window1,2)); %aprox position of horizontal edge
win1=[win1(1) win1(2) win1(3)+edge_pos1-15 win1(3)+edge_pos1+15]; %redefinition of
searching interval
[~, edge_pos2]=max(sum(window2,1));%aprox position of vertical edge
win2=[win2(1)+edge_pos2-15 win2(1)+edge_pos2+15 win2(3) win2(4)];
%% Brick edge detection
[a2, b2, edge2,
w2]=edgedetection_fun_param(im,xx,yy,xxhr,yyhr,edge_type2,edge_dir1,win1,res,SoN,m
od);
[a4, b4, edge4,
w4]=edgedetection_fun_param(im,xx,yy,xxhr,yyhr,edge_type2,edge_dir2,win2,res,SoN,m
od);

%% Calculate position 1 mm from brick edge (alignment)
%considering the orientation of edge
alfa2=atan(a2); %angle of horizontal edge
%if left side of brick I need to add 1mm to go to the right
%if right side of brick I need to remove 1mm to go to the left
if mean(edge1(:,2))<mean(edge2(:,2)) % control if the grid is on the left or on
the right
d=250;
else
d=-250;
end
% create a line parallel to horizontal edge
b21=b2+d/cos(alfa2);
line2=a2*xxhr(1,:)+b21;
x_int3=(b21-b3)/(a3-a2);%intersection with vertical grid
y_int3=a2*x_int3+b21;
x_int4=(b21-b4)/(a4-a2);%intersection with vertical edge
y_int4=a2*x_int4+b21;

%angle of vertical edge
if a4>0
alfa4=atan(a4);
else
alfa4=atan(a4)+pi;
end
%similar to above
if mean(edge3(:,1))<mean(edge4(:,1))
d=-250;
else
d=250;
end
% create a line parallel to vertical edge
b41=b4+d/cos(alfa4);
line4=a4*xxhr(1,:)+b41;
x_int1=(b41-b1)/(a1-a4);%intersection with horizontal grid
y_int1=a1*x_int1+b1;
x_int2=(b41-b2)/(a2-a4);%intersection with horizontal edge
y_int2=a2*x_int2+b2;

%% Recalculate edge in a smaller interval (measuring edge)
d1=10;
%definition of new window for edge detection
win2cx =find(xx(1,:)==round(x_int2));
win2cy =find(yy(:,1)==round(y_int2));
w2new= [max(win2cx-2*d1,win1(1)) min(win2cx+2*d1,win1(2)) max(win2cy-d1,win1(3))
min(win2cy+d1,win1(4))];
try

```

```

[a2new, b2new, edge2new]=edgedetection_fun_param(im, xx,
yy,xxhr,yyhr,edge_type2,edge_dir1,w2new,res,SoN,mod);
catch
disp('An error occurred.');
```

disp('Execution will continue.');

a2new=a2;b2new= b2;edge2new=edge2;

end


```
win4cx =find(xx(1,:)==round(x_int4));
win4cy =find(yy(:,1)==round(y_int4));
w4new= [max(win4cx-d1,win2(1)) min(win4cx+d1,win2(2)) max(win4cy-2*d1,win2(3))
min(win4cy+2*d1,win2(4))];
try
[a4new, b4new, edge4new]=edgedetection_fun_param(im, xx,
yy,xxhr,yyhr,edge_type2,edge_dir2,w4new,res,SoN,mod);
catch
disp('An error occurred.');
```

disp('Execution will continue.');

a4new=a4;b4new= b4;edge4new=edge4;

end

%% Calculate measuring points

x_int2new=(b41-b2new)/(a2new-a4);

y_int2new=a2new*x_int2+b2new;


```
%
if a4new==inf
x_int4new=mean(edge4new(:,1));
else
x_int4new=(b21-b4new)/(a4new-a2);
end
y_int4new=a2*x_int4new+b21;
```



```
%% Outputs
% ox = (b1-b3)/(a3-a1); %grid origin x coordinate
% oy = a1*ox+b1; %grid origin y coordinate
alfax=rad2deg(atan(a1));%angle of horizontal grid
alfay=rad2deg(atan(a3));%angle of vertical grid
if alfay<0
alfay=180+alfay;
end
xh=x_int2new; %x coordinate of meas. point on horizontal brick edge
yh=y_int2new; %y coordinate of meas. point on horizontal brick edge
alfah=rad2deg(alfa2); %angle of horizontal brick edge
xv=x_int4new; %x coordinate of meas. point on vertical brick edge
yv=y_int4new; %y coordinate of meas. point on vertical brick edge
alfav=rad2deg(alfa4); %angle of vertical brick edge
%
win=[w1 win1 w3 win2]; %edge searching window matrix used
```



```
%% Plot
figure(fig_num)
imagesc(xx(1,:),yy(:,1),im)
colormap(gray);axis image
hold on
plot(edge1(:,1), edge1(:,2),'LineWidth', 3,'Color',[0 0.1 0.9])
plot(edge2(:,1), edge2(:,2),'LineWidth', 3,'Color',[0 0.1 0.9])
plot(edge3(:,1), edge3(:,2),'LineWidth', 3,'Color',[0 0.1 0.9])
plot(edge4(:,1), edge4(:,2),'LineWidth', 3,'Color',[0 0.1 0.9])
plot(edge2new(:,1), edge2new(:,2),'LineWidth', 3,'Color',[0.9 0 0])
plot(edge4new(:,1), edge4new(:,2),'LineWidth', 3,'Color',[0.9 0 0])
plot(xxhr(1,:), line2,'LineWidth', 2,'LineStyle','--','Color',[0 0.1 0.9])
plot(xxhr(1,:), line4,'LineWidth', 2,'LineStyle','--','Color',[0 0.1 0.9])
plot(x_int1, y_int1, 'o','Color',[0 0.8
0.2],'MarkerSize',5,'MarkerFaceColor',[0 0.8 0.2])
plot(x_int2new,y_int2new,'o','Color',[0 0.8
0.2],'MarkerSize',5,'MarkerFaceColor',[0 0.8 0.2])
plot(x_int3, y_int3, 'o','Color',[0 0.8
0.2],'MarkerSize',5,'MarkerFaceColor',[0 0.8 0.2])
```

```

plot(x_int4new,y_int4new,'o','Color',[0 0.8
0.2],'MarkerSize',5,'MarkerFaceColor',[0 0.8 0.2])
plot(ox,oy,'o','Color',[0 0.8 0.2],'MarkerSize',5,'MarkerFaceColor',[0 0.8 0.2])
xlim([xx(1,1) xx(1,end)])
ylim([yy(1,1) yy(end,1)])

hold off
%%

figure(fig_num+50)
imagesc(xx(1,:),yy(:,1),sobel)
colormap(gray);axis image
hold on
plot(edge1(:,1), edge1(:,2),'LineWidth', 3,'Color',[0 0.1 0.9])
plot(edge2(:,1), edge2(:,2),'LineWidth', 3,'Color',[0 0.1 0.9])
plot(edge3(:,1), edge3(:,2),'LineWidth', 3,'Color',[0 0.1 0.9])
plot(edge4(:,1), edge4(:,2),'LineWidth', 3,'Color',[0 0.1 0.9])
plot(edge2new(:,1), edge2new(:,2),'LineWidth', 3,'Color',[0.9 0 0])
plot(edge4new(:,1), edge4new(:,2),'LineWidth', 3,'Color',[0.9 0 0])
plot(xxhr(1,:), line2,'LineWidth', 2,'LineStyle','--','Color',[0 0.1 0.9])
plot(xxhr(1,:), line4,'LineWidth', 2,'LineStyle','--','Color',[0 0.1 0.9])
plot(x_int1, y_int1, 'o','Color',[0 0.8
0.2],'MarkerSize',5,'MarkerFaceColor',[0 0.8 0.2])
plot(x_int2new,y_int2new,'o','Color',[0 0.8
0.2],'MarkerSize',5,'MarkerFaceColor',[0 0.8 0.2])
plot(x_int3, y_int3, 'o','Color',[0 0.8
0.2],'MarkerSize',5,'MarkerFaceColor',[0 0.8 0.2])
plot(x_int4new,y_int4new,'o','Color',[0 0.8
0.2],'MarkerSize',5,'MarkerFaceColor',[0 0.8 0.2])
plot(ox,oy,'o','Color',[0 0.8 0.2],'MarkerSize',5,'MarkerFaceColor',[0 0.8 0.2])
xlim([xx(1,1) xx(1,end)])
ylim([yy(1,1) yy(end,1)])
hold off
% % %

```

```

% % % % %
% Author:giucos
% date 2016/12/01
% Description:function to find edge (vertical or horizontal) from a selected
windows in a
% picture. A linear regression with exclusion of outliers is performed to
% find a straight edge.
%
% input:      im:      grey level image matrix
%            xx:      x coordinate matrix
%            yy:      y coordinate matrix
%            xxhr:    x coordinate matrix high resolution
%            yyhr:    y coordinate matrix high resolution
%            edge_type: brick or grid (could not exist)
%            edge_dir: horizontal or vertical
%            w:      edge searching window matrix (could be 0)
%
% output:     a:      angular coefficient of edge regression
%            b:      constant coefficient of edge regression
%            edge:    x y coordinates of found edge
%            r:      searching window used
%
% % % % %
function [a, b, edge,r]=edgedetection_fun(im, xx, yy,xxhr,yyhr,
edge_type,edge_dir,w)
%% Select edge and create x y matrix
bb=any(any(w));
switch bb
case 0
figure;
fig = gcf;
set ( fig, 'Units', 'normalized', 'Position', [0,0,1,1]);
imagesc(im);colorbar;colormap('gray');
ttl=strcat({'Select'},{' '},{edge_dir} ,{' '},{edge_type},{ ' '},{'edge'});
title(ttl, 'FontSize', 30,'Color', 'r');
axis image;
r=getrect;
close
r=round([r(1)  r(1)+floor(r(3)/2)*2  r(2)  r(2)+floor(r(4)/2)*2]);
otherwise
r=w;
end
%
%% create x y z matrix of selected window
bv_z=im(r(3):r(4), r(1):r(2));
bv_x=xx(r(3):r(4), r(1):r(2));
bv_xhr=xxhr((r(3)-1)*20+1 : r(4)*20 , (r(1)-1)*20+1 : r(2)*20);
bv_y=yy(r(3):r(4), r(1):r(2));
bv_yhr=yyhr((r(3)-1)*20+1 : r(4)*20 , (r(1)-1)*20+1 : r(2)*20);
[m, n]=size(bv_z);
%
%% Sobel filter
% generate horizontal/vertical edge emphasis kernel sobel 3x3
h = [1 2 1;0 0 0 ;-1 -2 -1];
v = [1 0 -1; 2 0 -2;1 0 -1];
J = imfilter(bv_z,h);
K = imfilter(bv_z,v);
sobel = (J.^2 + K.^2).^0.5;
% % generate horizontal/vertical edge emphasis kernel sobel 5x5
% h5=[2 3 4 3 2;1 2 3 2 1;0 0 0 0 0;-1 -2 -3 -2 -1;-2 -3 -4 -3 -2];
% v5=[2 1 0 -1 -2;3 2 0 -2 -3;4 3 0 -3 -4;3 2 0 -2 -3;2 1 0 -1 -2];
% J5 = imfilter(bv_z,h5);
% K5 = imfilter(bv_z,v5);
% sobel = (J5.^2 + K5.^2).^0.5;
%
%% Remove boundary elements because not significant
bv_x=bv_x(3:m-2,3:n-2);
bv_xhr=bv_xhr(41:(m-2)*20,41:(n-2)*20);
bv_y=bv_y(3:m-2,3:n-2);
bv_yhr=bv_yhr(41:(m-2)*20,41:(n-2)*20);

```

```

sobel=sobel(3:m-2,3:n-2);
[m, n]=size(sobel);

%
%% Different calculation for horizontal and vertical edges
switch edge_dir

%% Subpixel edge detection along columns
case 'horizontal'
ypos1=zeros(1,n);

for i=1:n
sobelNorm =(sobel(:,i)-min(sobel(:,i)))/std(sobel(:,i));%normalization
[maxlr,I] =max(sobelNorm); % max of sobel along columns
% if max too small edge doesn't exist
if maxlr>2
% if max is in the border of the selection of neighborhood isn't possible
SoN1=7;
if and(I>SoN1,I<m-SoN1)
int=sobelNorm(I-SoN1:I+SoN1); % select neighbour interval
%remove average value of ordinate to have a better condition in fitting
dy=-mean(bv_y(I-SoN1:I+SoN1,i));
y=bv_y(I-SoN1:I+SoN1,i)+dy;
%
yhr=bv_yhr(1+((I-1)-SoN1)*20:1+((I-1)+SoN1)*20,1+(i-1)*20);
[xData, yData] = prepareCurveData( y, int );
ft = fitttype( 'poly4' );
[fitresult, ~] = fit( xData, yData, ft );
coe=coeffvalues(fitresult);
%change fitting coefficients to match initial coordinates
coe1(1)= coe(1);
coe1(2)=4*coe(1)*dy + coe(2);
coe1(3)=6*coe(1)*dy^2+3*coe(2)*dy + coe(3);
coe1(4)=4*coe(1)*dy^3+3*coe(2)*dy^2+2*coe(3)*dy +coe(4);
coe1(5)= coe(1)*dy^4+ coe(2)*dy^3+ coe(3)*dy^2+coe(4)*dy +coe(5);
%search for max high resolution
ghr= coe1(1)*yhr.^4 + coe1(2)*yhr.^3 + coe1(3)*yhr.^2 + coe1(4)*yhr+coe1(5);
[~, Ihr]= max(ghr);
ypos1(i)=yhr(Ihr); %in pixel
end
end
end
%
%% Linear regression of edge just found
data=[bv_x(1,:) ' ypos1'];
data(any(data==0,2),:)=[];
ypos2=data(:,2)-mean(data(:,2));%remove average for better conditioned fitting
xpos2=data(:,1)-mean(data(:,1));
%
[xData, yData] = prepareCurveData( xpos2, ypos2);
ft = fitttype( 'poly1' );
opts = fitoptions( 'Method', 'LinearLeastSquares' );
opts.Lower = [-0.1 -0.1];
opts.Robust = 'Bisquare';
opts.Upper = [0.1 0.1];
[fitresult, ~] = fit( xData, yData, ft, opts );
coe=coeffvalues(fitresult);
%% Calculation of outliers from residuals
residuals=coe(1)*xpos2+coe(2)-ypos2;
stdev=std(residuals);
if stdev~=0
av=mean(residuals);
prob=1/length(residuals);
bound_low=norminv(prob,av,stdev);
bound_high=2*av-bound_low;
data=data(any((residuals <= bound_high & residuals >= bound_low),2),:);
%% New Regression
ypos2=data(:,2)-mean(data(:,2));%remove average for better conditioned fitting
xpos2=data(:,1)-mean(data(:,1));
[xData, yData] = prepareCurveData( xpos2, ypos2);

```

```

ft = fitttype( 'poly1' );
opts = fitoptions( 'Method', 'LinearLeastSquares' );
opts.Lower = [-0.1 -0.1];
opts.Robust = 'Bisquare';
opts.Upper = [0.1 0.1];
[fitresult, ~] = fit( xData, yData, ft, opts );
coe=coeffvalues(fitresult);
end
a=coe(1);
b=coe(2)-coe(1)*mean(data(:,1))+mean(data(:,2));
edge_vfit=a*bv_xhr(1,:)+b;
edge=[ bv_xhr(1,:) ' edge_vfit'];
%

%%
% plot(bv_xhr(1,:), edge_vfit)
%%

%% Subpixel edge detection along rows
case 'vertical'
xpos1=zeros(m,1);

for i=1:m
sobelNorm =(sobel(i,:)-min(sobel(i,:)))/std(sobel(i,:));%normalization
[maxlr,I] =max(sobelNorm); % max of sobel along columns
% if max too small edge doesn't exist
if maxlr>2
% if max is in the border of the selection of neighborhood isn't possible
SoN1=7;
if and(I>SoN1,I<n-SoN1)
int=sobelNorm(I-SoN1:I+SoN1); % select neighbour interval
% remove average value of ordinate to have a better condition in fitting
dx=-mean(bv_x(i,I-SoN1:I+SoN1));
x=bv_x(i,I-SoN1:I+SoN1)+dx;
%
xhr=bv_xhr(1+(i-1)*20,1+((I-1)-SoN1)*20:1+((I-1)+SoN1)*20);
[xData, yData] = prepareCurveData( x, int );
ft = fitttype( 'poly4' );
[fitresult, ~] = fit( xData, yData, ft );
coe=coeffvalues(fitresult);
%change fitting coefficients to match initial coordinates
coel(1)= coe(1);
coel(2)=4*coe(1)*dx + coe(2);
coel(3)=6*coe(1)*dx^2+3*coe(2)*dx + coe(3);
coel(4)=4*coe(1)*dx^3+3*coe(2)*dx^2+2*coe(3)*dx +coe(4);
coel(5)= coe(1)*dx^4+ coe(2)*dx^3+ coe(3)*dx^2+coe(4)*dx +coe(5);
%search for max high resolution
ghr= coel(1)*xhr.^4 + coel(2)*xhr.^3 + coel(3)*xhr.^2 + coel(4)*xhr+coel(5);
[~, Ihr]= max(ghr);
xpos1(i)=xhr(Ihr); %in pixel
end
end
end

%% Linear regression of edge
data=[xpos1 bv_y(:,1)];
data(any(data==0,2),:)=[];
ypos2=data(:,2)-mean(data(:,2));%remove average for better conditioned fitting
xpos2=data(:,1)-mean(data(:,1));
[xData, yData] = prepareCurveData( ypos2, xpos2);
ft = fitttype( 'poly1' );
opts = fitoptions( 'Method', 'LinearLeastSquares' );
opts.Lower = [-0.1 -0.1];
opts.Robust = 'Bisquare';
opts.Upper = [0.1 0.1];
[fitresult, ~] = fit( xData, yData, ft, opts );
coe=coeffvalues(fitresult);
%% Calculation of outliers from residuals
residuals=coe(1)*ypos2+coe(2)-xpos2;
stdev=std(residuals);
if stdev~=0

```

```

av=mean(residuals);
prob=1/length(residuals);
bound_low=norminv(prob,av,stdev);
bound_high=2*av-bound_low;
data=data(any((residuals <= bound_high & residuals >= bound_low),2),:);
%% New Regression
ypos2=data(:,2)-mean(data(:,2));%remove average for better conditioned fitting
xpos2=data(:,1)-mean(data(:,1));
[xData, yData] = prepareCurveData( ypos2, xpos2);
ft = fittype( 'poly1' );
opts = fitoptions( 'Method', 'LinearLeastSquares' );
opts.Lower = [-0.1 -0.1];
opts.Robust = 'Bisquare';
opts.Upper = [0.1 0.1];
[fitresult, ~] = fit( xData, yData, ft, opts );
coe=coeffvalues(fitresult);
end
al=coe(1);
b1=coe(2)-coe(1)*mean(data(:,2))+mean(data(:,1));
edge_vfit=al*bv_yhr(:,1)+b1;
edge=[edge_vfit, bv_yhr(:,1)];
% invert coordiantes (y-->x) (x-->y)
a=1/al;b=-b1/al;
%%
% plot(edge_vfit, bv_yhr(:,1))
%%
end
end

```

Digital Image correlation

```

%%
% Author: giucos
% Description: Calculate displacement field from pictures of deformed state
%              and a picture of original state. Possibility to divide the
%              pictures in subsets of smaller dimensions
%
%
%
%%
%
clc
close all
clear all
%% Select folder with pictures
folder_name = uigetdir;
cd(folder_name)
allFiles = dir( [folder_name '\*.bmp'] );
allNames = { allFiles.name };

%% Define subsets grid
prompt = {'Subset size(odd number):','Search window size (odd number):','Columns
number:', 'Rows number:'};
dlg_title = 'Patch grid inputs';
dim_dlg= repmat([1 length(dlg_title)+40],4,1);
defaultans = {'61','91','1','1'};
answer = inputdlg(prompt,dlg_title,dim_dlg ,defaultans);

ss=str2double(answer{1});           %size of the feature to correlate
ws=str2double(answer{2});           %size of the window to sweep
col_num=str2double(answer{3});      %number of columns of the grid
row_num=str2double(answer{4});

%%
chrono=tic; % Start measuring time

n= length (allNames); %n of picture to correlate
%reference picture = picture at time 0
f=imread(char(allNames(1)));
f=double(f);
f=sqrt((f(:, :, 1).^2+f(:, :, 2).^2+f(:, :, 3).^2)/3);
f=f(1:470,1:630); %reduced image to remove edge
%
pic_time=[0 0 0];
pic_time1=zeros(1,n);
out=zeros(col_num*row_num,14,n);
d=[0 0];
r=0;
A = cell(n,1); %element with all the pictures
for i=1:n
filename=char(allNames(i));
g=imread(filename);
g=double(g); %convert number format
g=sqrt((g(:, :, 1).^2+g(:, :, 2).^2+g(:, :, 3).^2)/3); %sum of intensity of 3 colour
channels
g=g(1:470,1:630); %not all picture because there are borders
%defining the time instant of the picture
FileInfo = dir(filename);
[Y, M, D, H, MN, S] = datevec(FileInfo.datenum);
pic_time = [H MN S];
pic_time1(1,i)=pic_time(1,1)/24+pic_time(1,2)/1440+pic_time(1,3)/86400; %time of
picture in days
%
[output,Time] =ImageCorrelationFun(ss, ws, col_num, row_num, g, f,chrono);
%2D correlation matrix
out(:, :, i)=output;
% d(i, :)= [out(2,3) out(2,4)];
A{i}=g;
end
totaltime=toc(chrono);

%%
time_poly(:, :)=out(:, 14, :);

```

```

time_gauss(:, :)=out(:,13,:);
time_corr(:, :)=out(:,12,:);
time_all=[time_corr time_gauss time_poly];%time to perform the calculation
dx_gauss=[out(:,1,1) out(:,2,1) zeros(length (out(:,1,1)),length
(out(1,1,:)))];%displacement in  $\mu\text{m}$ 
dy_gauss=[out(:,1,1) out(:,2,1) zeros(length (out(:,1,1)),length (out(1,1,:)))];
dx_poly=[out(:,1,1) out(:,2,1) zeros(length (out(:,1,1)),length (out(1,1,:)))];
dy_poly=[out(:,1,1) out(:,2,1) zeros(length (out(:,1,1)),length (out(1,1,:)))];
for k=1:length (out(1,1,:))
dx_gauss(:,k+2)=out(:,5,k)/0.2472;%0.2472 =magnification
dy_gauss(:,k+2)=out(:,6,k)/0.2472;
dx_poly(:,k+2)=out(:,7,k)/0.2472;
dy_poly(:,k+2)=out(:,8,k)/0.2472;
end
%% --- Plots ---
figure;imagesc(A{1});colormap(gray);hold on
for i= 1:n
disp_x(:,i)=[out(:,5,i)];
disp_y(:,i)=[out(:,6,i)];
quiver(out(:,1,i),out(:,2,i),out(:,5,i)*10,out(:,6,i)*10,'AutoScale',
'off','LineWidth',2,'Color',[1/i^0.5 1-1/i^0.5 1-1/i^0.7]);
end
hold off
%%
sub_center=[out(:,1,1) out(:,2,1)];

```

```

%%
% Author: giucos
% Description: the script perform 2d correlation of two picture using
%              smaller searching windows (faster correlation) and perform
%              a subpixel estimation of the displacemtn using gaussian
%              and polynomial fit on the correlation result
%
% Inputs:      ss = size of the feature to correlate (subset)
%              ws = size of the window to sweep
%              col_num = number of columns of the grid
%              row_num = number of row of the grid
%              f = "initial state" reference image
%              g = "deformed state" image
% Outputs:     center_x = x coordinate of center of correlation patches
%              center_y = y coordinate of center of correlation patches
%              disp_x   = x displacements from correlation
%              disp_y   = y displacements from correlation
%              disp_x_g = x displacements after gaussian fitting of correlation
%              disp_y_g = y displacements after gaussian fitting of correlation
%              disp_x_p = x displacements after polynomial fitting of correlation
%              disp_y_p = y displacements after polynomial fitting of correlation
%              max_0    = maximum values of correlation
%              max_m    = maximum values of gaussian fitting function
%              max_p    = maximum values of polynomial fitting function
%              Time     = time elapsed
%%
function [output,Time]=ImageCorrelationFun(ss, ws, col_num, row_num, g, f, chrono)
%% --- Initialization for cycle ---
time0=toc(chrono);
%%
[m n]=size(g);
center_x = zeros(row_num,col_num); %position of center of correlation patch
center_y = zeros(row_num,col_num);
disp_x   = zeros(row_num,col_num); %displacement from correlation
disp_y   = zeros(row_num,col_num);
disp_x_g = zeros(row_num,col_num); %displacement with gaussian fit
disp_y_g = zeros(row_num,col_num);
disp_x_p = zeros(row_num,col_num); %displacement with polynomial fit
disp_y_p = zeros(row_num,col_num);
max_0    = zeros(row_num,col_num); % maximum values of pathc correlations
max_m    = zeros(row_num,col_num);
max_p    = zeros(row_num,col_num);
time_corr= zeros(row_num,col_num);
time_g   = zeros(row_num,col_num);
time_p   = zeros(row_num,col_num);

if row_num~=1
pitchx=floor((n-(ws))/(col_num-1));
end
if col_num~=1
pitchy=floor((m-(ws))/(row_num-1));
end
%% --- For cycle (correlation) ---
for i=1:row_num
for j=1:col_num
%% Correlation
%center of correlated area
if row_num==1
cx= floor(n/2);
else
cx=floor(ws+1)/2+pitchx*(j-1);
end
if col_num==1
cy=floor(m/2);
else
cy=floor(ws+1)/2+pitchy*(i-1);
end
center_x(i,j)=cx;
center_y(i,j)=cy;
%

```

```

g1=g(cy-(ss-1)/2:cy+(ss-1)/2,cx-(ss-1)/2:cx+(ss-1)/2); %correlation subset
f1=f(cy-(ws-1)/2:cy+(ws-1)/2,cx-(ws-1)/2:cx+(ws-1)/2); %correlation searching
window

time=toc(chrono);
r_norm=normxcorr2(g1,f1); %2d normalized correlation
time_corr(i,j)=toc(chrono)-time;
% figure;surf(r_norm,'EdgeColor','none'); shading interp
[M1,I1] = max(r_norm(:)); %identification of maximum in the
corr. matrix
[I_row, I_col] = ind2sub(size(r_norm),I1); %index of maximum point
%time_corr(i,j)=toc;
s1=size(r_norm);
disp_x(i,j)=(s1(2)+1)/2-I_col;
disp_y(i,j)=(s1(1)+1)/2-I_row;
% if M1>0.5 %Threshold. If maximumvalue is small the correlation is
inefficient (not real overlapping)

%% subpixel maximum search correlation function fitting method
time=toc(chrono);
[Mg,X_max_g,Y_max_g]=mainD2GaussFitRot1(r_norm,I_row,I_col); %Gaussian fit
% Mg=0; X_max_g=0; Y_max_g=0; %Uncomment to remove gaussian fit
time_g(i,j)=toc(chrono)-time;
% plot
figure;
surf(Xhr,Yhr,Zgauss,'EdgeColor','none');
colormap parula;
axis('tight')
% axis([-2.3 2.3 -2.3 2.3])
hold on

scatter3(reshape(X,[25,1]),reshape(Y,[25,1]),reshape(Z,[25,1]),100,'k','filled');
mesh(X,Y,Z,'EdgeColor','k','facecolor','none')
xlabel('x','FontSize',20,'FontName','Times New Roman')
ylabel('y','FontSize',20,'FontName','Times New Roman')
zlabel('Correlation function','FontSize',20,'FontName','Times New Roman')

set(gca,'FontSize',20,'FontName','Times New Roman');
hold off
axes1 = axes('Parent',figure1);
view(axes1,[-37.5 30]);
box(axes1,'on');
grid(axes1,'on');
hold(axes1,'all');
box on
ax=gca;
ax.BoxStyle = 'back';
%

time=toc(chrono);
[Mp,X_max_p,Y_max_p]=mainD2PolyFit(r_norm,I_row,I_col); %Second order polynomial
fit
% Mp=0; X_max_p=0; Y_max_p=0;%Uncomment to remove polynomial fit
time_p(i,j)=toc(chrono)-time;
%
%%

center_x(i,j)=cx;
center_y(i,j)=cy;

disp_x(i,j)=(s1(2)+1)/2-I_col;
disp_y(i,j)=(s1(1)+1)/2-I_row;
disp_x_g(i,j)=(s1(2)+1)/2-I_col-X_max_g;
disp_y_g(i,j)=(s1(1)+1)/2-I_row-Y_max_g;
disp_x_p(i,j)=(s1(2)+1)/2-I_col-X_max_p;
disp_y_p(i,j)=(s1(1)+1)/2-I_row-Y_max_p;

max_0(i,j)=M1;
max_m(i,j)=Mg;

```

```

max_p(i,j)=Mp;

% else
% end

end
end

%% --- Outputs ---
center_x = reshape(center_x , row_num*col_num,1);
center_y = reshape(center_y , row_num*col_num,1);

disp_x   = reshape(disp_x   , row_num*col_num,1);
disp_y   = reshape(disp_y   , row_num*col_num,1);
disp_x_g = reshape(disp_x_g , row_num*col_num,1);
disp_y_g = reshape(disp_y_g , row_num*col_num,1);
disp_x_p = reshape(disp_x_p , row_num*col_num,1);
disp_y_p = reshape(disp_y_p , row_num*col_num,1);

max_0    = reshape(max_0    , row_num*col_num,1);
max_m    = reshape(max_m    , row_num*col_num,1);
max_p    = reshape(max_p    , row_num*col_num,1);

time_corr= reshape(time_corr , row_num*col_num,1);
time_g   = reshape(time_g   , row_num*col_num,1);
time_p   = reshape(time_p   , row_num*col_num,1);

%output dimensions n.subsets x 14
output=[center_x center_y disp_x disp_y disp_x_g disp_y_g disp_x_p disp_y_p...
max_0 max_m max_p time_corr time_g time_p];
% TF = output(:,3)==0;
% output(TF,:) = [] ;

Time = toc(chrono)-time0;

```

```

%% Fit a 2D gaussian function to data
%%
%
function [Mg1,X_max,Y_max]=mainD2GaussFitRot1(r_norm,I_row,I_col)
%%
FitSize=5; %Size of matrix to fit. Even number
if and(I_row>(FitSize-1)/2,and(I_row<(length(r_norm(:,1))-(FitSize-1)/2),...
and(I_col>(FitSize-1)/2,(I_col<(length(r_norm(1,:))-(FitSize-1)/2))))

Z=r_norm(I_row-(FitSize-1)/2:I_row+(FitSize-1)/2,I_col-(FitSize-
1)/2:I_col+(FitSize-1)/2);
[X,Y] = meshgrid(-(FitSize-1)/2:1:(FitSize-1)/2);

MdataSize = length(Z(:,1));
x0 = [1,0,50,0,50,0]; %Initial guess parameters[Amplitude, x0, sigmax, y0, sigmay,
angle(in rad)]
xdata = zeros(size(X,1),size(Y,2),2);
xdata(:, :,1) = X;
xdata(:, :,2) = Y;

%% --- Fit-----
lb = [0,-MdataSize/2,0,-MdataSize/2,0,-pi/4];
ub =
[realmax('double'),MdataSize/2,(MdataSize/2)^2,MdataSize/2,(MdataSize/2)^2,pi/4];
[x,~,~,exitflag] = lsqcurvefit(@D2GaussFunctionRot,x0,xdata,Z,lb,ub);

[Xhr,Yhr] = meshgrid(-MdataSize/2:0.05:MdataSize/2); % generate high res grid for
plot
sizehr=size(Xhr);
xdatahr = zeros(sizehr(1),sizehr(2),2);
xdatahr(:, :,1) = Xhr;
xdatahr(:, :,2) = Yhr;
Zgauss=D2GaussFunctionRot(x,xdatahr);
[Mg1,Img1] = max(Zgauss(:));
X_max=Xhr(Img1);Y_max=Yhr(Img1);
else
Mg1=0;X_max=0;Y_max=0; end

```

```

% Fit a 2D polynomial function to data

%%
function [Mpl,X_max,Y_max]=mainD2PolyFit(r_norm,I_row,I_col)
%% -----User Input-----
FitSize=5; %Size of matrix to fit. Even number
if and(I_row>(FitSize-1)/2,and(I_row<(length(r_norm(:,1))-(FitSize-1)/2),...
and(I_col>(FitSize-1)/2,(I_col<(length(r_norm(1,:))-(FitSize-1)/2))))
%definition of three matrix of coordinates to fit
Z=r_norm(I_row-(FitSize-1)/2:I_row+(FitSize-1)/2,I_col-(FitSize-
1)/2:I_col+(FitSize-1)/2);
[X,Y] = meshgrid(-(FitSize-1)/2:1:(FitSize-1)/2);
%
MdataSize = length(Z(:,1));
x0 = [1,1,0,1,0,1,0]; %Initial guess parametersx [a0, ax1, ax2, ay1, ay2, axy, fi]
xdata = zeros(size(X,1),size(Y,2),2);
xdata(:,1) = X;
xdata(:,2) = Y;

%% --- Fit-----
lb = [-inf,-inf,-inf,-inf,-inf,-inf,-pi/4];
ub = [ inf,inf,inf,inf,inf,inf,pi/4];
[x,~,~,exitflag] = lsqcurvefit(@D2PolynomialFunctionRot,x0,xdata,Z,lb,ub);

% [xData, yData, zData] = prepareSurfaceData(X,Y,Zm);
% [fitresult, gof] = fit([xData, yData],zData,'poly22');
% c_val=(coeffvalues(fitresult))';

[Xhr,Yhr] = meshgrid(-MdataSize/2:0.05:MdataSize/2); % generate high res grid for
plot
sizehr=size(Xhr);
xdatahr = zeros(sizehr(1),sizehr(2),2);
xdatahr(:,1) = Xhr;
xdatahr(:,2) = Yhr;
Zpoly=D2PolynomialFunctionRot(x,xdatahr);
[Mpl,Impl] = max(Zpoly(:));
X_max=Xhr(Impl);Y_max=Yhr(Impl);
[Min_g1,Imin_g1] = min(Zpoly(:));
else
Mpl=0;X_max=0;Y_max=0;
end

```


Appendix B: Instruments

Omega 5SRTC-TT-KI-40

Thermocouples

- ✓ Available from Stock in Convenient 5-Packs
- ✓ Calibration Available
- ✓ PFA Insulated Wire has Max Service Temp of 260°C
- ✓ Glass Braid Insulated Wire has Max Service Temp of 480°C
- ✓ Kapton® Insulated Wire has Max Service Temp of 316°C
- ✓ Available in 1 and 2 m Lengths
- ✓ Max Service Temp for Connector Body 220°C

Miniature Size

To Order (Specify Model Number)

Model Number IEC Colour Code	AWG Gauge	Diameter mm	Insulation
5SRTC-GG-(*)I-20-(**)	20	0.81	Glass Braid
5SRTC-GG-(*)I-24-(**)	24	0.51	Glass Braid
5SRTC-GG-(*)I-30-(**)	30	0.25	Glass Braid
5SRTC-TT-(*)I-20-(**)	20	0.81	PFA
5SRTC-TT-(*)I-24-(**)	24	0.51	PFA
5SRTC-TT-(*)I-30-(**)	30	0.25	PFA
5SRTC-TT-(*)I-36-(**)	36	0.13	PFA
5SRTC-TT-(*)I-40-(**)	40	0.076	PFA
5SRTC-KK-(*)I-20-(**)	20	0.81	Kapton®
5SRTC-KK-(*)I-24-(**)	24	0.51	Kapton®
5SRTC-KK-(*)I-30-(**)	30	0.25	Kapton®

* Insert calibration J, K, T, or E.



** Specify length, insert "1M" for 1 m or "2M" for 2 m length.

Note: Add cost per additional metre per pack of 5 on GG or TT wire. On KK wire add cost per additional metre per pack.

Ordering Example: 5SRTC-TT-KI-36-2M, 5-pack of Type K thermocouples with 2 m of 0.13 mm Dia. PFA insulated wire and a moulded mini connector with snap-on strain relief.

DeMeet 220

Multisensor CMM

	Video model	Combo model
General		
Video system	DeMeet Sony sensor camera	
Leica-Design telecentric lenses	2.0x (1.0x, 5.0x and 10.0x optional)	
Nikon telecentric lenses	3.0x (1.0x, 5.0x and 10.0x optional)	
Ring light ¹	3 rings, 16 segments and 48 cells (adjustable)	
Backlight and coaxial light	adjustable	
Probe system ²	-	Renishaw TP20
Construction ³	fixed bridge with granite base plate DIN 876/00	
Structure	extremely tension relieved, flat grinded cast iron	
Measuring table ⁴	tension relieved, hard anodized aluminum	
Linear guides	THK linear guides	
Linear encoders	Renishaw TONIC linear encoders	
Drive system	Faulhaber DC servo motors	
Operating mode	motorized joystick / CNC	
Measuring specifications		
Resolution (μm)	0.5 (0.1 optional)	
Accuracy standard ⁵ (μm)	X/Y/Z 4 + L/150	
(0.5 μm resolution) (L in mm)	XY 5 + L/150	XYZ 5 + L/150
Accuracy optional ⁵ (μm)	X/Y/Z 3 + L/200	
(0.1 μm resolution) (L in mm)	XY 4 + L/200	XYZ 4 + L/200
Travel speed max. (mm/s)	X/Y 250, Z 55	
Acceleration max. (mm/s ²)	X/Y/Z 500	
Power requirements		
Voltage (V)	90 - 120, 210 - 240 (50 - 60 Hz)	
Power (VA)	400	
Environmental conditions		
Operating temperature (°C)	15 - 35	
Measuring temperature (°C)	20 ± 0.5	
Humidity (%)	40 - 70 (no condensation)	
¹ For video models (except DeMeet-220) a ring light with 4 rings, 16 segments and 64 cells can be supplied as an option. ² Other probe systems can be supplied as an option. ³ The base plate of the DeMeet-220 is made of flat grinded cast iron. ⁴ Optional available in tension relieved nickel-plated steel. ⁵ The accuracy of the multi-sensor measuring system should be taken into account.		
Specifications apply to all DeMeet models, unless otherwise specified. Machines with higher specifications and/or modifications are available on request. Specifications are subject to change without prior notice. For more specifications refer to our website Schut.com .		
 	Measuring range (mm)	X 220, Y 150, Z 100
	Dimensions (mm)	W 520, L 700, H 615
	Weight (kg)	110
	Measuring table (mm)	X 357, Y 260
	Max. load (kg)	20

CE The DeMeet measuring machines are in compliance with EC Machine Directive 2006/42/EC, Electromagnetic Compatibility (EMC) directive 2014/30/EU and Low Voltage Directive (LVD) 2014/35/EU.

All trademarks, trade names, brand names, or logos mentioned or used are the property of their respective owners.

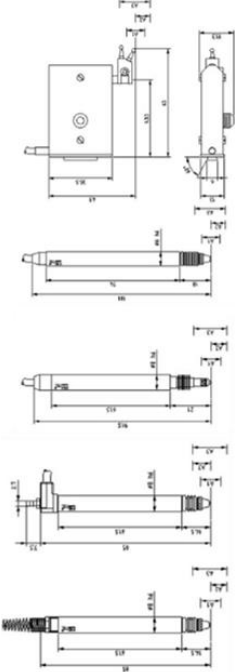
Pretec 2922N

Inductive probes

Technical specification									
Order Number	Measuring travel A1	Working Travel A2	Overall travel A3	Linearity typical	Hysteresis Error	Measuring force zero point	Protection	Cable	Application
2921	±0.8 mm	0.8 – 1.1 mm	3 mm	±0.3 %	< 0.02 µm	0.6-1.0 N	IP66	2 m - Axial	Splash waterproof
2922	±1 mm	1.1 – 1.3 mm variable	3 mm	±0.3 %	< 0.02 µm	0.45-0.75 N	IP64	2 m - Radial	Vacuum lift
2924	±1 mm	1.1 – 1.3 mm	3 mm	±0.3 %	< 0.02 µm	0.45-0.75 N	IP65	2 m - Axial	Splash waterproof
2940	±2 mm	1.1 – 1.3 mm variable	4.2 mm	±0.3 %	< 0.02 µm	0.45-0.75 N	IP64	2 m - Axial and radial	Universal
2970	±3 mm	3.5 mm	7 mm	±2 %	< 0.5 µm	0.8-1.2 N	IP64	2 m - Axial	Large measuring range
2952	±1 mm	1.05 – 1.1 mm	2 mm	±0.3 %	< 0.02 µm	0.0-0.25 N	IP64	2m - Axial	Low measuring force

Electrical/Environment					Materials				
Nominal sensitivity	Zero drift	Operating temperature	Maximum relative humidity	Housing	Contact point	Sensing technique	Male cable connector	Cable	
73.5 mV/mm	0.15 µm/°C	-15-45 °C	80%	Stainless steel cable braided stainless steel	M1.5 Cable length	Metric (DIN optional)	DIN 4332 without pin 6	2 m (available in longer cable in PUR as option)	

*14 to 20 m cable length will affect the output electrical signal by a minimum of 2% loss



2940/29242922292129702952

Compatibility

PRETEC probes integrate 2 sensitivities: PRETEC or TESA/others manufacturers! This is a standard feature on all our probes. Free yourselves from one brand!

Force setup

Inside spring replacement to change the measuring force to adapt to your application need is possible. This is an optional feature.

Travel setup

The travels set up is adjusted from the exit cable side! This is our insurance that you can perform the adjustments in any situation!

Cable exit

Our probes 2940/2924 allow axial or radial cable exit and avoid the hassles of ordering and stocking two types of probes. With a simple clip!

Cable length

Cable length is up to your application need. Our standard length is 2 m, but supply of up to 20 m in PUR is possible. This is an optional feature.

Accessories

Our accessories program range is substantial. Tailor-made accessories are as well available. Just call us!

Customisation

Let us talk if you need customized electronic measuring probes.

Our electronic measuring probes features

- Compatible with other manufacturers (TESA, etc.)
- Ø 8/6 mm probe stainless steel carbide-chromed housing
- Axial or radial cable exit
- Measuring bolt guided on ball bearing (except 2952)

- Special roller bearing locks the probe head against torsion
- Mechanical or vacuum retraction
- Pre/Post-travel setup from the back of the probe
- Wide range of accessories available

Omega SA1-RTD-4W-120-SB

RTD

SA1-RTD

Class A accuracy of $\pm 0.06^\circ\text{C}$ at 0°C . Thin film element is $2 \times 2 \times 0.8 \text{ mm}$ in a $25 \times 19 \text{ mm}$ self-adhesive carrier.

Extra Accuracy for Critical Measurements!

1 m (40"), 26 AWG stranded nickel-plated copper, PFA-insulated and jacketed cable.

SA1-RTD shown actual size.

Quick Delivery on Custom Lead Wire Lengths

- ✓ 100 Ω DIN Class A ($\pm 0.06^\circ\text{C}$ or $\pm 0.15^\circ\text{C}$ at 0°C) Accuracy Standard
- ✓ Easy-Installation Silicone-Based, Self-Adhesive Backing Rated to 260°C (500°F)
- ✓ Sensor Can be Reapplied
- ✓ 290°C (554°F) Short-Term Operation When Used as a "Cement-On" (OMEGABOND® Air Set Cements)
- ✓ Stripped 3- or 4-Wire Leads Standard (Connectors Optional)
- ✓ Stocked in 1 m (40") Lengths; Also Available in 2 and 3 m (80 and 120") and Custom Length Lead Wires
- ✓ Other Resistances/Accuracies Available on Request

The SA1-RTD surface-mount RTD temperature sensor mounts on flat or curved surfaces and provides Class A accuracy for critical temperature monitoring applications. Based on a $2 \times 2 \times 0.8 \text{ mm}$ thin-film platinum RTD and supplied in PFA-insulated 3- or 4-wire configurations (connectors optional), it can be customized for use in a wide variety of applications. The sensor can be easily applied using its self-adhesive backing, or permanently mounted using OMEGABOND® cements.

Use the SA1-RTD to monitor chip, heat sink, and environmental temperatures in electronic devices; check piping or ducting temperatures; monitor motor and transformer core

heat; test insulation capabilities; and check other applications in which surface and/or gradient temperatures need to be monitored or controlled.

Specifications
Minimum/Maximum Temperature: -73°C to 260°C (-100°F to 500°F) continuous, 290°C (554°F) short-term (when cemented in place)
Sensing Element: 100 Ω at 0°C (32°F), temp coefficient of $0.00385 \Omega/\Omega/^\circ\text{C}$ (IEC60751)
Accuracy: $\pm 0.06^\circ\text{C}$ at 0°C (DIN Class A)
Stability: Less than 0.2°C drift/year
Response Time: Less than 0.9 s (63% response time in water immersion), less than 2 s response time on a hot plate
Self-Heating Effect: 2.5 mW/ $^\circ\text{C}$
Lead Wire: 1 m (40"), 26 AWG stranded nickel-plated copper, PFA-insulated and jacketed cable

Available with Stainless Steel Overbraid!

For applications where electrical noise is prevalent, or where the sensor lead wires may be routed around sharp objects, consider the stainless steel overbraid option. To specify this option, add "-SB" to the end of the model number for an additional cost per meter (foot). Ordering example: SA1-RTD-80-SB.

To Order Visit omega.com/sa1-rtd for Pricing and Details

Model Number	Style	Length: m (inch)	Cold End Termination
SA1-RTD	3-wire	1 (40)	Stripped leads, 1/2" (1" insulated, singles 1/2" bare), 3 wires
SA1-RTD-80	3-wire	2 (80)	
SA1-RTD-120	3-wire	3 (120)	
SA1-RTD-MTP	3-wire	1 (40)	"MTP" style miniature flat 3-pin connector
SA1-RTD-80-MTP	3-wire	2 (80)	
SA1-RTD-120-MTP	3-wire	3 (120)	
SA1-RTD-4W	4-wire	1 (40)	Stripped leads, 1/2" (1" insulated, singles 1/2" bare), 4 wires
SA1-RTD-4W-80	4-wire	2 (80)	
SA1-RTD-4W-120	4-wire	3 (120)	
SA1-RTD-4W-TA4F	4-wire	1 (40)	TA4F connector; pins 1 and 2, common 3 and 4 common
SA1-RTD-4W-80-TA4F	4-wire	2 (80)	
SA1-RTD-4W-120-TA4F	4-wire	3 (120)	

Ordering Examples: SA1-RTD-80-MTP, Class A, surface-mount RTD sensor, 3-wire leads, 2 m (80") lead-wire length with a miniature 3-pin MTP connector. SA1-RTD-4W-80-TA4F, Class A, surface-mount RTD sensor, 4 wire leads, 2 m (80") lead-wire length with a 4-pin audio-style connector. For special lengths, add additional cost. For the "-SB" option, add additional cost.

Tesa GT 22-HP

Inductive probe



TESA probe with axial cable outlet, with the lowest linearity related max. permissible errors of the range.

DESCRIPTION

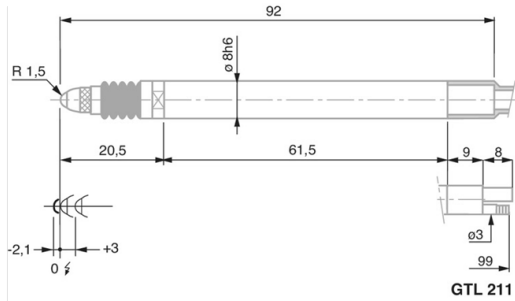
TESA Axial Probes Standard Probes Universal probes for common but constraining applications. • 8 mm diameter probe housing. Can be clamped over its entire length. • Measuring bolt mounted on a ball bearing. • Both the probe housing and ball-bearing guide are separate from one another, so that the measuring bolt moves easily even if the probe is not clamped appropriately. • Degree of protection IP65 according to IEC 60529. • Wide range of accessories including measuring inserts, spring sets, etc. • LVDT probes compatible with measuring equipment from other makers available on request.

SPECIFICATIONS

Standard	DIN 32876
Coefficient of linear expansion	0,15 µm/°C
Material	- Corps de fixation nickelé. - Tige de mesure en acier inoxydable. - Soufflet de protection en Nitrile (élastomère résistant) - Touche avec bille Ø3 mm en métal dur.
Degree of protection	IP64 (CEI 60529)
Weights	Mobile weight: 6g
Power supply	13 kHz (± 5%)
Included in delivery	- Measuring report - Declaration of conformity

References	Designation	Measuring range, mm	Max. errors, µm*	Repeatability, µm	Hysteresis, µm	Nominal measuring force, N
03230036	GT 21 HP	± 0,2	07 + 0,4 · L	0,01	0,01	0,63
03230021	GT 22 HP	± 0,2	07 + 0,4 · L	0,01	0,01	0,63

* Linearity error (L in mm)



MicroEpsilon TIM 160

Thermal camera

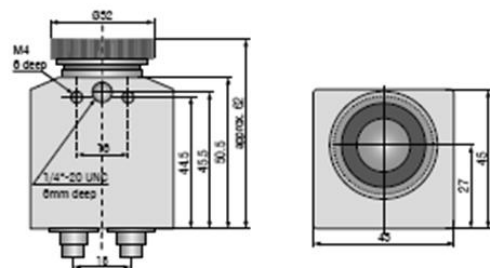
thermoIMAGER TIM 160

Miniaturized thermal imaging camera with USB interface

- Measuring range from -20°C to 900°C (special edition up to 1500°C)
- Excellent thermal sensitivity (NETD) of 0.08K
- Exchangeable lenses 6°/23°/48°FOV or 72°FOV
- Real-time thermography with 120Hz frame rate via USB 2.0 interface
- Power supply and data transfer via USB interface
- Extremely lightweight (195g) and robust (IP67)
- Extremely compact dimensions 45x45x62mm
- Analog input and output, trigger interface
- Software Developer Kit and LabVIEW examples included

Software

- Display of the thermal image in real time (120Hz) with recording function (video, snapshot)
- Complete set up of parameters and remote control of the camera
- Detailed analysis of fast, thermodynamic processes
- Output of analog temperature or alarm values via the process interface
- Digital communication via RS232 or DLL for software integration



Model	TIM 160
Optical resolution	160 x 120 pixels
Temperature ranges	-20°C to 100°C / 0°C to 250°C / 150°C to 900°C additional range: 200°C to 1500°C (option)
Spectral range	7.5 to 13µm
Frame rate	120Hz
System accuracy	±2°C or ±2%, whichever is greater
Resolution (Display)	0.1 °C
Lenses	72° / f = 3.3mm (min. distance 20mm); 48° / f = 5.7mm (min. distance 20mm); 23° / f = 10mm (min. distance 20mm); 6° / f = 35.5mm (min. distance 500mm)
Emissivity	0.10 to 1.00 adjustable
Thermal sensitivity (NETD)	0.1K with 48° FOV and 72° FOV ¹⁾ / 0.08K with 23° FOV ¹⁾ / 0.3K with 6° FOV ²⁾
Detector	Focal Plane Array (FPA) - uncooled micro bolometer 25x25µm ²
Measurement mode	Flexible spot with crosshair marking, measuring field with automatic display of maximum-, minimum- or average value
Color palettes	Iron, rainbow, black-white, black-white inverted etc.
Operation and set up (via menu)	Measurement modes fully automatic or manual, color palettes, emissivity, file management, date/time, °C/°F, language
Outputs/digital	USB 2.0 / optional GigE
Process interface (electrically isolated)	0-10V output, 0-10V input
Digital communication	via RS232 of PC / DLL interface used
Cable length	1m (standard), 5m, 10 m, 20m
Power supply	USB powered
Tripod mount	1/4-20 UNC
Protection class	IP67
Ambient temperature range	0°C to 50°C (up to 315°C with cooling jacket)
Storage temperature	-40°C to 70°C
Relative humidity	20 to 80%, non-condensing
Vibration	IEC 60068-2-6 (sinus-shaped) / IEC 60068-2-64 (broadband noise)
Shock	IEC 60068-2-27 (25g and 50g)
Weight	195g, incl. lens

PC requirements: minimum 1.5GHz, 1GB RAM, Windows XP SP 2 or Windows 7

¹⁾ Please note: measurement accuracy can be out of specification with distances below 200mm

²⁾ Please note: measurement accuracy can be out of specification with distances below 500mm

4

Miniaturized thermal imaging camera with USB interface

thermoIMAGER TIM 160

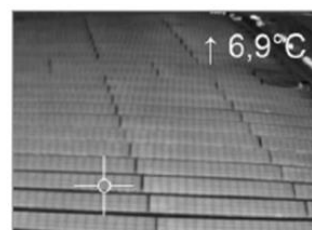
**thermoIMAGER TIM 160**

Miniaturized thermal imaging camera with USB interface

- Measuring range from -20°C to 900°C (special edition up to 1500°C)
- Excellent thermal sensitivity (NEDT) of 0.08K
- Exchangeable lenses 6°/23°/48°FOV or 72°FOV
- Real-time thermography with 120Hz frame rate via USB 2.0 interface
- Power supply and data transfer via USB interface
- Extremely lightweight (195g) and robust (IP67)
- Extremely compact dimensions 45x45x62mm
- Analog input and output, trigger interface
- Software Developer Kit and LabVIEW examples included

Software

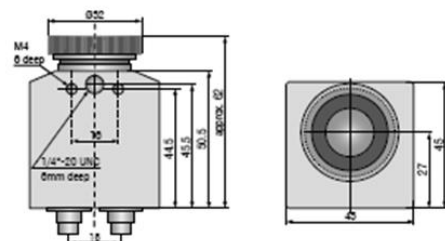
- Display of the thermal image in real time (120Hz) with recording function (video, snapshot)
- Complete set up of parameters and remote control of the camera
- Detailed analysis of fast, thermodynamic processes
- Output of analog temperature or alarm values via the process interface
- Digital communication via RS232 or DLL for software integration



Surface measurements in industrial applications



Suitable lenses for every measurement distance





5

Model	TIM 160
Optical resolution	160 x 120 pixels
Temperature ranges	-20°C to 100°C / 0°C to 250°C / 150°C to 900°C additional range: 200°C to 1500°C (option)
Spectral range	7.5 to 13µm
Frame rate	120Hz
System accuracy	±2°C or ±2%, whichever is greater
Resolution (Display)	0.1 °C
Lenses	72° / f = 3.3mm (min. distance 20mm); 48° / f = 5.7mm (min. distance 20mm); 23° / f = 10mm (min. distance 20mm); 6° / f = 35.5mm (min. distance 500mm)
Emissivity	0.10 to 1.00 adjustable
Thermal sensitivity (NETD)	0.1K with 48° FOV and 72° FOV ¹⁾ / 0.08K with 23° FOV ¹⁾ / 0.3K with 6° FOV ²⁾
Detector	Focal Plane Array (FPA) - uncooled micro bolometer 25x25µm ²
Measurement mode	Flexible spot with crosshair marking, measuring field with automatic display of maximum-, minimum- or average value
Color palettes	Iron, rainbow, black-white, black-white inverted etc.
Operation and set up (via menu)	Measurement modes fully automatic or manual, color palettes, emissivity, file management, date/time, °C/°F, language
Outputs/digital	USB 2.0 / optional GigE
Process interface (electrically isolated)	0-10V output, 0-10V input
Digital communication	via RS232 of PC / DLL interface used
Cable length	1m (standard), 5m, 10 m, 20m
Power supply	USB powered
Tripod mount	1/4-20 UNC
Protection class	IP67
Ambient temperature range	0°C to 50°C (up to 315°C with cooling jacket)
Storage temperature	-40°C to 70°C
Relative humidity	20 to 80%, non-condensing
Vibration	IEC 60068-2-6 (sinus-shaped) / IEC 60068-2-64 (broadband noise)
Shock	IEC 60068-2-27 (25g and 50g)
Weight	195g, incl. lens

PC requirements: minimum 1.5GHz, 1GB RAM, Windows XP SP 2 or Windows 7

¹⁾ Please note: measurement accuracy can be out of specification with distances below 200mm

²⁾ Please note: measurement accuracy can be out of specification with distances below 500mm

Scope of supply

TIM 160

- * TIM process camera
- incl. a selectable lens
- * Instruction Manual
- * USB cable 1m
- * Software for real-time processing and analyzing thermal images
- * Tripod mount
- * PIF cable 1m
- * Aluminum case

TIM 160/DK

- * TIM process camera
- incl. three lenses 6°, 23°, 48°
- * Certificate of calibration, adjusted to the included lenses
- * Tripod mount 200 to 1000mm
- * Aluminum case
- * Instruction Manual
- * USB cable 1m and 10m
- * Software for real-time processing and analyzing thermal images
- * PIF cable 1m

DTU Mechanical Engineering
Section of Manufacturing Engineering
Technical University of Denmark

Produktionstorvet, Bld. 427A
DK-2800 Kgs. Lyngby
Denmark
Phone (+45) 4525 4763
Fax (+45) 4593 0190
www.mek.dtu.dk
ISBN: 978-87-7475-539-5